Study of neutron induced reaction cross sections on Fe isotopes at the GELINA facility relevant to reactor applications

Georgios Gkatis

NNT : .....

THÈSE DE DOCTORAT

Soutenue à Aix-Marseille Université dans le cadre d'une cotutelle avec l'université "National Technical University of Athens" le 10 septembre 2024 par

Georgios Gkatis

Study of neutron induced reaction cross sections on Fe isotopes at the GELINA facility relevant to reactor applications

Discipline
Physique et Sciences de la Matière

Spécialité
Energie, Rayonnement et Plasma

École doctorale
ED-352 Physique et Sciences de la Matière

Laboratoire/Partenaires de recherche
CEA Cadarache
CEA/DES/IRESNE/DER/SPRC/LEPh

Composition du jury

Arnd JUNGHANS HZDR	Rapporteur
Maëlle KERVENO CNRS	Rapporteure
Roberto CAPOTE NOY IAEA	Examinateur
Cyrille DE SAINT JEAN CEA/DAM	Examinateur
Michail KOKKORIS NTUA	Examinateur
Jose BUSTO AMU	Président du jury
Gilles NOGUERE CEA/DES	Directeur de thèse
Maria DIAKAKI NTUA	Co-directrice de thèse
Arjan PLOMPEN EC-JRC	Invité

Affidavit

I, undersigned, Georgios Gkatis, hereby declare that the work presented in this manuscript is my own work, carried out under the scientific supervision of Dr. Gilles Noguere and Dr. Maria Diakaki, in accordance with the principles of honesty, integrity and responsibility inherent to the research mission. The research work and the writing of this manuscript have been carried out in compliance with both the French national charter for Research Integrity and the Aix-Marseille University charter on the fight against plagiarism.

This work has not been submitted previously either in this country or in another country in the same or in a similar version to any other examination body.

Place *Cadarache*,
date *10/06/2024*.

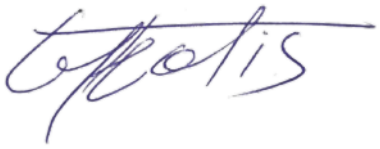

List of Publications and Participation in Conferences

List of publications produced as part of the thesis project:

- G. Gkatis, M. Diakaki, G. Noguere, A. Oprea, C. Paradela, E. Pirovano, and A. J. M. Plompen, *Double differential cross section measurements of neutron scattering on* ^{56}Fe, in preparation.
- G. Gkatis, E. Pirovano, M. Diakaki, G. Noguere, M. Nyman, A. Oprea, C. Paradela, and A. J. M. Plompen, *Angular distribution measurements of neutorn elastic scattering on natural carbon*, Physical Review C 110, 034609 (2024).
- G. Gkatis, E. Pirovano, M. Diakaki, G. Noguere, M. Nyman, A. Oprea, C. Paradela, and A. J. M. Plompen, *The ELISA spectrometer at the JRC-Geel: development, achievements and future plans*, HNPS Advances in Nuclear Physics 30, 11-18 (2024).
- G. Gkatis, M. Diakaki, G. Noguere, M. Nyman, A. Oprea, C. Paradela, E. Pirovano, and A. J. M. Plompen, *Cross section measurements of neutron elastic and inelastic scattering on* ^{54}Fe, Physical Review C 109, 034612 (2024).
- G. Gkatis, M. Diakaki, A. Mengoni, and G. Noguere, *Direct radiative capture calculations on* ^{56}Fe, EPJ Web of Conferences 294, 04002 (2024).

Participation in conferences and summer schools during the thesis period:

- NRAS 2024 - Neutron Resonance Analysis School (May 2024, Geel, Belgium)
- ARIEL (Accelerator and Research reactor Infrastructures for Education and Learning) Final Workshop (January 2024, Orsay, France) (Oral presentation)
- Nuclear data week - JEFF meeting organized by the OECD/NEA (November 2023, Paris, France) (Oral presentation)
- HNPS 2023 - 31st Annual Symposium of the Hellenic Nuclear Physics Society (September 2023, Athens, Greece) (Oral presentation)
- School on nuclear data for depletion calculations in the frame of the SANDA project (September 2023, Geel, Belgium) (Oral presentation)
- WONDER2023 - 6th International Workshop On Nuclear Data Evaluation for Reactor applications (June 2023, Aix-en-Provence, France) (Oral presentation)

- Nuclear data week - JEFF meeting organized by the OECD/NEA (November 2022, Paris, France) (Oral presentation)
- HNPS 2022 - 30th Annual Symposium of the Hellenic Nuclear Physics Society (October 2022, Ioannina, Greece) (Oral presentation)
- HISPANOS Hands-On school on the production, detection, and use of neutron beams (September 2022, Seville, Spain)
- NDRA 2022 – 4th Summer school on Neutron Detectors and Related Applications (June - July 2022, Riva del Garda, Italy)
- 2022 FLUKA.CERN Course – Beginner's introduction to the various functions and attributes of the FLUKA, a general purpose code for Monte Carlo simulation of radiation transport in complex geometries (May 2022, Brussels, Belgium)
- NuDataPath - 1st International on-line school on nuclear data: the path from the detector to the reactor calculation (February - March 2022, On-line)

Abstract

Studies of neutron induced reactions are of considerable interest, not only for their importance to fundamental research in Nuclear Physics but also for practical applications. Iron is a major structural material, used widely in nuclear technology applications, especially nuclear reactors where steel alloy components are used for building the core's structural support and as reflectors. For this reason, accurate neutron data are indispensable for the design and reliable operation of such facilities. The lack of experimental data, especially in the fast neutron energy region, has created discrepancies between the current evaluated nuclear data libraries.

New cross section measurements on Fe were carried out at the neutron time-of-flight facility GELINA. On the one hand, scattering experiments were performed to determine the differential cross section of neutron elastic and inelastic scattering on ^{54}Fe and ^{56}Fe in the fast neutron energy region (1-8 MeV), using enriched samples for both isotopes. For the detection of the scattered neutrons, the ELISA (ELastic and Inelastic Scattering Array) spectrometer was used. The array consists of 32 liquid organic scintillators for the detection of the scattered neutrons and a ^{235}U fission chamber for the measurement of the neutron flux. On the other hand, transmission experiments on ^{nat}Fe were performed at the 50 m measurement station of flight path 4. The moderated flux configuration was used providing a neutron spectrum with energies from a few eV to hundreds of keV. The neutrons were detected by a Li-glass scintillator enriched in ^{6}Li. Two natural iron metallic discs of 1.2 cm and 4.5 cm thickness were measured.

Finally, the direct radiative capture mechanism for ^{56}Fe was explored in an effort to provide a physical interpretation behind changes that were made in the capture cross section of ^{56}Fe. Specifically, two main changes were made in the evaluated cross sections. An artificial background was added in the resolved resonance region, in order to reproduce integral measurements in this energy range. The cross section above 850 keV was also increased based on experimental data provided by the Rensselaer Polytechnic Institute (RPI).

The goal of the present work is to perform new experiments and theoretical calculations to study neutron induced reaction cross sections on iron in an effort to tackle issues reported in the evaluated files by providing new experimental/theoretical data for key reactions and neutron energy regions.

Keywords: cross section, iron, elastic scattering, inelastic scattering, transmission, direct capture

Résumé

Les études des réactions induites par les neutrons sont d'un intérêt considérable, non seulement pour leur importance dans la recherche fondamentale en physique nucléaire, mais aussi pour leurs applications pratiques. Le fer est un matériau structurel majeur, largement utilisé dans les applications nucléaires, en particulier dans les réacteurs nucléaires où les composants en 'acier sont utilisés pour construire le support structurel du cœur et du réflecteur. Pour cette raison, des données précises sur les neutrons sont indispensables pour la conception et le fonctionnement fiable de ces installations. Le manque de données expérimentales, notamment dans la région des énergies des neutrons rapides, a créé des divergences entre les bibliothèques de données nucléaires évaluées actuelles.

De nouvelles mesures de sections efficaces sur le fer ont été réalisées à l'installation de temps de vol GELINA. D'une part, des expériences de diffusion ont été menées pour déterminer la section efficace différentielle de la diffusion élastique et inélastique des neutrons sur ^{54}Fe et ^{56}Fe dans la région des énergies des neutrons rapides (1-8 MeV), en utilisant des échantillons enrichis pour les deux isotopes. Pour la détection des neutrons diffusés, le spectromètre ELISA (ELastic and Inelastic Scattering Array) a été utilisé. L'ensemble se compose de 32 scintillateurs organiques liquides pour la détection des neutrons diffusés et d'une chambre à fission de ^{235}U pour la mesure du flux de neutrons. D'autre part, des expériences de transmission sur ^{nat}Fe ont été réalisées à 50 m de la source de neutron (base de vol 4). La configuration de flux modéré a été utilisée, fournissant un spectre de neutrons avec des énergies allant de quelques eV à des centaines de keV. Les neutrons ont été détectés par un scintillateur en verre au lithium enrichi en ^{6}Li. Deux disques métalliques en fer naturel de 1.2cm et 4.5cm d'épaisseur ont été mesurés.

Enfin, le mécanisme de capture radiative directe pour le ^{56}Fe a été exploré dans le but de fournir une interprétation physique des modifications apportées à la section efficace de capture de ^{56}Fe. Plus précisément, deux modifications principales ont été apportées aux sections efficaces évaluées. Un fond artificiel a été ajouté dans la région des résonances résolues, afin de reproduire les mesures intégrales dans cette gamme d'énergie. La section efficace au-dessus de 850 keV a également été augmentée sur la base des données expérimentales fournies par le Rensselaer Polytechnic Institute (RPI).

Le but de ce travail est de réaliser de nouvelles expériences et des calculs théoriques pour étudier les sections efficaces des réactions induites par neutrons sur le fer, dans le but de résoudre les problèmes signalés dans les fichiers évalués en fournissant de nouvelles données expérimentales/théoriques pour des réactions clés et des régions d'énergie specifiques.

Mots clés: section efficace, fer, diffusion élastique, diffusion inélastique, transmission, capture directe

Περίληψη

Οι μελέτες των αντιδράσεων νετρονίων παρουσιάζουν σημαντικό ενδιαφέρον, όχι μόνο για τη θεμελιώδη έρευνα στη Πυρηνική Φυσική αλλά και για πρακτικές εφαρμογές. Ο σίδηρος είναι ένα σημαντικό δομικό υλικό, που χρησιμοποιείται ευρέως σε εφαρμογές πυρηνικής τεχνολογίας, ειδικά σε πυρηνικούς αντιδραστήρες όπου τα εξαρτήματα από κράμα σιδήρου χρησιμοποιούνται για την κατασκευή της δομικής υποστήριξης του πυρήνα και ως ανακλαστήρες. Για το λόγο αυτό, ακριβή πυρηνικά δεδομένα για τις αντιδράσεις νετρονίων στο σίδηρο είναι απαραίτητα για το σχεδιασμό και την αξιόπιστη λειτουργία τέτοιων εγκαταστάσεων. Η έλλειψη πειραματικών δεδομένων, ειδικά στην ενεργειακή περιοχή των ταχέων νετρονίων, έχει δημιουργήσει διαφορές μεταξύ των πυρηνικών δεδομένων στις διάφορες αξιολογημένες βιβλιοθήκες.

Νέες μετρήσεις ενεργών διατομών αντιδράσεων νετρονίων στο Φε πραγματοποιήθηκαν στην εγκατάσταση χρόνου πτήσης GELINA. Αρχικά, πραγματοποιήθηκαν πειράματα σκέδασης για τον προσδιορισμό της διαφορικής ενεργού διατομής της ελαστικής και ανελαστικής σκέδασης νετρονίων στο ^{54}Fe και ^{56}Fe στην ενεργειακή περιοχή των ταχέων νετρονίων (1-8 MeV), χρησιμοποιώντας εμπλουτισμένα δείγματα και για τα δύο ισότοπα. Για την ανίχνευση των σκεδαζόμενων νετρονίων, χρησιμοποιήθηκε το φασματόμετρο ELISA (ELastic and Inelastic Scattering Array). Το ανιχνευτικό σύστημα αποτελείται από 32 οργανικούς υγρούς σπινθηριστές για την ανίχνευση των σκεδαζόμενων νετρονίων και έναν θάλαμο σχάσης ^{235}U για τη μέτρηση της ροής νετρονίων. Επιπλέον, πειράματα διέλευσης σε ^{nat}Fe πραγματοποιήθηκαν στο σταθμό μέτρησης των 50m της διαδρομής πτήσης 4. Τα νετρόνια ανιχνεύθηκαν από έναν σπινθηριστή γυαλιού λιθίου εμπλουτισμένο σε ^{6}Li. Μετρήθηκαν δύο δείγματα φυσικού σιδήρου 1.2cm και 4.5cm.

Τέλος, πραγματοποιήθηκαν θεωρητικοί υπολογισμοί για τη μελέτη της άμεσης σύλληψης στον ^{56}Fe σε μια προσπάθεια να παρασχεθεί φυσική ερμηνεία πίσω από τις αλλαγές που έγιναν στην ενεργό διατομή της αντίδρασης σύλληψης στο ^{56}Fe. Συγκεκριμένα, πραγματοποιήθηκαν δύο κύριες αλλαγές στα δεδομένα των αξιολογημένων βιβλιοθηκών. Προστέθηκε ένα τεχνητό υπόβαθρο στην χαμηλοενεργειακή περιοχή, ώστε να αναπαραχθούν μετρήσεις πειραμάτων integral σε αυτό το ενεργειακό εύρος. Η ενεργός διατομή πάνω από τα 850keV επίσης αυξήθηκε βάσει πειραματικών δεδομένων που παρέχονται από το εργαστήριο Rensselaer Polytechnic Institute (RPI).

Ο στόχος της παρούσας εργασίας είναι η πραγματοποίηση νέων πειραμάτων και θεωρητικών υπολογισμών για τη μελέτη των ενεργών διατομών αντιδράσεων που προκαλούνται από νετρόνια στον σίδηρο σε μια προσπάθεια να αντιμετωπιστούν τα ζητήματα που αναφέρονται στις αξιολογημένες βιβλιοθήκες παρέχοντας νέα πειραματικά/θεωρητικά δεδομένα για βασικές αντιδράσεις και ενεργειακές περιοχές νετρονίων.

Λέξεις κλειδιά: ενεργός διατομή, σίδηρος, ελαστική σκέδαση, ανελαστική σκέδαση, πειράματα διέλευσης, άμεση σύλληψη

Résumé Étendu
(Extended summary in French)

Introduction

Les données nucléaires jouent un rôle important dans l'ingénierie nucléaire. Elles sont utilisées dans une multitude d'applications scientifiques et technologiques. Dans le cadre de mon sujet de thèse, je me suis intéressé aux sections efficaces des réactions induites par neutron. L'objectif principal est l'amélioration de la section efficace de diffusion élastique du ^{56}Fe en lien avec les propriétés neutroniques des réflecteurs aciers utilisés dans les réacteur nucléaires. Les paramètres neutroniques sont également sensibles aux autres isotopes du fer : ^{54}Fe (5.85%) , ^{57}Fe (2.12%) et ^{58}Fe (0.28%).

Du point de vue théorique, les modèles existants ne peuvent pas reproduire précisément la section efficace de diffusion des matériaux tel que Fe, Cr et Ni dans une zone en énergie entre 1 et 6 MeV. Pour ce type de matériaux, le formalisme de la Matrice-R est utilisé pour décrire le domaine des résonances jusqu'à 1-2 MeV et le modèle optique est utilisé pour décrire le continuum des sections efficaces au-delà de 5-6 MeV. Des données expérimentales sont généralement utilisées pour compléter les évaluations entre ces deux modèles. La section efficace élastique est déduite de la section efficace totale mesurée par transmission.

Le but de ce travail est de réaliser des calculs théoriques ainsi que de nouvelles mesures de section efficace élastique et de transmission afin de valider et compléter les évaluations du ^{54}Fe et du ^{56}Fe. Ce manuscrit de thèse est divisé en trois parties distinctes:

- Mesurer pour la première fois les sections efficaces et les distributions angulaires pour la diffusion élastique et inélastique entre 1 et 8 MeV pour les deux isotopes les plus abondants dans le fer naturel, c'est-à-dire ^{54}Fe et ^{56}Fe. Le spectromètre ELISA installé auprès de l'installation GELINA (JRC-Geel, Belgique) a été utilisé et des échantillons enrichis ont été utilisés.

- Effectuer des mesures de transmission neutronique en utilisant des échantillons de fer naturel de différentes épaisseurs. Seules les mesures réalisées en dessous de 100 keV ont pu être réalisées et seront présentées dans ce document.

- Effectuer des calculs de capture radiative directe pour le ^{56}Fe dans le but de fournir une interprétation physique possible aux modifications apportées par le projet CIELO dans la section efficace ^{56}Fe(n,γ).

Dispositif expérimental

Comme déjà mentionné, les expériences de diffusion ont été réalisées auprès de l'installation de temps de vol de neutrons GELINA, située en Belgique. L'installation fournit une source de neutrons blancs pulsée, couvrant la région d'énergie de 10 meV à 20 MeV. Pour la détermination de l'énergie incidente des neutrons, la technique du temps de vol est utilisée. À cette fin, l'installation dispose d'aires expérimentales positionnées entre 10 m et 400 m. Différents dispositifs expérimentaux sont installés permettant la mesure de différents types de réactions nucléaires induites par les neutrons.

Pour la mesure de diffusion, le spectromètre ELISA (ELastic and Inelastic Scattering Array) a été utilisé (Fig. 1). Il est placé à 30 m de la source de neutron. Le détecteur se compose de deux parties principales : 32 scintillateurs organiques liquides pour la détection des neutrons diffusés et une chambre à fission (^{235}U) pour la mesure du flux de neutrons. La chambre à fission est placée à 1.3 m en amont de l'échantillon. Les détecteurs sont divisés en 4 ensembles de 8 détecteurs chacun montés à des angles spécifiques par rapport à la direction du faisceau de neutrons (Table 1). En utilisant ce spectromètre, l'objectif est de produire des données de sections efficaces de diffusion de neutrons à haute résolution dans la région d'énergie des neutrons rapides.

Le spectromètre ELISA possède deux types de scintillateurs organiques liquides. La moitié des détecteurs utilisent le matériau de scintillation EJ301 et l'autre moitié utilise le EJ315. Ce sont des scintillateurs rapides avec une résolution temporelle inférieure à 1 ns. La raison derrière l'utilisation de deux types de détecteurs différents, hydrogène (EJ301) et deutérium (EJ315), est

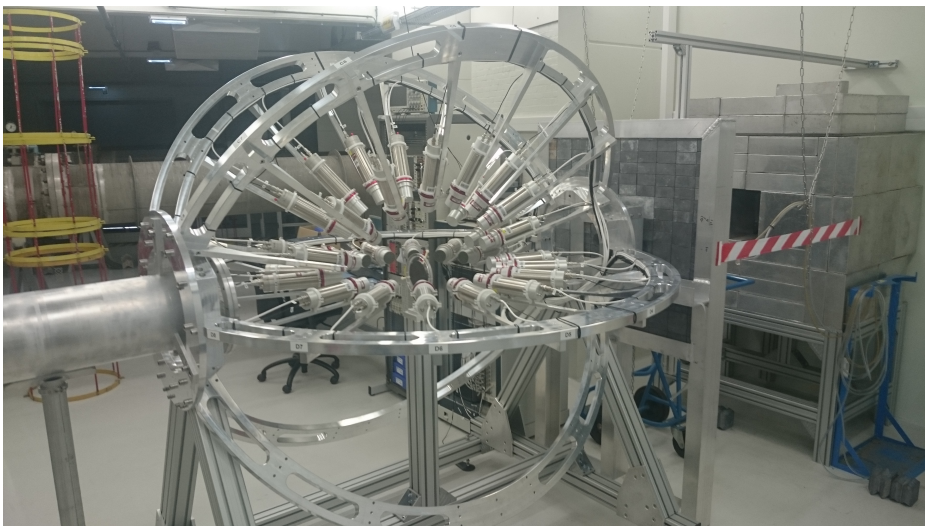

Figure 1: Le spectromètre ELISA est actuellement installé dans la base de vol numéro 1 de GELINA. Le faisceau de neutrons provient de la droite, passant d'abord à travers la chambre à fission qui est placée derrière le mur de plomb, puis atteignant l'échantillon de diffusion au centre de la configuration.

Table 1: Liste des 8 angles de détection par rapport à la direction du faisceau de neutrons. Leurs cosinus correspondants et leur poids utilisés pour la quadrature numérique sont également donnés.

Angle (θ_i) (deg)	163.8	142.8	121.7	100.6	79.4	58.3	37.2	16.2
cosθ_i	-0.9603	-0.7967	-0.5255	-0.1834	0.1834	0.5255	0.7967	0.9603
Weight (w_i)	0.1012	0.2224	0.3137	0.3627	0.3627	0.3137	0.2224	0.1012

que les neutrons détectés créent deux réponses d'amplitude d'impulsion différentes qui fournissent une vérification croisée entre les deux types de détecteurs, et aident à la découverte d'erreurs systématiques lors de l'analyse des données.

La chambre à fission contient un ensemble de 8 dépôts d'UF_4 sur 5 feuilles d'aluminium de 84 mm de diamètre et 20 µm d'épaisseur. Les dépôts ont été fabriqués au JRC-Geel, en utilisant la technique d'évaporation. Le diamètre des dépôts est de 70 mm, déterminé par le masque d'évaporation qui a été utilisé. La densité surfacique totale d'^{235}U a été déterminée expérimentalement par comptage alpha et a été trouvée égale à 4095(4) μg/cm^2. Chaque dépôt est face à l'anode correspondante, c'est-à-dire une électrode en aluminium de 25 µm d'épaisseur, placée à une distance de 7 mm pour l'enregistrement des fragments de fission. La chambre à fission est remplie de gaz P10 (10% de méthane - 90% d'argon) à pression atmosphérique.

Pour extraire les informations utiles, une caractérisation complète de la fonction de réponse du détecteur $R(L,E)$, qui représente la probabilité qu'une particule avec une énergie E produise une impulsion lumineuse avec une amplitude L, doit être effectuée. La méthode suivie dans ce travail était une combinaison de mesures de calibration dédiées et de simulations Monte Carlo. La caractérisation des détecteurs est répétée pour chaque campagne expérimentale, afin de surveiller la stabilité des détecteurs et d'identifier les problèmes qui pourraient survenir pendant les mesures. Les étapes suivies pour les caractérisations du système de détection sont:

- Pour les fonctions de réponse γ, la fonction de sortie lumineuse a été paramétrée, puis une combinaison de mesures expérimentales utilisant des sources de radionucléides et des simulations Monte Carlo avec le code MCNP6.2 ont été réalisées.

- Pour la réponse aux neutrons, après la paramétrisation de la fonction de sortie lumineuse pour les particules chargées, une mesure dédiée de la diffusion des neutrons sur le carbone naturel a été combinée avec des simulations Monte Carlo.

Expériences de diffusion

Dans le cadre de ce travail, trois expériences différentes ont été menées pour étudier la diffusion des neutrons sur le ^{54}Fe, le ^{nat}C et le ^{56}Fe. Les mesures ont été effectuées entre 2019 et 2023. Pour chaque expérience, deux types de mesures ont été réalisés. Une avec l'échantillon en place (sample-in) et une deuxième sans l'échantillon (sample-out). Les mesures sans échantillon ont été effectuées afin d'établir la contribution du bruit de fond provenant des neutrons du faisceau qui ont diffusés une ou plusieurs fois dans l'air et les matériaux environnants avant d'être détectés par l'un des scintillateurs. Dans les expériences actuelles, la plage d'énergie des neutrons de 1 MeV à 8 MeV a été étudiée. Bien que GELINA ait un spectre d'énergie des neutrons s'étendant au-delà de 20 MeV, la limitation pratique se pose lorsque le flux diminue au-delà de 8 MeV, rendant difficile d'atteindre des statistiques désirables dans les temps de mesure de ce travail. Le seuil inférieur, établi à 1 MeV, est dû à l'efficacité du détecteur.

Les sections efficaces différentielles de diffusion des neutrons ont été calculées via l'expression:

$$\frac{d\sigma_{el/inl}(E,\theta)}{d\Omega} = \frac{N'_{el/in}(E,\theta)}{\Delta\Omega\rho_T\Phi(E)A_b},$$

où E est l'énergie incidente du neutron, $N'_{el/inl}$ est le nombre d'événements corrigés des événements de diffusion élastique/inélastique, $\Delta\Omega$ est l'angle solide du détecteur, ρ_T est la densité surfacique de l'échantillon, $\Phi(E)$ est la densité de flux neutronique, et A_b représente la dimension du faisceau de neutrons. La section efficace intégrée en l'angle a été extraite en appliquant la règle de

quadrature de Gauss-Legendre:

$$\sigma(E) = 2\pi \sum_{i=1}^{8} w_i \frac{d\sigma}{d\Omega}(E, \cos\theta_i),$$

où $\frac{d\sigma}{d\Omega}(E, \cos\theta_i)$ est la section efficace différentielle en fonction de l'énergie incidente du neutron E et de l'angle de diffusion θ_i, et w_i sont les facteurs de pondération correspondants (Table 1).

L'analyse en plusieurs étapes suivie pour la détermination des différentes composantes est donnée ci-dessous:

- Séparer les événements induits par les neutrons des événements induits par les photons via une analyse de forme d'impulsion (méthode d'intégration de charge)
- Soustraction du bruit de fond (données sample-out)
- Séparer les neutrons provenant de la diffusion élastique ou inélastique (calculs cinématiques et déconvolution des distributions de sortie lumineuse)
- Appliquer une correction pour la diffusion multiple dans la cible (simulation Monte Carlo)
- Calcul de la densité de flux neutronique incidente sur chaque échantillon

La procédure d'analyse entière a été validée en extrayant la section efficace de diffusion élastique à partir de la mesure du carbone naturel. Dans de nombreux laboratoires, les mesures de la section efficace de diffusion élastique des neutrons sur le carbone sont utilisées pour calibrer les détecteurs, surveiller leur stabilité et valider les résultats expérimentaux. Elle est bien adaptée à de telles applications car la section efficace est connue de manière fiable avec une incertitude inférieure à 1% jusqu'à une énergie incidente des neutrons de 4.8 MeV. De plus, la section efficace différentielle est proposée comme standard par l'AIEA, pour les énergies des neutrons inférieures à 1.8 MeV.

Dans la Fig. 2, les distributions angulaires résultantes de la diffusion élastique des neutrons provenant des trois expériences sont données pour deux angles spécifiques. Les résultats sont comparés aux évaluations JEFF-3.3 et ENDF/B-VIII.0 convoluées avec la résolution énergétique expérimentale. Il existe un accord relativement bon entre les valeurs expérimentales et évaluées. Dans le cas du carbone, les résultats expérimentaux sont en bon accord avec les distributions angulaires bien connues, ce qui démontre la fiabilité des modèles des fonctions réponse développés dans le cadre de cette analyse.

Les sections efficaces de diffusion élastique des neutrons intégrées en angle provenant de toutes les mesures sont présentées dans la Fig. 3. Les résultats sont comparés aux évaluations JEFF-3.3 et ENDF/B-VIII.0 convoluées avec la résolution énergétique expérimentale. Dans le cas du ^{54}Fe, l'évaluation JEFF-3.3 a été calculée en soustrayant la section efficace non élastique basée sur le modèle optique de la section efficace totale évaluée, tandis que l'évaluation ENDF/B-VIII.0 a été produite en utilisant le code EMPIRE. Les résultats de ce travail sont en très bon accord avec JEFF-3.3. Dans le cas du ^{nat}C, la section efficace expérimentale obtenue est en accord avec les sections efficaces évaluées. Enfin, dans le cas du ^{56}Fe, les résultats sont en relativement bon accord avec les deux évaluations, dans lesquelles la diffusion élastique évaluée est la différence entre la section efficace totale et les sections efficaces partielles restantes.

La section efficace de diffusion inélastique a également été explorée pour les mesures du fer. Dans la Fig. 4, les résultats des sections efficaces partielles intégrées en angle de la diffusion inélastique depuis les premiers états excités du ^{54,56}Fe et le deuxième état du ^{56}Fe sont présentés et comparés aux évaluations JEFF-3.3 et ENDF/B-VIII.0 convoluées avec la résolution énergétique

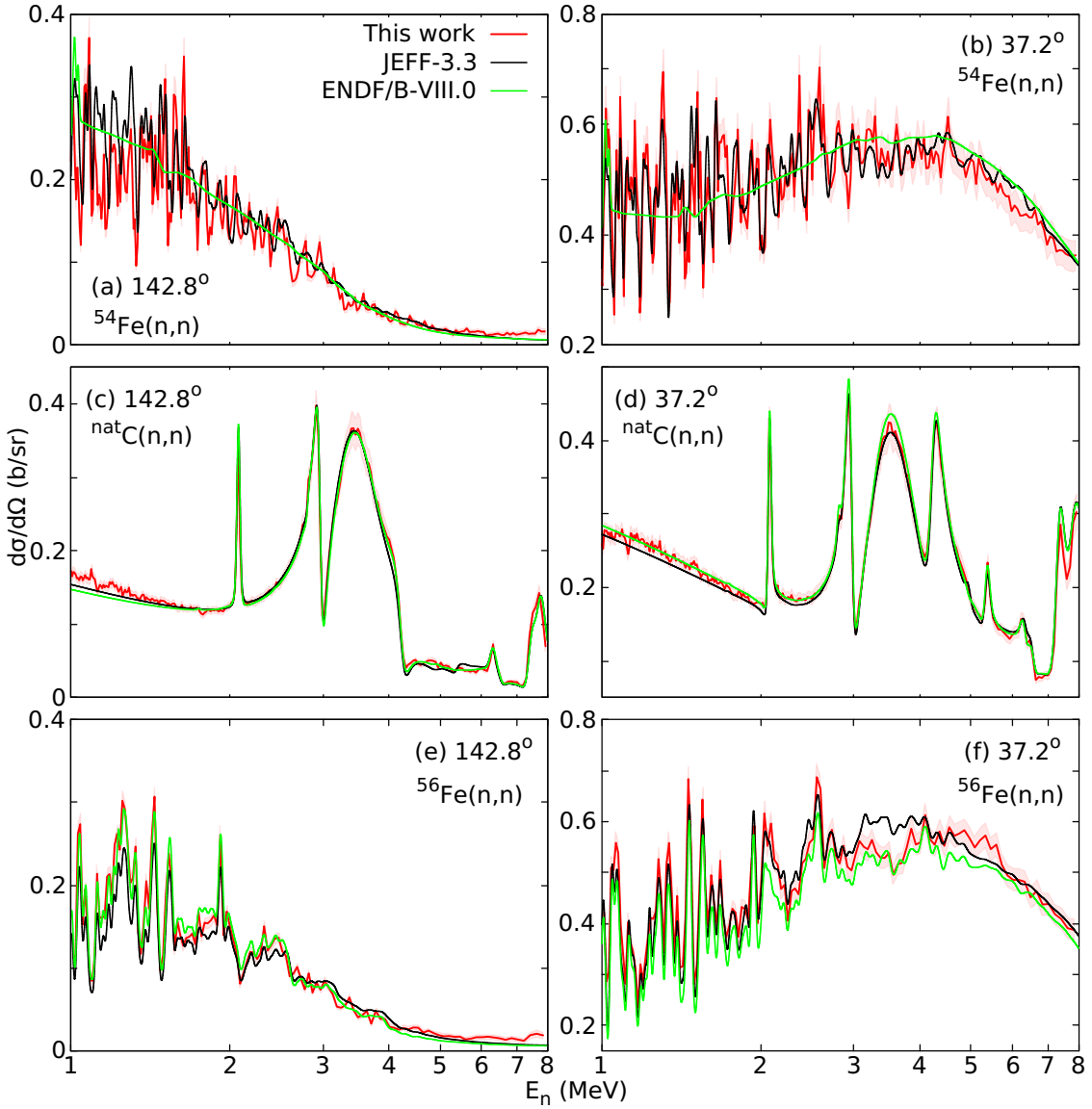

Figure 2: Exemples de sections efficaces différentielles de diffusion élastique des neutrons sur (a-b) ^{54}Fe, (c-d) ^{nat}C, et (e-f) ^{56}Fe, en fonction de l'énergie des neutrons à deux des huit angles de détection. Les sections efficaces expérimentales sont comparées aux valeurs évaluées fournies par les bibliothèques d'évaluation JEFF-3.3 et ENDF/B-VIII.0 convoluées avec la résolution énergétique expérimentale.

expérimentale. Les résultats de ce travail sont en relativement bon accord avec les valeurs fournies par l'évaluation dans le cas du ^{54}Fe. Les résultats obtenus pour le ^{56}Fe montrent une possible sous-estimation des sections efficaces par les évaluations. Les distributions angulaires ont également été extraites et sont présentées en détail au Chapitre 3.

Expériences de transmission sur le fer naturel

En plus de la mesure de diffusion, des mesures de transmission neutronique du fer naturel ont été effectuées pour explorer la région de basse énergie, autour de 24 keV, où des problèmes dans les évaluations ont été observés. Les expériences de transmission représentent le type de mesures

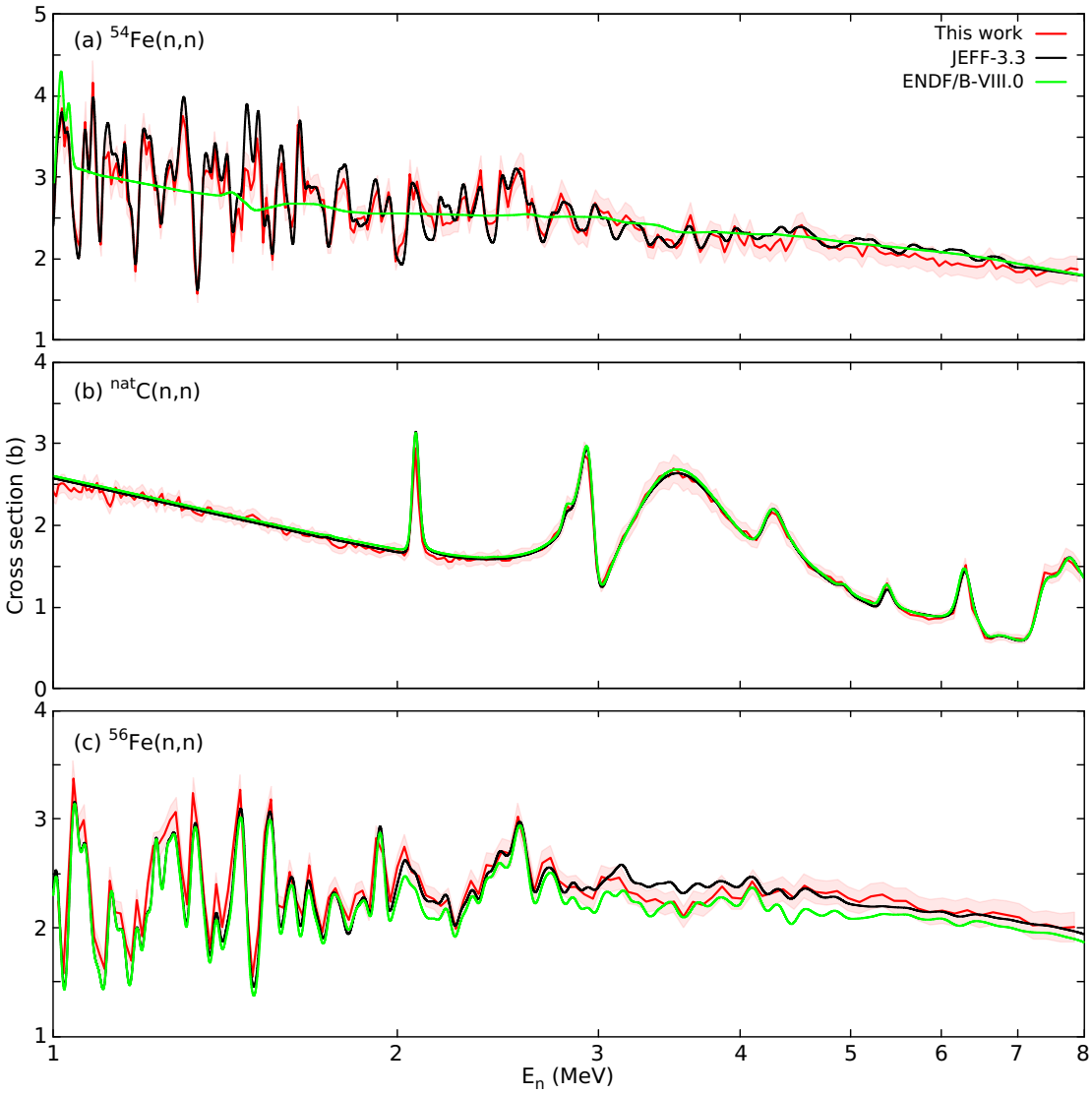

Figure 3: Section efficace intégrée en angle de la diffusion élastique des neutrons sur (a) ^{54}Fe, (b) ^{nat}C, et (c) ^{56}Fe en fonction de l'énergie des neutrons comparée aux évaluations JEFF-3.3 et ENDF/B-VIII.0 convoluées avec la résolution énergétique expérimentale.

de temps de vol le plus simple et le plus précis. Les expériences ont été réalisées à 50 m de la source de neutron (base vol numéro 4). Le spectre des neutrons modérés a été utilisé. Le faisceau de neutrons traversant l'échantillon a été détecté par un scintillateur en verre au lithium enrichi en ^{6}Li. Deux échantillons de fer naturel de 1.2 cm et 4.5 cm d'épaisseur ont été mesurés. La transmission expérimentale a été calculée en utilisant la formule suivante :

$$T_{exp}(t_m) = N_T \frac{C_{in}(t_m) - k_T B_{in}(t_m)}{C_{out}(t_m) - k_T B_{out}(t_m)},$$

où C_{in}, C_{out} sont les taux de comptages avec et sans échantillon, B_{in}, B_{out} représentent la contribution du bruit de fond, N_T est un facteur de normalisation, k_T est un facteur qui tient compte de l'incertitude corrélée pour les effets systématiques dus au modèle de bruit de fond, et t_m est le temps de vol.

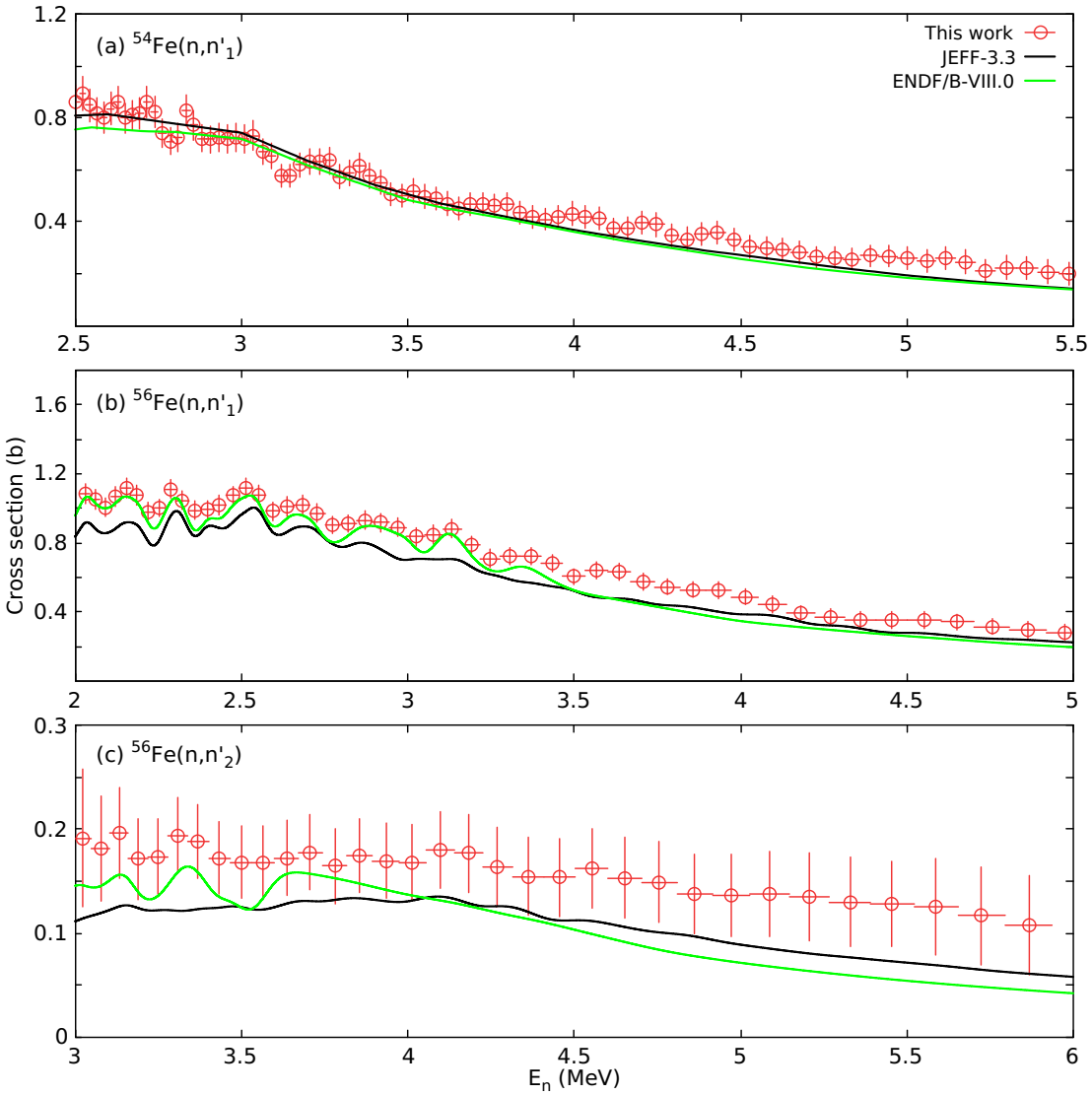

Figure 4: Section efficace intégrée en angle de la diffusion inélastique des neutrons depuis le premier état excité de (a-b) ^{54,56}Fe, et depuis le deuxième état de (c) ^{56}Fe en fonction de l'énergie incidente des neutrons comparée aux évaluations JEFF-3.3 et ENDF/B-VIII.0 convoluées avec la résolution énergétique expérimentale.

Dans la Fig. 5, la transmission expérimentale des deux échantillons de fer naturel est présentée pour la plage en énergie des neutrons incidents de 1 à 100 keV. Les résultats sont comparés aux transmissions théoriques calculées avec les évaluations JEFF-3.3 et ENDF/B-VIII.0. Des écarts entre la transmission expérimentale et les évaluations sont observés dans la région d'énergie de 5 à 25 keV. On observe que les fichiers de paramètres de résonance des deux évaluations ne parviennent pas à décrire correctement la transmission dans cette région d'énergie, ce qui entraîne une transmission théorique inférieure par rapport aux résultats expérimentaux de ce travail.

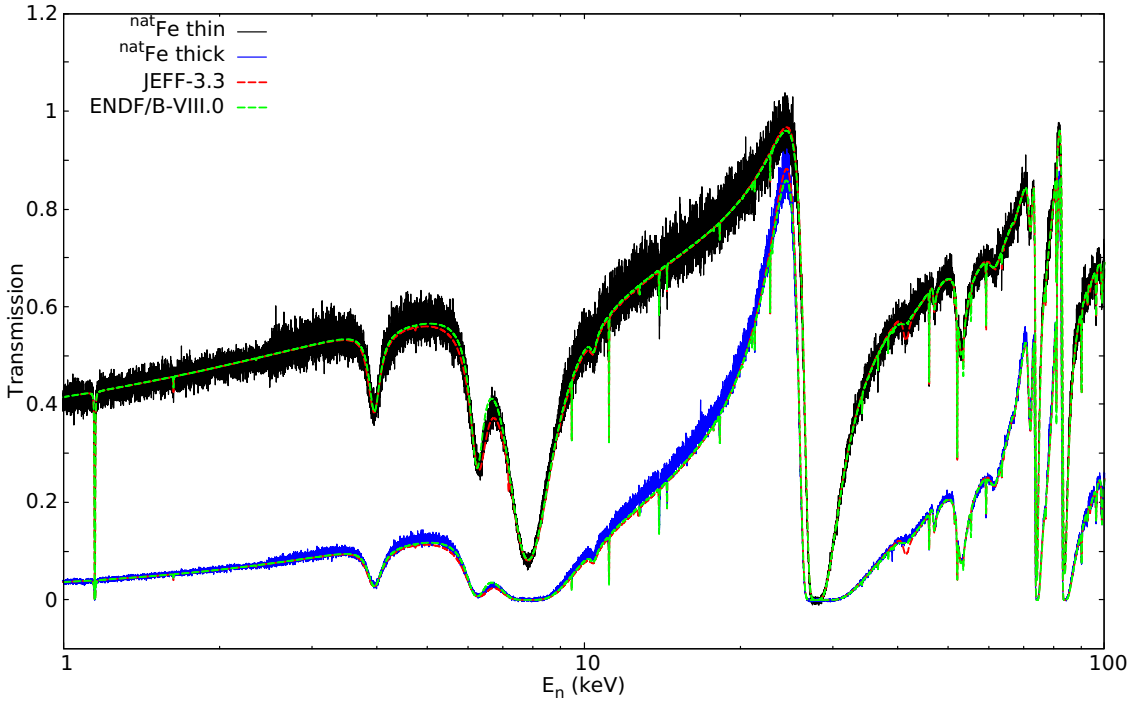

Figure 5: Les transmissions expérimentales obtenues avec les échantillons de fer naturel minces et épais sont comparées aux évaluations JEFF-3.3 et ENDF/B-VIII.0 convoluées avec la résolution expérimentale.

Calculs théoriques

Pour fournir une interprétation physique des changements apportés à la section efficace de capture du ^{56}Fe par le projet CIELO dans la région d'énergie de 10 à 100 keV, le mécanisme de capture directe a été exploré. En pratique, deux mécanismes de capture existent. Le premier est la capture par formation d'un noyau composé, où le neutron incident est capturé et un système composé à longue durée de vie est formé. Le second est la capture directe, où le neutron incident est capturé par la cible sans formation de noyaux composé. La capture directe se produit en excitant un nombre limité de degrés de liberté dans un laps de temps plus court, ce qui reflète la durée nécessaire au projectile pour traverser la cible.

Pour l'émission d'un rayonnement dipolaire électrique (E1) de l'état initial à l'état final, et pour une énergie incidente de neutron spécifique E_n, la section efficace de capture directe est donnée par :

$$\sigma_{n,\gamma} = \frac{16\pi}{9\hbar} k_\gamma^3 \bar{e}^2 |Q_{i\to f}^{(E1)}|,$$

où $k_\gamma = \varepsilon_\gamma/\hbar c$ est le nombre d'onde du rayonnement γ émis avec l'énergie ε_γ, $\bar{e} = -Ze/A$ est la charge E1 du neutron, et $Q_{i\to f}^{(E1)}$ est l'élément de matrice de transition de l'état initial à l'état final. Dans le présent travail, le code PDIX a été utilisé pour calculer la capture directe. Il effectue le calcul en deux étapes. Tout d'abord, les fonctions d'onde de l'état lié sont déterminées sur la base des données expérimentales disponibles, puis la section efficace de capture directe est calculée pour un potentiel optique donné. Ensuite, la section efficace de capture totale (composée

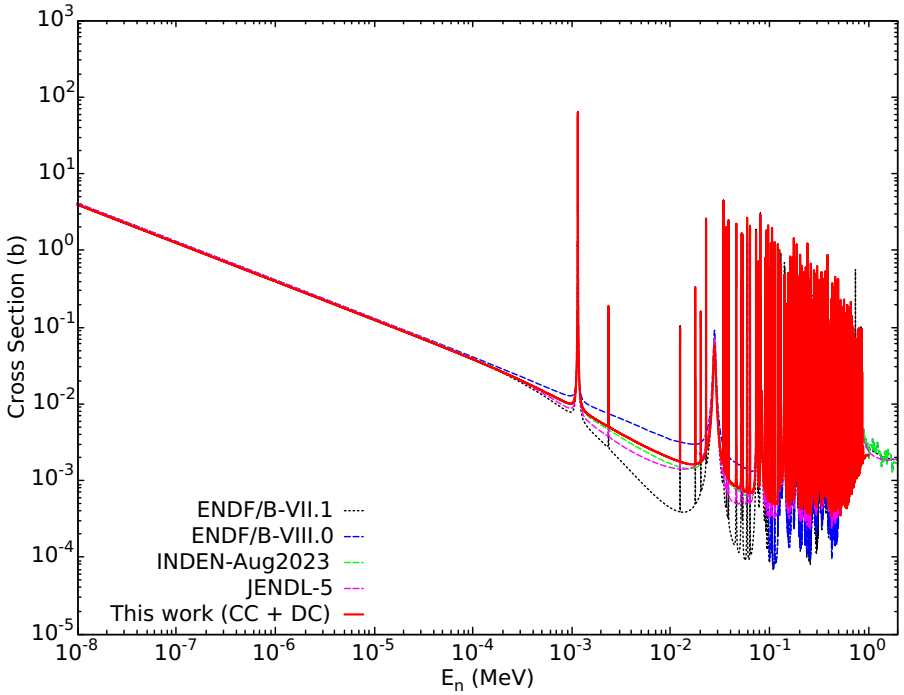

Figure 6: Résultat de la section efficace de capture totale pour une énergie incidente des neutrons allant du thermique jusqu'à 2 MeV comparée à la section efficace évaluée du ^{56}Fe(n,γ) disponible dans ENDF/B-VII.1, ENDF/B-VIII.0, INDEN-Aug2023 et JENDL-5.

et directe) a été calculée en utilisant PDIX, en employant l'approximation Single-Level Breit-Wigner (SLBW) pour la description de la capture composée. Les résultats de ce travail sont présentés dans la Fig. 6.

Conclusions - Perspectives

Dans le cadre de ce travail, de nouvelles expériences ont été réalisées sur l'installation de temps de vol GELINA pour mesurer les sections efficaces des réactions induites par neutrons sur le fer dans le but d'étudier les problèmes signalés dans les fichiers évalués du fer. Les données étudiées sont les distributions angulaires et les sections efficaces de diffusion élastique et inélastique des neutrons sur ^{54,56}Fe dans la région des neutrons rapides. Pour la diffusion élastique, il s'agit des premières mesures expérimentales fournissant des données à haute résolution dans la plage d'énergie de 1 à 8 MeV. La procédure d'analyse entière a été validée avec succès en utilisant une mesure de ^{nat}C. Les données obtenues reproduisent la section efficace recommandée par l'AIEA. Les résultats sur le fer ont été comparés avec les données disponibles dans la bibliothèque EXFOR, les évaluations (JEFF-3.3, ENDF-B/VIII.0) et des calculs théoriques utilisant les codes de réaction TALYS et EMPIRE.

De plus, des expériences de transmission neutronique sur le ^{nat}Fe ont été réalisées dans le but d'étudier la région d'énergie autour de 24 keV où des problèmes ont été identifiés par les évaluateurs travaillant sur les données nucléaires du fer. Les expériences ont été effectuées sur la base de vol à 50 m avec deux échantillons de fer naturel de différentes épaisseurs. Les résultats ont été comparés aux évaluations JEFF-3.3 et ENDF/B-VIII.0. Des différences avec nos mesures ont effectivement été observées autour de la région d'énergie de 24 keV. Les résultats ont également

été comparés aux données expérimentales disponibles dans la littérature et semblent être en bon accord.

Enfin, le mécanisme de capture radiative directe pour le cas du ^{56}Fe a été exploré dans ce travail. Dans l'ensemble, la capture directe (onde s) est capable d'expliquer la composante qui a été ajoutée dans la région d'énergie de 10 eV à 100 keV, tandis que la capture directe (onde d) semble être un bon candidat pour le "pic" observé à 850 keV dans une mesure de capture réalisée à RPI. De plus, une tentative de calcul de la section efficace de capture totale (capture directe et composé) a été réalisée en utilisant le formalisme Single-Level Breit-Wigner, disponible dans le code PDIX, pour décrire la région des résonances résolues. Les résultats finaux de ce travail semblent être très proches de ceux disponibles dans la libraire JENDL-5.

Les perspectives futures incluent une analyse plus approfondie des données collectées, des mises à niveau des systèmes de détection afin de réaliser de nouvelles mesures. Plus précisément, les distributions angulaires de ^{54,56}Fe seront utilisées pour extraire les coefficients de Legendre expérimentaux pour l'évaluation des distributions angulaires, tandis que les améliorations apportées au spectromètre ELISA permettront d'explorer la diffusion élastique en dessous de 1 MeV. Des efforts visant à réduire le bruit de fond dans les mesures de diffusion sont prévus grâce à l'installation de conditions sous vide autour de l'installation. Les nouvelles mesures de diffusion se concentreront sur les noyaux de masse moyenne et lourde, visant à résoudre les divergences des modèles théoriques et le manque de données expérimentales. De plus, des mesures supplémentaires de transmission des neutrons sur le fer naturel sont proposées, ainsi que le développement d'une nouvelle station de transmission à GELINA pour une acquisition de données améliorée. Enfin, la mise en œuvre du formalisme de capture radiative directe dans des codes d'ajustement de résonance comme CONRAD améliorera le calcul de la section efficace de capture totale.

Εκτεταμένη Περίληψη
(Extended summary in Greek)

Εισαγωγή

Τα πυρηνικά δεδομένα παίζουν σημαντικό ρόλο στην πυρηνική φυσική και μηχανική, καθώς χρησιμοποιούνται σε πληθώρα επιστημονικών και τεχνολογικών εφαρμογών. Ενώ η σημασία τους είναι ιδιαίτερα έντονη στις εφαρμογές πυρηνικών αντιδραστήρων, τα πυρηνικά δεδομένα είναι επίσης πολύ σημαντικά σε ένα ευρύ φάσμα πεδίων από τη βασική έρευνα έως τομείς όπως η πυρηνική ιατρική, η πυρηνική ασφάλεια, η περιβαλλοντική παρακολούθηση και πολλοί άλλοι. Στον τομέα της πυρηνικής ενέργειας, αυτά τα δεδομένα είναι απαραίτητα για τον σχεδιασμό και τη βελτιστοποίηση των αντιδραστήρων, εξασφαλίζοντας την ασφαλή λειτουργία και ενισχύοντας τη συνολική απόδοση τους. Οι ακριβείς ενεργές διατομές αντιδράσεων νετρονίων δεν είναι μόνο σημαντικές για τη λειτουργία των παραδοσιακών αντιδραστήρων σχάσης, αλλά παρέχουν επίσης βασικές πληροφορίες στην ανάπτυξη μελλοντικών συσκευών σύντηξης και προηγμένων συστημάτων όπως οι αντιδραστήρες τέταρτης γεννιάς και οι ADS (Accelerator Driven Systems).

Ο σίδηρος χρησιμοποιείται σε διάφορες εφαρμογές στη πυρηνική τεχνολογία, κυρίως λόγω των ευνοϊκών μηχανικών και θερμικών ιδιοτήτων του. Ως δομικό υλικό, ο σίδηρος και τα κράματά του χρησιμοποιούνται ευρέως στην κατασκευή πυρηνικών αντιδραστήρων και άλλων πυρηνικών εγκαταστάσεων. Λόγω της αντοχής τους και της ικανότητας διατήρησης της δομικής ακεραιότητας ακόμη και σε υψηλές θερμοκρασίες, τα υλικά που βασίζονται στον σίδηρο είναι κατάλληλα για την κατασκευή δοχείων πίεσης, δομικών υποστηριγμάτων για τον πυρήνα του αντιδραστήρα, συστημάτων σωληνώσεων και άλλων εξαρτημάτων μέσα σε έναν πυρηνικό αντιδραστήρα. Κατά τη λειτουργία του αντιδραστήρα, τα εξαρτήματα από σίδηρο εκτίθενται σε υψηλή ροή νετρονίων. Για αυτό το λόγο αλλά και για πολλούς άλλους, οι ακριβείς ενεργές διατομές αντιδράσεων νετρονίων στο σίδηρο, που χρησιμοποιούνται σε μοντέλα μεταφοράς νετρονίων, είναι απαραίτητα για τη βελτιστοποίηση της απόδοσης των αντιδραστήρων, την ασφαλή λειτουργία και την ανάπτυξη νέων συστημάτων.

Αν και ο σίδηρος είναι το πιο κοινό δομικό υλικό στις εφαρμογές πυρηνικής τεχνολογίας, οι αξιολογημένες ενεργές διατομές αντιδράσεων νετρονίων στα ισότοπα του σιδήρου που διατίθενται από διάφορες βιβλιοθήκες θεωρούνται ανεπαρκείς σε ορισμένα σημαντικά σημεία. Μελέτες έχουν δείξει ότι οι αβεβαιότητες στα αξιολογημένα δεδομένα των ενεργών διατομών στον σίδηρο έχουν μεγάλη επίδραση στις πιο σημαντικές παραμέτρους που σχετίζονται με την ανάπτυξη καινοτόμων συστημάτων αντιδραστήρων. Επιπλέον, έχει αποδιχθεί ότι οι θεωρητικοί υπολογισμοί σε ισότοπα της περιοχής Cr-Ni δεν μπορούν να αναπαράξουν σωστά τις ενεργές διατομές στο ενεργειακό εύρος νετρονίων από 1 έως 6 MeV. Ο μόνος τρόπος για να μειωθούν επαρκώς οι αβεβαιότητες των ενεργών διατομών είναι με τη χρήση ακριβή πειραματικών δεδομένών σε αυτήν την ενεργειακή περιοχή. Αν και ο ^{56}Fe αντιπροσωπεύει

το 91.75% του φυσικού σιδήρου, έχει αποδιχθεί ότι τα αποτελέσματα πειραμάτων benchmark που περιέχουν σίδηρο είναι ευαίσθητα στα υπόλοιπα ισότοπα του σιδήρου ^{56}Fe (5.85%), ^{57}Fe (2.12%) και ^{58}Fe (0.28%).

Στόχος αυτής της εργασίας είναι η διεξαγωγή νέων μετρήσεων και θεωρητικών υπολογισμών για την μελέτη των ενεργών διατομών στα ισότοπα του σιδήρου. Η παρούσα διδακτορική διατριβή χωρίζεται σε τρία διαφορετικά μέρη:

- Μετρήσεις για πρώτη φορά με υψηλή ενεργειακή διακριτική ικανότητα των ενεργών διατομών και γωνιακών κατανομών νετρονίων για την ελαστική και την ανελαστική σκέδαση, στην ενεργειακή περιοχή των γρήγορων νετρονίων, για τα δύο πιο σημαντικά ισότοπα στο φυσικό σίδηρο, δηλαδή το ^{54}Fe και το ^{56}Fe. Για τις μετρήσεις χρησιμοποιήθηκε το φασματομέτρο ELISA που βρίσκεται στο εργαστήριο GELINA, καθώς και υψηλά εμπλουτισμένα δείγματα και για τα δύο ισότοπα.

- Μετρήσεις διελεύσεων νετρονίων χρησιμοποιώντας δείγματα φυσικού σιδήρου με διάφορα πάχη, για τη μελέτη της ενεργειακής περιοχής των 24 keV και της ενεργού διατομής στις περιοχές μεταξύ των συντονισμών.

- Διεξαγωγή θεωρητικών υπολιγσμών για τη μελέτη της direct capture με σκοπό να παροχή μιας φυσική ερμηνεία στις αλλαγές που πραγματοποιήθηκαν από το CIELO prjoect στην ενεργό διατομή της αντίδρασης ^{56}Fe(n,γ).

Πειραματική διάταξη

Όπως ήδη αναφέρθηκε, τα πειράματα σκέδασης πραγματοποιήθηκαν στο εργαστήριο GELINA που βρίσκεται στο Βέλγιο. Το εργαστήριο παρέχει μια παλμική λευκή πηγή νετρονίων, καλύπτοντας την ενεργειακή περιοχή από 10 meV έως 20 MeV. Για τον προσδιορισμό της ενέργειας των νετρονίων χρησιμοποιείται η τεχνική χρόνου πτήσης. Γι΄ αυτόν τον σκοπό, δέκα διαδρομές πτήσης είναι διαθέσιμες, μεταβαλλόμενες σε μήκος από την πιο σύντομη στα 10 m έως την πιο μακρινή στα 400 m. Σε αυτές τις διαδρομές πτήσης είναι εγκατεστημένες διαφορετικές πειραματικές διατάξεις που επιτρέπουν τη μέτρηση διαφορετικών ειδών αντιδράσεων νετρονίων.

Για τις μέτρησεις σκέδασης χρησιμοποιήθηκε το ανιχνευτικό σύστημα ELISA (ELastic and Inelastic Scattering Array) (Σχήμα 1). Το σύστημα είναι τοποθετημένο σε απόσταση 30 m από τη πηγή νετρονίων στο διάδρομο πτήσης 1. Αποτελείται από δύο κύρια μέρη: 32 υγρούς οργανικούς ανιχνευτές για την ανίχνευση των σκεδαζόμενων νετρονίων και έναν θάλαμο σχάσης ^{235}U για τη μέτρηση του ροής νετρονίων. Ο θάλαμος σχάσης είναι τοποθετημένος 1.37 m μπροστά από το δείγμα. Οι ανιχνευτές χωρίζονται σε 4 σετ των 8 ανιχνευτών έκαστος, τοποθετημένους σε συγκεκριμένες γωνίες σε σχέση με τη κατεύθυνση της δέσμης νετρονίων (Πίνακας 1). Χρησιμοποιώντας αυτό το ανισχνευτικό σύστημα, στόχος είναι να παραχθούν δεδομένα υψηλής ενεργειακής διακριτκής ικανότητας για τις ενεργές διατομές αντιδράσεων σκέδασης στην περιοχή των γρήγορων νετρονίων.

Πίνακας 1: Οι 8 διαφορετικές γωνίες ανίχνευσης σε σχέση με την κατεύθυνση της δέσμης νετρονίων. Δίνονται επίσης τα αντίστοιχα συνημίτονα και βάρη που χρησιμοποιούνται για την αριθμητική τετραγωνική ολοκλήρωση.

Γωνία (θ_i)	163.8	142.8	121.7	100.6	79.4	58.3	37.2	16.2
$cos\theta_i$	-0.9603	-0.7967	-0.5255	-0.1834	0.1834	0.5255	0.7967	0.9603
Βάρος (w_i)	0.1012	0.2224	0.3137	0.3627	0.3627	0.3137	0.2224	0.1012

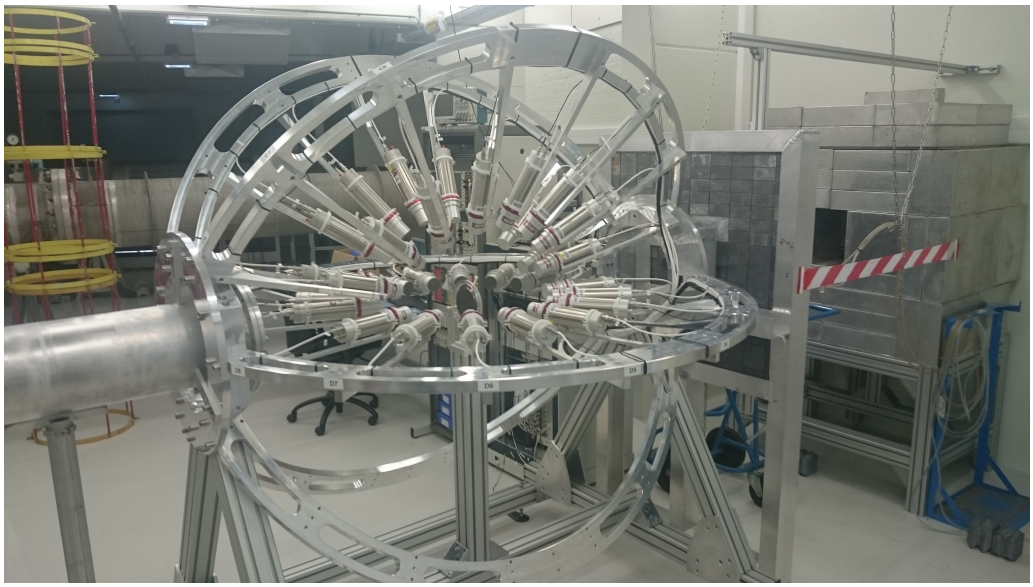

Σχήμα 1: Το φασματόμετρο ELISA εγκατεστημένο στη διαδρομή πτήσης 1 της GELINA. Η δέσμη νετρονίων έρχεται από δεξιά, προς τα αριστερά, περνώντας πρώτα από το θάλαμο σψάσδης που βρίσκεται πίσω από τον μολυβένιο τοίχο και στη συνέχεια φτάνει στο δείγμα σκέδασης στο κέντρο του συστήματος.

Στο φασματόμετρο ELISA, χρησιμοποιούνται δύο διαφορετικοί τύποι υγρών οργανικών ανιχνευτών. Οι μισοί ανιχνευτές χρησιμοποιούν το υλικό EJ301 και οι άλλοι μισοί χρησιμοποιούν το EJ315. Πρόκειται για γρήγορους ανιχνευτές με χρονική ανάλυση (time resolution) κάτω από 1 ns. Ο λόγος πίσω από τη χρήση δύο διαφορετικών τύπων ανιχνευτών, πρωτονίου (EJ301) και δευτερίου (EJ315), είναι ότι τα ανιχνευμένα νετρόνια δημιουργούν δύο διαφορετικές αποκρίσεις ύψους παλμού που παρέχουν έναν ανταγωνιστικό έλεγχο μεταξύ των δύο τύπων και βοηθούν στον εντοπισμό συστηματικών σφαλμάτων κατά την ανάλυση των δεδομένων.

Ο θάλαμος σχάσης περιέχει ένα σύνολο από 8 δείγματα UF_4 σε 5 αλουμινένιες βάσεις διαμέτρου 84 mm και πάχους 20 μm. Τα Δείγματα κατασκευάστηκαν στο JRC-Geel, χρησιμοποιώντας την τεχνική της εξάτμισης. Η διάμετρος των δειγμάτων είναι 70 mm, που καθορίζεται από τη μάσκα εξάτμισης που χρησιμοποιήθηκε. Η συνολική επιφανειακή πυκνότητα ^{235}U προσδιορίστηκε πειραματικά μέσο alpha counting και βρέθηκε να είναι 4095(4) μg/cm^2. Κάθε δείγμα κοιτάει την αντίστοιχη ανόδιο, δηλαδή έναν αλουμινένιο ηλεκτρόδιο πάχους 25 μm, τοποθετημένο σε απόσταση 7 mm για την καταγραφή των φραφμάτων σχάσης. Ο θάλαμος σχάσης γεμίζεται με αέριο P10 (10% μεθάνιο - 90% αργό) σε ατμοσφαιρική πίεση.

Είναι σημαντικό να πραγματοποιηθεί ένας πλήρης χαρακτηρισμός της συνάρτησης απόκρισης $R(L,E)$ του ανιχνευτή, η οποία αντιπροσωπεύει την πιθανότητα ενός σωματιδίου με ενέργεια E να παράγει ένα φωτεινό παλμό με ένταση L. Η μέθοδος που ακολουθήθηκε ήταν ένας συνδυασμός πειραματικών μετρήσεων βαθμονόμησης και προσομοιώσεων Monte Carlo. Ο χαρακτηρισμός των ανιχνευτών επαναλαμβάνεται για κάθε πείραμα προκειμένου να παρακολουθείται η σταθερότητα των ανιχνευτών και να εντοπιστούν προβλήματα που ενδέχεται να προέκυψαν κατά τις μετρήσεις. Τα βήματα που ακολουθήθηκαν για το χαρακτηρισμό του συστήματος ανίχνευσης είναι:

- Για τη συνάρτηση απόκρισης των φωτονίων, συνδυάστηκαν πειραματικές μετρήσεις χρησιμοποιώντας ραδιενεργές πηγές και προσομοιώσεις Monte Carlo με τον κώδικα MCNP6.2.

- Για τη συνάρτηση απόκριση των νετρονίων, συνδυάστηκαν πειράματα σκέδασης σε φυσικό άνθρακα με προσομοιώσεις Monte Carlo.

Πειράματα σκέδασης

Στα πλαίσια της παρούσας εργασίας, πραγματοποιήθηκαν τρεια διαφορετικά πειράματα για τη μελέτη της σκέδασης νετρονίων σε ^{54}Fe, ^{nat}C και ^{56}Fe. Οι μετρήσεις πραγματοποιήθηκαν από το 2019 έως το 2023. Για κάθε πείραμα, πραγματοποιήθηκαν δύο είδη μετρήσεων. Μία με το δείγμα στη θέση του (sample-in) και μία δεύτερη χωρίς το δείγμα (sample-out). Οι μετρήσεις sample-out πραγματοποιήθηκαν για να καθοριστεί η συμβολή του υποβάθρου από νετρόνια που σκεδάστηκνα μία ή πολλαπλές φορές στον αέρα και τα περιβάλλοντα υλικά και στη συνέχεια ανιχνεύθηκαν. Στα παρόντα πειράματα, μελετήθηκε το εύρος ενεργειών νετρονίων από 1 MeV έως 8 MeV. Παρόλο που η GELINA έχει ένα φάσμα ενεργειών νετρονίων που επεκτείνεται πέρα από τα 20 MeV, πρακτικός περιορισμός προκύπτει καθώς η ροή μειώνεται πέρα των 8 MeV, κάτι που καθιστά δύσκολο το να επιτευχθεί επιθυμητή στατιστική μέσα στους χρόνους μέτρησης των πειραμάτων. Το χαμηλό ενεργειακό κατώφλι καθορίστηκε στο 1 MeV λόγω της απόδοσης των ανιχνευτών.

Οι διαφορικές ενεργές διατομές υπολογίστηκαν μέσω της σχέσης:

$$\frac{d\sigma_{el/inl}(E,\theta)}{d\Omega} = \frac{N^{'}_{el/in}(E,\theta)}{\Delta\Omega\rho_T\Phi(E)A_b}, \tag{1}$$

όπου E είναι η ενέργεια του εισερχόμενου νετρονίου, $N^{'}_{el/inl}$ είναι ο διορθωμένος αριθμός των ελαστικά/ανελαστικά σκεδαζόμενων γεγονότων, $\Delta\Omega$ είναι η στερεά γωνία του ανιχνευτή, ρ_T είναι η επιφανειακή πυκνότητα του δείγματος, $\Phi(E)$ είναι η ροή νετρονίων, και A_b είναι η εντατική εμβέλεια της δέσμης νετρονίων. Η ανελκτική συνολική τομή διάθλασης εξήχθη με την εφαρμογή του κανόνα τετραγωνικής ολοκλήρωσης Gauss-Legendre:

$$\sigma(E) = 2\pi \sum_{i=1}^{8} w_i \frac{d\sigma}{d\Omega}(E, \cos\theta_i),$$

όπου $\frac{d\sigma}{d\Omega}(E,\cos\theta_i)$ είναι η διαφορική ενεργός διατομή για ενέργεια E και γωνία θ_i και w_i είναι το βάρος κάθε γωνίας (Πίνακας 1).

Τα βήματα που ακολουθήθηκαν για τον προσδιορισμό των ενεργών διατομών δίνονται παρακάτω:

- Διαχωρισμός γεγονόταν μεταξύ νετρονίων και φωτονίων (μέθοδος ολοκλήρωσης φορτίου)
- Διόρθωση υποβάθρου (sample-out data)
- Διαχωρισμός νετρονίων που προκύπτουν από ελαστική και ανελαστική σκέδαση (κινηματικοί υπολογισμοί και αποσυνέλιξη των κατανομών φωτός)
- Διόρθωση για τα γεγονότα που προκύπτουν από πολλαπλές σκεδάσεις στο στόχο (προσομοιώσεις Monte Carlos)

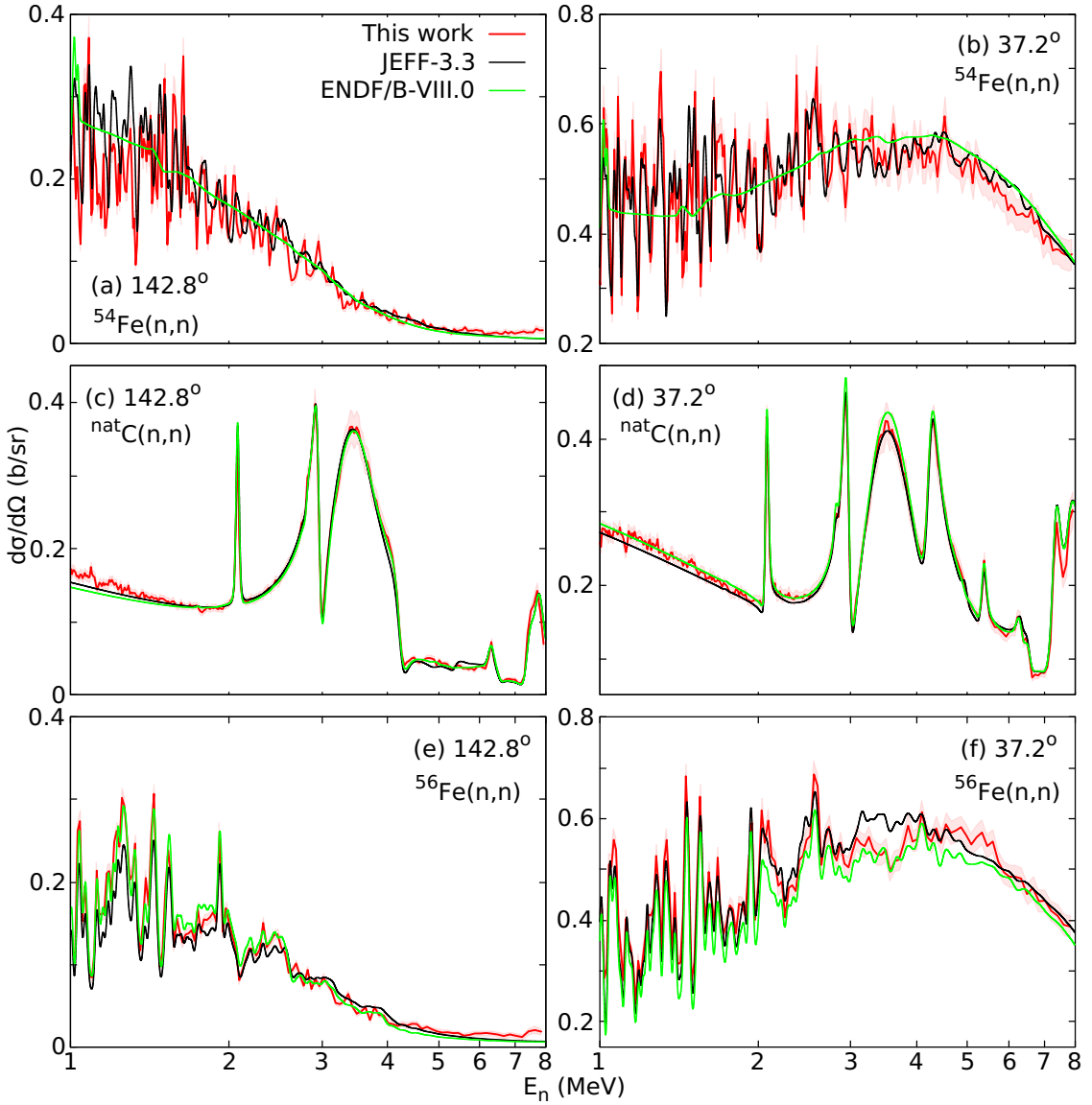

Σχήμα 2: Παραδείγματα διαφορικών ενεργών διατομών ελαστικής σκέδασης νετρονίων σε (a-b) ^{54}Fe, (c-d) ^{nat}C και (e-f) ^{56}Fe, ως συνάρτηση της ενέργειας του εισερχόμενου νετρονίου σε δύο από τις οκτώ γωνίες ανίχνευσης. Τα αποτελέσματα συγκρίνονται με τα αξιολογημένα δεδομένω των βιβλιοθηκών JEFF-3.3 και ENDF/B-VIII.0.

Ολόκληρη η ανάλυσης επικυρώθηκε εξάγοντας τη ενεργό διατομή της ελαστικής σκέδασης από τη μέτρηση του φυσικού άνθρακα. Σε πολλά εργαστήρια, μετρήσεις της ενεργού διατομής της ελαστικής σκέδασης νετρονίων σε άνθρακα χρησιμοποιούνται για τη βαθμονόμηση ανιχνευτών, την παρακολούθηση της σταθερότητάς τους και την επικύρωση πειραματικών αποτελεσμάτων. Είναι κατάλληλο για τέτοιες εφαρμογές διότι η ενεργός διατομή είναι γνωστή με αβεβαιότητα κάτω του 1% έως την ενέργεια 4.8 MeV. Επιπλέον, η διαφορική ενεργός διατομή προτείνεται ως standard από την IAEA για ενέργειες νετρονίων κάτω των 1.8 MeV.

Στο Σχήμα 2, παρουσιάζονται οι γωνιακές κατανομές της ελαστικής σκέδασης νετρονίων από τα τρία διαφορετικά πειράματα για ένα επιλεγμένο αριθμό γωνιών ανίχνευσης. Τα αποτελέσματα συγκρίνονται με τα τα αξιολογημένα δεδομένω των βιβλιοθηκών JEFF-3.3 και ENDF/B-VIII.0. Υπάρχει σχετικά καλή συμφωνία μεταξύ των πειραματικών και αξιολογη-

μένων δεδομένων, μέσα στα όρια των σφαλμάτων, σε ολόκληρη την ενεργειακή περιοχή. Στην περίπτωση του άνθρακα, τα πειραματικά αποτελέσματα συμφωνούν καλά με τις γνωστές γωνιακές κατανομές, πράγμα που δείχνει ότι οι συναρτήσεις απόκρισης που αναπτύχθηκαν στο πλαίσιο αυτής της ανάλυσης και χρησιμοποιήθηκαν στα πειράματα του σιδήρου είναι σε θέση να αναπαράγουν κατάλληλα τις πειραματικές κατανομές φωτός.

Οι ενεργές διατομές ελαστικής σκέδασης νετρονίων από όλες τις μετρήσεις παρουσιάζονται στο Σχήμα 3. Τα αποτελέσματα συγκρίνονται με τα τα αξιολογημένα δεδομένω των βιβλιοθηκών JEFF-3.3 και ENDF/B-VIII.0. Στην περίπτωση του ^{54}Fe, η βιβλιοθήκη JEFF-3.3 υπολογίστηκε αφαιρώντας τις μη ελαστικές ενεργές διατομές από την εκτιμώμενη συνολική ενεργό διατομή, ενώ η βιβλιοθήκη ENDF/B-VIII.0 παράχθηκε χρησιμοποιώντας τον κώδικα EMPIRE για αυτήν την ενεργειακή περιοχή. Τα αποτελέσματα αυτής της εργασίας είναι σε πολύ καλή συμφωνία με τη JEFF-3.3. Στην περίπτωση του φθσικού άνθρακα, η πειραματική ενεργός διατομή αυτής της εργασίας είναι σε συμφωνία με την γνωστή ενεργό διατομή.

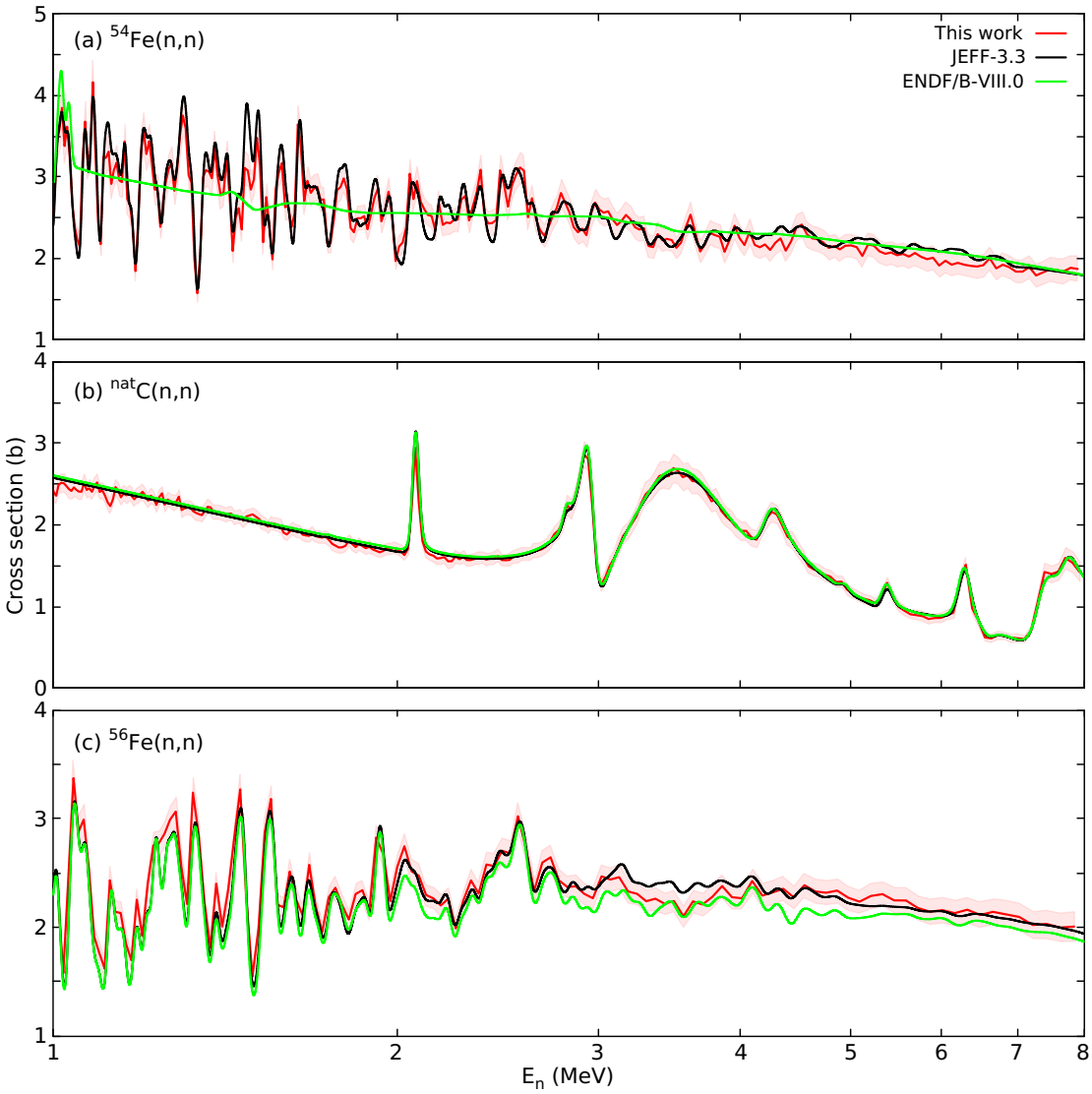

Σχήμα 3: Ενεργές διατομές ελαστικής σκέδασης νετρονίων από (a) ^{54}Fe, (b) $^{\text{nat}}$C και (c) ^{56}Fe, ως συνάρτηση της ενέργειας του εισερχόμενου νετρονίου. Τα αποτελέσματα συγκρίνονται με τα αξιολογημένα δεδομένω των βιβλιοθηκών JEFF-3.3 και ENDF/B-VIII.0.

Τέλος, στην περίπτωση του ^{56}Fe, τα αποτελέσματα είναι σε σχετικά καλή συμφωνία και με τις δύο βιβλιοθήκες, οι οποίες ακολούθησαν την ίδια μέθοδο υπολογισμού της ελαστικής διάθλασης, δηλαδή υιοθετώντας τη διαφορά μεταξύ των συνολικών και των υπολοίπων μερικών τομών.

Εκτός από την ελαστική σκέδαση, εξετάστηκε επίσης και η ανελαστική σκέδαση στις μετρήσεις του σιδήρου. Στο Σχήμα 4, παρουσιάζονται τα αποτελέσματα μερικών ενεργών διατομών ανελαστικής σκέδασης από τη πρώτη διεγερμένη στάθμη των ^{54,56}Fe, και από τη δεύτερη στάθμη του ^{56}Fe, και συγκρίνονται με τα αξιολογημένα δεδομένω των βιβλιοθηκών JEFF-3.3 και ENDF/B-VIII.0. Οι εντίδτοιχες γωνιακές κατανομές παρουσιάζονται λεπτομερώς στο Κεφάλαιο 3.

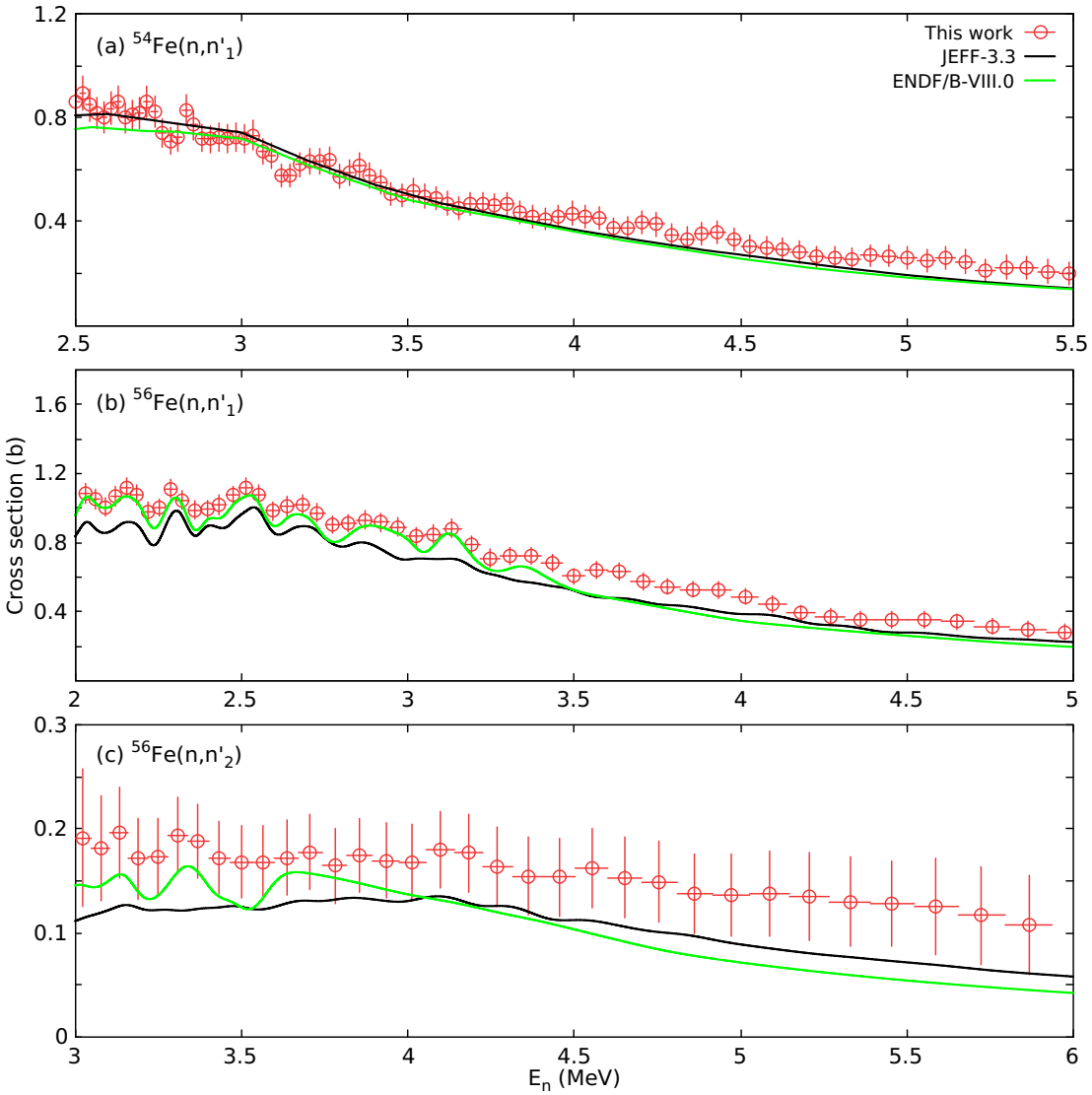

Σχήμα 4: Ενεργές διατομές ανελαστικής σκέδασης νετρονίων από τη πρώτη διεγερμένη στάθμη των (a-b) ^{54,56}Fe, και από τη δεύτερη στάθμη του (c) ^{56}Fe, ως συνάρτηση της ενέργειας του εισερχόμενου νετρονίου. Τα αποτελέσματα συγκρίνονται με τα αξιολογημένα δεδομένω των βιβλιοθηκών JEFF-3.3 και ENDF/B-VIII.0.

Πειράματα μετάδοσης νετρονίων σε φυσικό σίδηρο

Εκτός από τα πειράματα σκέδασης, πραγματοποιήθηκαν επίσης μετρήσεις μετάδοσης νετρονίων σε φυσικό σίδηρο για να εξερευνηθεί η χαμηλή ενεργειακή περιοχή, περίπου στα 24 keV, όπου παρατηρήθηκαν προβλήματα στα δεδομένα των αξιολογημένων βιβλιοθηκών. Οι μετρήσεις μετάδοσης αντιπροσωπεύουν τον πιο απλό και ακριβή τύπο μετρήσεων χρόνου πτήσης. Οι πειραματικές μετρήσεις πραγματοποιήθηκαν στον σταθμό 50 m της διαδρομής 4. Η δέσμη των νετρονίων που περνά από το δείγμα ανιχνεύτηκε από ένα ανιχνευτή Li-glass εμπλουτισμένο με 6Li. Μετρήθηκαν δύο διαφορετικά δείγματα φυσικού σιδήρου με πάχος 1.2 cm και 4.5 cm. Η πειραματική μετάδοση (transmission) υπολογίστηκε χρησιμοποιώντας τον τύπο:

$$T_{exp}(t_m) = N_T \frac{C_{in}(t_m) - k_T B_{in}(t_m)}{C_{out}(t_m) - k_T B_{out}(t_m)},$$

όπου C_{in}, C_{out} είναι ο αριθμός των γεγονότων με και χωρίς το στόχο, B_{in}, B_{out} είναι η αντίστοιχη συνεισφορά υποβάθρου, N_T είναι ένας παράγοντας κανονικοποίησης, k_T είναι ένας παράγοντας που λαμβάνει υπόψη τη συσχετισμένη αβεβαιότητα για συστηματικές επιδράσεις λόγω του μοντέλου που περιγράφει το υπόβαθρο και t_m είναι ο χρόνος πτήσης.

Στο Σχήμα 5 παρουσιάζεται τα πειραματικά απότελέσματα και για τις δυο μετρήσεις στο ενεργειακό εύρος νετρονίων από 1 έως 100 keV. Τα αποτελέσματα συγκρίνονται με τη θεωρητική μετάδοση των βιβλιοθηκών JEFF-3.3 και ENDF/B-VIII.0. Παρατηρούνται κάποιες διαφορές μεταξύ των πειραματικών και των αξιολογημένων δεδομένων στην ενεργειακή περιοχή από 5 έως 25 keV. Παρατηρείται ότι οι παράμετροι που περιγράφουν τους συντονισμούς στις δύο βιβλιοθήκες δεν είναι σε θέση να περιγράψουν επαρκώς τη μετάδοση σε αυτή την ενεργειακή περιοχή, με αποτέλεσμα να προκύπτει μια θεωρητική μετάδοση που είναι χαμηλότερη σε σύγκριση με τα πειραματικά αποτελέσματα αυτής της εργασίας.

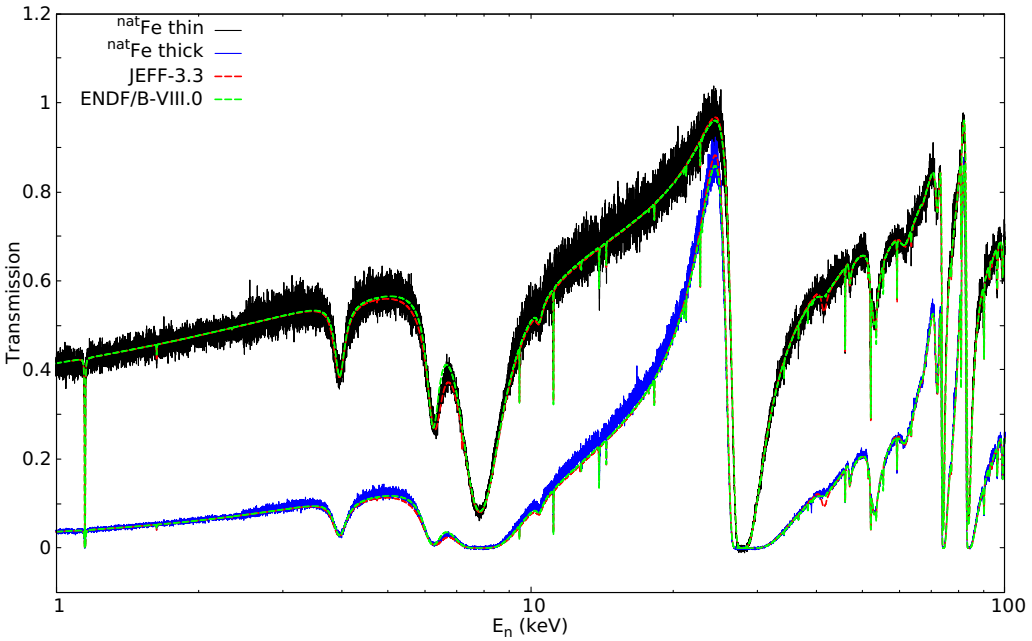

Σχήμα 5: Πειραματικά φάσματα μετάδοσης νετρονίων από το λεπτό και τον παχύ στόχο σιδήρου. Τα αποτελέσματα συγκρίνονται με τα αξιολογημένα δεδομένα των βιβλιοθηκών JEFF-3.3 και ENDF/B-VIII.0

.

Θεωρητικοί υπολογισμοί

Ο μηχανισμός άμεσης σύλληψης (direct capture) μελετήθηκε ώστε να παρεχθεί μια φυσική ερμηνεία στις αλλαγές που έγιναν στη ενεργό διατομή της αντίδρασης ^{56}Fe(nγ) από το πρόγραμμα CIELO στην ενεργειακή περιοχή 10-100keV. Στην πράξη, υπάρχουν δύο μηχανισμοί σύλληψης. Πρώτον είναι η σύλληψη μέσω σύνθετου πυρήνα, όπου το εισερχόμενο νετρόνιο συλλαμβάνεται και δημιουργείται ένα μακροβιό σύστημα σύνθετου πυρήνα. Δεύτερον, η άμεση σύλληψη, όπου το εισερχόμενο νετρόνιο καταλαμβάνεται από τον στόχο χωρίς καμία δημιουργία σύνθετου πυρήνα. Η άμεση σύλληψη πραγματοποιείται με την διέγερση ενός περιορισμένου αριθμού βαθμών ελευθερίας εντός ενός πιο σύντομου χρονικού διαστήματος.

Για την εκπομπή ακτινοβολίας ηλεκτρικού διπόλου (E1) από την αρχική στην τελική κατάσταση, και για μια συγκεκριμένη ενέργεια προσπίπτοντος νετρονίου E_n, η ενεργός διατομή άμεσης σύλληψης δίνεται από:

$$\sigma_{n,\gamma} = \frac{16\pi}{9\hbar} k_\gamma^3 \bar{e}^2 |Q_{i\to f}^{(E1)}|,$$

όπου $k_\gamma = \varepsilon_\gamma/\hbar c$ είναι ο κυματαριθμός της εκπεμπόμενης ακτινοβολίας γ με ενέργεια ε_γ, $\bar{e} = -Ze/A$ είναι το φορτίο E1 του νετρονίου, και $Q_{i\to f}^{(E1)}$ ίναι το στοιχείο του πίνακα μετάβασης από την αρχική στην τελική κατάσταση.

Στην παρούσα εργασία, ο κώδικας PDIX χρησιμοποιήθηκε για τον υπολογισμό της άμεσης σύλληψης. Η διαδικασία υπολογισμού πραγματοποιείται σε δύο βήματα. Πρώτα, οι κυματοσυναρτήσεις της δεσμευμένης κατάστασης καθορίζονται με βάση τα διαθέσιμα πειραματικά δεδομένα και στη συνέχεια ο υπολογισμός της ενεργού διατομής άμεσης σύλληψης πραγματοποιείται για ένα δεδομένο οπτικό μοντέλο. Στη συνέχεια, η συνολική διατομή σύλληψης (σύνθετη και άμεση) υπολογίστηκε χρησιμοποιώντας τον κώδικα PDIX, με την αξιοποίηση του Single-Level Breit-Wigner (SLBW) για την περιγραφή της σύνθετης σύλληψης. Τα αποτελέσματα της παρούσας εργασίας παρουσιάζονται στο Σχήμα 6.

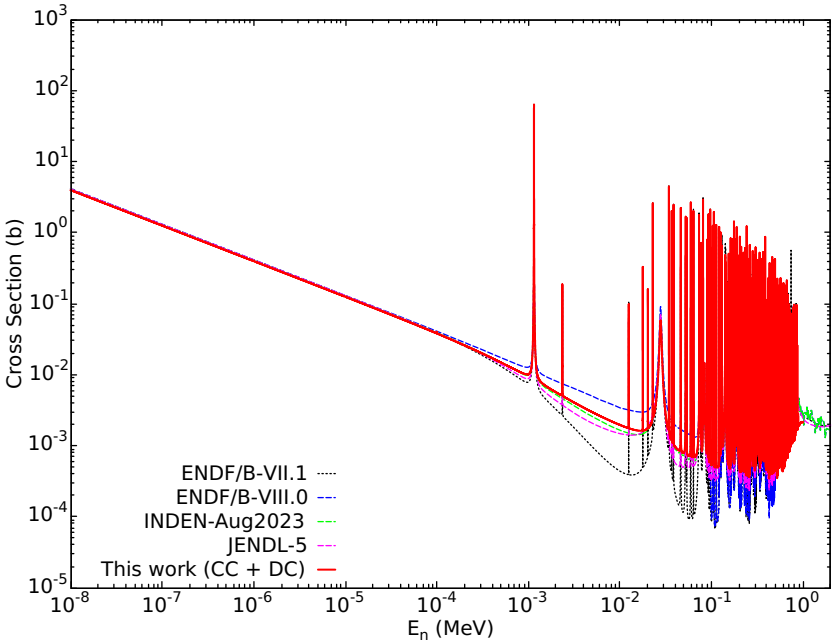

Σχήμα 6: Τα αποτελέσματα της συνολικής ενεργού διατομής σύλληψης νετρονίου από τη περιοχή των θερμιών νετρονίων έως τα 2 MeV συγκρίνονται με τα δεδομένα των βιβλιοθηκών ENDF/B-VII.1, ENDF/B-VIII.0, INDEN-Aug2023 και JENDL-5.

Συμπεράσματα - Προοπτικές

Στην παρούσα εργασία, πραγματοποιήθηκαν νέα πειράματα στο εργαστήριο χρόνου πτήσης GELINA για τη μέτρηση των ενεργών διατομών αντιδράσεων που προκαλούνται από νετρόνια στον σίδηρο, με στόχο την αντιμετώπιση προβλημάτων που αναφέρθηκαν στα αξιολογημένα δεδομένα του σιδήρου, παρέχοντας νέα πειραματικά δεδομένα για βασικές αντιδράσεις και ενεργειακές περιοχές. Αρχικά, μετρήθηκαν οι γωνιακές κατανομές και οι ενεργές διατομές της ελαστικής και ανελαστικής σκέδασης νετρονίων στο ^{54,56}Fe στην περιοχή γρήγορων νετρονίων, χρησιμοποιώντας υψηλά εμπλουτισμένα δείγματα και για τα δύο ισότοπα. Για την ελαστική σκέδαση, αυτές είναι οι πρώτες πειραματικές μετρήσεις που παρέχουν δεδομένα υψηλής ενεργειακής ανάλυσης στην ενεργειακή περιοχή 1 έως 8 MeV. Η διαδικασία ανάλυσης επικυρώθηκε επιτυχώς χρησιμοποιώντας μια μέτρηση με φυσικό άνθρακα αναπαράγοντας την καλά γνωστή ενεργό διατομή της αντίδρασης ^{nat}C(n,n). Τα αποτελέσματα συγκρίθηκαν με τα πειραματικά δεδομένα διαθέσιμα στη βιβλιοθήκη EXFOR, τα αξιολογημένα δεδομένω των βιβλιοθηκών JEFF-3.3 και ENDF-B/VIII.0, καθώς και με θεωρητικούς υπολογισμούς χρησιμοποιώντας τους κώδικες TALYS και EMPIRE.

Επιπλέον, πραγματοποιήθηκαν πειράματα μετάδοσης νετρονίων σε ^{nat}Fe με στόχο τη μελέτη της ενεργειακής περιοχής γύρω από τα 24 keV, όπου έχουν εντοπιστεί προβλήματα από τους αξιολογητές που δουλεύουν στα πυρηνικά δεδομένα του σιδήρου. Τα πειράματα πραγματοποιήθηκαν στο σταθμό των 50 μέτρων της GELINA και μετρήθηκαν δύο δείγματα φυσικού σιδήρου με διαφορετικό πάχος. Τα τελικά αποτελέσματα συγκρίθηκαν με τα αξιλογημένα δεδομένα των JEFF-3.3 και ENDF/B-VIII.0 και, παρόλο που και οι δύο αξιολογήσεις φαίνεται να αποδίδουν σχετικά καλά σε όλη την ενεργειακή περιοχή των νετρονίων, παρατηρήθηκαν ορισμένες διαφορές ιδιαίτερα γύρω από την περιοχή των 24 keV. Τα αποτελέσματα συγκρίθηκαν επίσης με πειραματικά δεδομένα διαθέσιμα στη βιβλιογραφία.

Τέλος, ο μηχανισμός της άμεσης σύλληψης για την περίπτωση του ^{56}Fe εξετάστηκε σε αυτή την εργασία. Φάνηκε πως η άμεση σύλληψη s-wave μπορεί να εξηγήσει το υπόβαθρο που προστέθηκε στην ενεργειακή περιοχή 10eV - 100keV, ενώ η άμεση σύλληψη d-wave φαίνεται ως καλή υποψήφιος για την ξαφνική άνοδο της ενεργού διατομής σύλληψης γύρω από τα 850 keV που παρατηρήθηκε σε πρόσφατο πείραμα. Επιπλέον, έγινε μια προσπάθεια υπολογισμού της συνολικής διατομής σύλληψης (άμεση και σύνθετη σύλληψη) χρησιμοποιώντας το μοντέλο Single-Level Breit-Wigner (SLBW), που είναι διαθέσιμη στον κώδικα PDIX, για την περιγραφή της περιοχής των συντονισμών. Τα τελικά αποτελέσματα αυτής της εργασίας φαίνεται να είναι πολύ κοντά στα πιο πρόσφατα αξιολογημένα δεδομένα για τη ενεργό διατομή της αντίδρασης ^{56}Fe(n,γ) που παρέχονται από τις βιβλιοθήκες INDEN και το JENDL.

Οι μελλοντικές προοπτικές περιλαμβάνουν περαιτέρω ανάλυση των συλλεχθέντων δεδομένων, αναβαθμίσεις των συστημάτων ανίχνευσης και νέες μετρήσεις. Συγκεκριμένα, οι γωνιακές κατανομές των ^{54,56}Fe θα χρησιμοποιηθούν για την εξαγωγή πειραματικών συντελεστών Legendre που είναι κρίσιμοι για την αξιολόγηση των γωνιακών κατανομών, ενώ οι αναβαθμίσεις του φασματόμετρου ELISA θα επιτρέψουν την εξερεύνηση της ελαστικής σκέδασης κάτω από 1 MeV. Προβλέπονται προσπάθειες για τη μείωση του υποβάθρου στις μετρήσεις σκέδασης μέσω της εγκατάστασης συνθηκών κενού γύρω από την εγκατάσταση ή τη διαδρομή της δέσμης. Νέες μετρήσεις σκέδασης θα επικεντρωθούν σε μεσαίου και βαρέως τύπου πυρήνες, με στόχο την αντιμετώπιση αποκλίσεων και της έλλειψης πειραματικών δεδομένων. Επιπλέον, προτείνονται περαιτέρω μετρήσεις μετάδοσης νετρονικίων σε φυσικό σίδηρο, μαζί με την ανάπτυξη νέου σταθμού μετάδοσης στη GELINA για βελτιωμένη συλλογή δεδομένων. Τέλος, η εφαρμογή της άμεσης σύλληψης σε κώδικες προσαρμογής συντονισμών όπως ο CONRAD θα βελτιώσει τον υπολογισμό της συνολικής διατομής σύλληψης.

"To my parents, I couldn't have done it without their constant support"

Acknowledgments

The completion of this PhD has been a collective effort, bringing together the expertise and collaboration of three institutions: **CEA** (France), **NTUA** (Greece), and **JRC** (Belgium). This work would not have been possible without the invaluable support, mentorship, and encouragement of many individuals who played a significant role in my academic and research journey.

I would first like to express my deepest gratitude to **Maria Diakaki**, who was the first person I contacted when I applied for this PhD position. Even though she did not know me personally at the time, she placed her trust in me, and I am certain that her influence played a significant role in the decision made by the team at CEA to hire me, even if she might not admit it. Over the course of these three years, despite the physical distance, she was always there when I needed her. We spent countless hours on phone and video calls discussing my work in great detail. Her insightful feedback, constructive criticism, and encouragement played a crucial role in shaping both my research and my growth as a researcher. I will always be deeply grateful for the time and energy she invested in me, and I feel fortunate to have had her support on both a professional and personal level throughout this journey.

I would also like to extend my sincere thanks to **Gilles Noguere**, who welcomed me to CEA when I began my PhD in October 2021. He was instrumental in helping me navigate the administrative maze that comes with a CEA contract, ensuring a smooth start to my journey. I had the privilege of spending the first three months of my PhD with him at Cadarache, where he not only helped me grasp the objectives of this project but also provided invaluable guidance that laid the foundation for the rest of my work. Even during my time at the JRC, he remained in constant contact, keeping up with my progress and offering support from afar. I was a bit intimidated by him at first, but over the past three years, I've come to appreciate both his mentorship and his unique sense of humor. Working with him has been a fantastic experience, and I'm genuinely grateful for all his dedication and support throughout this project.

Also, I would like to express my heartfelt thanks to **Arjan Plompen**, who served as my supervisor during the two and a half years I spent at the JRC. Despite his busy schedule, he always made time to check in on my progress and offer assistance whenever I faced challenges. Our discussions were crucial in deepening my understanding of the physics behind my experiments. His guidance through various stages of the project was invaluable in shaping my approach and understanding of the subject. His ability to be both professionally rigorous and personally supportive played a key role in making my PhD journey rewarding and manageable. His contribution was instrumental to the success of this project, and I will be forever grateful for his support and guidance. I hope that he is as proud of our work as I am.

Special thanks are owed to **Elisa Pirovano**. It is evident that this PhD would not have been possible without her. She was the one who developed the spectrometer I used in my measurements and endured countless emails and meeting hours until I became familiar with the setup and data analysis. She was always responsive, happy to assist, and provided invaluable guidance throughout the process. I will be forever in her debt. Although we mostly communicated from a distance, I

had the opportunity to work with her in person at PTB in July 2024. This experience was not only highly educational but also enjoyable and memorable. Thanks to her and the rest of the team at PTB, that month turned out to be one of the highlights of my PhD journey.

During this PhD, I spent two and a half years at the GELINA facility of the JRC-Geel, and there are several people to whom I am grateful for my time there. First, I would like to thank **Carlos Paradela Dobarro**. He was the one who welcomed me to the JRC upon my arrival and, unfortunately for him, was often the first person I turned to when problems arose. Despite this, he was always there to help, answer my questions, and provide guidance in a way that ensured I understood both the problems and their solutions. I consider him both a mentor and a friend, and I am grateful for the time and support we shared. I consider myself fortunate to have had the opportunity to work with **Peter Schillebeeckx** before his retirement. As an expert in the nuclear data field, he possesses a wealth of knowledge that he generously shares with young researchers like myself. He taught me many valuable lessons, and I will always cherish the time we spent together. Furthermore, I would like to thank **Stefan Kopecky** for the time we spent discussing my work and its results. He was always willing to clarify things that were unclear to me and offered a more optimistic perspective when I had doubts. It's a pity that we didn't have more time to work on the resonance analysis, but I remain hopeful for future opportunities. I also want to highlight his unique sense of humor, he made me laugh more than anyone else during my stay at the JRC. I'm still working on getting into the *Dying Fetus* genre of music, though! I would also like to thank my office mate, **Andreea Oprea**, for the enjoyable discussions and good times we shared while working in the same office. She took a genuine interest in my work and was always willing to help whenever technical problems arose with the setups. Lastly, I would like to extend my gratitude to all the staff at the GELINA facility. My thanks go to the secretaries for managing the administrative aspects of my visit, the technicians who were always available and willing to assist with issues related to the experimental setups, and, of course, the operators of the accelerator who, under challenging conditions, did their utmost to ensure the optimal conditions for the experiments related to this work.

I would also like to thank **Alberto Mengoni**, who provided not only the code for the direct capture calculations but also invaluable guidance and support throughout the process. He was always available to answer my questions regarding the calculations, offering clear explanations and helping me understand the underlying physics. His expertise and willingness to assist were crucial in this part of my PhD, and I am deeply grateful for his support.

I will be forever grateful to the two professors who introduced me to the exciting world of experimental nuclear physics, **Roza Zanni-Vlastou** and **Mike Kokkoris**. They welcomed me as a new member of the Nuclear Physics group at NTUA back in 2018 for my bachelor's thesis and guided me through the early stages of my academic journey. We continued working together during my master's thesis, and even throughout my PhD, they remained invested in my progress, consistently asking about the project's development and offering valuable advice. Their trust and support have been instrumental, and it is clear to me that I wouldn't be where I am today without their encouragement and mentorship. I hope they are proud of the work I have accomplished so far.

I would also like to thank the members of the jury who are not mentioned above: the reviewers **Maëlle Kerveno** and **Arnd Junghans**, and the examiners **Roberto Capote Noy**, **Cyrille de Saint Jean**, and **José Busto**. Thank you for accepting the task of reviewing my work and for participating in the defense of my PhD. It was both an honor and a privilege to have your expertise and insights contribute to this process.

Once again, I would like to extend my heartfelt thanks to all the individuals mentioned above, and I hope our paths will cross again in the future. Beyond the scientific support, it is evident that

navigating the emotional roller coaster of pursuing a PhD would not have been possible without the support of some very special people in my personal life.

I would like to start by thanking **Georgios Giouvanakis**, who has taken on many roles in my life over the past six years: partner, friend, therapist, doctor, chef, and so much more. He has been my rock and my first contact for sharing both the highs and lows. His unwavering support and belief in me, even when I struggled to believe in myself, have been crucial in shaping the person I am today. I am deeply grateful for his significant impact on my life. I often wish I could have had even a fraction of the positive influence on his life that he has had on mine. I feel incredibly fortunate that our paths crossed, and I hold him in my heart with immense love and affection. No matter where our paths may lead, he will always have a special place in my life and my heart.

I would also like to thank one of my best friends, **Sofia Apergi**. We met during our undergraduate studies at NTUA, and since then, our lives have run in parallel paths. In 2019, she moved abroad to pursue her PhD, and by a stroke of luck, I ended up living only 30 minutes away from her—me in Geel and she in Eindhoven. I'm not sure I would have survived the loneliness that comes with working in Geel if it weren't for her and her friends. She has always been a source of support and advice whenever I needed it. I believe we've both done quite well so far, though I'm still eagerly waiting for her to become rich and famous and fulfill her promise of buying me a villa in Mykonos. Fingers crossed!

The next part is devoted to two people with whom I have spent thousands of hours in video calls over the past three years. First, I would like to extend my heartfelt thanks to **Anastasia Ziagkova**. We first met in 2018 when we both joined the nuclear physics group at NTUA, and since then, our bond has deepened into something truly special. Describing Anastasia is challenging because she has a character that's truly one-of-a-kind. She has been a constant source of kindness and support, both personally and scientifically. While she might argue that she belongs in the scientific section of the acknowledgments—rightfully so, given the countless hours we've spent discussing our projects-I believe her influence extends well beyond the academic part. Nevertheless, I sincerely hope that we'll have the opportunity to collaborate on a project together in the future! The third member of this video call trio is **Evangelia Taimpiri**. We met when we started our master's together, and even though it becomes harder to make close friends as you grow older, there was an instant connection with her. I feel incredibly grateful to have her in my life—she has always been supportive and never hesitates to give her honest opinion, which I truly appreciate. I will forever cherish the fun and often hilarious moments we've shared, and I'm excited to create even more unforgettable memories with her in the future.

Special thanks are owed to my Parisian friends **Aggeliki Peppa** and her partner **Corto**. I wouldn't have survived the ordeal that is French bureaucracy without their help. I owe them a great deal and am deeply grateful for their unwavering support. On a related note, I would also like to thank the head of LEPh, **Veronique Bellanger-Villard**, who, despite the distance, was always incredibly responsive and helpful whenever I encountered issues with CEA's HR.

I would also like to thank my fellow Greek colleagues at the GELINA facility, **Andrea Tsinganis** and **Emmanuel Cambas**, for the nice conversations and company during my time in Geel. Their presence made my stay more enjoyable, and I appreciated having them around both professionally and personally.

Additionally, I would like to thank all the members of the Nuclear Physics group at NTUA, both past and present, for their guidance and support, especially during my early years in research. One member of this group is my European travel buddy, **Sotiris Chasapoglou**, with whom I am grateful to have shared rooms in various countries during conferences and schools throughout our PhDs. I would also like to extend my thanks to the PhD students at LEPh—**Francois**, **Fiona**, **Carole**, **Valentin**, and **David**—for making me feel welcome and part of the team when I first

arrived at CEA, despite not speaking French.

For the end, I have saved the most important people in my life: my family—my parents, **Evangelia** and **Apostolos**, and my siblings, **Vaggelis** and **Ioanna**. As the youngest member of the family, I have been surrounded by their unwavering love, support, and encouragement since the day I was born. My parents have always believed in me, providing not only the foundation upon which I've built my academic journey but also a sense of security that allowed me to pursue my dreams without fear. My siblings have been my closest companions, cheering me on through every challenge, always ready to lend an ear or offer advice when I needed it most. I know that no matter what happens, I can count on them to stand by me, and for that, I am eternally grateful. I feel truly blessed to have them in my life, and I love them deeply. This accomplishment is as much theirs as it is mine.

This work was partially supported by the Commissariat à l'énergie atomique et aux énergies alternatives (CEA) through the SINET project, and by the European Commission through the EU-FRAT, and ARIEL (EURATOM research and training program 2014-2018 under grant agreement No 847594) projects.

Contents

List of Figures

List of Tables

Chapter 1

Introduction

1.1 Importance of nuclear data

Nuclear data are playing a pivotal role in nuclear science and engineering, since they are used in a plethora of scientific and technological applications. While their significance is particularly pronounced in nuclear reactor applications, nuclear data are also very important in various domains from fundamental research to fields like nuclear medicine, nuclear safety and security, space exploration, environmental monitoring, and many more (see Fig. 1.1), shaping our understanding of fundamental processes and enabling innovations in diverse fields [1].

In the field of nuclear energy applications, these data are indispensable for the design and optimization of reactors, ensuring safe operation and enhancing overall efficiency. Precise information on neutron cross sections, decay properties, and reaction rates are not only important for the operation of traditional fission power plants, but also provide key information in the development of future fusion devices and advanced reactor systems like GEN-IV reactors, SMRs (Small Modular Reactors), and ADS (Accelerator Driven Systems) [2].

Additionally, nuclear data are playing an important role in different aspects of nuclear medicine, from diagnostic imaging to radiation therapy and medical isotope production. For example, isotopes with specific decay properties like positron emitters for PET (Positron Emission Tomography) scans or gamma emitters for SPECT (Single Photon Emission Computed Tomography) imaging, rely on the accuracy of nuclear data for a safe and reliable diagnosis. Furthermore, nuclear reactions are employed in the production of radioisotopes that are used in therapeutic procedures, such as cancer treatment, thus precise knowledge of reaction cross sections is very important [3].

In the case of environmental monitoring and nuclear forensics, like identification and quantification of radioactive isotopes, these procedures also heavily rely on nuclear data. From assessing the impact of nuclear accidents to monitoring radioactive contamination in the environment, and many other applications in this field, nuclear data provide crucial insights into the origin, distribution, and behavior of radioactive materials [4].

In these critical domains and many other, outdated, imprecise, and incomplete nuclear data can

Figure 1.1: The Nuclear Data Tree: representation of the various fields where nuclear data are used (figure courtesy of the EC-JRC).

slow down progress, limit precision, and compromise safety. Experimental facilities, such as particle accelerators and research reactors, serve as crucial platforms for generating new nuclear data and validating theoretical models. In these facilities measurements of nuclear reaction cross sections and decay properties are performed in an effort to enrich international nuclear data libraries and enhance predictive capabilities. Nuclear data libraries are comprehensive collections of evaluated nuclear data, which include information on nuclear reactions, decay processes, and properties of isotopes. The accuracy of the experimental data determines the accuracy of the evaluated data, which are used for the above-mentioned applications.

1.2 Status of the nuclear data of iron

Iron is used in various applications within the nuclear industry, primarily due to its favorable mechanical and thermal properties. As a structural material, iron and its alloys are widely employed in the construction of nuclear reactors and other nuclear facilities. Due to their strength, corrosion resistance, and ability to maintain structural integrity even at high temperatures iron-based materials are suitable for the construction of pressure vessels, structural supports for the reactor

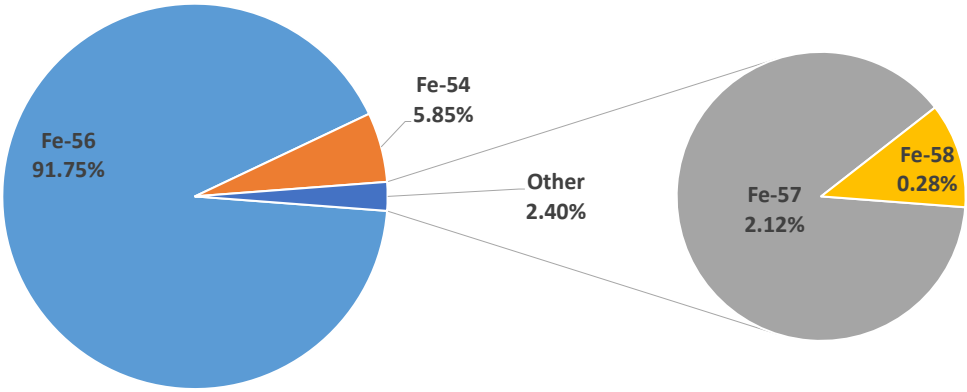

Figure 1.2: Chart of the isotopic composition of natural iron.

core, steam generators, piping systems, and other components inside a nuclear power plant. During reactor operation the steel alloy components are exposed to a high neutron flux. Additionally, these materials are used in the design of casks and containers for the storage and transportation of spent nuclear fuel. These containers provide structural integrity and radiation shielding to ensure the safe handling and storage of radioactive materials. For the above reasons and many others as well, accurate neutron cross section data of iron, that are used in neutron transport models, are indispensable for optimizing reactor performance, ensuring safe and efficient operation, and developing effective shielding systems that reduce radiation exposure.

Even though iron is a common structural material in nuclear technology applications it remains very difficult to evaluate. Despite the importance, the iron evaluations available from various libraries were deemed deficient in certain important respects. Sensitivity and uncertainty studies have shown that uncertainties on the evaluated data of neutron cross sections on iron have a big impact on the most significant integral parameters related to the development of innovative reactor systems [5]. Additionally, for the fast neutron energy region (from 1 to 8 MeV) theoretical calculations are known to perform poorly in the Cr-Ni region [6]. In the case of the iron isotopes, resonances are causing strong fluctuations on the cross sections in this neutron energy range. On the one hand, the current resolved resonance range evaluation methodology using the R-Matrix theory is only able to properly reproduce the experimental cross sections up to several hundreds of keV neutron incident energy, and on the other hand statistical model calculations using the Hauser-Feshbach theory are able to properly reproduce the continuum cross section only above 6 MeV neutron energy [7]. Since none of the two theoretical approaches performs well in the energy range of 1 to 6 MeV, accurate experimental data in this region are the only way to sufficiently constrain the uncertainties on the current evaluated data files of iron. In an effort to address some of the reported issues on the evaluated files, iron was included in the Collaborative International Evaluated Library Organization (CIELO) [8] project, the results of which were implemented in the ENDF/B-VIII.0 [9] evaluation. Within this project, it was realized that even though ^{56}Fe amounts for 91.75% of natural iron, validation results for iron containing benchmarks are sensitive to the minor iron isotopes ^{54}Fe (5.85%), ^{57}Fe

(2.12%), and ^{58}Fe (0.28%) in both the resolved resonance and fast neutron energy region. In the case of ^{56}Fe, strong scattering resonances with very deep interference minima are observed. In these energy regions, like the most well known one around 24 keV (see Fig. 1.3), where the cross section is nearly zero, the contribution of the minor isotopes dominates. This is the reason why the evaluations of ^{56}Fe cannot be separated from the evaluations of the minor iron isotopes. The outcome of this project and the current status of the evaluated nuclear data libraries for the different neutron induced reactions on Fe isotopes relevant to this work are discussed below [12].

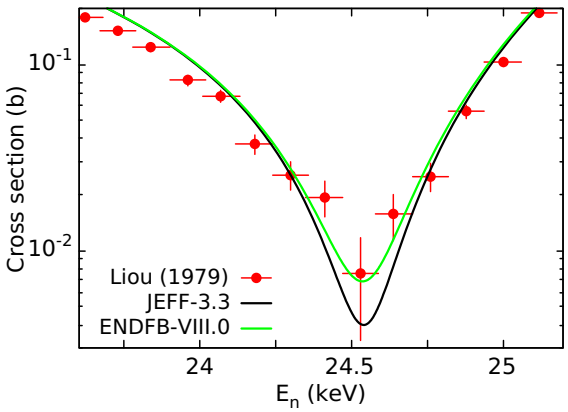

Figure 1.3: Total cross section of ^{56}Fe in the region around 24 keV. The JEFF-3.3 [10] and ENDF/B-VIII.0 evaluations are compared with the experimental data of Liou et al. (1979) [11].

Elastic scattering

Elastic scattering occurs when a neutron collides with a nucleus and rebounds, with the total kinetic energy conserved. The energy lost by the neutron in the collision depends on the angle through which it is scattered. Even though elastic scattering on the Fe isotopes is the dominant reaction mechanism only a handful of experimental data are available in the EXFOR [13] library. The experimental determination of neutron elastic scattering cross sections poses a challenge due to several factors:

- Since neutrons lack electric charge, direct detection is almost impossible. In most cases, neutrons are detected indirectly based on the measurement of secondary particles produced by neutron interactions using scintillation detectors, proportional counters, or solid-state detectors.
- The angular dependence of neutron scattering has to be taken into account, which creates a need to measure multiple detection angles.
- The scattering samples must be of high purity in order to avoid extra corrections and uncertainties.
- Background interference plays a crucial role in the extraction of meaningful data. Neutron scattering experiments need to be conducted in environments with low background radiation, ideally in a vacuum, to avoid signals generated from in-beam neutrons scattering on air and then reaching the detectors.

Given these challenges, experimentalists need to employ meticulous techniques and sophisticated data analysis methods to properly measure elastic scattering cross sections.

An example of the impact of the cross sections of neutron elastic scattering on iron is given in Ref. [14]. It is stated that neutron elastic scattering on iron nuclides is a major contributor to the uncertainty of the coolant expansion coefficients for the MYRRHA reactor [15]. Specifically, maximum uncertainties of 8% for ^{56}Fe and, unrealistically high, relative uncertainties up to 500% for ^{54}Fe and up to 1000% for ^{57}Fe, are observed in the JEFF-3.3 [10] evaluation in the MYRRHA relevant energy range (0.1 keV to 4.0 MeV). A reduction of the uncertainty in these quantities is recommended to meet target accuracies for the design of the MYRRHA reactor.

For the fast neutron energy region only a few scattered points are available, measured with quasi-monoenergetic neutron beams for the case of ^{54}Fe (Table 1.1) and ^{56}Fe (Table 1.2), while no data are available for ^{57}Fe and ^{58}Fe. In Fig. 1.4 the available experimental cross sections of elastic scattering in the EXFOR library are compared with the JEFF-3.3 and ENDF/B-VIII.0 evaluations. In the case of ^{56}Fe, both evaluations are following the same approach, i.e. the elastic scattering

Table 1.1: Elastic scattering data of ^{54}Fe available in the EXFOR library [13]. The name of the first author, the year of publication, the neutron energy range under study, the quantity (CS - Cross section and/or DA - Differential c/s with respect to angle) and the number of points are listed.

Reference		E_n range (MeV)	Quantity (Points)	
Rodgers (1967)	[16]	2.33	CS(1)	DA(5)
Boschung (1971)	[17]	4.04-5.60	CS(3)	DA(30)
Fedorov (1973)	[18]	2.90		DA(8)
Kinney (1974)	[19]	5.50-8.50	CS(3)	DA(62)
Korzh (1977)	[20]	1.50-3.00	CS(4)	DA(35)
El-Kadi (1982)	[21]	7.96-13.90	CS(4)	DA(105)
Korzh (1987)	[22]	5.00-7.00	CS(3)	DA(39)
Guenther (1989)	[23]	1.30-3.97		DA(370)
Vanhoy (2018)	[24]	2.00-6.00		DA(121)

Table 1.2: Elastic scattering data of ^{56}Fe available in the EXFOR library [13]. The name of the first author, the year of publication, the neutron energy range under study, the quantity (CS - Cross section and/or DA - Differential c/s with respect to angle) and the number of points are listed.

Reference		E_n range (MeV)	Quantity (Points)	
Rodgers (1967)	[16]	2.33	CS(1)	DA(5)
Kinney (1968)	[25]	4.60-7.57	CS(7)	DA(85)
Boschung (1971)	[17]	5.05-5.58	CS(2)	DA(19)
Morozov (1972)	[26]	1.80		DA(17)
Korzh (1977)	[20]	1.50-3.00	CS(4)	
Schweitzer (1978)	[27]	1.50-3.00	CS(1)	DA(12)
El-Kadi (1982)	[21]	7.96-13.90	CS(4)	DA(104)
Ramirez (2017)	[28]	0.80-7.96	CS(20)	DA(192)

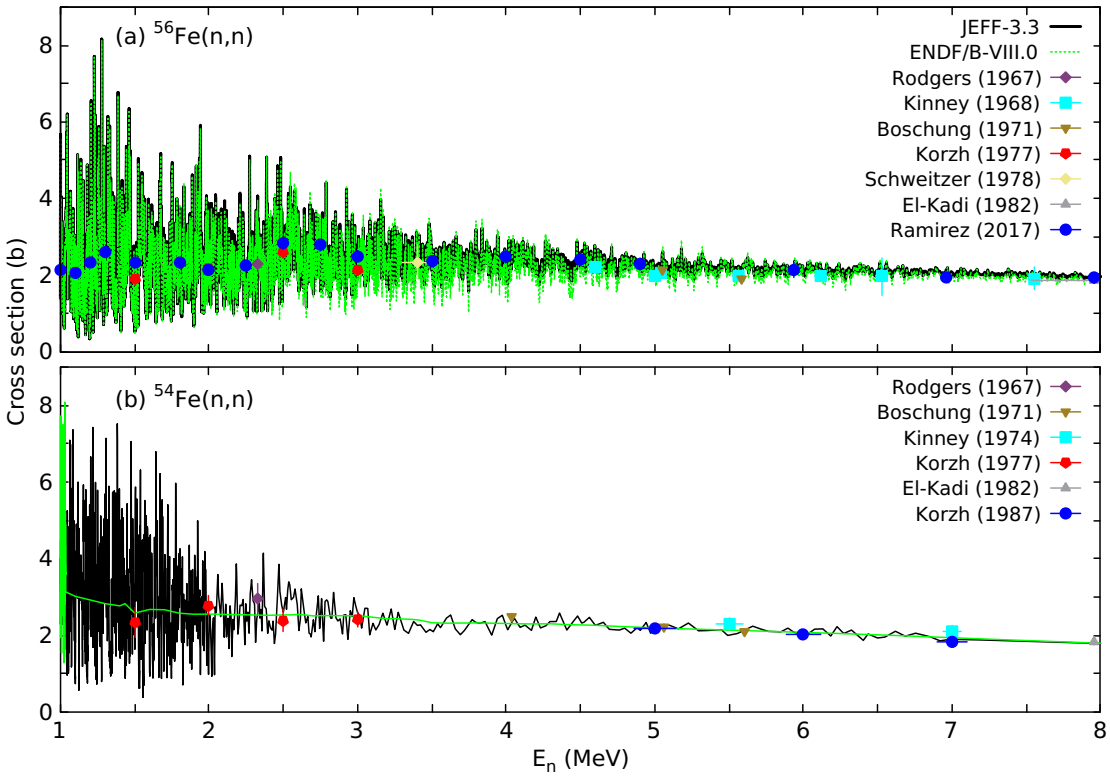

Figure 1.4: Comparison between the available experimental cross section data of neutron elastic scattering on (a) ^{56}Fe, (b) ^{54}Fe and the JEFF-3.3 [10] and ENDF/B-VIII.0 [9] evaluations in the energy region from 1 to 8 MeV.

cross section was defined as the difference between the total and the sum of the cross sections of the other reaction channels in this region. Even though in both evaluations the same total cross section on ^{nat}Fe by Berthold et al. (1995) [29] was used, corrected for the contribution of the minor isotopes, discrepancies are observed. These discrepancies are originating from differences in the evaluations of the partial cross sections between JEFF-3.3 and ENDF/B-VIII.0, that then are propagated into the elastic scattering cross section when subtracting them from the total. In the case of ^{54}Fe, while in the JEFF-3.3 evaluation the same methodology is adopted, the ENDF/B-VIII.0 evaluation has adopted optical model calculations using the EMPIRE [30] code. It is shown that even though the few experimental data available in the literature are in agreement with the evaluations, the resolution of the measurements is not enough to properly describe the fluctuating behavior of the cross section in this region. Furthermore, discrepancies between the data are also observed, exceeding uncertainties that in some cases reach 20%.

Inelastic scattering

In inelastic neutron scattering, the incident neutron collides with a target nucleus and transfers part of its energy, causing the nucleus to be excited to a higher energy state. This can occur through different mechanisms. In a direct reaction, the neutron interacts with specific nucleons in the nucleus, transferring energy rapidly without forming a compound nucleus, resulting in targeted

excitations. In a pre-equilibrium reaction, the neutron exchanges energy with a few nucleons, and the system has not yet reached full equilibrium, leading to partial energy sharing before the nucleus stabilizes. In a compound nucleus reaction, the neutron is fully absorbed, forming a highly excited compound nucleus that redistributes the energy among all its nucleons before decaying by the emotion of gamma rays. These mechanisms contribute to the complexity of neutron inelastic scattering, with the dominant process depending on the energy of the neutron and the properties of the target nucleus.

Inelastic scattering can be measured through two primary methods: detecting inelastically scattered neutrons or measuring the gamma rays emitted during the de-excitation of the residual nucleus. When measuring the scattered neutrons, the data obtained is directly related to the inelastic scattering cross section, which helps to characterize the interaction between the neutron and the target nucleus. By analyzing the angular distributions of these neutrons, additional insights into the reaction mechanism can be gained, as these distributions specify the quantum numbers involved. However, at low energy or angular resolutions, it can be challenging to clearly distinguish between inelastic and elastic scattering events, adding complexity to the analysis. Alternatively, inelastic scattering can be measured by detecting gamma rays emitted as the residual nucleus de-excites. This approach provides valuable information about the total inelastic scattering process, but requires model calculations to estimate the population of parent nuclear states involved. Accurate nuclear structure data is essential for this method, as the measurement is sensitive to factors like spin transfer during the interaction. Both methods—neutron and photon detection—complement each other and provide different perspectives on inelastic scattering events, depending on the specific details of the reaction.

It has been proven that inelastic scattering on iron also plays an important role in benchmark calculations. In Ref. [31] the inelastic scattering data on ^{56}Fe are cited as one of the major sources of the uncertainty in the determination of the important integral parameters relative to reactor applications. For that reason the neutron inelastic scattering cross section on ^{56}Fe has been included on the High Priority Request List (HPRL) of the OECD/NEA Data Bank [32]. The targeted uncertainty for Accelerator-Driven Minor Actinides Burner is 2% and for European Fast Reactors is 7%-9%. For the total inelastic scattering only a few experimental data are available in the EXFOR library for ^{56}Fe [33–38] (Table 1.4), two data set for ^{54}Fe [23,39] (Table 1.3), one set for ^{57}Fe [40], and zero data for ^{58}Fe. In Fig. 1.5 the available experimental data for the total inelastic scattering cross section in the EXFOR library are presented along with the JEFF-3.3 and ENDF/B-VIII.0 evaluations. In the case of ^{54}Fe, optical model calculations have been adopted in both evaluations. Large discrepancies are observed between the two evaluations and the available data in EXFOR. Based on the data by Olacel et al. (2018) [39] fluctuating structures in the cross section are observed, as expected in all isotopes of iron. These data were not taken into account during the evaluations since they became available after the end of the CIELO project. The same phenomena are also observed for the ^{57}Fe isotope. In the case of ^{56}Fe, both evaluations are strongly based on the high resolution measurements of Dupont et al. (1998) [35] and Negret et al. (2013) [34], even though problems have been reported for both data sets, normalization issues in the measurement of

Dupont, and energy calibration problems in the measurement of Negret [12]. In ENDF/B-VIII.0 the cross section has a fluctuating behavior up to 3.5 MeV and then optical model calculations are adopted, while in the JEFF-3.3 the fluctuating cross section continues up to 10 MeV. As mentioned earlier, the discrepancies between the two evaluations observed here are the main reason for the discrepancies in the elastic scattering cross section (see Fig. 1.4).

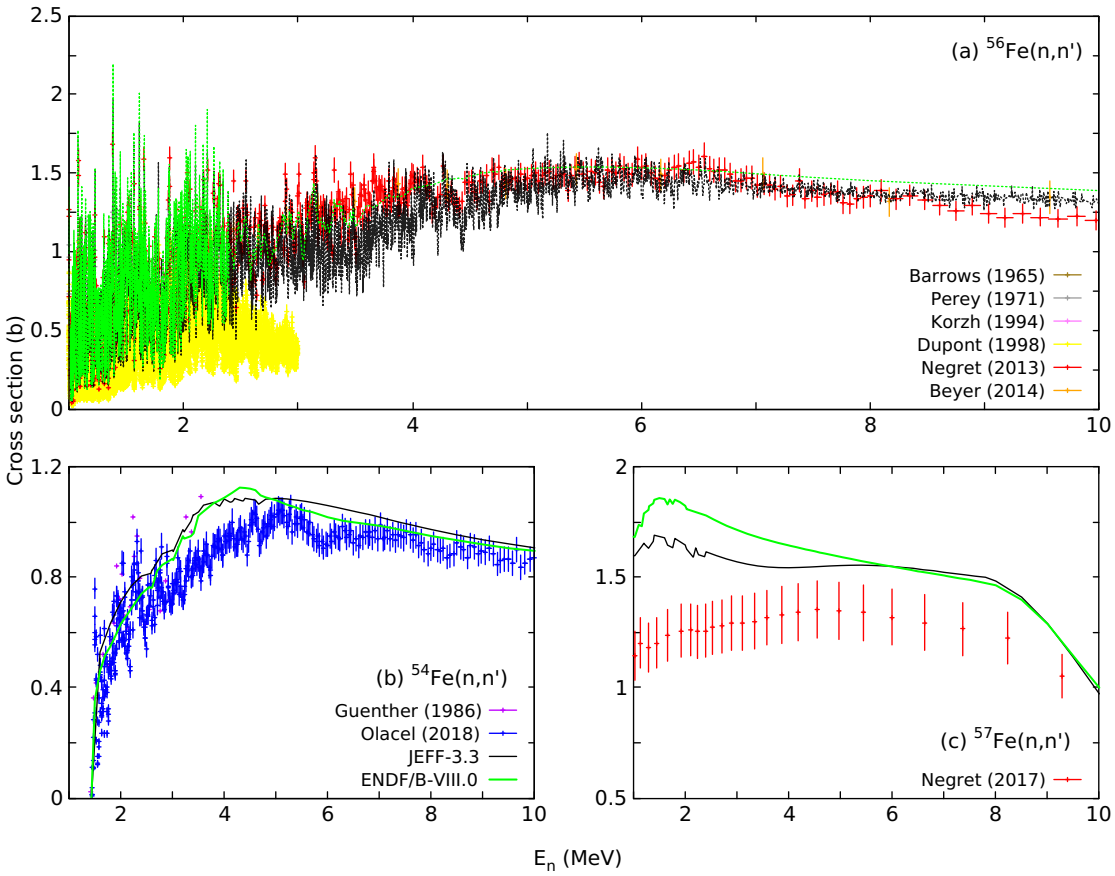

Figure 1.5: Comparison between the available experimental cross section data of neutron total inelastic scattering on (a) ^{56}Fe, (b) ^{54}Fe, (c) ^{57}Fe and the JEFF-3.3 [10] (black line) and ENDF/B-VIII.0 [9] (green line) evaluations in the energy region from 1 to 10 MeV.

Angular distributions

Furthermore, in the conclusion of the CIELO project concerns were expressed about the angular distributions of the elastic and inelastic scattering channels, data that are playing a crucial role in shielding, reflection and leakage. Especially for elastic scattering, the lack of angular distributions below 4 MeV was emphasized, since it was concluded that these data are important in calculating criticality and deep penetration. For ^{57}Fe and ^{58}Fe there are no experimental angular distributions reported in the EXFOR library and for ^{54}Fe only a few experimental data are available for elastic (Table 1.1) and inelastic scattering from the first excited state (Table 1.3) for a small number of detection angles using monoenergetic neutron beams. In the case of ^{56}Fe, the evaluations of

the angular distributions heavily rely on high-resolution scattering measurements of ^{nat}Fe that are available in the EXFOR library covering energies up to 4 MeV. These data need to be corrected for the contribution of the minor isotopes, a correction that increases the overall uncertainty in the final result. Specifically for ^{56}Fe, a few experimental angular distributions of neutron elastic (Table 1.2) and inelastic scattering from the first (Table 1.4) and the second (Table 1.5) excited levels are available in the EXFOR library. Even though the current evaluations are in relatively good agreement with the few experimental data for elastic scattering, in the case of inelastic scattering big discrepancies are observed both between the evaluations and the different experimental data (see Fig. 1.6).

Table 1.3: Partial inelastic scattering cross sections from the first excited level of ^{54}Fe (1.4082 MeV), available in EXFOR [13]. The name of the first author, the year of publication, the neutron energy range under study, the methodology, the quantity (CSP - Partial cross section and/or DAP - Partial differential c/s with respect to angle) and the number of points are listed.

E_{LVL1}=1.4082 MeV					
Reference		E_n range (MeV)	Method	Quantity (Points)	
Rodgers (1967)	[16]	2.33	n spectroscopy	CSP(1)	DAP(5)
Tsukada (1969)	[41]	2.65-3.26	n spectroscopy	CSP(1)	DAP(22)
Boschung (1971)	[17]	4.04-5.60	n spectroscopy	CSP(14)	DAP(29)
Fedorov (1973)	[18]	2.90	n spectroscopy	CSP(1)	DAP(8)
Kinney (1974)	[19]	5.50-8.50	n spectroscopy	CSP(3)	DAP(64)
Almen-Ramström (1975)	[42]	2.50-4.50	n spectroscopy	CSP(9)	
Korzh (1977)	[20]	2.00-3.00	n spectroscopy	CSP(3)	DAP(27)
El-Kadi (1982)	[21]	7.96-13.9	n spectroscopy	CSP(4)	DAP(104)
Guenther (1986)	[23]	1.30-3.97	γ spectroscopy	CSP(60)	
Korzh (1987)	[22]	5.00-7.00	n spectroscopy	CSP(3)	DAP(39)
Mittler (1987)	[43]	1.46-3.69	γ spectroscopy	CSP(29)	
Olacel (2018)	[39]	1.41-18.00	γ spectroscopy	CSP(326)	
Vanhoy (2018)	[24]	2.25-6.00	n spectroscopy		DAP(107)

Capture

The resonance analysis for the capture cross sections of all the iron isotopes have been performed using the Reich-Moore approximation. It is interesting to mention that the capture cross section of ^{56}Fe is very small due to the underlying nuclear structure in which the nucleons populate a nearly closed shell. Within the CIELO project, major changes were made and then adopted by the ENDF/B-VIII.0 evaluation. A background cross section component was added in the energy range from 10 eV to 100 keV. The enhancement of the capture cross section in this region was based on the criticality benchmark HEU-MET-INTER-001 (ZPR-9/34). It was observed that when the

Table 1.4: Partial inelastic scattering cross sections from the first excited levels of ^{56}Fe (0.8468 MeV), available in EXFOR [13]. The name of the first author, the year of publication, the neutron energy range under study, the methodology, the quantity (CSP - Partial cross section and/or DAP - Partial differential c/s with respect to angle) and the number of points are listed.

E_{LVL1}=0.8468 MeV					
Reference		E_n range (MeV)	Method	Quantity (Points)	
Stelson (1952)	[44]	1.87	n spectroscopy		DAP(1)
Weddell (1956)	[45]	6.5	n spectroscopy		DAP(1)
Cranberg (1956)	[46]	2.25-2.45	n spectroscopy		DAP(26)
Kardashev (1962)	[47]	1.00-3.95	γ spectroscopy	CSP(12)	
Bredin (1964)	[48]	1.95	n spectroscopy		DAP(10)
Gilboy (1965)	[49]	2.01-3.99	n spectroscopy	CSP(4)	
Tucker (1965)	[50]	0.864-1.10	γ spectroscopy	CSP(31)	
Smith (1966)	[51]	1.13-1.50	n spectroscopy	CSP(26)	
Rodgers (1967)	[16]	2.33	n spectroscopy	CSP(1)	DAP(5)
Degtjarev (1967)	[52]	1.37-3.76	n spectroscopy	CSP(7)	
Kinney (1968)	[25]	4.60-7.55	n spectroscopy	CSP(7)	DAP(85)
Barrows (1968)	[53]	2.90	γ spectroscopy	CSP(1)	
Tsukada (1969)	[41]	1.37-3.26	n spectroscopy		DAP(73)
Rogers (1971)	[54]	0.92-1.79	γ spectroscopy	CSP(10)	
Boschung (1971)	[17]	5.05-5.58	n spectroscopy	CSP(2)	DAP(19)
Tomita (1973)	[55]	1.43-2.15	n spectroscopy		DAP(225)
Elbakr (1973)	[56]	0.891-1.74	γ spectroscopy	CSP(8)	
Konobeevskii (1974)	[57]	0.862-1.18	γ spectroscopy	CSP(67)	
Korzh (1975)	[58]	1.50-3.00	n spectroscopy	CSP(4)	
Almen-Ramström (1975)	[42]	2.02-4.50	n spectroscopy	CSP(11)	
Mittler (1975)	[43]	0.878-3.96	γ spectroscopy	CSP(36)	
Korzh (1977)	[20]	1.50-3.00	n spectroscopy	CSP(4)	DAP (34)
Lebedev (1977)	[59]	4.70	n spectroscopy		DAP (3)
Schweitzer (1978)	[27]	3.40	n spectroscopy	CSP(1)	DAP (12)
Salama (1981)	[60]	2.02-3.96	n spectroscopy	CSP(6)	DAP (100)
Nemilov (1982)	[61]	0.893-5.00	γ spectroscopy	CSP(32)	
El-Kadi (1982)	[21]	7.96-13.90	n spectroscopy	CSP(4)	DAP(89)
Negret (2013)	[34]	0.861-4.50	γ spectroscopy	CSP(645)	
Beyer (2014)	[33]	0.847-9.56	γ spectroscopy	CSP(30)	
Ramirez (2017)	[28]	1.50-7.96	n spectroscopy	CSP(14)	DAP (180)
Vanhoy (2018)	[24]	1.50-4.70	n spectroscopy	CSP(17)	
Pirovano (2019)	[62]	1.99-6.01	n spectroscopy		DAP(1530)

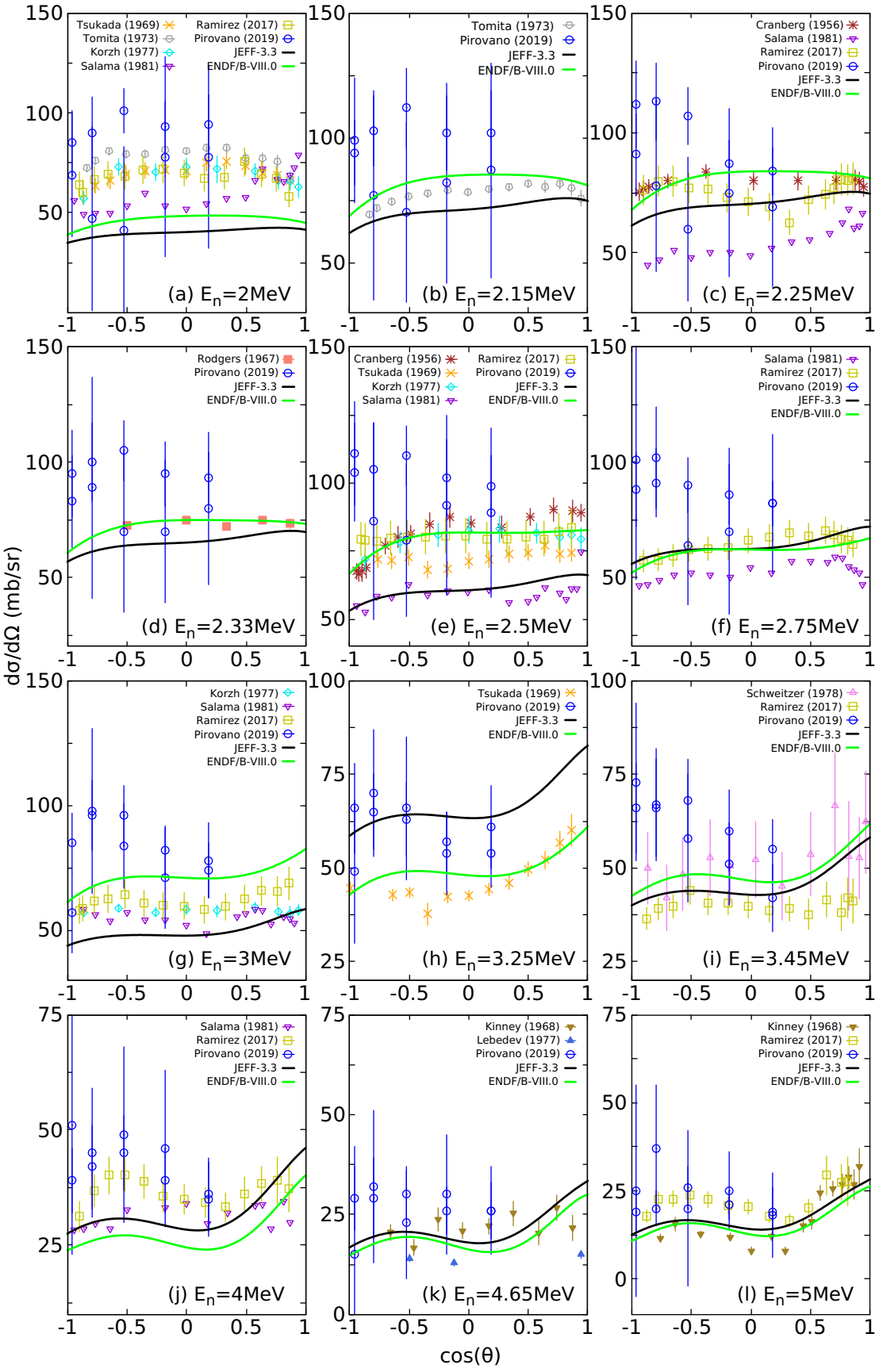

Figure 1.6: Comparison of differential cross sections of neutron inelastic scattering from the first excited state of ^{56}Fe as a function of the cosine of the scattering angle θ, between data available in the EXFOR [13] library and the angular distributions provided in the JEFF-3.3 [10] and ENDF/B-VIII.0 [9] evaluations. The corresponding incident neutron energy is reported in each graph.

Table 1.5: Partial inelastic scattering cross sections from the second excited levels of ^{56}Fe (2.0851 MeV), available in EXFOR [13]. The name of the first author, the year of publication, the neutron energy range under study, the methodology, the quantity (CSP - Partial cross section and/or DAP - Partial differential c/s with respect to angle) and the number of points are listed.

E_{LVL2}=2.0851 MeV					
Reference		E_n range (MeV)	Method	Quantity (Points)	
Weddell (1956)	[45]	6.5	n spectroscopy		DAP(1)
Kardashev (1962)	[47]	1.00-3.95	γ spectroscopy	CSP(6)	
Gilboy (1965)	[49]	2.01-3.99	n spectroscopy	CSP(3)	
Tucker (1965)	[50]	0.864-1.10	γ spectroscopy	CSP(23)	
Degtjarev (1967)	[52]	1.37-3.76	n spectroscopy	CSP(4)	
Kinney (1968)	[25]	4.60-7.55	n spectroscopy	CSP(12)	
Barrows (1968)	[53]	2.90	γ spectroscopy	CSP(1)	
Tsukada (1969)	[41]	1.37-3.26	n spectroscopy		DAP(34)
Boschung (1971)	[17]	5.05-5.58	n spectroscopy	CSP(2)	DAP(19)
Korzh (1975)	[58]	1.50-3.00	n spectroscopy	CSP(1)	
Almen-Ramström (1975)	[42]	2.02-4.50	n spectroscopy	CSP(7)	
Mittler (1975)	[43]	0.878-3.96	γ spectroscopy	CSP(21)	
Korzh (1977)	[20]	1.50-3.00	n spectroscopy	CSP(1)	DAP (9)
Nemilov (1982)	[61]	0.893-5.00	γ spectroscopy	CSP(7)	
Negret (2013)	[34]	0.861-4.50	γ spectroscopy	CSP(288)	
Beyer (2014)	[33]	0.847-9.56	γ spectroscopy	CSP(14)	
Ramirez (2017)	[28]	1.50-7.96	n spectroscopy	CSP(6)	
Vanhoy (2018)	[24]	1.50-4.70	n spectroscopy	CSP(13)	

ENDF/B-VII.1 evaluation [63] was used, the benchmark's eigenvalue was overestimated by more than 1000 pcm. It was realized that by making a minor readjustment in this energy region, it became possible to bring the HEU-MET-INTER-001 result within the experimental uncertainty, while minimally impacting other benchmarks. As seen in Fig 1.7. the added background cross section demonstrates a nearly 1/v behavior. Furthermore, the background from 700 to 850 keV was readjusted (see Fig. 1.8) to reproduce the experiments performed at RPI by McDermott et al. (2017) [64]. In this measurement, a "bump" in the capture yield was observed at around 850 keV. The increase of the (n,γ) cross section in this region cannot be described via the R-Matrix theory. Also, it is interesting to mention that in this energy the inelastic scattering channel opens, so one would expect the capture cross section to decrease and not the opposite.

Currently, the cross section data of iron are under study by the International Nuclear Data Evaluation Network (INDEN) [65], coordinated by the International Atomic Energy Agency (IAEA). In the latest evaluation released by INDEN in August 2023, the background component in the 10 eV - 100 keV region was reduced by more than 50% of what was introduced in the

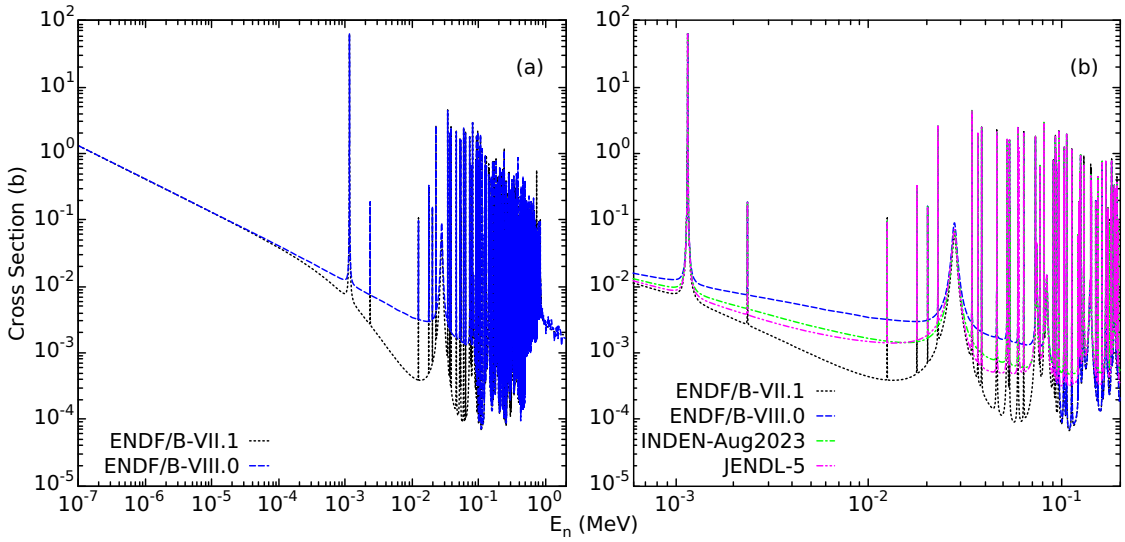

Figure 1.7: (a) Evaluated ^{56}Fe(n,γ) cross section of ENDF/B-VII.1 [63] (black) and ENDF/B-VIII.0 [9] (blue) from thermal up to 2 MeV neutron energy. (b) Comparison of the ^{56}Fe(n,γ) evaluated cross section of ENDF/B-VII.1 (black), ENDF/B-VIII.0 (blue), INDEN-Aug2023 [65] (green), and JENDL-5 [66] (magenta) in the 10 eV - 100 keV region.

ENDF/B-VIII.0 evaluation (Fig. 1.7b). This intermediate choice for the background component was still able to reproduce the HEU-MET-INTER-001 benchmark, and it also proved to be optimal for the ASPIS/Fe-88 benchmark. This change was also supported by the latest JENDL evaluation, JENDL-5 [66], where direct and semi-direct calculations for ^{56}Fe were considered.

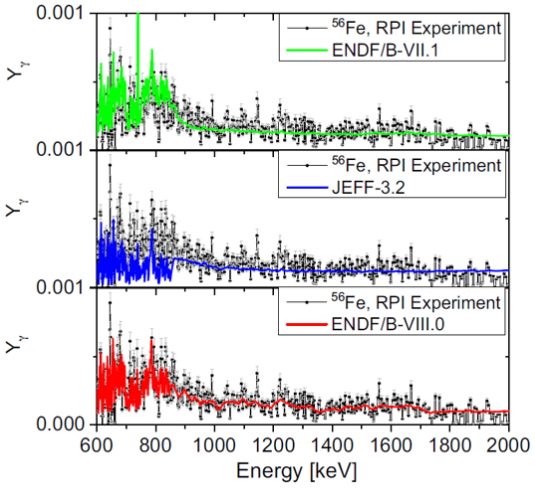

Figure 1.8: Comparison of calculated capture yields from the semi-integral experiment at RPI on ^{nat}Fe [12].

1.3 Objectives of the thesis

For the above mentioned reasons, new experimental cross section data are crucial for clearing out discrepancies, lowering uncertainties on the current evaluated libraries of iron and finally assisting in the development of models used for predicting the cross sections in different energy regions. The aim of this work is part of an effort to tackle some of the issues reported earlier in the most

important nuclear data of Fe affecting the quality of the evaluations, by performing new measurements and theoretical calculations. The present thesis is divided into three different parts. First, are the measurements for the first time high-resolution cross sections and neutron angular distributions for both elastic and inelastic scattering, in the fast neutron energy region, for the two most abundant isotopes in natural iron, i.e. ^{54}Fe and ^{56}Fe, to address the lack of experimental data. For the measurements, the ELISA spectrometer stationed at the GELINA facility was utilized and highly enriched samples for both isotopes were used. Furthermore, in order to study the 10 keV-100 keV energy region of the capture cross section of ^{56}Fe where the background component was added in the CIELO project, since this region cannot be measured experimentally via (n,γ) measurements, because the cross section in this region is too low thus it is not easy to properly discriminate the capture yield from the background contribution, two different approaches were followed. Neutron transmission measurements using natural iron samples of various thicknesses were performed to study the 24 keV energy region and the dips between the resonances. Additionally, direct radiative capture calculations for ^{56}Fe were performed. The goal is to combine the transmission experiments with the direct capture calculations, especially in the 24 keV energy region where the elastic scattering has a large dip and the total cross section practically equals the capture cross section (see Fig. 1.9) in an effort to provide a physical interpretation and possible physical constraints to the changes that were made.

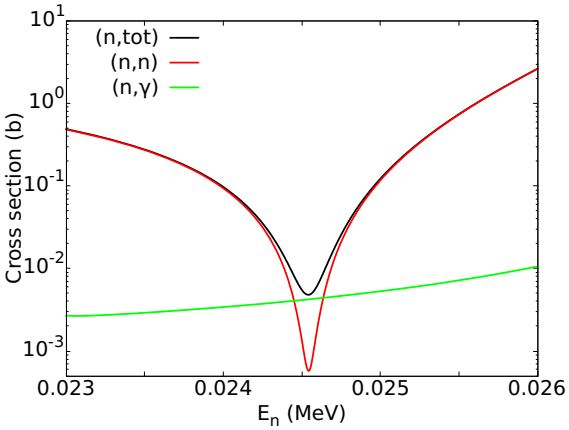

Figure 1.9: Cross sections of the total, elastic, and capture reaction of ^{56}Fe in the 24 keV neutron energy region from the latest INDEN [65] evaluation.

1.4 Organization of the thesis

A description of the GELINA facility, the time-of-flight technique, the ELISA spectrometer used for the scattering experiments and the characterization of the detectors placed in the setup is given in Chapter 2. The details of the different measurements, the analysis of the acquired data and the results of the scattering measurement on ^{54}Fe and ^{56}Fe are presented in Chapter 3. In Chapter 4 the transmission experiments are described along with the analysis and the extracted results. Finally, in Chapter 5 the calculations of the direct radiative capture on ^{56}Fe are presented and discussed.

Chapter 2

Neutron scattering on Iron: Experimental setup

The neutron scattering experiments were carried out at the white neutron source of the Geel Electron Linear Accelerator (GELINA) of the European Commission's Joint Research Centre (EC-JRC) in Geel, Belgium. This chapter contains a short description of the facility and the neutron production process. Additionally, the ELISA (ELastic and Inelastic Scattering Array) spectrometer, utilised in these experiments, along with the full characterization procedure for the determination of the detectors' neutron response is described in detail.

2.1 The GELINA white neutron source

The GELINA time-of-flight facility is a pulsed white neutron source built in 1965 [67]. It is a multi-user facility designed for high-resolution cross section measurements in the neutron incident energy range between 10 meV and 20 MeV. The facility consists of four main parts: the linear electron accelerator, a post-acceleration compression magnet, a neutron producing target, and 12 flight paths with different experimental equipment (see Fig. 2.1) [68–70].

The accelerator is an S-band linac producing short electron bursts of 10 ns duration with a 10 A peak current. It consists of three sections: a 2 m long standing wave buncher and two 6 m long traveling wave sections. The electron bursts are produced by a triode gun with an average energy range of about 80 keV. The maximum repetition rate of the accelerator is 800 Hz and each electron burst consist of a train of 30 pulses. Due to beam loading, the energy of the electrons in each burst decreases linearly, from 130 MeV for the first pulse to 70 MeV for the last pulse. After the acceleration and before colliding with the neutron producing target, the electrons are passing through a 360°deflection dipole magnet. The magnet consists of five magnetic sectors and is 3 m in diameter. The electrons traverse circles in the magnet with diameters determined by their momenta, meaning that high energy electrons will follow a trajectory with large diameter, while the less energetic ones will travel a shorter circle. This process ensures that all pulses will exit the magnet at the same time with a Gaussian time distribution of less than 1 ns duration.

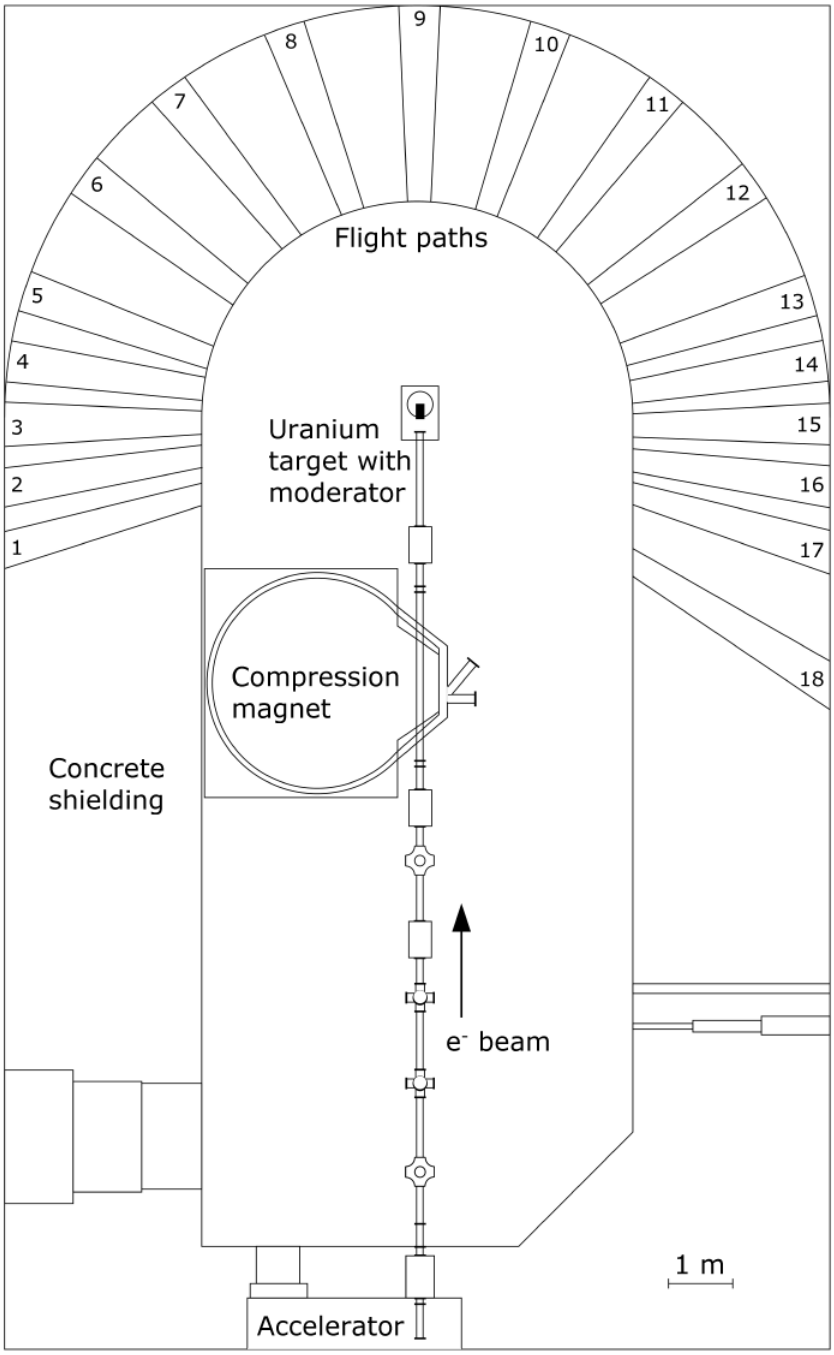

Figure 2.1: Schematic representation of the target area and compression magnet of the GELINA facility. The electron beam line, the compression magnet, the neutron producing target and the different flight paths are presented. Out of the 18 flight paths shown here, only 12 are used for measurements, while flight paths 7, 8, 9, 10, 11 and 18 are excluded.

After the compression magnet, the electrons are impinging on the neutron producing target (see Fig. 2.3) [71]. It is a rotating, mercury cooled target made out of a U-Mo alloy with 10%-weight Mo. Due to the high power density (10 kW/cm^3) deposited in the target, to avoid localized heating, the target rotates to spread the heat over its circumference. Mercury is chosen as a coolant,

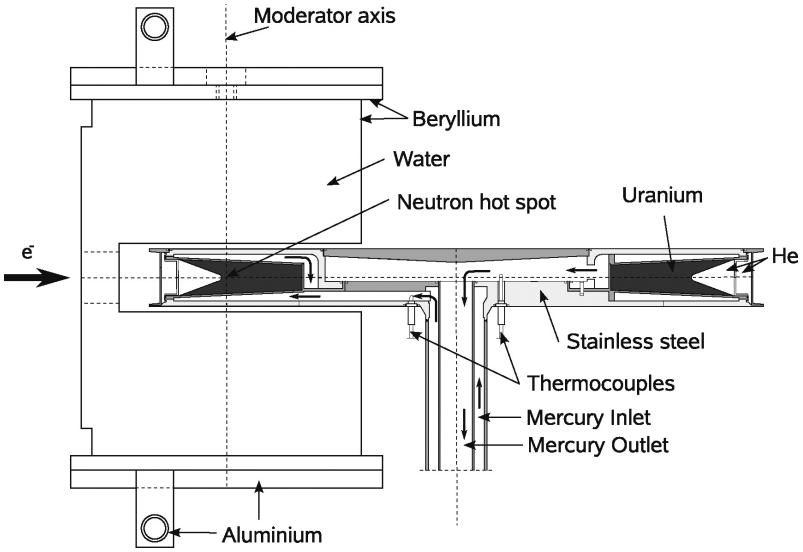

Figure 2.3: Scheme of the rotating neutron producing target of GELINA [72].

mainly to avoid neutron moderation. Uranium is chosen as the main material because it favours the production of photons in the bremsstrahlung process and has a high cross section for neutron production via photon-induced reactions [(γ, n) and (γ, f)] in the uranium nuclei. On average 3.4×10^{13} neutrons/s are produced with an evaporation spectrum and are emitted isotropically. To ensure a substantial number of neutrons with energy below 100 keV, a configuration involving two light-water moderators positioned above and below the target is employed. These moderators are beryllium containers filled with water. Two flux setups are at disposal (see Fig. 2.2). In one of them, collimators obstruct the moderators, and the flight path is exclusively exposed to the uranium disk, yielding a fast neutron spectrum referred to as Direct Flux Configuration (DFC). In the other one, shadow bars obstruct the uranium disk, allowing the flight path to be solely exposed to the moderators, resulting in an epithermal spectrum with a thermal component. This is known as the Moderated Flux Configuration (MFC) [72]. The produced neutron beam is constantly monitored using BF_3 proportional counters mounted at different positions in the ceiling of the target hall. These detectors may also be used for normalization of the measured spectra to the same neutron intensity.

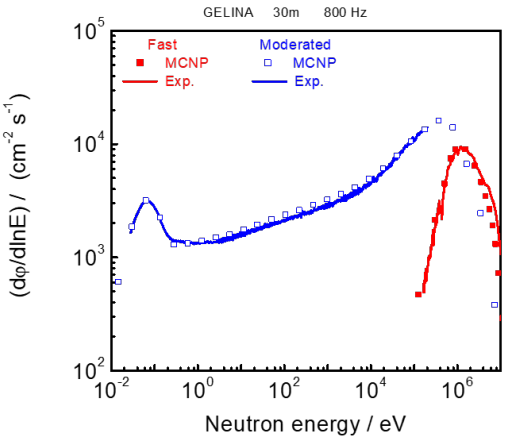

Figure 2.2: Comparison of the simulated and experimental neutron flux distributions of the DFC and MFC configurations of GELINA [72].

GELINA provides twelve flight paths in a star-like configuration around the neutron producing target. The produced neutrons travel in tubes of 50 cm diameter kept under vacuum conditions.

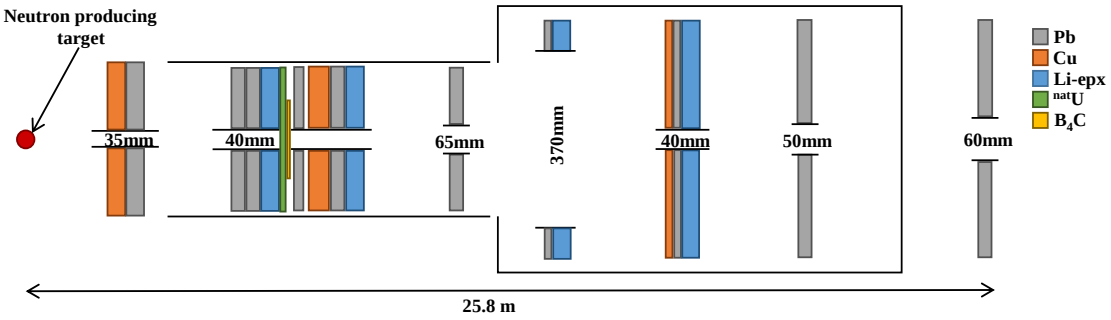

Figure 2.4: Schematic description of the filter system installed inside the tube of flight path one.

The flight paths are varying in length, from the shortest one at 10 m to the longest one at 400 m. Along each flight path, multiple measurement stations are positioned in different distances. These stations are equipped with diverse detectors and specialized data acquisition systems, meticulously combined for the precise measurements of neutron induced reaction cross sections. The experimental setup used in this work is installed at flight path one at 108°with respect to the electron beam direction, at the 30 m station. In this flight path the direct flux configuration was used supplying a useful neutron spectrum with energies from 100 keV to almost 10 MeV. Inside the flight tube a collimation system is installed to define the size of the beam (see Fig. 2.4). The collimators consist of layers of specially chosen materials absorbing different components of the beam. These materials are: lithium epoxy for the absorption of slow neutrons, copper for fast neutrons, and lead for photons. Furthermore, two filters, one made of depleted uranium and the other one of boron carbide, are placed in the flight path tube, at the exit of the target hall, in order to minimize the intensity of the bremsstrahlung and the thermal neutron component. The beam size was measured at the sample position using a photographic film, resulting in 4.9(2) cm diameter.

2.2 Time-of-flight technique

For the determination of the incident neutron energy the time-of-flight technique was used.The basic principle of neutron spectroscopy using the time-of-flight method lies in the measurement of the time t that a neutron needs to travel a given distance L. The velocity u of the neutron is simply given by:

$$u = \frac{L}{t} \tag{2.1}$$

and therefore the kinetic energy E is:

$$E = m_n c^2(\gamma - 1), \tag{2.2}$$

where m_n is the neutron mass, c is the speed of light, and γ is the relativistic Lorentz factor:

$$\gamma = \frac{1}{\sqrt{1-(u/c)^2}}. \tag{2.3}$$

In the experiment, the time-of-flight t_m is determined from the difference between a start T_0 and a stop t_n signal:

$$t_m = t_n - T_0. \tag{2.4}$$

At GELINA the start signal is generated every time an electron burst passes through a coil just before impinging on the neutron producing target. To account for the time offset related to the difference in cable lengths, the strong bremsstrahlung (γ-flash) produced from every burst is used as a time reference and the starting signal is expressed as:

$$T_0 = t_\gamma - L/c, \tag{2.5}$$

where t_γ is the detection time of the γ-flash and L/c is the time required for a photon to travel from the source to the detector. The stop signal is produced when a neutron enters one of the detectors. In a scattering experiment, the time-of-flight is determined by combining the time the neutron needs to travel from the source to the scattering sample, with the time the scattered neutron needs to travel from the sample to the detector. In this case the time of flight is calculated using the formula:

$$t_m = \frac{L}{c\sqrt{1-1/(1+E_0/m_nc^2)^2}} + \frac{L'}{c\sqrt{1-1/(1+E'/m_nc^2)^2}}, \tag{2.6}$$

where E_0 and E' is the kinetic energy before and after the collision, L is the distance between the neutron producing target and the scattering sample, and L' is the distance between the sample and the detector. For elastic scattering, by knowing the nuclear mass M of the scattering sample and the detection angle θ, the kinetic energy after the collision E' can be described as a function of the kinetic energy before the collision E_0 based on the conservation of energy and momentum:

$$E'(Mc^2+mc^2) - E_0(Mc^2-mc^2) + E_0E' = c^2p_0p'\cos\theta, \tag{2.7}$$

where $p_0 = \sqrt{E_0(E_0+2mc^2)}/c$ and $p' = \sqrt{E'(E'+2mc^2)}/c$ are the momentum before and after the collision. By combining equations (2.6) and (2.7) the incident neutron energy can be extracted. In the case of inelastic scattering, the excitation energy E^* of the target nucleus needs to be taken into account and therefore the conservation of energy and momentum is given by:

$$2E'(Mc^2+mc^2) - 2E_0(Mc^2-mc^2) + 2E_0E' + E^*(2Mc^2+E^*) = 2c^2p_0p'\cos\theta \tag{2.8}$$

and by combining equations (2.6) and (2.8) the incident neutron energy for inelastic scattering is calculated. The detailed calculations to extract the formulas mentioned above are given in Appendix A.

2.3 The ELISA spectrometer

For the detection of the scattered neutrons, the ELastic and Inelastic Scattering Array (ELISA) was used [62, 73–75]. ELISA was developed in 2016 and is one of the various experimental

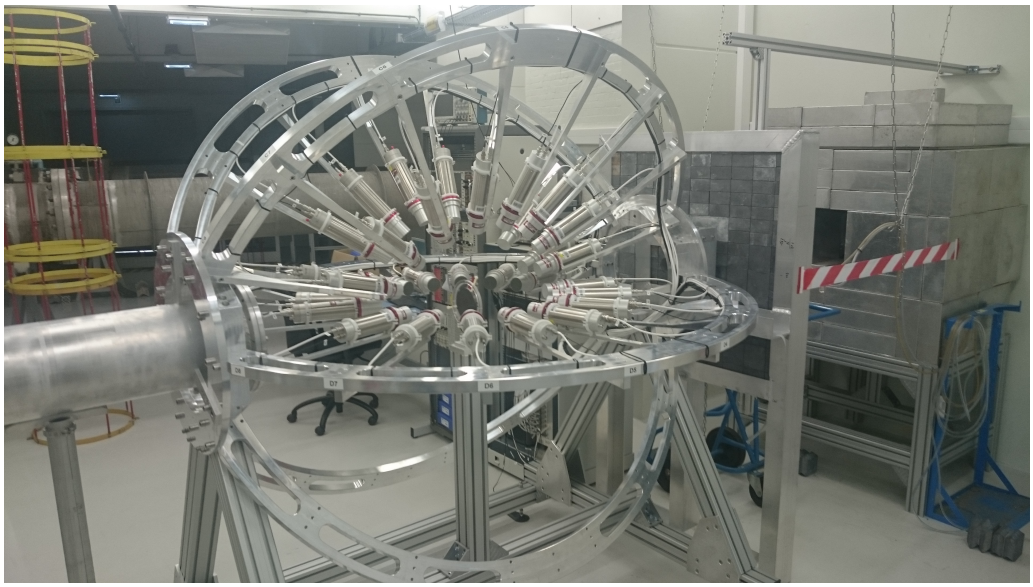

Figure 2.5: The ELISA spectrometer currently installed at the flight path 1 of GELINA. The neutron beam comes from the right, first passing through the fission chamber which is placed behind the lead wall and then reaching the scattering sample at the center of the setup.

setups currently installed at the GELINA neutron time-of-flight facility. The setup is designed for the high-resolution measurement of elastic and inelastic scattering cross sections and angular distributions in the fast neutron energy region. The concept of measuring double differential neutron-emission cross sections dates back to the end of the eighties, when a similar detector array, featuring 8 liquid organic scintillators, was designed and developed at GELINA [76]. The development of ELISA was based on this past experience. One of the main differences between the two setups is that in the old array, the detectors were placed as close as possible to the sample without interfering with the neutron beam, while at ELISA, the detection angles were carefully chosen based on the possibility of applying numerical techniques for the angle integration. To achieve high accuracy in the detection angles, the distance between the detectors and the sample position had to be increased.

Currently, the spectrometer consists of two main parts: 32 liquid organic scintillators for the detection of the scattered neutrons, and a ^{235}U fission chamber for the measurement of the neutron flux (see Fig. 2.5). The scintillators are divided into 4 sets of 8 detectors each, mounted at specific angles with respect to the neutron beam direction (see Fig. 2.6). In general the scattering differential cross section with respect to the incident neutron energy E and the scattering angle θ is described as a Legendre expansion:

$$\frac{d\sigma}{d\Omega}(E,\theta) = \frac{\sigma(E)}{2\pi}\sum_{l=0}^{N_l}\frac{2l+1}{2}\alpha_l(E)P_l(\cos\theta_i), \tag{2.9}$$

where $\sigma(E)$ is the scattering cross section, $P_l(\cos\theta_i)$ is the l^{th} order Legendre polynomials, $\alpha_l(E)$ is the corresponding coefficient, and N_l is the highest order for which the Legendre coefficient

Table 2.1: The 8 different detection angles with respect to the neutron beam direction. Their corresponding cosine and weight used for the numerical quadrature are also given.

Angle (θ_i) **(deg)**	163.8	142.8	121.7	100.6	79.4	58.3	37.2	16.2
cosθ_i	-0.9603	-0.7967	-0.5255	-0.1834	0.1834	0.5255	0.7967	0.9603
Weight (w_i)	0.1012	0.2224	0.3137	0.3627	0.3627	0.3137	0.2224	0.1012

is available. In the ELISA setup, the detection angles have been carefully chosen, so that their corresponding cosines match the zeros of the Legendre polynomial of the 8th order. This allows the calculation of the integral cross section $\sigma(E)$ using the Gauss-Legendre quadrature rule:

$$\sigma(E) = 2\pi \sum_{i=1}^{8} w_i \frac{d\sigma}{d\Omega}(E, \cos\theta_i), \qquad (2.10)$$

where $\frac{d\sigma}{d\Omega}(E, \cos\theta_i)$ is the differential cross section as a function of the incident neutron energy E and scattering angle θ_i, and w_i are the corresponding weight factors (Table 2.1). The method is exact for Legendre polynomials of order 15 and remains highly accurate for higher orders, extended samples and numbers of detectors [73].

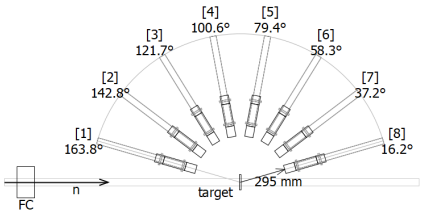

Figure 2.6: Schematic of one of the sets with the 8 detectors mounted at the detection angles. A relative description of the position of the scintillators-target-fission chamber (FC) system is presented [73].

2.3.1 Liquid organic scintillators

Liquid organic scintillators are frequently employed in the detection of fast neutrons due to their unique properties that make them well-suited for this purpose. They have a high sensitivity for fast neutrons, fast response time, ability to discriminate between different types of radiation, and their efficiency is reaching maximum value at energies between 1 to 2 MeV, making them valuable tools in various scientific and industrial contexts, including nuclear physics and radiation monitoring. These scintillators consist of aromatic hydrocarbons, such as benzene or xylene, doped with specific organic compounds. When fast neutrons interact with the scintillator material, they produce recoil hydrogen nuclei (protons/deuterons) via scattering reactions. The organic scintillator, in turn, captures these nuclei and undergoes a rapid excitation, producing flashes of light.

In the ELISA spectrometer, two different types of commercially available liquid organic scintillators, manufactured by Scionix, are used. Half of the detectors (model:51A51/2MQOE1-EJ301-NX) use the EJ301 scintillator material, a liquid based on xylene (C_8H_{10}) (NE213 equivalent) [77] and the other half use the EJ315 (model:51A51/2MQOE1-EJ315-NX), which is highly purified deuterated benzene (C_6D_6) [78] (details in Table 2.2). These are fast scintillators with a time resolution below 1 ns. They are suitable for neutron spectrometry since photon/neutron separation can be achieved via pulse shape analysis. The reason behind using two different types of detectors, hydrogen (EJ301) and deuterium (EJ315) based, is that the detected neutrons create two

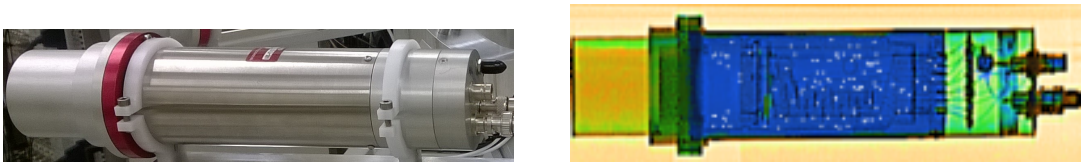

Figure 2.7: Left: photograph of one of the detectors placed at the ELISA setup. Right: X-ray scan of one of the detectors where the void in the liquid volume cell and the electronic circuits of the PMT are visible.

different pulse height responses which provides a cross check between the two types, and assists in the discovery of systematic errors during the data analysis.

The detectors have a cylindrical shape with a liquid cell of 5.08 cm height and of 2.54 cm radius, filled up to 97% with the corresponding hydrocarbon liquid (see Fig. 2.7). They have an aluminum housing of 1.52 mm thickness, sealed with a quartz window that provides an optical coupling to the photomultiplier tube (PMT, Electron Tubes Ltd., model 9213). The PMT and the corresponding voltage divider are mounted in a μ-metal housing of 0.64 mm thickness, shielding them from external magnetic fields. The scintillation liquid emits light pulses, which are then gathered by the light guide (represented by the quartz window) and transformed into electrons, commonly referred to as photoelectrons, by the photocathode within the Photomultiplier Tube (PMT). These photoelectrons undergo acceleration towards the PMT dynodes, where they undergo a cascade process, multiplying through secondary electron emission. The voltage provided to the dynode chain via the voltage divider needs careful optimization to maximize the multiplication process while maintaining linearity. This fine-tuning ensures that the charge pulses registered at the PMT's anode remain proportionate to the light output originating from the scintillator.

2.3.2 Ionization chamber

The ionization chamber contains a set of 8 UF_4 deposits on 5 aluminum foils of 84 mm diameter and 20 μm thickness (see Fig. 2.8). The deposits were manufactured at the JRC-Geel, using the evaporation technique. The isotopic composition of the material used for the manufacturing of the deposits is presented in Table 2.3. The diameter of the deposits is 70 mm, determined by the

Table 2.2: Composition and physical properties of the EJ301 and EJ315 scintillation materials [77, 78].

	EJ301	**EJ315**
Number of ^{1}H atoms per cm^2	$4.82{\cdot}10^{22}$	$0.0287{\cdot}10^{22}$
Number of ^{2}H atoms per cm^2	-	$4.06\ 10^{22}$
Number of C atoms per cm^2	$3.98{\cdot}10^{22}$	$4.10\ 10^{22}$
Density at 25°C (g/cm^3)	0.874	0.954
Scintillation liquid volume (cm^3)	105.9	105.9
Scintillation efficiency (photons/1 MeV electrons)	12000	9200
Wavelength of maximum emission (nm)	425	425

evaporation mask that was used. The total areal density of ^{235}U was experimentally determined by alpha counting and it was found to be 4095(4) μg/cm^2. Two single-sided foils are placed in the front and the back of the chamber, facing forward with respect to the neutron beam, and three double-sided are placed in the middle, each with a 14 mm distance between them. Each deposit is facing the corresponding anode, i.e. a 25 μm thick aluminum electrode, placed at a distance of 7 mm for the recording of the fission fragments. The electrodes are supplied with a positive voltage, while the aluminum foils supporting the deposits are grounded. The front window of the chamber has a 0.3 mm thickness while the back one is 0.2 mm thick. The fission chamber is filled with P10 gas (10% methane - 90% argon) at atmospheric pressure with a small flow rate continuously refreshing the counter gas to maintain stable operation.

Table 2.3: Areal density of the UF_4 deposits inside the ionization chamber. The ^{235}U content was determined by defined solid-angle alpha counting using the total alpha activity and an isotopic composition determined by mass spectrometry (see below).

Target	μg U/cm^2	μg ^{235}U/cm^2
Target 1	622(1)	622(1)
Target 2 side 1	488(1)	488(1)
Target 2 side 2	464(1)	463(1)
Target 3 side 1	489(1)	488(1)
Target 3 side 2	459(1)	458(1)
Target 4 side 1	487(1)	487(1)
Target 4 side 3	461(1)	461(1)
Target 5	628(1)	628(1)

U-isotope	^{233}U	^{234}U	^{235}U	^{236}U	^{238}U
Abundance	< 0.001	0.035973(75)	99.9336(14)	0.009629(53)	0.0207(14)

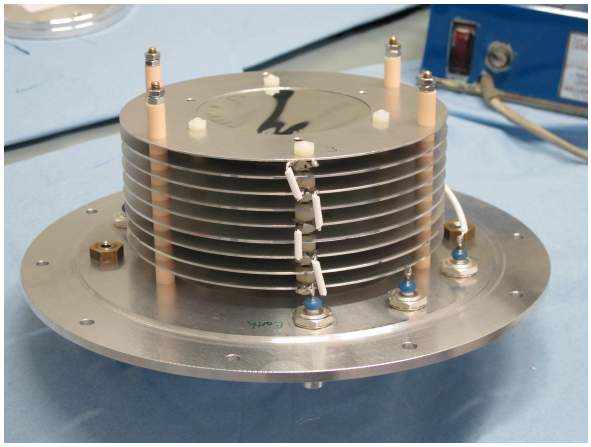

Figure 2.8: Stack of the UF_4 deposits and the aluminum electrodes inside the parallel plate ionization chamber.

2.3.3 The data acquisition system

For the data acquisition of the scintillators, a dedicated digitizer-based system was developed at GELINA. It features 8 digitizer cards with 4 channels each, manufactured by SP Devices (model: ADQ14DC-4A-VG-PXIe). The cards have a 500 MS/s sampling rate and 14 bit amplitude resolution. They are installed in a PXIe chassis (ADLINK PXES-2780) and controlled by a Red Hat Enterprise Linux 6.4 operating system. The digitizer's clocks are synchronized by an external 10 MHz reference coming from a clock generator (Stanford Research Systems Inc. CG635). The signals are recorded from the anode output of the PMT of each detector. Every channel triggers independently of the other when a signal surpasses the given threshold. The timestamps of the recorded signals are directly related to the linac reference signal ("T_0 signal"), which is connected to the digitizers as an external signal and resets the time for every neutron burst. To account for the fact that the T_0 signal arrives at the digitizers later than the signals produced by the γ-flash, but before the neutron burst, a digital delay generator (Stanford Research Systems Inc. DG535) is utilized to ensure that it arrives later also than the neutrons. This means that the time reference of the time-of-flight is given after every neutron burst. All recorded signal information, including waveforms and timestamps, are saved on the disk for offline analysis.

The data acquisition system used for the fission chamber is based on NIM electronics (see Fig. 2.9). First, the recorded signals pass through a charge integrating preamplifier (CSTA2HV) and then are split in two directions. On one direction, the signal passes through a spectroscopic amplifier (Ortec 671) and from there to an Analog-to-Digital Converter (ADC, FAST ComTec 7072). On the other direction, the signal is first passing through a fast filter amplifier (Ortec 579), then a constant fraction discriminator (CFD, Ortec 584), and ends up to a Time-to-Digital Converter (TDC, developed at the JRC). The TDC functions as a stopwatch: the T_0 signal starts the clock, and the timestamps of fission chamber signals are gauged in relation to it. To address any disparity in the arrival times of T0 and fission chamber signals, adjustments are made by delaying (via cable delay) the CFD signals. This ensures the precedence of the T_0 signal arrival at the TDC. The information coming from the ADC and the TDC are synchronized in time for each incoming signal using a multiplexer (MMPM, developed at the JRC) and gets stored for offline analysis.

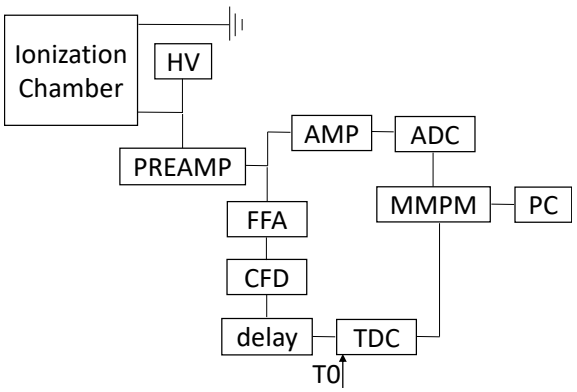

Figure 2.9: Schematic description of the data acquisition system for the ionization chamber. HV: high-voltage, PREAMP: preamplifier, FFA: fast filter amplifier, CFD: constant fraction discriminator, TDC: time-to-digital converter, MMPM: multiplexer, AMP: amplifier, ADC: analog-to-digital converter.

2.4 Characterization of the detectors

As mentioned above, scintillation fluorescent light is emitted when ionizing radiation interacts with the liquid scintillation material of the detectors. In reality, only a portion of the deposited energy is transformed into light, while the remaining energy is mainly dissipated as heat. The proportion of energy converted into photons is influenced by both the particle's energy and the stopping power of the scintillation material. The light output exhibits a linear relationship with energy for electrons surpassing 40 keV, while for protons, deuterons, and heavier ions, the output is consistently lower than that of electrons with equivalent kinetic energy, and the response does not follow a linear behavior with respect to energy [79].

Two types of ionizing radiation can be detected with the scintillators used at the ELISA spectrometer, neutrons and photons. In the case of photons, they transfer their energy by interacting with the orbital electrons of the molecules in the liquid, mainly via Compton scattering. In the case of neutrons, the detection mechanism is based on elastic scattering on the hydrogen nuclei of the liquid molecules (protons for the EJ301 and deuterons for the EJ315). Since these are hydrocarbon liquids, neutrons interact also with the carbon nuclei, but the produced light of the carbon recoil is typically low and the signals are below the detection threshold.

To extract meaningful information, a full characterization of the detector's response function $R(L,E)$, which represents the probability of a particle with an energy E producing a light pulse with amplitude L, needs to be performed. The method followed in the present work was a combination of measurements and Monte Carlo simulations as described in [80–83]. The characterization of the detectors is repeated for every different experimental campaign at the ELISA spectrometer, in order to monitor the stability of the detectors and identify problems that might have occurred during the measurements. In the next subsections the steps followed for the characterizations of the detection system are described in detail.

2.4.1 Signal processing

The signals generated by liquid organic scintillators exhibit a rapid rise time, primarily influenced by the characteristics of the photomultiplier tube, and a tail composed of a fast and a slow component. The predominant contributor to light emission is the fast component, known as prompt fluorescence, characterized by a typical decay time in the order of a few nanoseconds. Conversely, the slow component, identified as delayed fluorescence, undergoes decay over a few hundred nanoseconds. The ratio between the intensity of the slow and fast components is once again contingent on stopping power, being higher for particles inducing greater ionization density in the liquid [84].

The first step in the characterization of the detectors is the processing of the signals recorded by the scintillators. For every produced waveform the total integrated charge (light output equivalent) and the corresponding timestamps are extracted (see Fig. 2.10). A correction is implemented to the timestamps, to improve the time resolution using the constant fraction discrimination algorithm

(CFD) [85–88]. Based on this algorithm, the signals undergo two different processes on either side: on one side, they are inverted and delayed by a 3 ns delay, and on the other side, they are attenuated by a constant fraction of 30%. These two modified components are then summed together, and the zero-crossing point of the resulting waveforms is identified. This zero-crossing point represents an accurate measure of the signal's timing information. By focusing on a fraction of the pulse height and introducing a delay, CFD improves timing resolution by emphasizing the rising edge of the signal, where signal-to-noise ratio is typically higher, contributing to more accurate estimation of the arrival time of the signal.

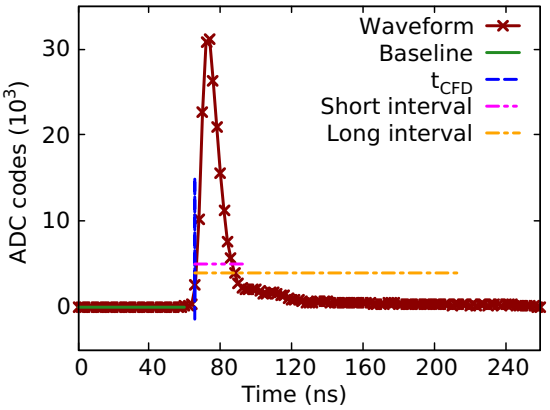

Figure 2.10: Example of a recorded signal. The time correction based on the CFD algorithm, along with the intervals for the pulse shape discrimination are presented.

To distinguish neutrons from photon induced events the recorded signals undergo a pulse shape analysis. In this work, the charge integration method was used [89, 90]. The recorded waveforms are integrated over two intervals, a short (Q_S-30 ns) one and a long (Q_L-150 ns) one that has the same start as the short one (starting point as it occurs from the CFD algorithm) but stops right before the tail of the waveform begins (see Fig. 2.10). The pulse shape discrimination (PSD) factor is defined as the ratio of the integral of the tail (Q_L-Q_S) to the long interval (Q_L) (Eq. (2.11)). In Fig. 2.11, the resulting pulse shape discrimination spectra, obtained from a measurement with an AmBe source, are presented with respect to the light output, for one of the EJ301 and one of the EJ315 detectors.

$$PSD = \frac{Q_L - Q_S}{Q_L} \tag{2.11}$$

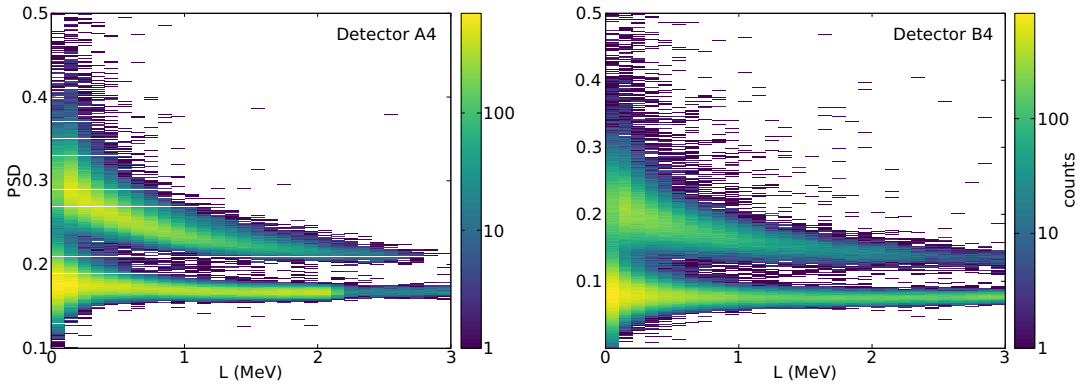

Figure 2.11: Two-dimensional pulse shape discrimination (PSD) spectrum of an AmBe source measurement as a function of the light output (L) for one an EJ301 (left) and an EJ315 (right) detectors. The top part of the spectra corresponds to the neutron induced events (higher tail-to-total ratio) and the bottom part correspond to photon induced events (lower tail-to-total ratio).

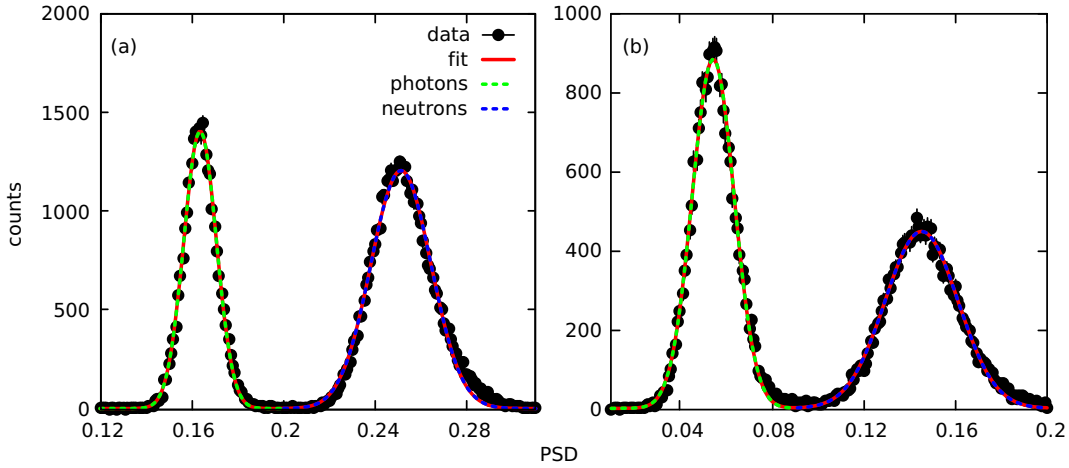

Figure 2.12: Two slice histograms of the PSD distributions, one for each type of detectors [EJ301 (a) & EJ315 (b)]. Fits are shown for the full histogram (sum of two Gaussians) as well as for individual photon and neutron clusters (individual Gaussians).

The charge integration pulse shape discrimination method works particularly well for high-energy depositions, but is prone to misclassification of events for relatively low-energy depositions. To determine the optimal PSD factor and minimize the number of misclassified events the methodology described in Ref. [91] was followed. According to this method, the data are sliced into smaller subsets based on the total integrated charge and the resulting PSD distributions of each slice is fitted with the sum of two Gaussian functions, one corresponding to photons f_γ and the second one for neutrons f_n (see Fig. 2.12). Then the fitted data are used to determine the optimal discrimination point within each slice, which is defined as the ratio that misclassifies the smallest number of particles in the slice. This ratio is found by solving:

$$PSD_{opt} = \arg\min_{x\in[0,1]} \left(\int_x^1 f_\gamma(x)\,dx + \int_0^x f_n(x)\,dx \right). \tag{2.12}$$

The first and second integrals in Eq. (2.12) compute the portion of the photon and neutron, respectively, that will be misclassified when setting x as the discrimination point. However, if the data set contains an overwhelming number of pulses from one type of particle, usually observed in the low light output region, the minimization could result in a discrimination point that misclassifies a large percentage of the less prevalent particle (see Fig. 2.13). To avoid possible effects this might have to the final resuls, during the analysis of the acquired data, proper thresholds (typically at 0.2 MeV)

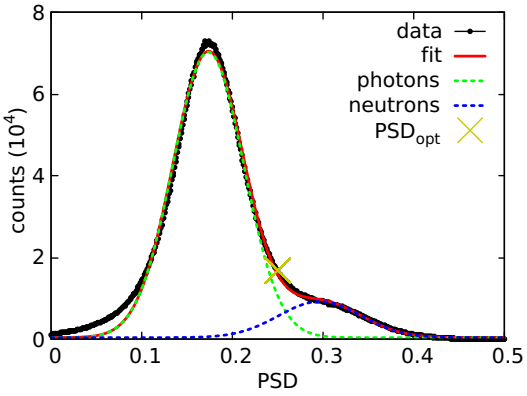

Figure 2.13: Example of PSD distribution for light outputs between 0 and 0.2 MeV.

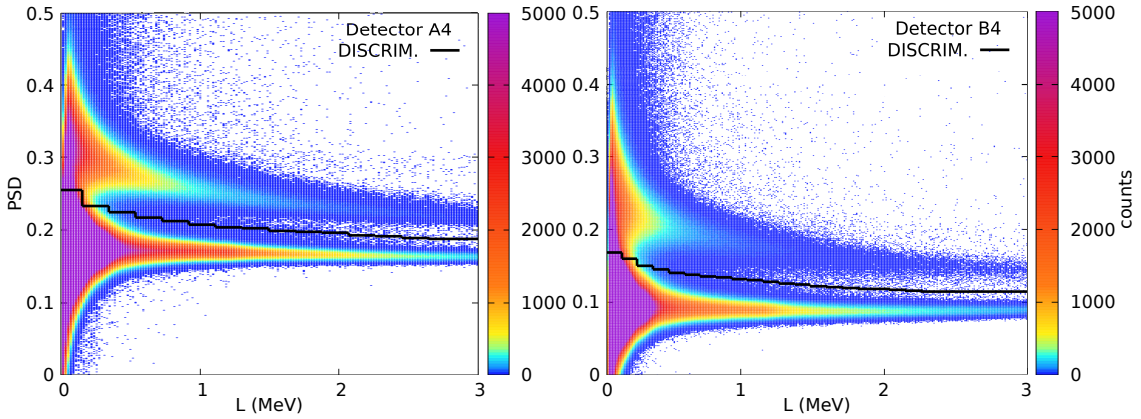

Figure 2.14: The two-dimensional pulse shape discrimination (PSD) spectra as a function of the light output (L) for one an EJ301 (left) and an EJ315 (right) detectors. The black line (DISCRIM.) represents the optimal separation point between neutron (upper part) and photon (lower part) induced events.

were implemented. In Fig. 2.14 the two-dimensional histograms of the signals recorded during the measurement of one of the samples studied in the present work as a function of the light output for an EJ301 and an EJ315 detector are presented. The black line that separates neutron from photon induced events, represents the optimal separation point determined using Eq. (2.12).

2.4.2 Determination of the response function

Once all signals are processed, the next step is the characterization of the detector's response function $R(L,E)$. This functions reflects the likelihood that after the detection of a photon or neutron with energy E a light output signal L is produced. This probability is influenced by factors such as the probability (cross section) of a photon or neutron interacting with the scintillation liquid, transferring a specific amount of energy E' to the electrons (for photons) or hydrogen (for neutrons), and on the relationship between deposited energy and light output, i.e. the light output function $L' = L(E')$. In the present work, the response function of each detector was approximated by the convolution of two functions [80]:

$$R(L,E) = \int r(L,L')N_{theor}(L',E)dL', \tag{2.13}$$

where $N_{theor}(L',E)$ is the "theoretical" light output distribution produced by the irradiation of a detector with monoenergetic photons or neutrons, determined via Monte Carlo simulations, and $r(L,L')$ is the resolution function parametrized with a Gaussion distribution with varying width [79]:

$$r(L,L') = \frac{1}{\sqrt{2\pi\sigma_{L'}^2}} e^{-\frac{(L-L')^2}{2\sigma_{L'}^2}}. \tag{2.14}$$

The variance $\sigma^2_{L'}$ of the light output distribution was determined using the empirical approximation [92, 93]:

$$\sigma^2_{L'} = B_0^2 + B_1^2 L' + B_2^2 L'^2, \tag{2.15}$$

where every parameter represents an independent contribution due to the:

- B_0: noise of the photomultiplier and the electronic circuits
- B_1: statistical fluctuations of the light production and amplification
- B_2: position-dependent light transmission from the scintillator to the photocathode

Both the light output and resolution function are characteristic for each individual detector, therefore in the present work a separate response function was developed for each detector used at the ELISA spectrometer.

2.4.2.1 Response functions for γ-rays

Starting with the response to γ-rays the light output function needs to be parametrized. Light output functions have been extensively studied for a variety of scintillators of different type and size, and they have been found to be strongly dependent on the charged particle creating the light pulse, i.e. electrons in the case of γ-ray detection [94–97]. For the scintillators used at the ELISA spectrometer, the light output produced by electrons with energy 0.04 MeV$\leq E_e \leq$ 1.6 MeV is described by the linear function:

$$L(E_e) = A_1(E_e + A_0), \tag{2.16}$$

where A_1 is a constant scaling arbitrarily chosen parameter set to 1 in the present work, following the convention of measuring light in terms of equivalent electron energy deposition [98] and A_0 is an energy offset set to -5 keV, accounting for the quenching effects in the scintillators at small energies [99].

Following the parametrization of the light output function for γ-rays, a combination of experimental measurements and Monte Carlo simulations were performed. First, a set of calibration measurements using radionuclide γ-ray sources was performed. The sources that were used and their properties are presented in Table 2.4. They were placed in the sample position of the spectrometer, 29.5(1) cm away from the detectors. Then, detailed Monte Carlo simulations of these measurements were carried out for the determination of the "theoretical" light output distributions N_{theor}. For the simulations the MCNP6.2 [100, 101] code was used. A detailed description of the geometry of the detectors was given as input (see Fig. 2.15). Both type of detectors used at the ELISA spectrometer (EJ301 & EJ315) have the same dimensions. In the simulation model, the detector is placed horizontally at a distance of 29.5 cm from the particle source. The sources were defined as isotropic with the same properties and geometrical characteristics as the ones used in the actual measurements. The simulated light output distributions can be obtained with MCNP by tallying the energy distribution of the pulses created in the liquid volume cell (tally "F8"). In Fig. 2.16[(a) to (c)] the simulated Compton spectra of the

Table 2.4: Characteristics of the γ-ray sources. The half-life, the activity, the energy of the emitted γ-rays, the corresponding energy of the Compton edge, and their intensity are given for each isotope.

Source	$T_{1/2}$ (y)	A_d (kBq)	E_γ (keV)	E_c (keV)	I (%)
^{137}Cs	30.05	365.57	662	477	85.10
^{207}Bi	32.90	359.78	570	394	97.75
			1064	858	74.50
			1770	1547	6.87
^{22}Na	2.61	139.22	511	341	180.76
			1275	1062	99.94
^{232}Th	$1.4 \cdot 10^{10}$	N.A.	2615	2382	-
AmBe	432.60	N.A.	4438	4196	-

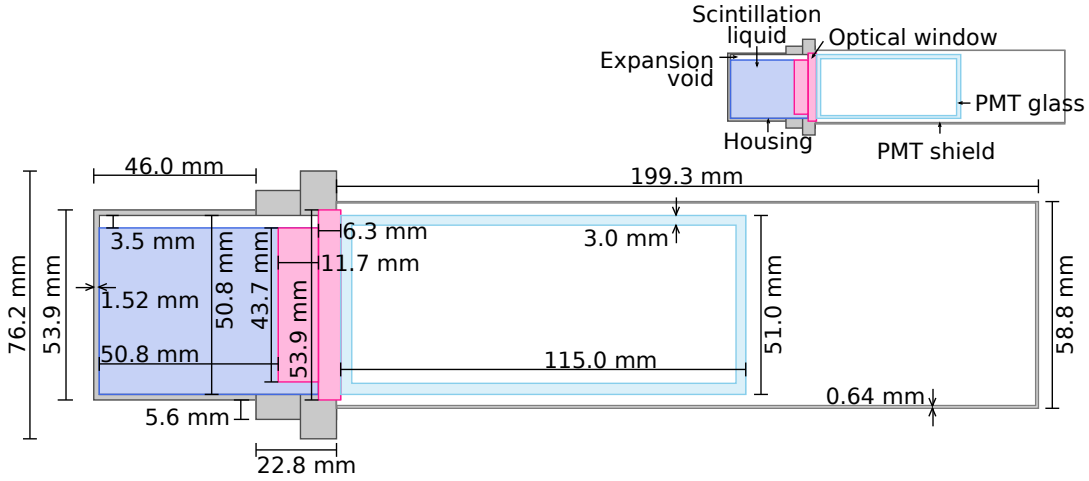

Figure 2.15: Schematic description of the detector's geometry given as input in the simulations [73].

^{137}Cs, ^{22}Na, and ^{207}Bi sources are presented. It is evident that there is almost no distinction between the EJ301 and EJ315 detectors in the context of photon spectrometry. The light output distributions produced by each source from the simulations were then folded with the resolution function and fitted to the corresponding experimental light output histograms (see Fig. 2.16 [(d) to (f)]). Via this fitting process, the parameters B_0, B_1, B_2 of the resolution function were obtained for each detector. This fit was also used to extract the calibration curve between the integrated charge Q_L and the light output L via the formula:

$$Q_L = F \cdot L + O, \tag{2.17}$$

where F is the conversion factor from photons to electrons and O is the offset of the data acquisition system. In Fig. 2.17 the results of this calibration for one of the EJ301 (a) and EJ315 (c) detectors are presented. The calibration curve for each specific detector was derived by fitting Eq. (2.17) to the data points of the Compton edges. Additionally, the relative resolutions σ_L/L of the same

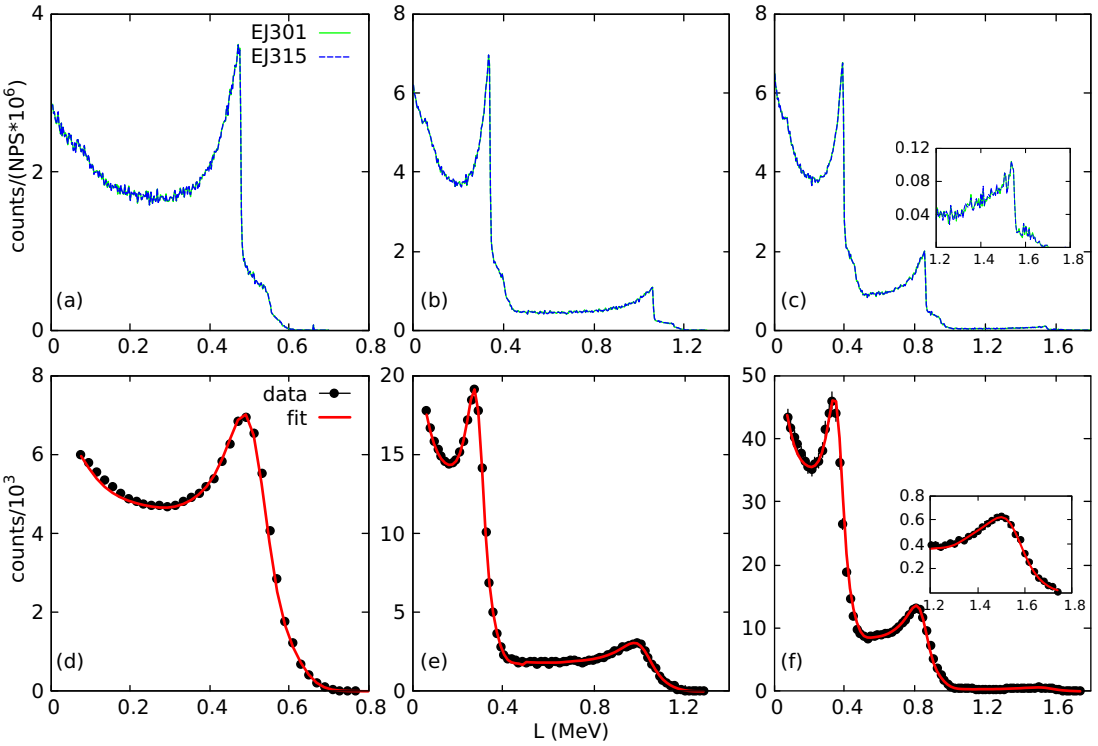

Figure 2.16: Top part: simulated light output distributions of the ^{137}Cs (a), ^{22}Na (b), and ^{207}Bi (c) sources for both the EJ301 and the EJ315 detector. Bottom part: fit of the simulated resolution-folded response (red line) to the experimental data (black points) for the same sources. Each peak corresponds to the Compton edges of the primary γ-rays emitted by the radionuclide sources.

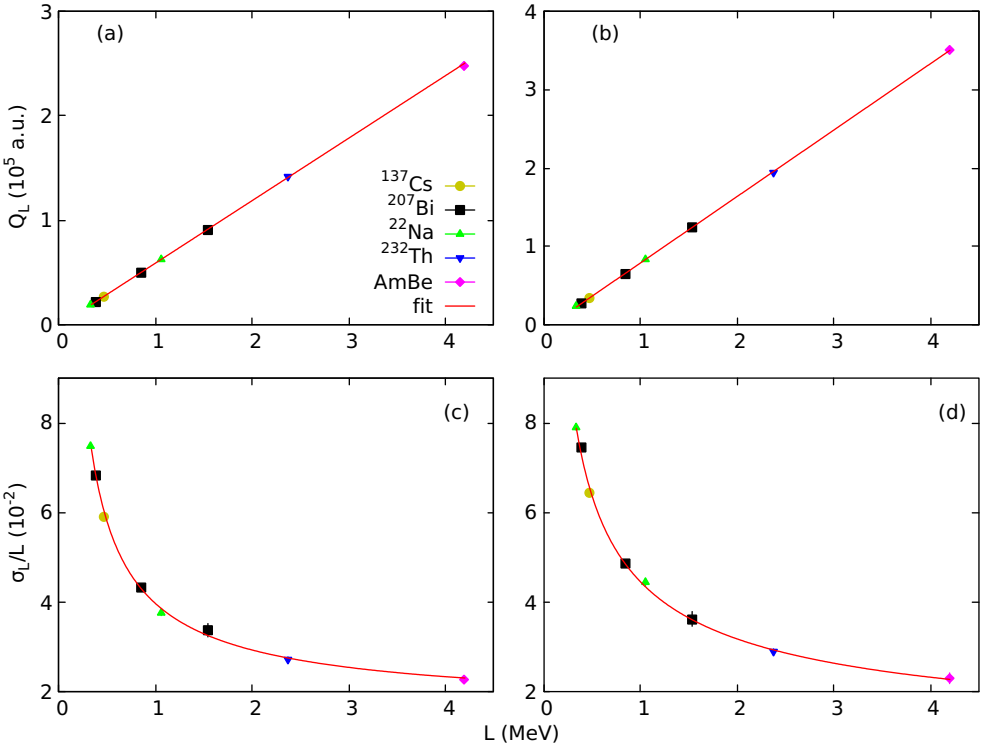

Figure 2.17: Calibration of the Q_L scale and relative resolution σ_L/L as functions of the light output for one of the EJ301 [(a) & (c)] and EJ315 [(b) & (d)] detectors.

detectors (EJ301-(b) & EJ315-(d)) are presented as a function of the light output. The data in this case were fitted with Eq. (2.15).

2.4.2.2 Response functions for neutrons

For the neutron response functions the non-linear behavior of the light output produced by charged particles heavier than the electrons (protons for the EJ301 and deuterons for the EJ315 detectors) needs to be taken into account. Several parametric formulas have been suggested to characterize this relationship, spanning from a semi-empirical method relying on the specific energy loss [82, 94–96, 102, 103] to complete empirical analytical expressions based on the charged particle energy [82, 104, 105]. In the present work, the modified empirical formula of Kornilov et al. [82] was used, which has proven to be a good approximation to describe the non-linear behavior of the light output produced by proton and deuteron based scintillators:

$$L(E_r) = A_1 E_r + \frac{A_2 E_r^2}{E_r + A_3}, \tag{2.18}$$

where E_r is the energy of the recoil hydrogen nucleus and A_1, A_2, A_3 are parameters unique to each detector and must be established experimentally. For every neutron energy E_n the maximum recoil energy of the hydrogen nuclei was estimated using the non-relativistic formula:

$$E_r^{max} = \frac{4A}{(A+1)^2} E_n, \tag{2.19}$$

where A is the ratio between the proton or the deuteron mass, depending on the detector, and the neutron mass.

After the parametrization of the light output function for charged particles, the same modeling method as the one used for the γ-rays response functions was followed, i.e. combining experimental measurements and Monte Carlo simulations. The aim of the simulations was to replicate the scattering of beam neutrons on the sample. While the sources could have been treated as isotropic, for enhanced simulation efficiency, neutron direction was uniformly sampled only within the solid angle covered by the detector and under vacuum conditions. For each type of detector different simulations where performed covering an energy range from 0.5 to 8 MeV with a 10 keV step. The non-linearity of the light output function for charged particles implies that when a neutron undergoes multiple collisions inside the detector, the light output cannot be determined solely by the total energy deposition. Instead, the contribution of each collision must be computed individually. To that purpose, the "PTRAC" card of MCNP was utilized to track each neutron history event. This feature was employed to identify collision events occurring within the liquid cell volume. For each collision, the light output was determined using Eq. (2.18), and the light output distribution was obtained by adding the contributions of events from the same history. In Fig. 2.18 the spectra obtained for neutrons with 2, 3, and 4 MeV neutron energies are displayed for both type of detectors. It is observed that the light output

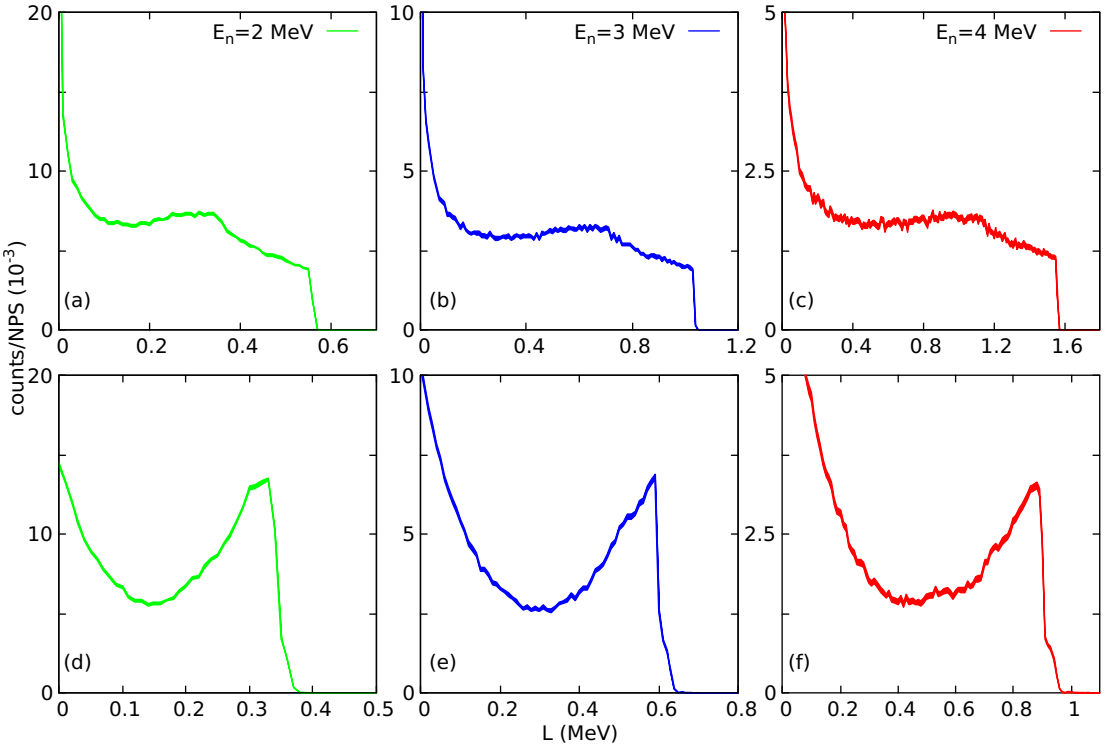

Figure 2.18: Simulated light output spectra with infinitesimal resolution for 2,3, and 4 MeV neutron incident energy for the EJ301 [(a) to (c)] and EJ315 [(d) to (f)] detectors.

distribution follows a different behavior for each type of detectors. This is because the elastic scattering recoil energy distribution is directly proportional to the angular distributions measured for the target nucleus in the center-of-mass (CM) reference frame. For the n-p scattering (EJ301 detectors) the distribution is isotropic in the CM, thus the "flat" light output distribution. For the n-d scattering (EJ315 detectors) the distribution is not isotropic and in the light output distributions the backscattering peak that corresponds roughly to 8/9 of the neutron energy is observed.

Additional simulations were performed to test possible effects of the way the neutrons are emitted in the simulations might have in the light output distributions. Except for the method followed in this work, i.e. emission of neutrons in the solid angle of the detector, four other different emission methods were tested: emission of neutrons as a cylinder beam covering the whole detector's window, as a pencil beam, as isotropic, and after the scattering in a sample (carbon in the case of this test). The results of these simulations are presented in Fig. 2.19. The simulations were performed for 2 MeV neutrons. It is observed that there are practically no differences in the produced light output distributions, only some discrepancies in the low energies below 0.1 MeV are observed, a region that was not used in the present work. As already mentioned above, in the simulations of the present work the neutrons are emitted under vacuum conditions. To test the possible effect in the light output distribution of the air between the sample under study and the detector, additional simulations were performed. In Fig. 2.20 the resulting light output distributions

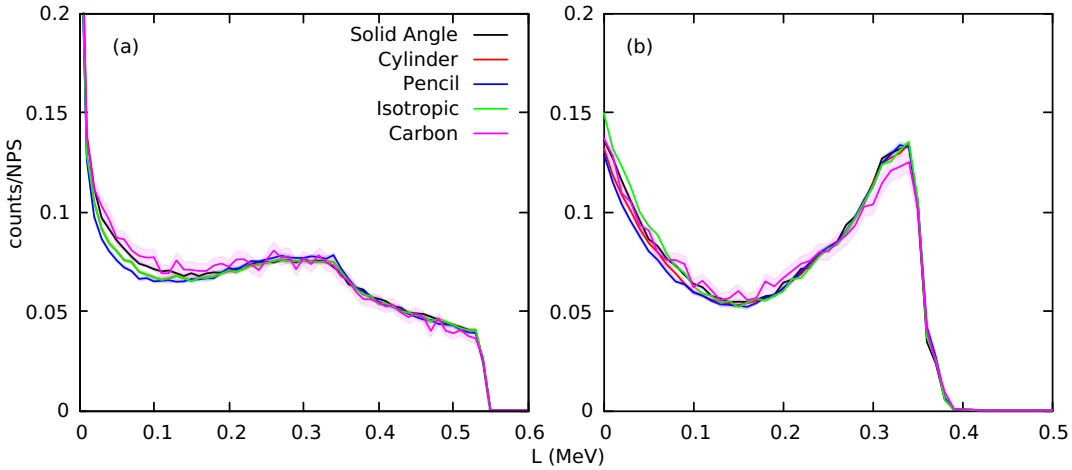

Figure 2.19: Simulated light output distributions with a different source description of 2 MeV neutron incident energy for the EJ301 (a) and EJ315 (b) detectors.

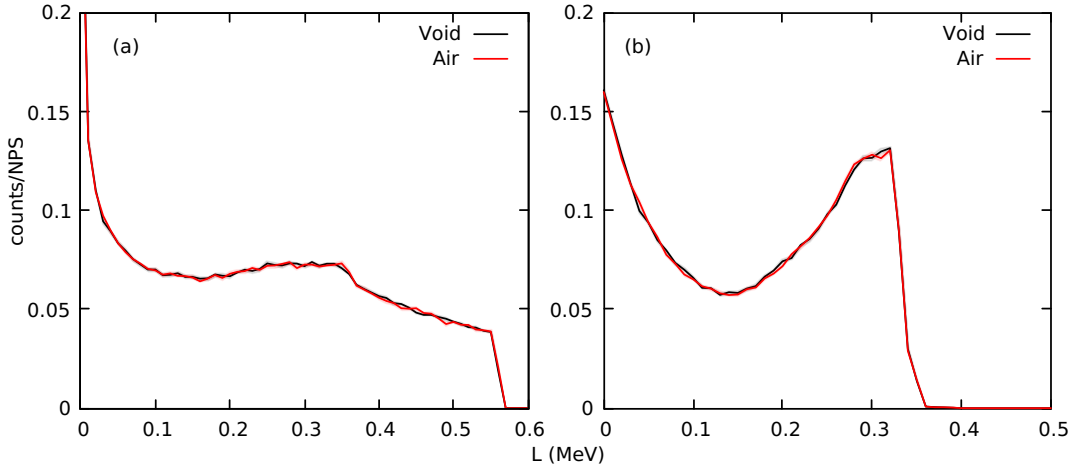

Figure 2.20: Simulated light output distributions of 2 MeV neutron incident energy for the EJ301 (a) and EJ315 (b) detectors under vacuum and normal conditions.

of 2 MeV neutrons emitted in both air and void conditions are presented for both detector types. It is observed that there are practically no differences between the two conditions.

After the simulations were completed, in order to determine the parameters of the light output function [Eq. (2.18)] for protons and deuterons, calibration measurements with monoenergetic neutrons need to be performed. Via those measurements experimental light output distributions were obtained and then the simulated distributions are fitted to the corresponding experimental ones and the parameters of Eq. (2.18) were extracted. To acquire quasi-monoenergetic neutrons in a time-of-flight experiment, short time intervals that correspond to a narrow energy range can be selected. In this work, the experimental light output distributions were obtained from scattering measurements using a carbon sample. Carbon was chosen for its high inelastic scattering threshold of 4.81 MeV, meaning that below this energy only neutrons that are elastically scattered arrive at

the detectors. Furthermore, the difference in energy between the ground and the first excited state is big enough to sufficiently separate elastic and inelastic events through neutron spectrometry.

In the present work, 18 short time-of-flight intervals of 5 ns duration, that correspond to narrow energy ranges were selected, and for the mean neutron energy of these intervals, the corresponding simulated light output distribution was fitted to the experimental one (see Fig. 2.22 for the EJ301 and Fig. 2.23 for the EJ315 detectors). In the end, the different parameters obtained from each energy were fitted to extract a set of values that would work best for the whole neutron energy range (see Fig. 2.21). With this method, a model describing the neutron response function was developed for each detector individually.

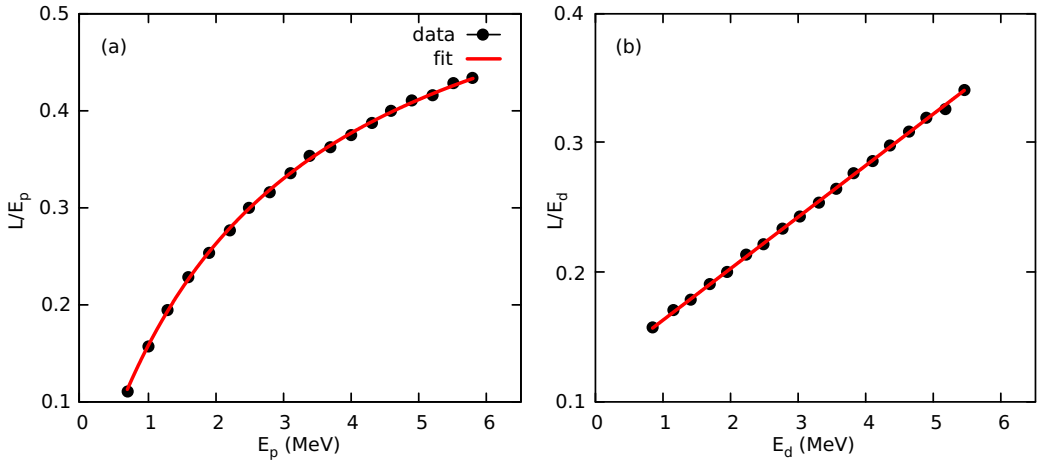

Figure 2.21: Ratio of the light output to the recoil energy as a function of the recoil energy E_p for protons [EJ301 - (a)] and E_d for deuterons [EJ315 - (b)]. The experimental points and the fit of Eq. (2.18) are presented.

After the neutron response function has been determined for each detector, the detector's intrinsic efficiency can be calculated using the following formula:

$$\varepsilon(E) = \int_{L_{thr}} R(L,E)dL, \tag{2.20}$$

where L_{thr} is the light output threshold used for each detector during the analysis. The resulting efficiencies are presented as a function of the neutron energy in Fig. 2.24. It is observed that the efficiency is following the same trend for all the detectors, with a small spread in absolute values caused by the differences in the response function parameters. The efficiency rises rapidly starting from energies around 500 keV, it reaches maximum value between 1 and 2 MeV, and from there it is slowly decreasing. Also, it is observed that the EJ301 detectors have higher efficiency, ranging between 30-40% maximum value, while the EJ315 have maximum efficiency between 20-30%.

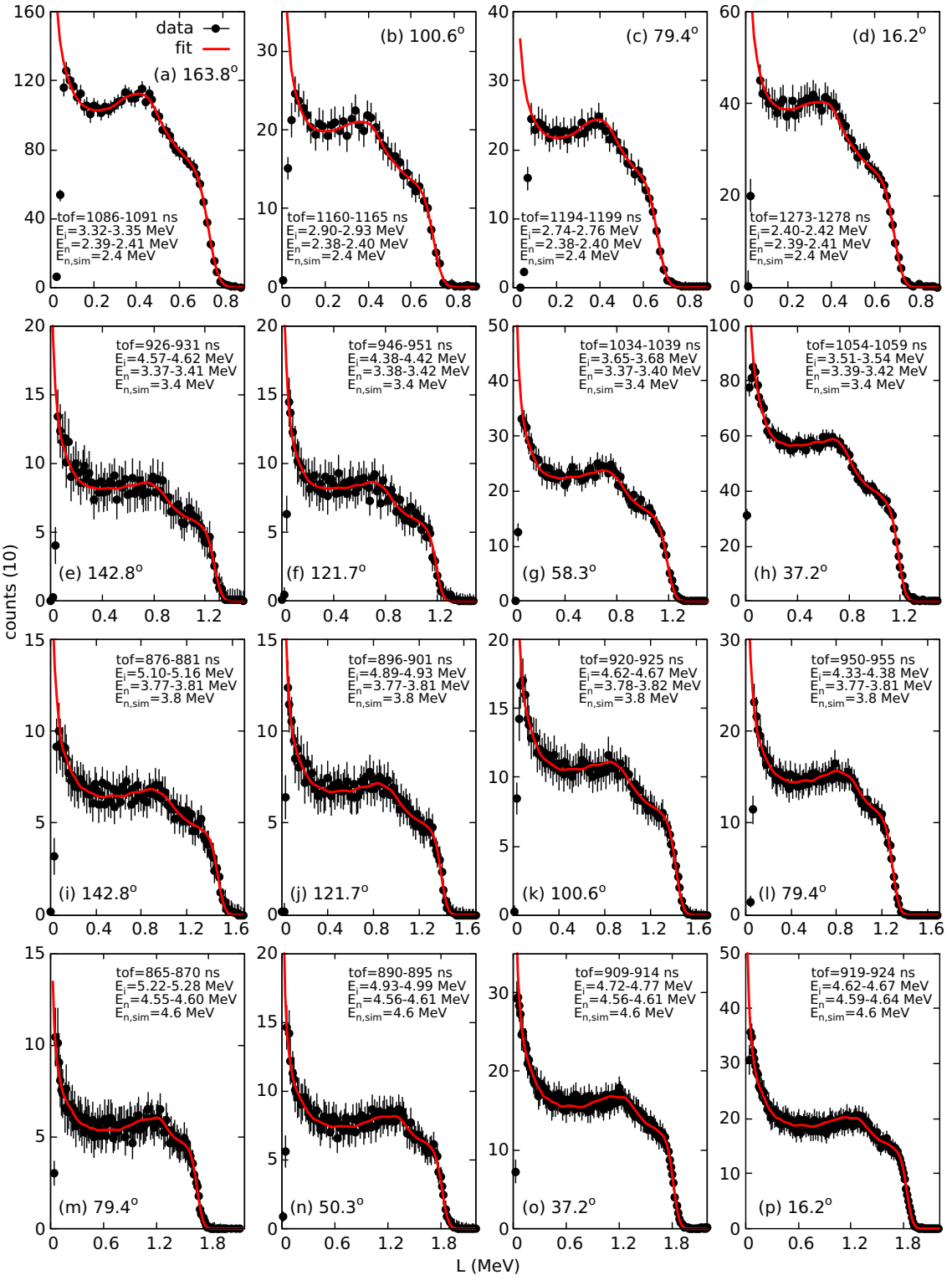

Figure 2.22: Examples of experimental light output histograms (data) measured with EJ301 detectors at different angles, compared with the simulated detector responses (fit). Each graph represents a different 5 ns interval. The time-of-flight information is provided in each graph. E_i and E_n are the neutron energies before and after the collision with carbon considering only elastic scattering. $E_{n,sim}$ is the simulated monoenergetic neutrons light output distribution used to fit the experimental data.

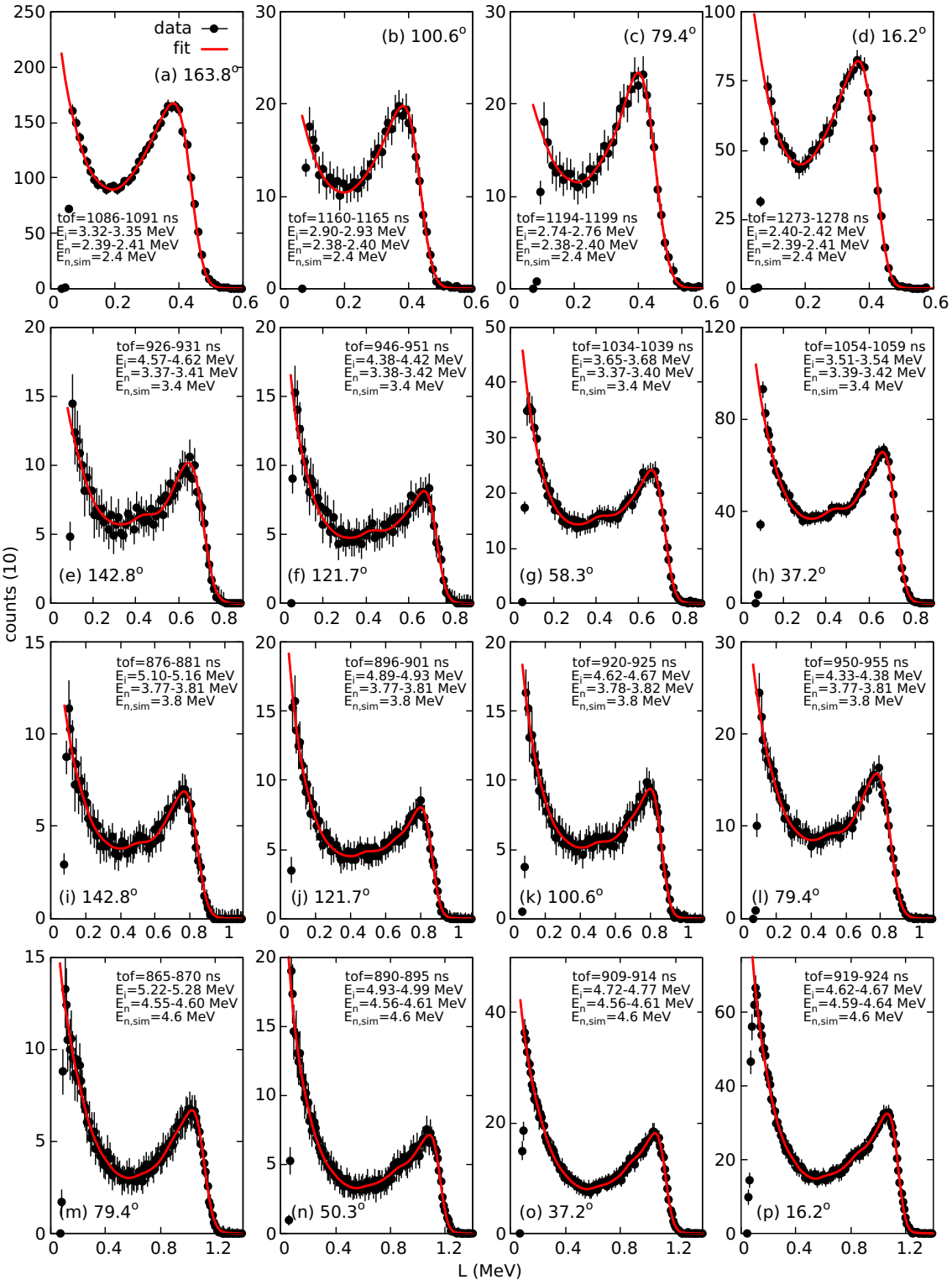

Figure 2.23: Examples of experimental light output histograms (data) measured with EJ315 detectors at different angles, compared with the simulated detector responses (fit). Each graph represents a different 5 ns interval. The time-of-flight information are provided in each graph. The meaning of the quantities reported in each graph is the same as for Fig. 2.22.

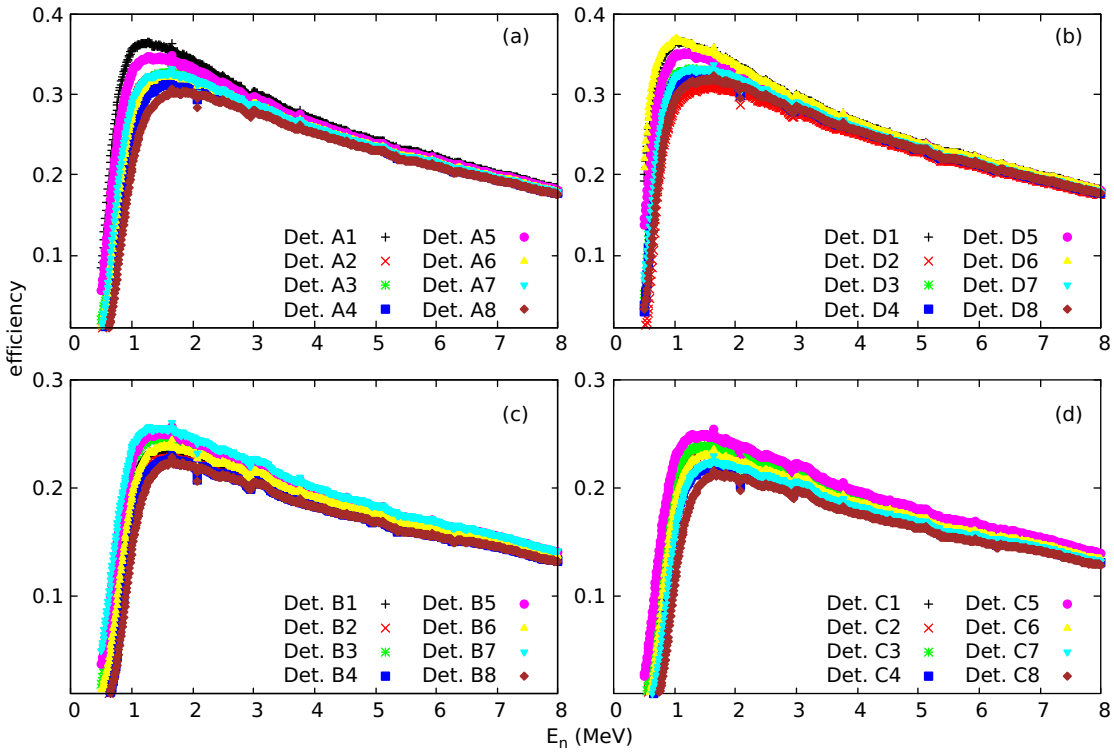

Figure 2.24: The intrinsic efficiency of the detectors as a function of the neutron energy. Each graph contains the efficiencies of the 8 detectors placed in one of the 4 sets of the ELISA spectrometer. The values for the EJ301 are given in (a) and (b) and for the EJ315 in (c) and (d).

2.5 Conclusions

In this chapter, a short description of the GELINA facility, neutron production process and time-of-flight technique was given. The ELISA spectrometer used in the present work was described in detail. The setup consists of 32 liquid organic scintillators for the detection of the scattered neutrons and a ^{235}U ionization chamber for the measurement of the neutron flux. Additionally, the methodology for the characterization of the detectors' response functions to neutrons and γ-rays was laid out. This procedure included dedicated calibration measurements with radionuclide sources and a natural carbon sample as well as Monte Carlo simulations of these measurements done with the MCNP6 code. The response functions that were developed in the end, were a key ingredient in the analysis of the scattering measurements described in the next chapter.

Chapter 3

Neutron scattering on Iron: Experiments, analysis and results

Three different measurements were performed at the GELINA time-of-flight facility utilizing the ELISA spectrometer to study neutron scattering on ^{54}Fe, ^{nat}C, and ^{56}Fe. The measurements were carried out between 2019 and 2023. The details of each experiment and a complete overview of the data analysis required for the extraction of the cross sections will be presented in this chapter. The results of each experiment will be presented as well, compared with the available experimental data in the literature, the most recent nuclear data evaluations, and theoretical calculations.

3.1 Experimental details

As mentioned in Sec. 2.1 the ELISA spectrometer is placed at the 30 m station of flight path 1. In the present experiments, the actual neutron flight path from the neutron source to the fission chamber and to the scattering sample was 25.66(7) m and 27.037(5) m, respectively. The beam spot diameter was measured at the sample position using a photographic film, resulting in 4.9(2) cm. For each experiment, two types of measurements were performed. One with the sample in place (sample-in) and a second one without the sample (sample-out). The sample-out measurements were carried out in order to establish the background contribution from in-beam neutrons that scattered once or multiple times in the air and the surrounding materials and then got detected by one of the scintillators. The allocated beam-time for each experiment is given bellow and summarized in Table 3.1.

In the first scattering experiment, performed in 2019, an enriched ^{54}Fe sample was measured. This highly enriched ^{54}Fe sample was leased from the Isotope Office of the Oak Ridge National Laboratory. It was a metallic disk of 51 mm diameter and 1.3 mm thickness. The areal density of the sample was derived from a measurement of the weight and the area. The area was determined by an optical surface inspection with a microscope system from Mitutoyo [106]. The calculated areal density used in this work was 0.954 g/cm^2 with 2% uncertainty. In this experiment, the sample-in measurement lasted almost 360 hours, while the sample-out lasted almost 330 hours.

Table 3.1: Year of measurement and allocated beam-time of each experimental campaign.

Sample	Year	Beam time (h)	
		Sample-in	Sample-out
^{54}Fe	2019	360	330
^{nat}C	2020	250	240
^{56}Fe	2023	500	350

Table 3.2: Isotopic composition of the enriched iron samples used in the present work.

Fe isotope	^{54}Fe sample	^{56}Fe sample
^{54}Fe	**97.68(7)%**	0.16(1)%
^{56}Fe	2.24(6)%	**99.77(1)%**
^{57}Fe	0.04(1)%	0.07(1)%
^{58}Fe	0.04(1)%	<0.01%

In the second experiment, performed in 2020, the measurement of neutron scattering on a carbon sample took place, for the determination of the neutron response function models of the detectors as described in Sec. 2.4.2.2. The sample was a graphite disk made of natural carbon, purchased from Goodfellow, with 100 mm diameter and 2.0 mm thickness. The thickness of the sample was relatively small in order to minimize multiple scattering effects that might have an impact in the final results. The areal density of the sample was determined with the same method as the one used in the ^{54}Fe sample and was found to be 0.351 g/cm^2 with 0.2% uncertainty. The sample-in measurement lasted almost 250 hours and the sample-out almost 240 hours.

For the last scattering experiment, performed in 2023, an enriched ^{56}Fe sample was measured (see Fig. 3.1). The sample was a metallic disk of 70 mm diameter and 1 mm thickness. The sample was characterized following the same technique that was used for the other two and the extracted areal density was 0.814 g/cm^2 with 0.2% uncertainty. In this experiment, the sample-in measurement lasted almost 500 hours and the sample-out almost 350 hours.

Figure 3.1: Photo of the ^{56}Fe sample placed in the sample position of the ELISA spectrometer.

The isotopic composition of the enriched samples and the detailed geometrical characteristics of all samples are listed in Tables 3.2 and 3.3. All three samples used in this work had a diameter larger than the neutron beam, ensuring that the whole beam was intercepted.

Table 3.3: Geometrical characteristics of the scattering samples used in the present work.

Sample	^{54}Fe	^{nat}C	^{56}Fe
Mass (g)	19.494(10)	27.70(1)	31.396(10)
Diameter (mm)	51.00(51)	100.0(1)	70.068(1)
Thickness (mm)	1.30(1)	2.0(1)	1.00(1)
Molar mass (g/mol)	53.987(1)	12.01(1)	55.935(1)
Areal density (g/cm^2)	0.954(18)	0.351(1)	0.814(2)
Areal density (atoms/b)	0.0106(2)	0.0176(1)	0.00878(1)

The UF_4 samples placed inside the ionization chamber for the monitoring of the neutron flux were also bigger in diameter (70 mm) than the beam, making sure that the homogeneity and size of the beam did not play a role in the analysis.

In the present experiments, the neutron energy range from 1 MeV to 8 MeV was studied. Although GELINA has a neutron energy spectrum extending beyond 20 MeV, the practical limitation arises as the flux decreases beyond 8 MeV, making it difficult to achieve desirable statistics within the measurement times of this work. The lower threshold, established at 1 MeV, is due to the detector efficiency, as illustrated in Fig. 2.24.

3.2 Data reduction

The neutron differential scattering cross sections were calculated via the expression:

$$\frac{d\sigma_{el/inl}(E,\theta)}{d\Omega} = \frac{N'_{el/in}(E,\theta)}{\Delta\Omega\rho_T\Phi(E)A_b}, \tag{3.1}$$

where E is the incident neutron energy, $N'_{el/inl}$ are the corrected counts of elastic/inelastic scattering events, $\Delta\Omega$ is the detector's solid angle, ρ_T is the areal density of the sample (Table 3.3), $\Phi(E)$ is the neutron fluence, and A_b is the cross-sectional area of the neutron beam. Throughout the text, angle θ will implicitly represent one of the eight angles of the ELISA setup. Below, a detailed description for the calculation of the different components of Eq. (3.1) is given.

3.2.1 Calculation of the neutron scattered events

The number of neutron scattering events, both for elastic and inelastic scattering, were determined by analyzing the scintillator data and extracting the neutron time-of-flight spectra. This is a multi-step analysis involving: processing of the recorded signals and the separation between photon and neutron induced events (as described in Sec. 2.4.1), subtraction of the background contribution, separation between elastically and inelastically scattered neutrons, and finally the multiple scattering correction.

3.2.1.1 Neutron t.o.f. distributions

The events recorded by the scintillators during the measurements, are a mix of neutrons coming from elastic and inelastic scattering in the sample, photons from inelastic scattering or neutron capture in the sample, and bremsstrahlung photons from scattering. As already mentioned in Sec. 2.4.1, to separate between neutron and photon induced events a pulse shape analysis was performed using the charge integration method. In Fig. 3.2 examples of the resulting time-of-flight histograms of the three different measurements after the pulse shape discrimination are presented. For each scattering sample, an example of a counting histogram for an EJ301 and an EJ315 detector at specific scattering angles was selected. It is observed that every time-of-flight spectrum exhibits

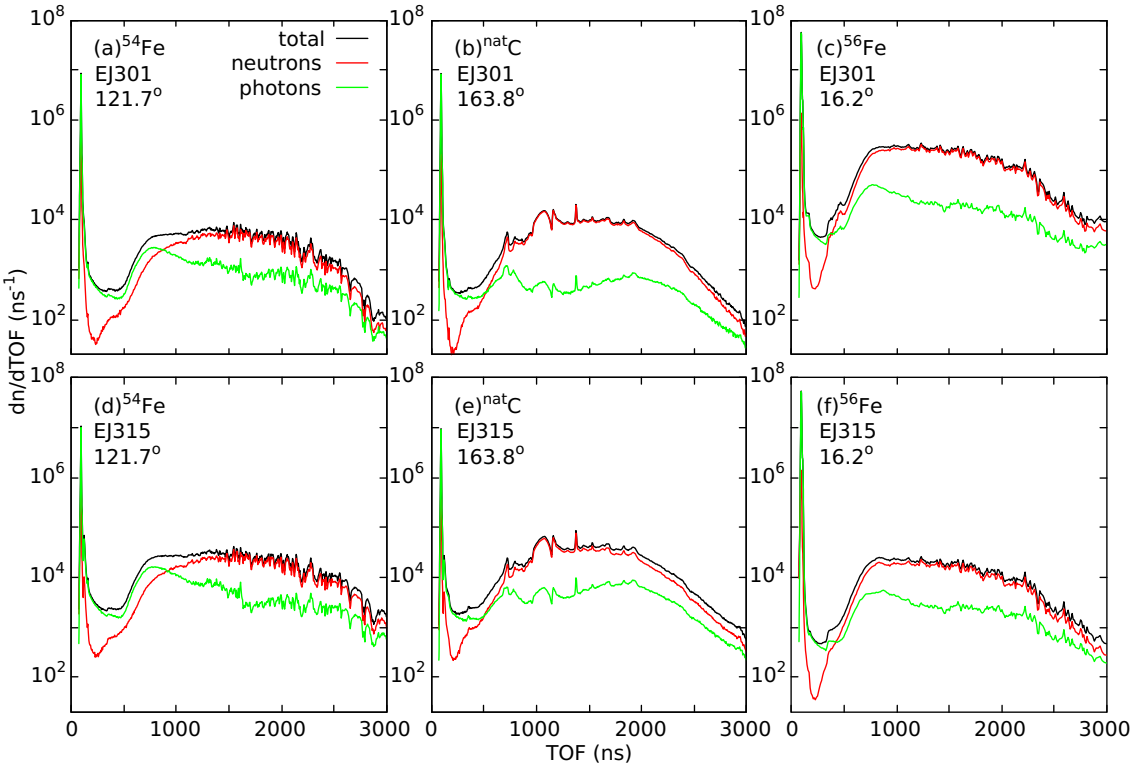

Figure 3.2: Time-of-flight distributions for the two kind of detectors placed at different angles during the measurement of the ^{54}Fe [(a) & (d)], ^{nat}C [(b) & (e)], and ^{56}Fe [(c) & (f)] samples. The total number of recorded events (black line) along with the number of neutron (red line) and photon (green line) events individually, resulting from the pulse shape discrimination, are presented.

a distinct peak at around 91 ns, which represents the arrival time of bremsstrahlung photons at the detectors ("so called γ-flash"). The main component of the γ-flash is described by the photon distributions (green lines) as expected, but fragments of it are also observed in the neutron distributions (red lines). The presence of the γ-flash in the neutron distributions is the result of an imperfect pulse shape discrimination. Even though the time resolution of the beam during optimal operation of GELINA is between 1-2 ns, the γ-flash peak appears broadened in the time-of-flight spectra. This is attributed to the time evolution of the bremsstrahlung production process and the time resolution of both the detectors and the DAQ system. The full width at half maximum (FWHM) of the γ-flash peak serves as the lower limit for time resolution achieved in each experiment. During the measurement of the ^{54}Fe and ^{nat}C samples, GELINA was operating under optimal conditions and the FWHM of the γ-flash peak at the detectors of the ELISA setup was 5 ns (resolution of the measurements). At the given distance from the source, a time resolution of 5 ns in time-of-flight corresponds to a 5 keV energy resolution at 1 MeV, 26 keV at 3 MeV, 57 keV at 5 MeV, and 93 keV at 7 MeV. During the measurement of the ^{56}Fe sample, due to accelerator related issues, the time resolution of the beam, and thus the measurement, was 10 ns based on independent monitors used by the operators of GELINA. This

was also verified by the detectors at the ELISA spectrometer as the γ-flash peak appeared to be broader, with a FWHM of 10 ns. At the same distance, a time resolution of 10 ns corresponds to a 10 keV energy resolution at 1 MeV, 53 keV at 3 MeV, 113 keV at 5 MeV, and 189 keV at 7 MeV. The difference in the γ-flash width from 5 to 10 ns is shown in Fig. 3.3. The value of the FWHM is extracted by applying a Gaussian fit to the experimental data.

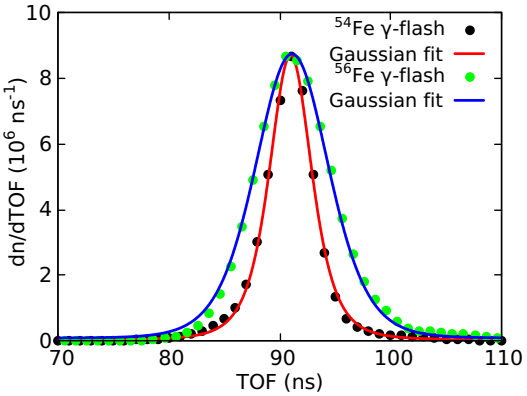

Figure 3.3: Time-of-flight distributions of the γ-flash peaks recorded during the measurement of the ^{54}Fe and ^{56}Fe samples.

In the time-of-flight distributions presented in Fig. 3.2, except for the γ-flash, a fluctuating behavior in the neutron distributions for the case of ^{54}Fe and ^{56}Fe above 1000 ns is also observed. This is expected considering the fluctuating behavior of the scattering cross sections in middle mass nucleus. In the case of carbon [Fig. 3.2 (b) & (e)] clear structures are observed in the time-of-flight region from 650 ns to 1500 ns. For example, the peak observed at around 1375 ns corresponds to a well known resonance in the carbon cross section at 2.078 MeV that is used for the energy calibrations of detectors. In all the examples presented in Fig. 3.2, the photon distributions exhibit similar patterns with the neutrons, but the counts are significantly lower by one to two orders of magnitude. The time-correlated photons are exclusively attributed to the inelastic scattering in the samples. The remaining photons result from inelastic scattering on structural components such as the detector support, collimators, and beam stop.

After acquiring the neutron time-of-flight spectra for each detector the background contribution needs to be extracted. In the current experiments, background related events are generated when beam neutrons interact one or more times in the air and surrounding materials and then arrive in the detectors. To account for this contribution, measurement without the samples were performed and were subtracted from the ones with the samples in place. To account for the difference in measurement time and fluctuations in the neutron beam between the sample-in and sample-out measurements, a normalization factor was calculated based on the fission events recorded in the ionization chamber. On average, the background component accounted for 30-40% of the recorded events in each detector mainly generated from beam neutrons scattering on air. As an example, in Fig. 3.4 the experimental neutron background at the 163.8°

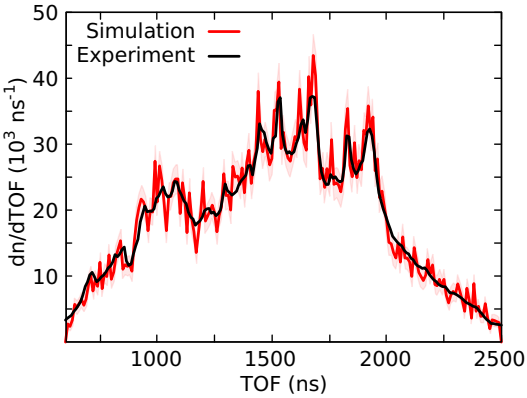

Figure 3.4: Comparison between the experimental and the simulated neutron background at the 163.8° detection angle.

detection angle is compared with the corresponding simulated one. The simulated background represents only beam neutrons that scattered on air and then reached the detector. This component was extracted using the MCNP6.2 code and the PTRAC output option. It is observed that the two background spectra are in agreement within the uncertainty of the simulation, which validates the fact that the majority of the background events are generated from neutron scattering in the air.

3.2.1.2 Elastic/Inelastic separation

Following the removal of photon induced and background events, the separation between events coming from elastic and inelastic scattering took place. In the carbon experiment only elastic scattering was considered, due to the high inelastic scattering threshold, but in the ^{54}Fe and ^{56}Fe experiments inelastic scattering was also explored. In Table 3.4 the levels of the two isotopes up to 3 MeV energy are presented. Each time-of-flight spectrum was split in small intervals of 5 ns duration for the ^{54}Fe and ^{nat}C experiments, and 10 ns for the ^{56}Fe experiment, and their corresponding light output distributions were analyzed. The main principle of the method followed in this work was the fact that in a given time-of-flight interval the fastest neutrons arrive at the detector after a single elastic scattering in the sample, while slower neutron arrive after inelastic scattering or after multiple scattering collisions in the sample. Via kinematic calculations, using equations (2.6), (2.7) and (2.8), it is possible to determine the energy of the neutrons that were scattered elastically E'_{el} or inelastically E'_{inl_1}, E'_{inl_2}, etc. for every time-of-flight interval. These different neutron energies generate different light output distributions in the detector that overlap below a certain threshold, which depends on the energy difference from the ground state to the first level, from the first level to the second, and so on.

To separate the different scattering components, proper thresholds were applied in the light output distributions. For elastic scattering, this light output threshold L_{thr} depends on the energy E'_{inl_1} of the neutron after inelastic scattering from the first excited state of the sample under study, therefore the threshold is different for each time-of-flight interval. To determine each light output threshold first the energy E'_{inl_1} was calculated using Eq. (2.8) and for that energy the maximum

Table 3.4: List of the levels of ^{54}Fe and ^{56}Fe up to 3 MeV reported in the ENSDF [107] library. The energy E^*, the angular momentum and parity J^π, and the half-life $T_{1/2}$ of each level are listed.

^{54}Fe			^{56}Fe		
E^* (keV)	J^π	$T_{1/2}$	E^* (keV)	J^π	$T_{1/2}$
0	0^+	stable	0	0^+	stable
1408.19(19)	2^+	0.76(2) ps	846.7778(19)	2^+	6.07(23) ps
2538.1(3)	4^+	4.0(8) ps	2085.1045(25)	4^+	0.63(12) ps
2561.3(4)	0^+	$\leq$ 1.4 ps	2657.5894(25)	2^+	21(1) fs
2900	2^+	-	2941.50(1)	0^+	0.45(9) ps
2949.2(5)	6^+	1.22(2) ns	2959.972(4)	2^+	28(3) fs
2959.0(5)	2^+	0.052(7) ps			

deposited energy E_r^{max} in the detectors (maximum recoil energy of protons or deuterons depending on the detector type) was calculated using Eq. (2.19). Then, the maximum light output L_{inl}^{max} was calculated using the light output function (2.18): $L_{inl}^{max} = L(E_r^{max})$. Finally, the threshold was placed at the maximum light output produced by an inelastic event taking into account the resolution broadening of the detector Eq. (2.15):

$$L_{thr} = L_{inl}^{max} + 2\sigma_L \tag{3.2}$$

Once the thresholds are defined, the detector's modeled response $R(L, E'_{el})$ (see Sec. 2.4.2.2) for neutrons with energy E'_{el} is scaled by a factor λ to match the experimental data above the threshold and the resulting distribution $R_{fit}(L, E'_{el}) = \lambda \cdot R(L, E'_{el})$ describes the contribution of elastic scattering events to the total light output distributions. The same procedure was followed to discriminate neutrons coming from inelastic scattering from the first excited state to those scattering from the second state, the second to the third, and so on. In Fig. 3.5 and 3.6 the light output distributions for specific 5 ns (^{54}Fe) and 10 ns (^{56}Fe) time intervals are presented along with the decomposition

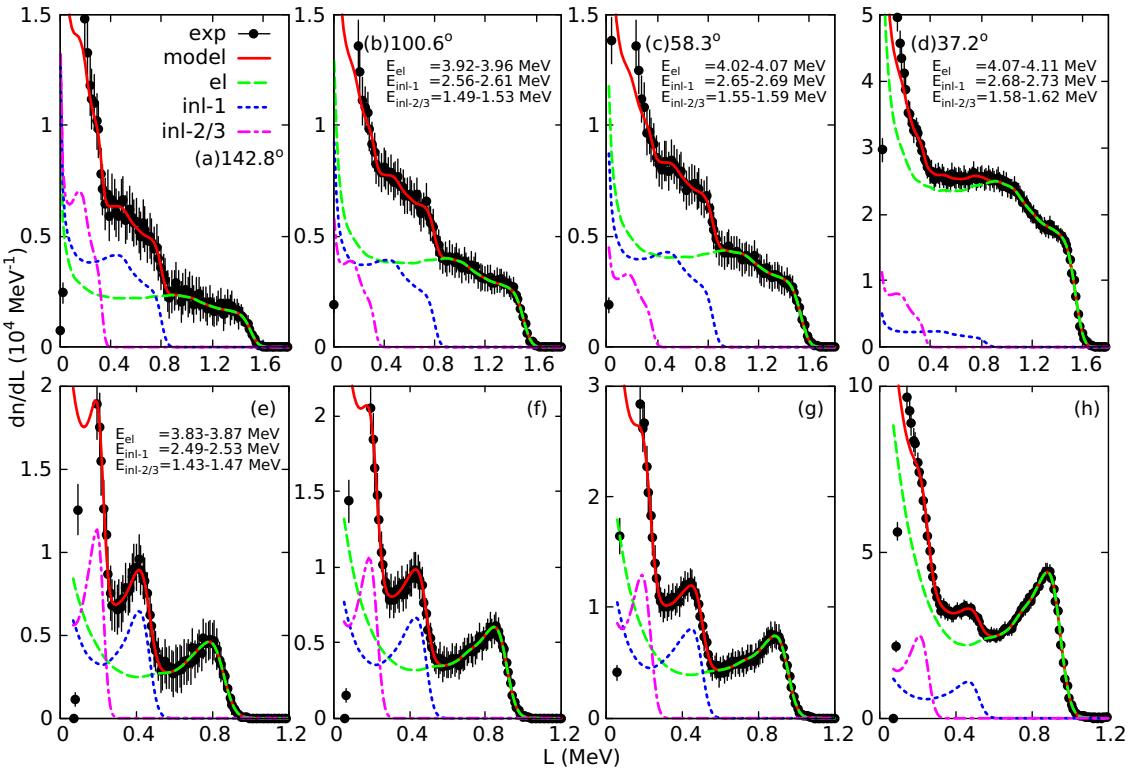

Figure 3.5: Light output distributions for the time-of-flight interval from 976 to 981 ns from the ^{54}Fe measurement. The graphs correspond to the same four different detection angles for both the EJ301 (n,p) [(a) to (d)] and EJ315 (n,d) [(e) to (h)] detectors. The experimental values (exp) are presented along with their associated response (model) and their different components from elastic scattering (el), and inelastic scattering from the first and second excited stated (inl-1, inl-2/3). The corresponding neutron energies after an elastic (E_{el}), and inelastic scattering from the first and second levels (E_{inl-1}, $E_{inl-2/3}$) are also given in the graphs.

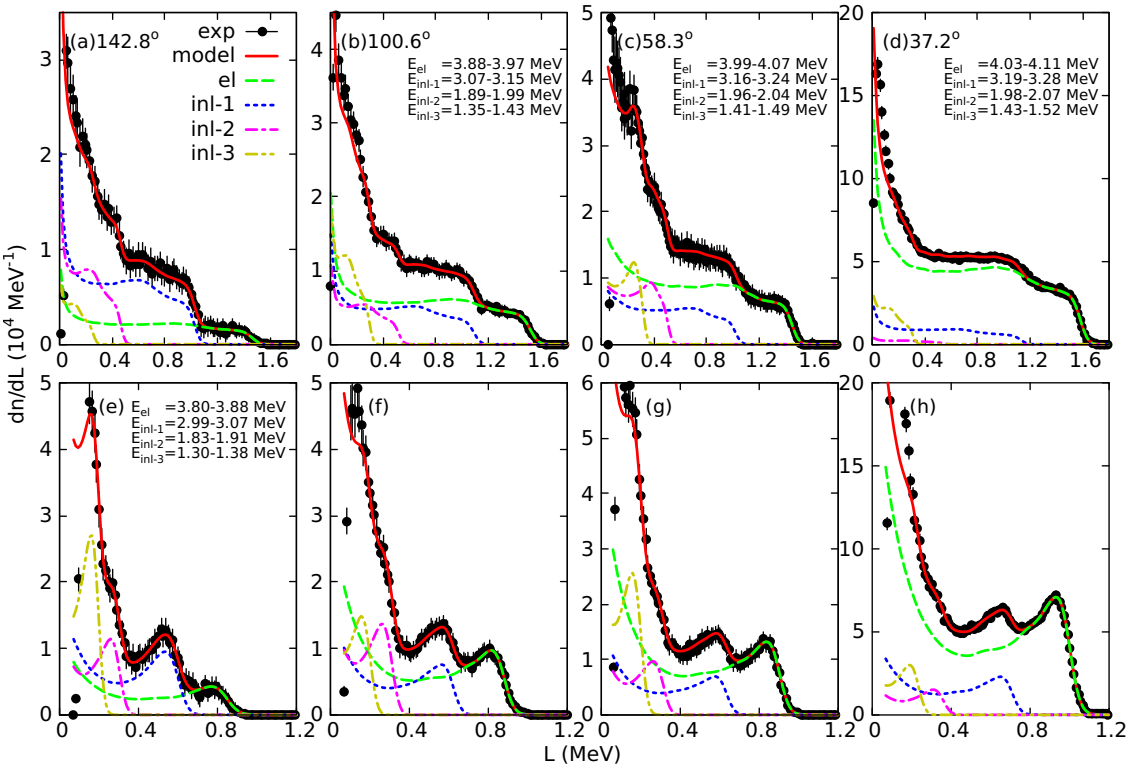

Figure 3.6: Light output distributions for the time-of-flight interval from 976 to 986 ns from the ^{56}Fe measurement. The graphs correspond to the same four different detection angles for both the EJ301 (n,p) [(a) to (d)] and EJ315 (n,d) [(e) to (h)] detectors. The experimental values (exp) are presented along with their associated response (model) and their different components from elastic scattering (el), and inelastic scattering from the first, second and third excited states (inl-1, inl-2, inl-3). The corresponding neutron energies after an elastic (E_{el}), and inelastic scattering from the first, second and third levels (E_{inl-1}, E_{inl-2}, E_{inl-3}) are also given in the graphs.

of the detector's modeled response into the different scattering components. Both time intervals correspond to incident energies above the threshold for inelastic scattering from the third levels of both iron isotopes. For the case of ^{54}Fe since the second and third levels only have 30 keV difference in energy (see Table 3.4), not enough to clearly separate the two different distributions, in Fig. 3.5 under the label "inl-2/3" a pseudo level was considered with the average energy of the two levels. For that reason only inelastic scattering from the first exited state of ^{54}Fe was explored in the present work. In general, the model seems to reproduce well the experimental data in both cases. During the elastic/inelastic separation process it was observed that the contribution of inelastic reactions became significant only above $\sim$1 MeV after their corresponding thresholds. Because of this, the cross sections could not be extracted for energies close to the inelastic scattering threshold. Similar distributions for the natural carbon experiment were already shown in Sec. 2.4.2.2 when describing the development of the neutron response models, in Fig. 2.22 and 2.23.

If LV represents the different scattering components, from $LV = 0$ for elastic scattering, $LV = 1$ for inelastic scattering from the first exited state and so forth until the highest level for which the incident neutron energy is higher than the inelastic threshold, the number of scattering events is

extracted using the following formula:

$$\langle N_{LV}\rangle_{\Delta t}(\theta) = \frac{1}{\varepsilon(E'_{LV})|_{L_{thr,LV}}\Delta\Omega}\int_{L_{thr,LV}} R_{meas}(L,E'_{LV})dL, \tag{3.3}$$

where $\langle N_{LV}\rangle_{\Delta t}$ is the number of scattering events for each level LV per $\Delta t = 5$ or 10 ns time-of-flight interval and detection angle, $R_{meas}(L,E'_{LV})$ is the experimental light ouput distribution, $\Delta\Omega$ is the detector opening angle, and $\varepsilon(E'_{LV})|_{L_{thr,LV}}$ is the intrinsic efficiency of each detector with respect to the detected neutron energy E'_{LV} calculated for the threshold value $L_{thr,LV}$ using Eq. (2.20).

3.2.1.3 Multiple scattering correction

The obtained numbers of neutron induced events for the different scattering processes were corrected for multiple scattering effects before being used in the cross section calculation. Multiple scattering contribution is generated from beam neutrons that interact twice or more times in the samples and then reach one of the detectors. In the present work, the correction factor for such events (f_{msc}) was calculated via Monte Carlo simulations using the MCNP6.2 code. In the simulation, the full geometry of the spectrometer was given as input (see Fig. 3.7), and the description of the neutron source was based on the actual properties of the beam during the measurement. Additionally, the resolution of the facility was taken into account in the simulations, based on the work described in Ref. [72]. In Fig. 3.8 the probability density functions (pdfs) in delay distance normalized to have an integral of one are presented for flight path 1, for the incident neutron energies studied in this work. It is observed that the dominant contribution of the resolution for the DFC (Direct Flux Configuration) is a pronounced peak near zero delay distance arising from source neutrons having suffered no more than a few forward scattering collisions with the uranium target.

Figure 3.7: MCNP version of the ELISA spectrometer. The sample holder, the scattering sample, the 32 liquid organic scintillators and their respective mounting are included in the geometry.

The PTRAC option of MCNP was selected as output where the history of each neutron arriving in any of the detectors is recorded. Then, the number of neutron events that interacted more than once with the sample and then arrived at any detector was written down, and the correction factor was defined as the ratio of the detected multiple scattering events to the total number of detected events. In Fig. 3.9 the resulting multiple scattering correction is presented for each sample. It is observed that at the carbon measurement

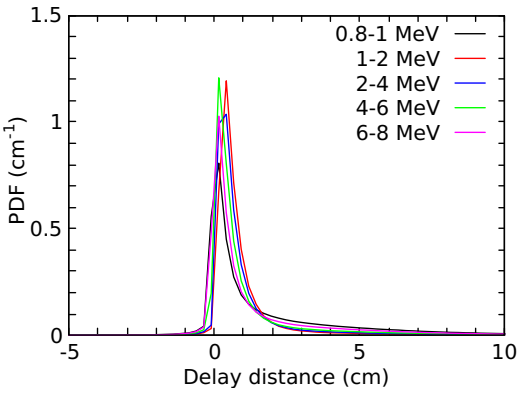

Figure 3.8: Resolution functions for selected energies at flight path 1, calculated using MCNP.

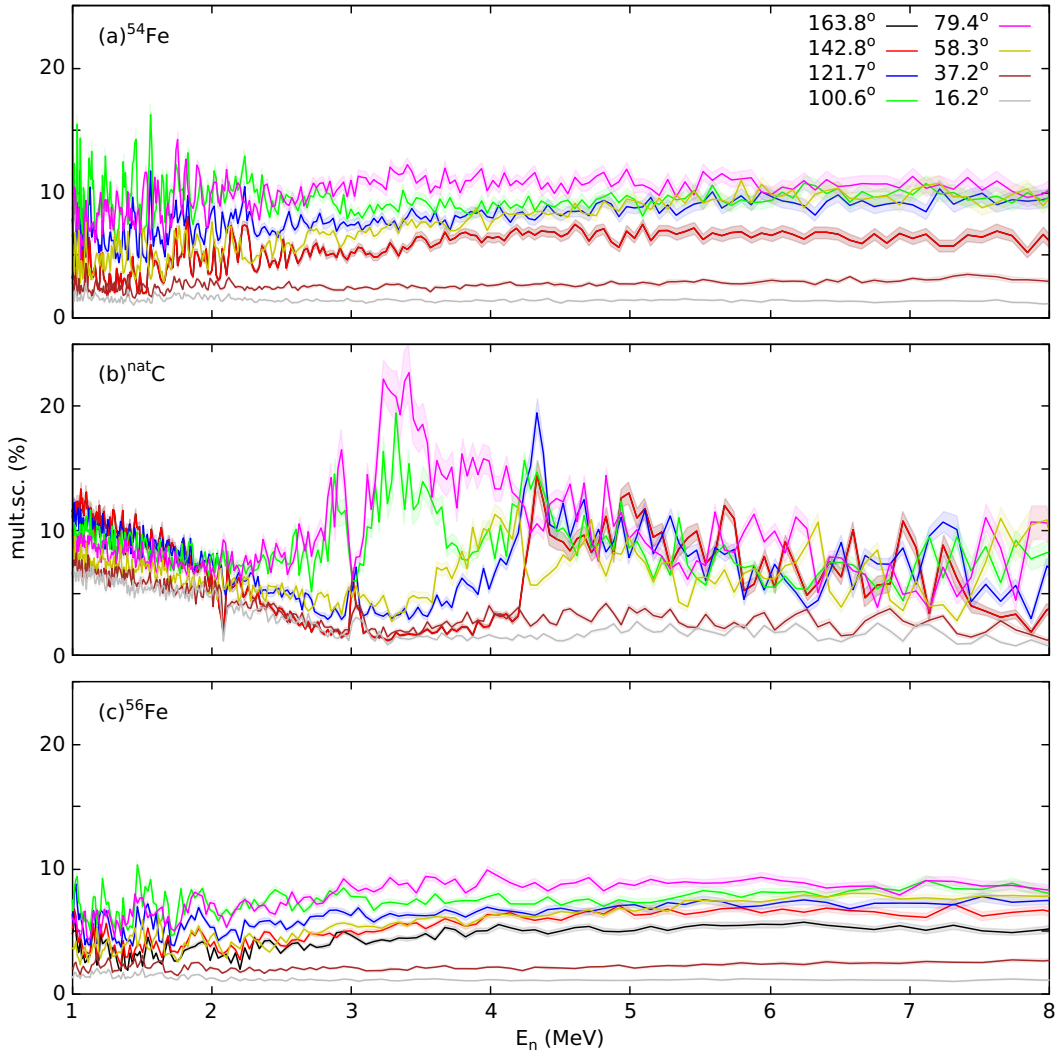

Figure 3.9: Percentage of the multiple scattering correction as a function of the incident neutron energy, for the ^{54}Fe (a), ^{nat}C (b), and ^{56}Fe (c) sample measurements, at the eight different detection angles.

the correction is higher than the corrections in the iron measurements almost over the whole neutron energy range and for all detection angles. This mainly because of the higher thickness and diameter of the carbon sample, which means that neutron after scattering have to "travel" a larger distance inside the sample, increasing the possibility of a second scattering. For the same reason, the corrections are reaching maximum values at angles close to 90° in all measurements. The method followed in this present work provides a time-of-flight dependent correction for every detector individually and is applied to the number of scattering events using the formula:

$$\langle N_{LV}\rangle'_{\Delta t}(\theta) = (1 - f_{msc}) \cdot \langle N_{LV}\rangle_{\Delta t}(\theta), \tag{3.4}$$

where $\langle N_{LV}\rangle_{\Delta t}$ is the initial number of elastic/inelastic scattering events per 5 or 10 ns time-of-flight interval and detection angle, and $\langle N_{LV}\rangle'_{\Delta t}$ is the final number of elastic/inelastic scattering events.

Furthermore, with the PTRAC option of MCNP the isotope with which the neutrons interacted is also recorded, which also allows for the identification of events that interacted with the other iron isotopes in the enriched samples and then reached any of the detectors. The same method as the one for the multiple scattering contribution [Eq. (3.4)] was followed to correct for the contamination of the minor iron isotopes in the ^{54}Fe and ^{56}Fe sample. This contamination factor (f_{con}) was found to be less than 1% of the recorded neutron events for the ^{54}Fe and less than 0.1% for the ^{56}Fe measurements, at each detection angle over the whole neutron energy region.

3.2.2 Estimation of the neutron fluence

Once the scattering yields have been determined, the neutron fluence impinged on the scattering samples needs to be calculated. This is achieved by analyzing the ionization chamber data. In Fig. 3.10 the pulse height histograms of the ^{235}U ionization chamber during the sample-in measurements for all samples are presented. Each histogram can be split in three parts: the α-particle area at low amplitudes, the fission fragments area at high amplitudes, and the "plateau" which acts

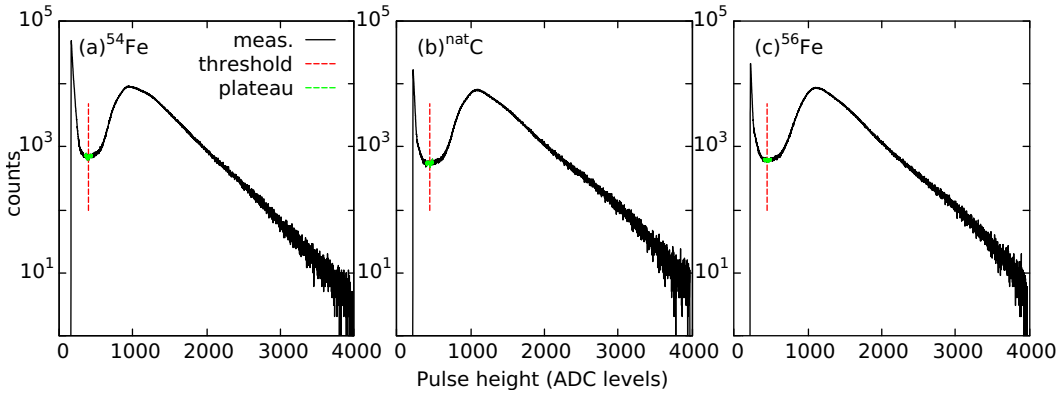

Figure 3.10: Full pulse-height histograms of the sample-in measurements of each sample. The experimental counts (black) are presented along with the corresponding threshold (red) and the plateau region (green).

as the separation area between the α-particles and the fission fragments. In every experiment, the contribution from α-particles was rejected by applying a threshold in the middle of the plateau, which was choosen based on beam-off data. The neutron fluence is extracted using the standard cross-section of the neutron induced fission on ^{235}U and is determined using the formula:

$$\Phi(E) = \frac{Y_{FC}(E)}{\varepsilon_{FC} \cdot \sigma_{^{235}U(n,f)} \cdot \rho_{^{235}U} \cdot A_b}, \tag{3.5}$$

where $Y_{FC}(E)$ is the total number of fission fragments above the threshold as a function of the neutron energy E, ε_{FC} is the detection efficiency of the fission chamber, $\sigma_{^{235}U(n,f)}$ is the neutron induced fission cross section of ^{235}U, $\rho_{^{235}U}$ is the areal density of the ^{235}U deposits in atoms per unit surface (see Table 2.3), and A_b is the cross-sectional area of the neutron beam which is also included in the calculation of the cross section [Eq. (3.1)], and therefore is canceled out. The detection efficiency was determined using the formula:

$$\varepsilon_{FC} = \frac{Y_{FC}}{Y_{FC} + Y_A + Y_B}, \tag{3.6}$$

where Y_{FC} is the total number of fission fragments above the threshold, Y_A is the number of fission fragments below the threshold, determined with a linear fit of the counts in the plateau region and extrapolating to zero amplitude (see Fig. 3.11), and Y_B is the number of fission fragments that were stopped in the ^{235}U deposits, determined using the method described in Ref. [108]. According to this method, the number of fission fragments that were stopped in the deposits is calculated using the formula:

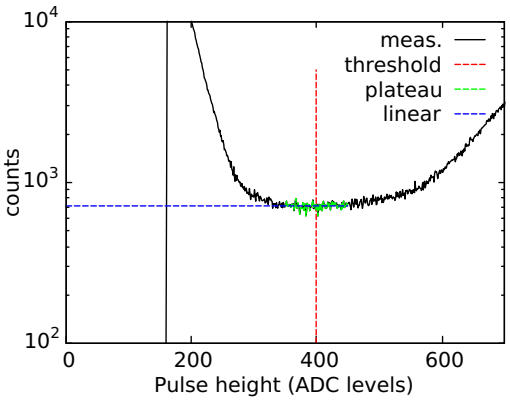

Figure 3.11: The plateau area of the sample-in measurement of ^{54}Fe separating the α-particles from the fission fragments. The linear fit of the area and the extrapolation to zero amplitude is also presented.

$$Y_B = \frac{Y_{FC} + Y_A}{F_{YB}} - Y_{FC} - Y_A, \tag{3.7}$$

where F_{YB} is a correction factor calculated using the formula: $F_{YB} = 1 - \Delta_{UF4}$. In this method, the Δ_{UF4} was determined experimentally and it amounts to $\Delta_{UF4} = 0.105(7) \cdot t_{UF4}$, where t_{UF4} is the thickness of the deposits in mg/cm^2. The efficiency was calculated individually for the sample-in (SI) and sample-out (SO) measurements of each sample and the results are presented in Table 3.5. The resulting neutron fluence energy distribution impinged on each scattering sample is presented in Fig. 3.12.

Table 3.5: Fission chamber efficiencies from the different experimental campaigns.

Sample	Efficiency	
	Sample-in	Sample-out
Fe-54	0.891(10)	0.890(10)
C-nat	0.890(10)	0.890(10)
Fe-56	0.888(10)	0.889(10)

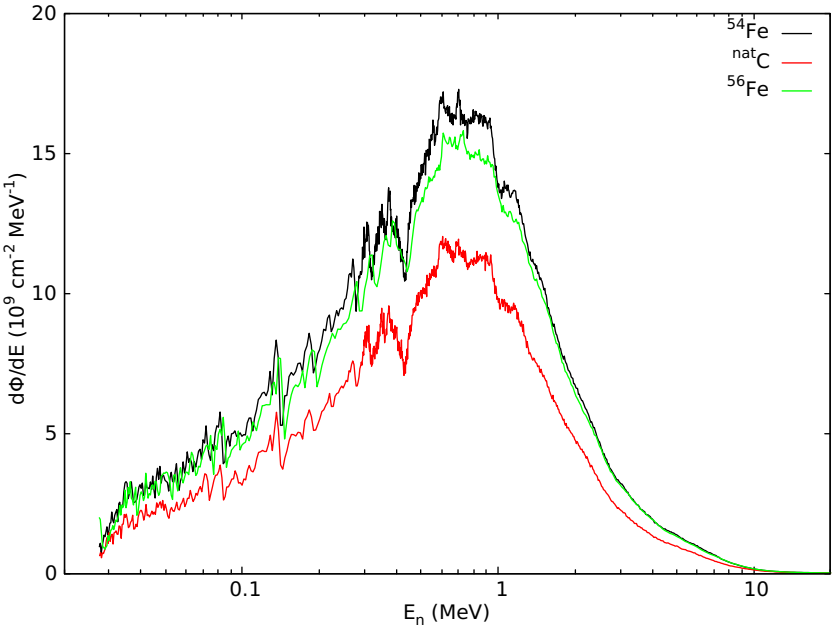

Figure 3.12: Neutron fluence impinged on the scattering samples with respect to the neutron incident energy.

3.2.3 Calculation of the cross section

Upon the determination of all the different components, the differential cross sections were calculated using Eq. (3.1) and then the angle-integrated cross sections were calculated using Eq. (2.10). As mentioned in Sec. 2.3, four detectors are placed in every scattering angle, therefore the final cross section for each angle was calculated by taking the average of the results of the four detectors. The corresponding total uncertainty of the resulting cross section was calculated by uncertainty propagation using the root-sum-square method, taking into account all individual contributions. In practise the final uncertainty was extracted by calculating the square root of the sum of the squares of the partial derivatives multiplied by the corresponding uncertainties. The statistical uncertainty of the cross section results from the number of scattered neutrons from the samples that arrived in the detectors and the fission fragment yield of the ^{235}U deposits. The various systematic contributions in the data analysis are presented in Table 3.6.

Table 3.6: Relative systematic uncertainties involved in the data analysis.

Contribution	^{54}Fe	^{nat}C	^{56}Fe
Sample areal density	2%	0.3%	0.2%
Fission chamber efficiency		1%	
^{235}U(n,f) cross section		1.1-1.2%	
^{235}U deposits mass		0.1%	
Multiple scattering correction (uncertainty of the simulation)	4-6%	3-8%	3-7%

3.3 Validation of the analysis with carbon

Except for the development of the response function models (see Sec. 2.4.2.2) the scattering experiment on natural carbon was used for the validation of the whole analysis procedure. In many laboratories, measurements of the cross section of neutron elastic scattering on carbon are used to calibrate detectors, monitor their stability, and validate experimental results. It is well-suited for such applications because the cross section is reliably known with an uncertainty below 1% up to 4.8 MeV incident neutron energy. Furthermore, the differential cross section is proposed as a standard by the IAEA, for neutron energies below 1.8 MeV [109].

In addition to the validation of the analysis, the new cross sections can be used to address issues in the nuclear data evaluations of carbon and assist in new evaluation efforts to extend the standard cross section to energies above 1.8 MeV. When it comes to the nuclear data evaluations of carbon, two different approaches have been adopted in the recent years. In the JEFF-3.3 evaluated library, released in 2017, only one file that corresponds to the elemental cross section is available, based on the ENDF/B-VI.1 evaluation by C. Y. Fu [110,111] for incident neutron energies below 20 MeV. In the ENDF/B-VIII.0 library, released in 2018, separate files for the isotopic description of the cross section for both ^{12}C (98.94%) and ^{13}C (1.06%) are provided. This is the first ENDF/B version providing isotopic instead of elemental cross sections for the case of carbon and it was achieved by performing a detailed R-matrix analysis for the description of the ^{13}C system using the EDA code [112], resulting in a new evaluation for the neutron cross sections of ^{12}C at energies below 6.5 MeV [113]. Additionally, changes were made in the Legendre coefficients that represent the angular distributions of neutron elastic and inelastic scattering. Even though in all these evaluations special care was given to reproduce the standard cross section until 1.8 MeV, discrepancies in the neutron angular distributions up to 22% are observed above this energy.

The resulting angular distributions of neutron elastic scattering on natural carbon, with respect to the incident neutron energy, for the 8 different detection angles, are presented in Fig. 3.13. The results are compared with the JEFF-3.3 and ENDF/B-VIII.0 evaluations folded with the experimental energy resolution. There is a relatively good agreement between experimental and evaluated values over the whole neutron energy range, especially for neutron incident energies below 1.8 MeV where the cross sections are considered as standards. Out of the two evaluations included in the figure, ENDF/B-VIII.0 seems to perform better compared to the data of this work in all detection angles, while in the case of JEFF-3.3 discrepancies are observed especially for the 100.6°detection angle. The total uncertainties on the angular distributions vary from 3% to 14%.

In Fig. 3.14, the differential neutron elastic scattering cross sections are given for a selection of neutron energies as a function of the detection angle θ, along with the available data in the EXFOR library and the cross section values provided by the JEFF-3.3 and ENDF/B-VIII.0 evaluations. Twelve 5 ns time-of-flight intervals have been selected for this comparison, that cover most of the neutron incident energies that have been reported from other experiments in the literature (see Table 3.7). There is a good agreement between the results of this work and the experimental values available in the EXFOR library. The results are in agreement within uncertainty with the most

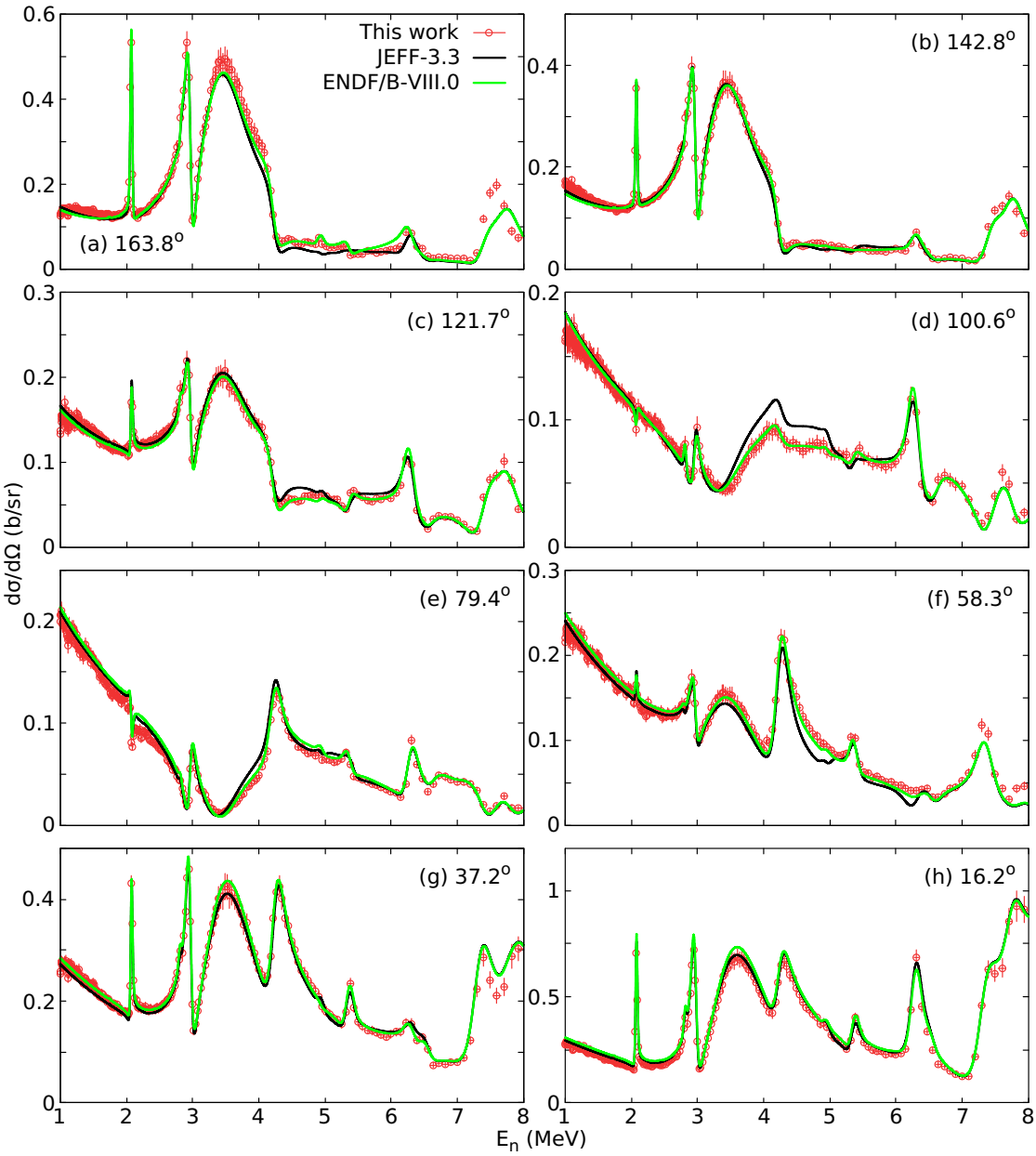

Figure 3.13: Differential cross sections of neutron elastic scattering on ^{nat}C as a function of the incident neutron energy at the 8 detection angles. The experimental cross sections are compared with the evaluated values provided by the JEFF-3.3 [10] and ENDF/B-VIII.0 [9] libraries folded with the experimental energy resolution.

recent data reported by Ramirez et al. (2022) [114] using quasi-monoenergetic neutron beams. Significant discrepancies between experimental data and evaluations are observed only in Fig. 3.14(e), for the interval that corresponds to 3 MeV incident neutron energy, where the evaluations are following a somewhat different trend compared to the majority of the experimental data. This is due to the quick change in the shape of the differential cross section in both backward and forward angles in this energy region. The cross section is falling rapidly from 2.9 to 3 MeV, where it reaches the minimum value, and then increases fast from 3 to 3.5 MeV. The resolution of the

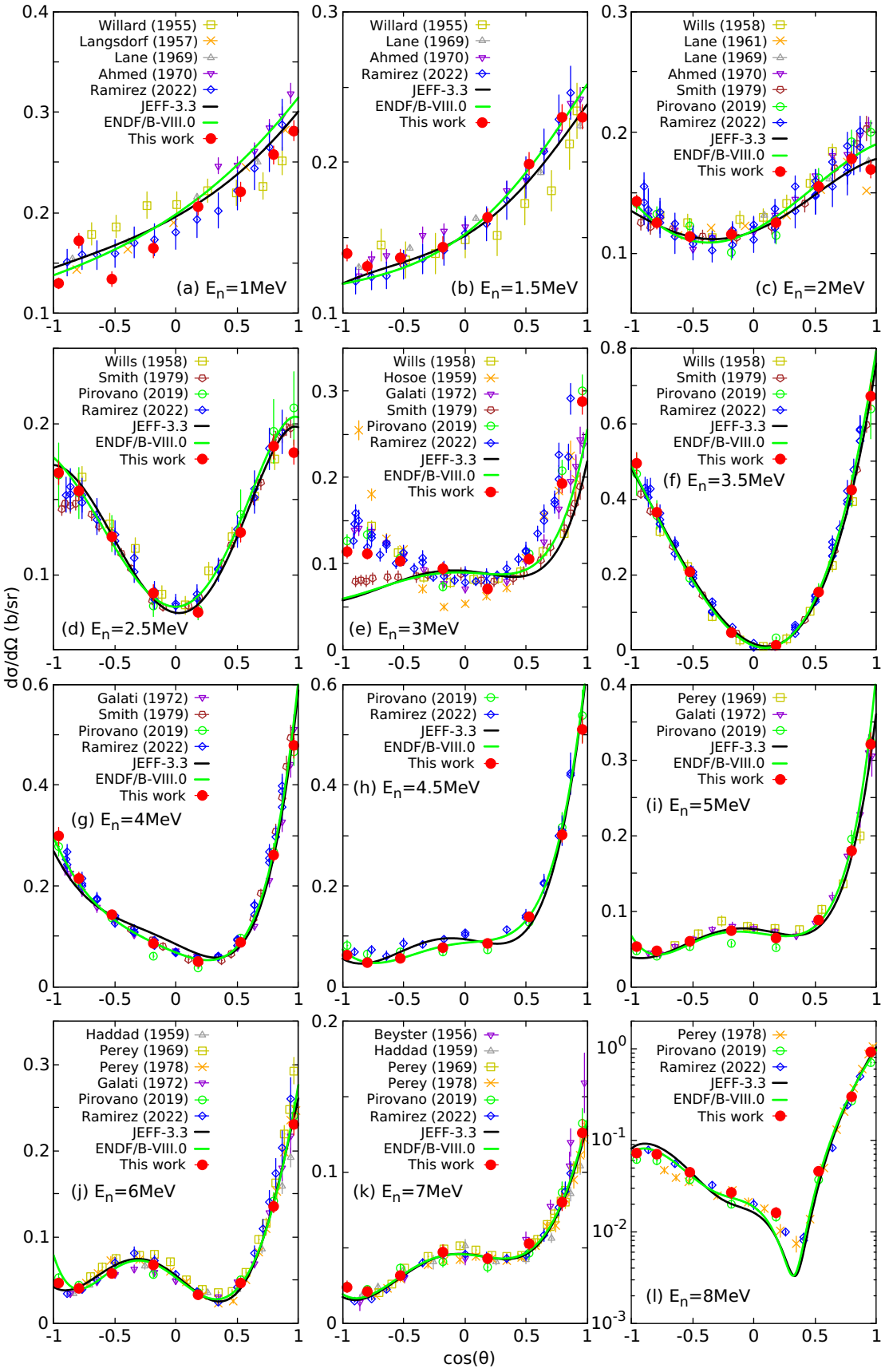

Figure 3.14: Comparison of differential cross sections of neutron elastic scattering on ^{nat}C as a function of the cosine of the scattering angle θ, with data available in the EXFOR [13] library and the angular distributions provided in the JEFF-3.3 [10] and ENDF/B-VIII.0 [9] evaluations. Twelve 5 ns t.o.f. intervals have been selected. The corresponding incident neutron energy is reported in each graph.

Table 3.7: Neutron elastic scattering cross section data of ^{nat}C available in the EXFOR library [13], in chronological order. The name of the first author, the year of publication, the neutron energy range under study, the quantity (CS and/or DA) and the number of points are listed.

Reference		E_n range (MeV)	Quantity (Points)	
Macphail (1940)	[115]	2.34-2.80	CS(6)	
Little Jr. (1955)	[116]	2.70		DA(9)
Jennings (1955)	[117]	4.40		DA(1)
Walt (1955)	[118]	4.10	CS(1)	DA(8)
Willard (1955)	[119]	0.55-1.50	CS(3)	DA(25)
Muehlhause (1956)	[120]	1.66		DA(35)
Beyster (1956)	[121]	7.00		DA(105)
Langsdorf Jr. (1957)	[122]	0.03-1.78	CS(34)	DA(370)
Wills Jr. (1958)	[123]	1.45-4.10		DA(107)
Hosoe (1959)	[124]	2.85-3.00		DA(56)
Haddad (1959)	[125]	6.00-7.00	CS(3)	DA(30)
Bostrom (1959)	[126]	4.21-7.58	CS(3)	DA(38)
Lane (1961)	[127]	1.96-2.24		DA(256)
Lane (1969)	[128]	0.50-2.00	CS(39)	DA(243)
Perey (1969)	[129]	4.60-8.56	CS(13)	DA(265)
Ahmed (1970)	[130]	0.50-2.00		DA(427)
Mcdaniel (1972)	[131]	7.48		DA(13)
Galati (1972)	[132]	3.03-6.94		DA(476)
Knox (1973)	[133]	2.63	CS(1)	DA(8)
Velkley (1973)	[134]	7.20-9.00		DA(106)
Hollandsworth (1975)	[135]	7.55		DA(6)
Perey (1978)	[136]	5.22-8.69	CS(40)	DA(670)
Smith (1979)	[137]	1.50-3.99	CS(31)	DA(438)
Pirovano (2019)	[62]	1.99-7.99	CS(140)	DA(1120)
Ramirez (2022)	[114]	0.50-7.96	CS(66)	DA(739)

current measurements is not good enough to properly describe this dip in the cross section. In Fig. 3.15 the proposed cross sections of the ENDF/B-VIII.0 evaluation for the lowest (2.981 MeV) and the highest (3.007 MeV) neutron energies of the 5 ns time-of-flight interval chosen to describe the cross section at 3 MeV are presented along with the experimental results. The strong fluctuating behavior of the cross section is observed. As expected, due to the limitations of the resolution of the measurement, the experimental results are lying in the middle of the proposed values by ENDF/B-VIII.0.

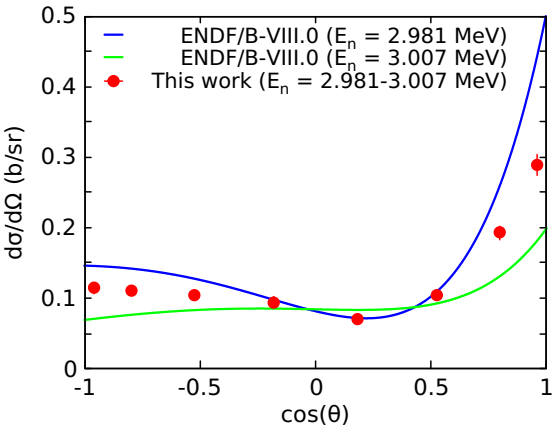

Figure 3.15: Comparison of the differential cross sections for the 5 ns interval that corresponds to the neutron energy range $E_n = 2.981 - 3.007$ MeV.

The results of the angle-integrated neutron elastic scattering cross-sections are presented in Fig. 3.16. The data are compared to the available cross section data in the EXFOR library and the evaluated values provided by the JEFF-3.3 and ENDF/B-VIII.0 libraries folded with the experimental energy resolution. The results of this work are in good agreement, within uncertainties, with the other experimental values and the evaluation libraries. These results are consistent with the most recent work by Ramirez et al. (2022) [114] which provides data in key energy points of the cross section in this energy region, specifically around the well-known resonance of carbon at 2.078 MeV, in the maximum of the cross section at energies around 3.5 MeV, and also in energies around the resonance at 6.48 MeV. Also, the data are compatible within uncertainties with the work

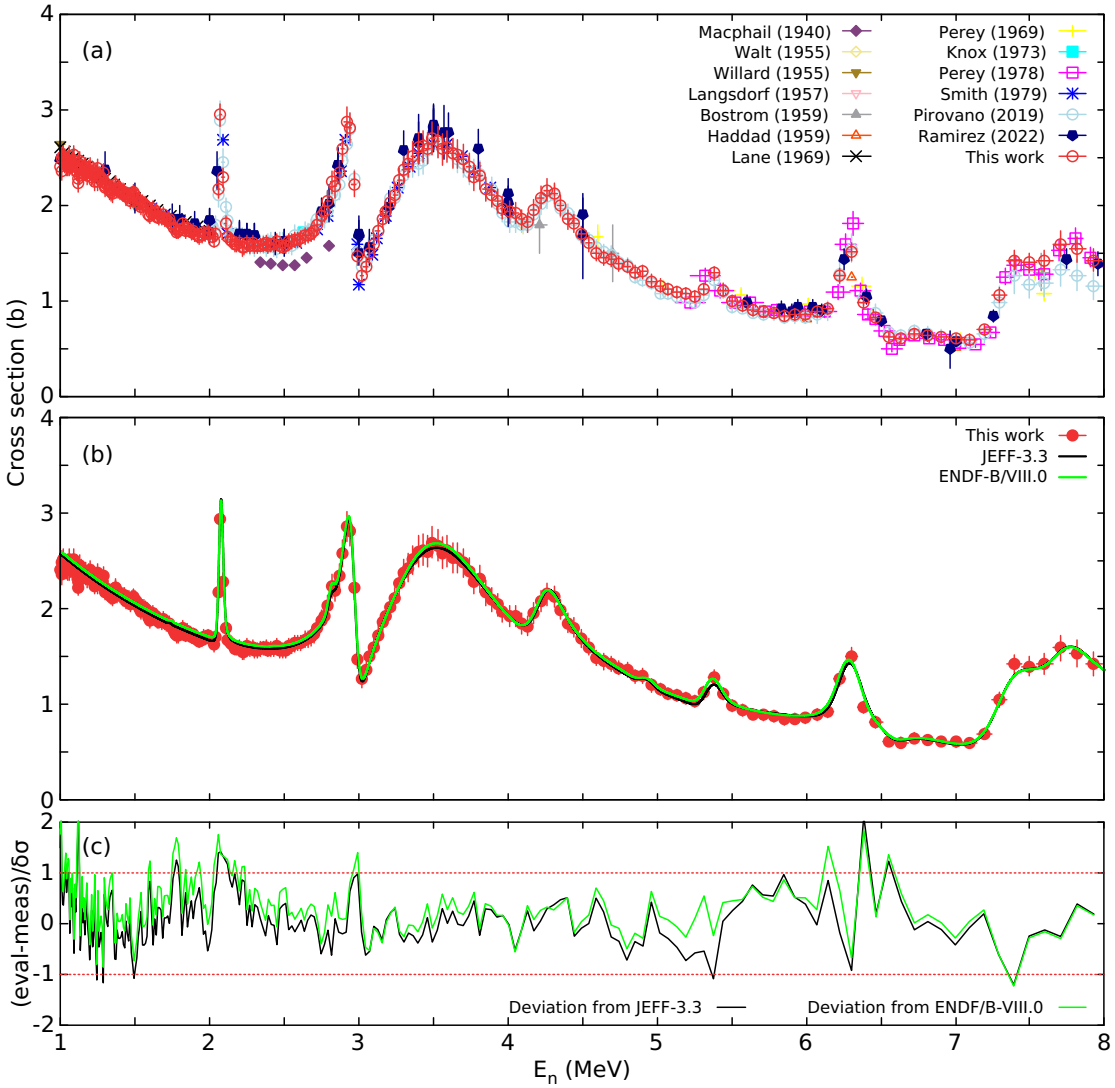

Figure 3.16: Angle-integrated cross section of neutron elastic scattering on ^{nat}C as a function of the incident neutron energy compared with (a) the data available in the EXFOR library [13], and (b) the JEFF-3.3 [10] and ENDF/B-VIII.0 [9] libraries folded with the experimental energy resolution. In (c) the deviation of the experimental results from the evaluated values is presented as the difference between evaluation and measurement divided by the experimental uncertainty ($\delta\sigma$).

by Perey et al. (1978) [136] which is the only measurement that provides a detailed description of the cross section in the energy range from 5.5 to 8 MeV. The total uncertainties on the angle-integrated cross sections varied from 3% to 8%. Additionally, in Fig. 3.16(c) the deviation between the results of this work and the evaluations is presented relative to the experimental uncertainty ($\delta\sigma$). It is observed that the results of this work are in agreement with the evaluations within the uncertainty over the whole neutron energy range. Discrepancies outside the experimental uncertainties are observed only for a handful of experimental points although it never exceeds $|2\delta\sigma|$. The sharp resonances in the cross section on neutron elastic scattering on carbon at the 2.816 MeV and 4.937 MeV incident energies could not be measured with the current energy resolution of the spectrometer. This was the first measurement providing high-resolution data for neutron elastic scattering on natural carbon in the energy range of 1 to 2 MeV and only the second high-resolution measurement in the energy range from 2 to 8 MeV, with the first one also been performed at the ELISA spectrometer by Pirovano et al. [62] using a thicker natural carbon sample.

The agreement between the experimentally determined cross sections and the evaluated values demonstrates that the response function models that were developed in the framework of this analysis and then used in the ^{54}Fe and ^{56}Fe data, are able to properly reproduce the experimental light output distributions. Overall, this agreement shows that the analysis procedure followed in the present work is able to produce precise results of both the differential and angle-integrated elastic scattering cross sections for fast neutrons in the energy region from 1 to 8 MeV.

3.4 Results for neutron scattering on ^{54}Fe

In the case of the ^{54}Fe experiment, elastic scattering angular distributions and integral cross sections were produced in the energy range from 1 to 8 MeV, whereas for inelastic scattering, partial differential and angle integrated cross sections were estimated from the first excited state of ^{54}Fe in the energy range from 2.5 to 5.5 MeV [138]. The results are presented below and are compared with the available experimental and evaluated nuclear data.

3.4.1 Elastic scattering

The results for the differential cross section of neutron elastic scattering on ^{54}Fe are presented in Fig. 3.17 with respect to the incident neutron energy for 8 different detection angles, in the energy range from 1 to 8 MeV. The results are compared with the values provided by the JEFF-3.3 and ENDF/B-VIII.0 evaluations folded with the experimental energy resolution. For the evaluated differential cross sections, ENDF/B-VIII.0 has adopted optimized theoretical calculations, produced by the EMPIRE nuclear reaction code [30], while JEFF-3.3 used a Legendre representation for energies below 20 MeV, based on the sum of calculated Legendre coefficients for compound nucleus and shape-elastic scattering. The difference between the adopted methods of the evaluations explain the difference in the shape of the resulting cross sections: the ENDF/B-VIII.0 cross sections follow a smooth trend, while the JEFF-3.3 cross sections have a fluctuating

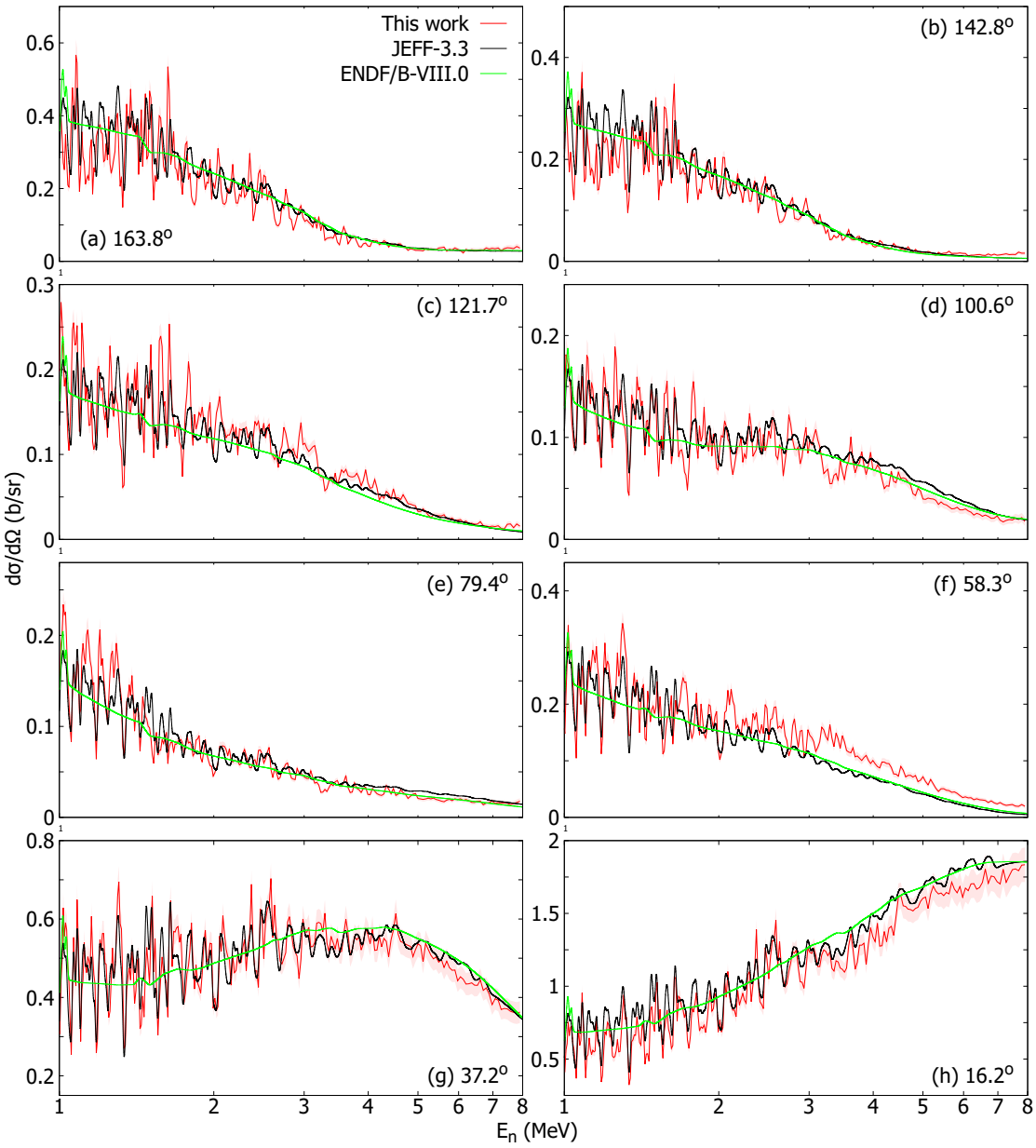

Figure 3.17: Differential cross sections of neutron elastic scattering on ^{54}Fe as a function of the incident neutron energy at the 8 detection angles. The experimental cross sections are compared with the evaluated values provided by the JEFF-3.3 [10] and ENDF/B-VIII.0 [9] libraries folded with the experimental energy resolution.

behavior. There is an overall good agreement between experimental and evaluated values over the whole neutron energy range. Only in the case of 58.3°, for energies approximately above 2 MeV, the experimental cross section is systematically higher than the values proposed by the evaluation. The same issue was also observed in [62], at a comparison of experimental differential cross section of neutron elastic scattering on ^{nat}Fe at 58.3° and evaluated values proposed by ENDF/B-VIII.0. Meanwhile, in the case of the ^{nat}C(n,n) validation measurement the resulting cross section at 58.3° (see Fig. 3.13) was in good agreement with the well known evaluated values, and, on

the other hand, there is this consistency between ^{54}Fe and ^{nat}Fe at 58.3°. This is an indication of possible issues with the evaluations of neutron angular distributions on Fe isotopes. For the differential cross sections the total uncertainties vary from 5% to 25%, and are mainly generated from the duration of the experiments and their related statistics. The highest uncertainties, above 15%, are observed in the energy range between 6 and 8 MeV at backward angles, where the cross section is reaching very low values due to the fact that elastic scattering on Fe is a forward-peaked reaction.

In Fig. 3.18, the differential cross section is given as a function of the cosine of the detection angle θ. The data are compared with values available in the EXFOR library and the angular distributions provided by the JEFF-3.3 and ENDF/B-VIII.0 evaluations. Twelve 5 ns t.o.f. intervals have been selected, that cover most of the neutron incident energies measured in other experiments reported in EXFOR (Table 1.1). In general, there is a satisfactory agreement between the cross section values calculated in this work and the experimental data available in literature. The results are in agreement with the latest measurement performed by Vanhoy et al. (2018) [24] using quasi-monoenergetic neutron beams. Also, in the energy intervals above 2.5 MeV for the cosine that corresponds to the 58.3° (0.5255) detection angle, it is observed again that the cross section values calculated in this work are higher than the ones reported in JEFF-3.3, and ENDF/B-VIII.0 evaluations, but values from other experiments also support higher cross sections in this region.

The angle-integrated neutron elastic scattering cross section is presented in Fig. 3.19. The results are compared with the data available in the literature, and the JEFF-3.3 and ENDF/B-VIII.0 evaluations folded with the experimental resolution of the measurement. In the JEFF-3.3 evaluation, the elastic scattering cross section was calculated by subtracting the optical model based non-elastic cross section from the evaluated total cross section, which was purely based on the experimental data of Carlton et al. (1985) [139], while the ENDF/B-VIII.0 evaluated values were produced using the EMPIRE code. The results of this work are in overall good agreement with the few previous experimental values available in the EXFOR library, the JEFF-3.3, and ENDF/B-VIII.0 evaluations, especially in the energy region between 1 and 3 MeV where resonances are causing strong fluctuations in the cross section. Also, the deviation between the results of this work and the evaluations is presented in Fig. 3.19(c) relative to the experimental uncertainty ($\delta\sigma$). It is observed that the results of this work are in excellent agreement with the JEFF-3.3 evaluation within the uncertainty over the whole neutron energy range. When it comes to the ENDF/B-VIII.0 evaluation discrepancies outside the experimental uncertainties are observed in the 1-3 MeV energy region where the evaluated cross section has a smooth behaviour and a proper comparison with the fluctuating experimental cross section is not possible. This agreement validates the evaluation methodology employed in JEFF-3.3, which involved the combination of high-resolution transmission data and optical model calculations to extract the elastic scattering cross section. The total uncertainty of the angle-integrated cross section varies between 5% and 8%.

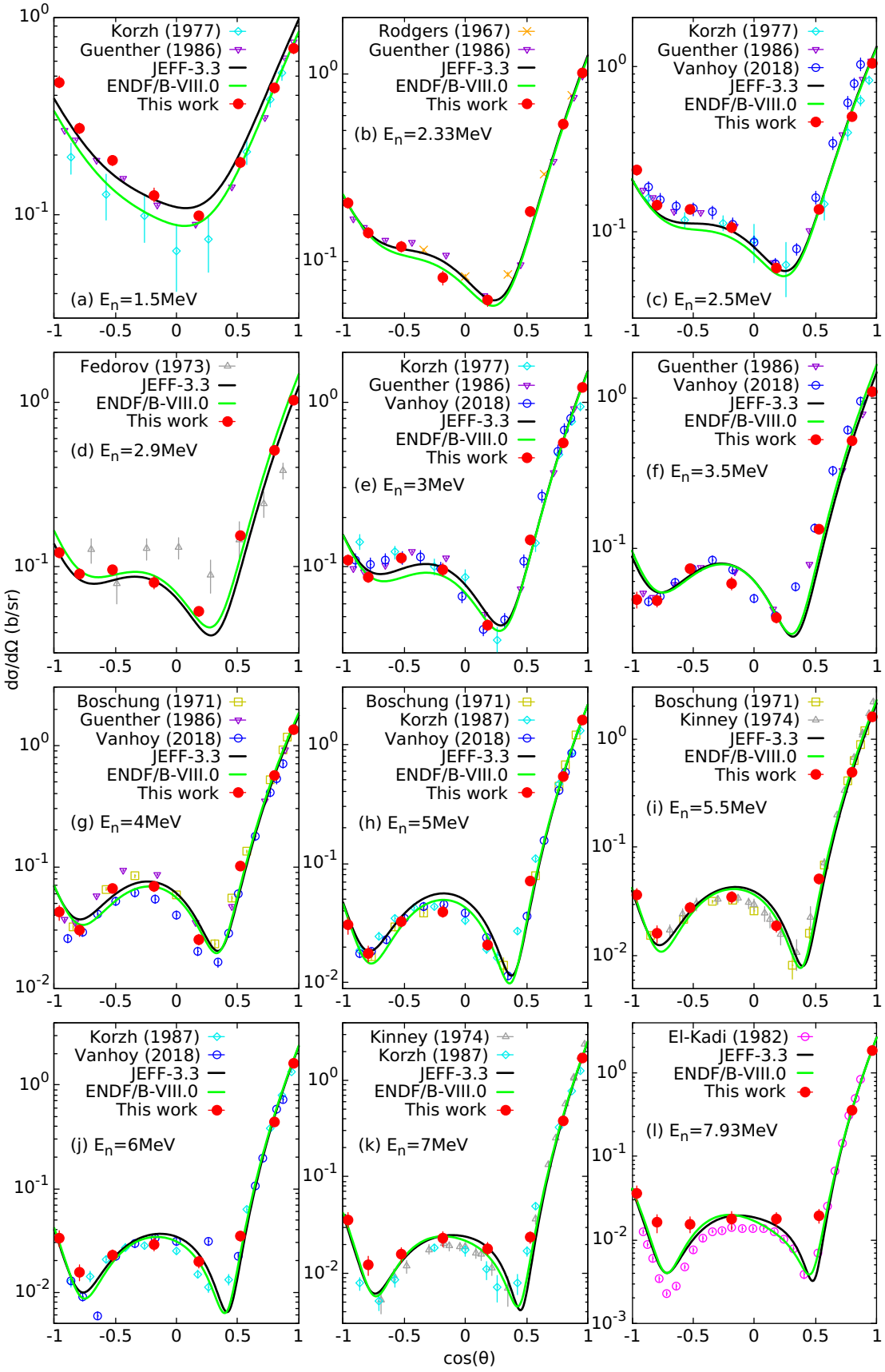

Figure 3.18: Comparison of differential cross sections of neutron elastic scattering on ^{54}Fe as a function of the cosine of the scattering angle θ, with data available in the EXFOR [13] library and the angular distributions provided in the JEFF-3.3 [10] and ENDF/B-VIII.0 [9] evaluations. Twelve 5 ns t.o.f. intervals have been selected. The corresponding incident neutron energy is reported in each graph.

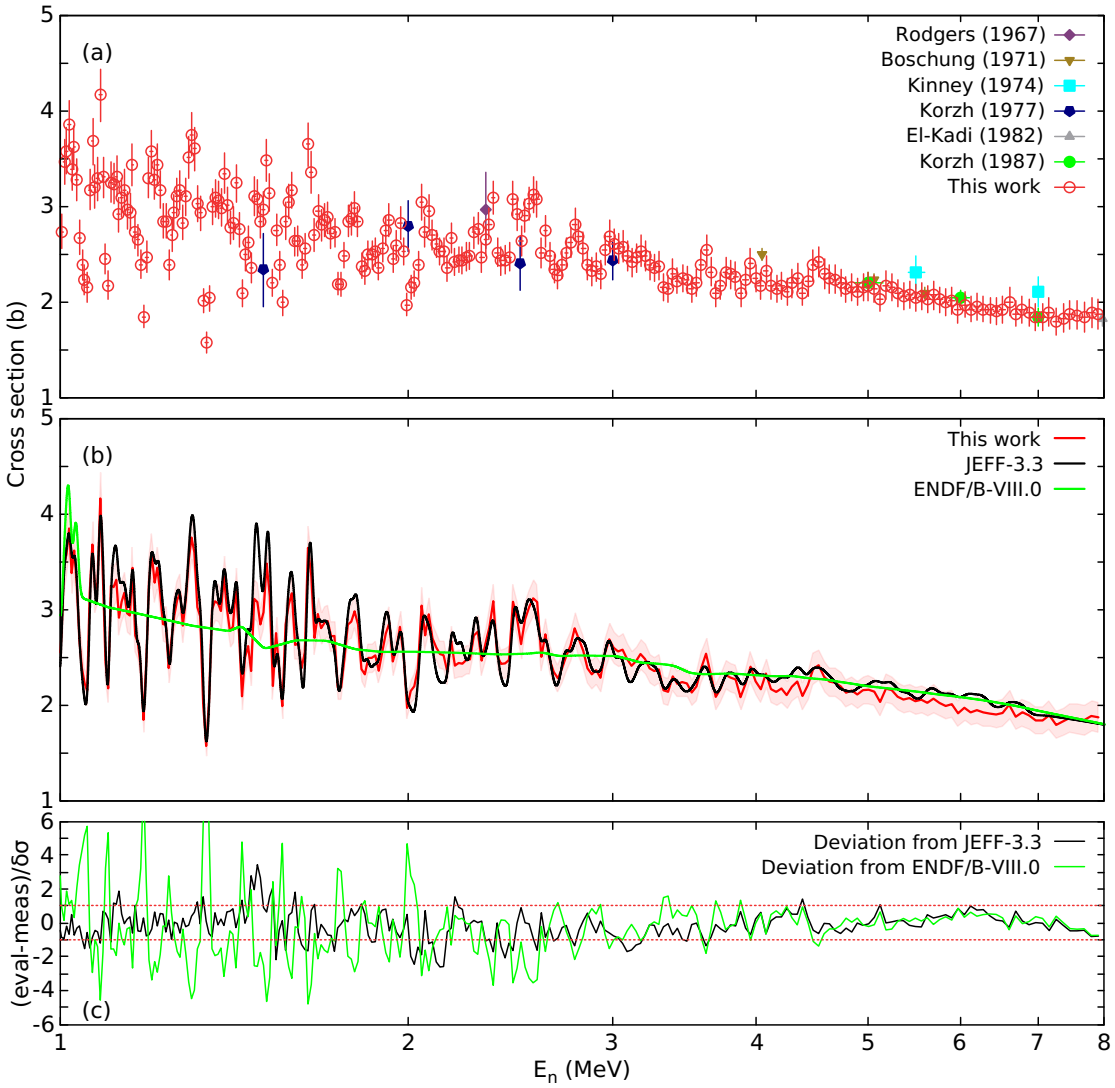

Figure 3.19: Angle-integrated cross section of neutron elastic scattering on ^{54}Fe as a function of the incident neutron energy compared with (a) the data available in the EXFOR library [13], and (b) the JEFF-3.3 [10] and ENDF/B-VIII.0 [9] libraries folded with the experimental energy resolution. In (c) the deviation between the experimental and evaluated values is presented as the difference between evaluation and measurement divided by the experimental uncertainty ($\delta\sigma$).

3.4.2 Inelastic scattering

The results for the differential cross section of neutron inelastic scattering from the first excited state of ^{54}Fe (1.408 MeV), in the energy range from 2.5 to 5.5 MeV, are presented in Fig. 3.20. The cross sections are given with respect to the incident neutron energy at 8 different detection angles. The values are compared with the ENDF/B-VIII.0 evaluated library, which is based on optimized theoretical calculations using the EMPIRE code. A comparison with the JEFF-3.3 library was not possible in this case, as the corresponding data were not available in the JEFF-3.3 file. For most of the detection angles the measured values are slightly higher than the ones provided by ENDF/B-VIII.0 over the whole neutron energy range. The total uncertainties range from 7% to 50%. Just as

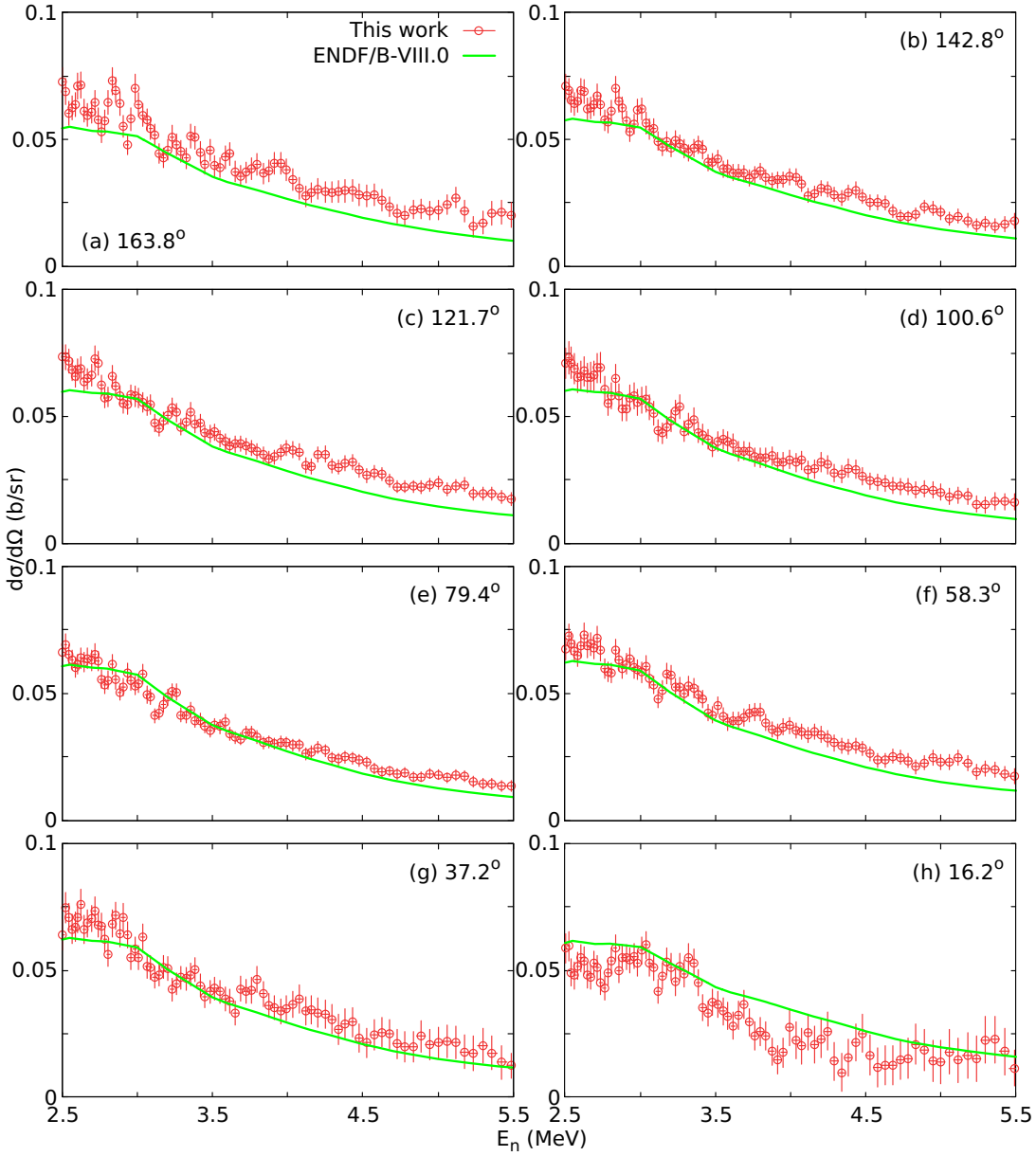

Figure 3.20: Differential cross sections of neutron inelastic scattering from the first excited state of ^{54}Fe as a function of the incident neutron energy at the 8 detection angles. The experimental cross sections are compared with the evaluated values provided by the ENDF/B-VIII.0 [9] library.

elastic scattering, high uncertainties, above 20%, are observed in the two forward detectors for energies above 4 MeV. The reason for that is the fact that the inelastic scattering yield is extracted after the subtraction of the elastic scattering component in the corresponding light output distribution (see Fig. 3.5). At these angles, the inelastic scattering cross section is decreasing but the elastic scattering one is increasing with the neutron energy reaching values 20 times higher than the inelastic scattering one, making it the predominant reaction in this energy range. In this case, the only way to lower the uncertainties is to perform much longer measurements.

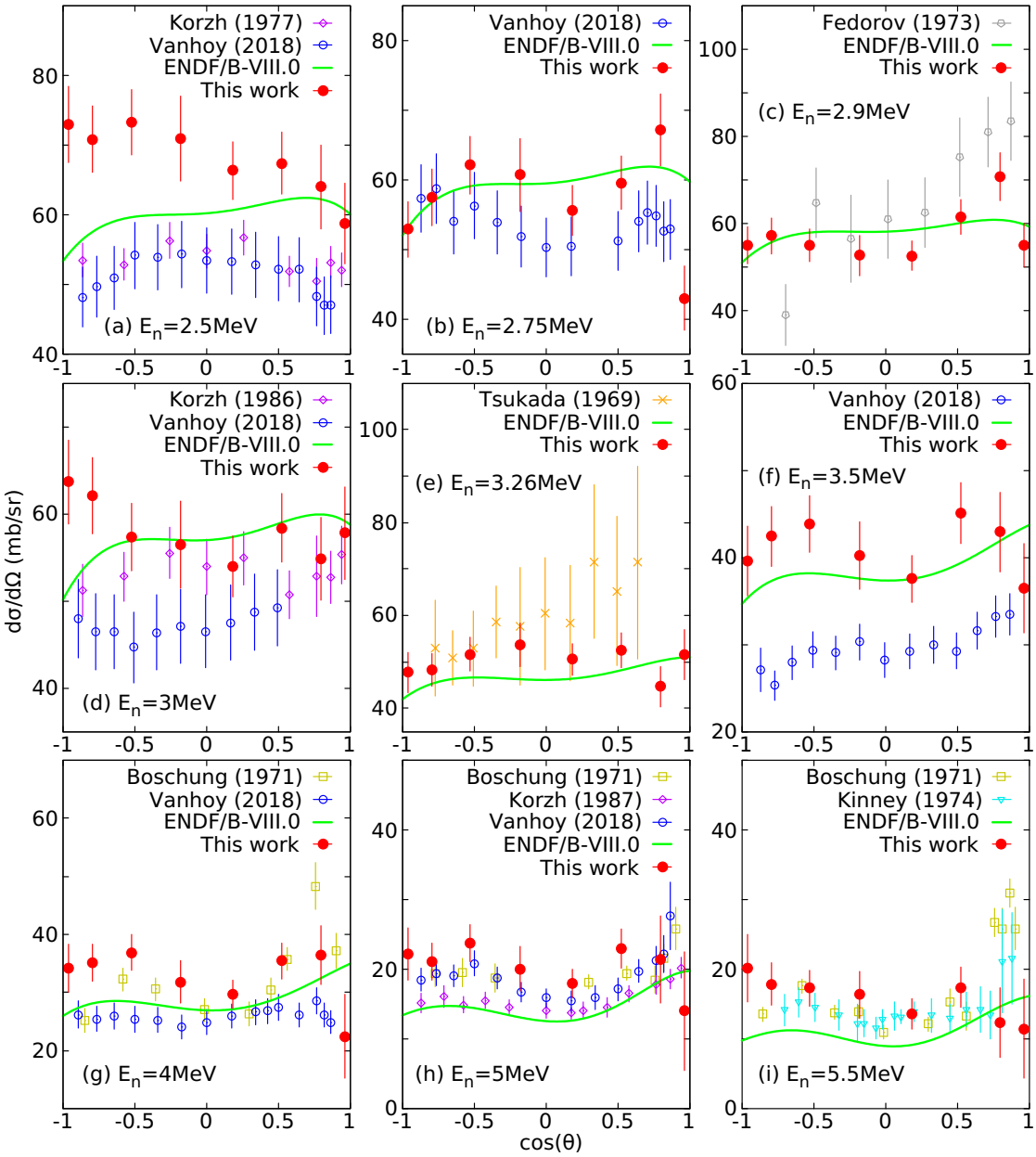

Figure 3.21: Comparison of differential cross sections of neutron inelastic scattering from the first excited state of ^{54}Fe as a function of the cosine of the scattering angle θ, with data available in the EXFOR [13] library and the angular distributions provided in the ENDF/B-VIII.0 [9] evaluation. Nine 5 ns t.o.f. intervals have been selected. The corresponding incident neutron energy is reported in each graph.

In Fig. 3.21 the differential cross section is presented as a function of the cosine of the detection angle θ, and compared with all the data available in the literature and the ENDF/B-VIII.0 evaluation. Similarly to elastic scattering, nine 5 ns t.o.f. intervals have been selected, covering all the neutron incident energies that have been measured in other experiments reported in EXFOR (Table 1.3). Even though in most cases the results of this work remain in agreement within uncertainty with the ENDF/B-VIII.0 evaluation, large discrepancies are observed between the different

experimental data available in the literature, the results of this work, and the ENDF/B-VIII.0 evaluation. In the 5 ns t.o.f. intervals that correspond to neutron incident energies below 5 MeV the most recent data by Vanhoy et al. (2018) [24] are included in the graphs which support lower cross sections compared to the results of this work and to the ENDF/B-VIII.0 evaluation. Only in the last two 5 ns t.o.f. intervals that correspond to 5 MeV and 5.5 MeV neutron energies there is a relatively good agreement between the different experimental data. Overall, these discrepancies between the different experiments and the evaluation that are observed in Fig. 3.21 indicate issues in the angular distributions of neutron inelastic scattering on ^{54}Fe that need to be further investigated.

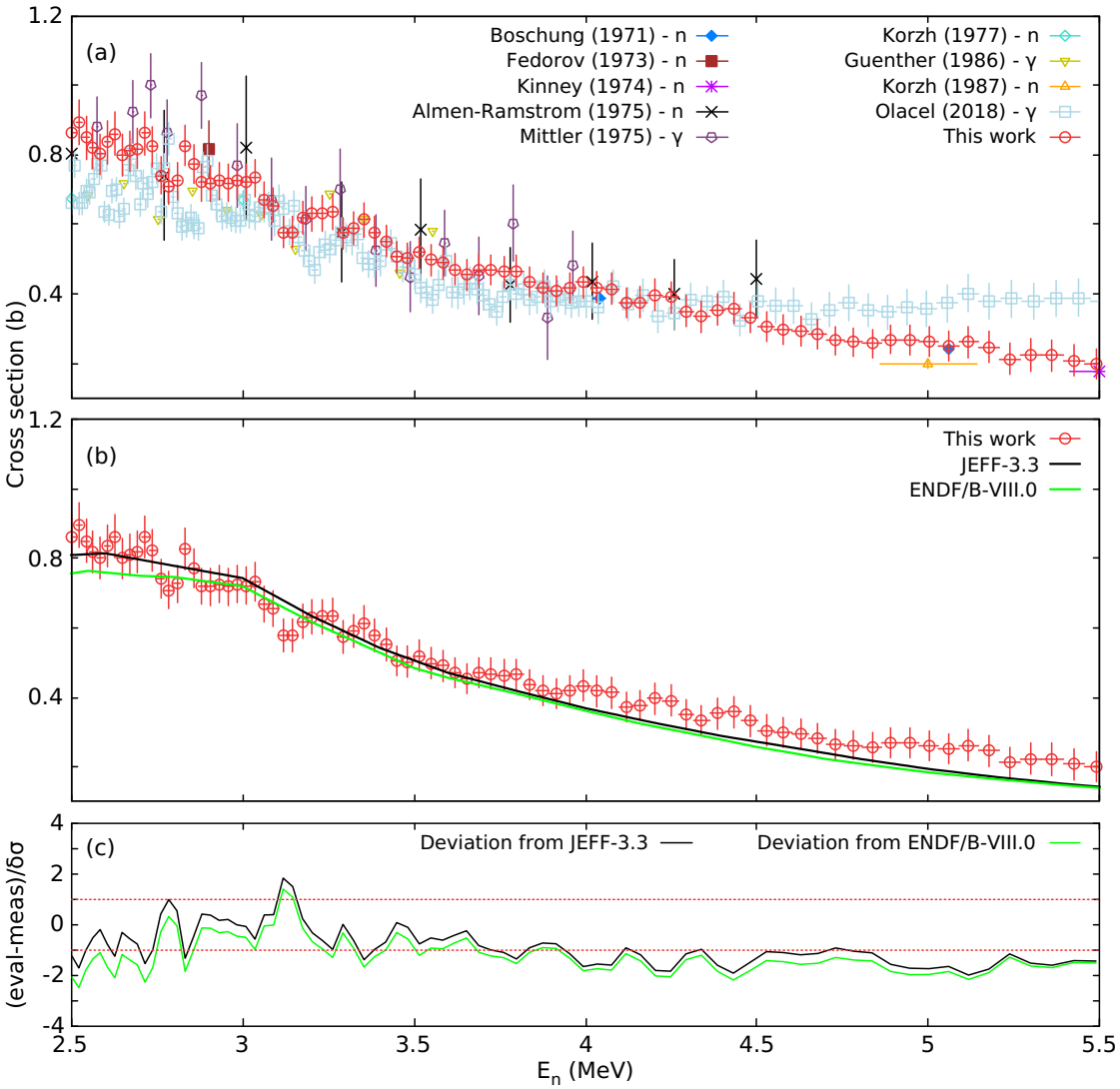

Figure 3.22: Angle-integrated cross section of neutron inelastic scattering from the first excited state of ^{54}Fe as a function of the incident neutron energy compared with (a) the data available in the EXFOR library [13], and (b) the JEFF-3.3 [10] and ENDF/B-VIII.0 [9] libraries. In (c) the deviation of the experimental results from the evaluated values is presented as the difference between evaluation and measurement divided by the experimental uncertainty ($\delta\sigma$).

The angle-integrated neutron inelastic scattering cross section from the first excited state of ^{54}Fe is presented in Fig. 3.22 in the energy range from 2.5 to 5.5 MeV. The total uncertainty of the cross section varies between 6% and 20%. The results are compared with the data available in the literature, and the JEFF-3.3 and ENDF/B-VIII.0 evaluations. It is observed that the results are following the trend of the evaluation values, with a good agreement within uncertainty with JEFF-3.3 which proposes slightly higher cross section values than ENDF/B-VIII.0. In comparison with the other experimental values reported in the EXFOR library, there is an overall good agreement within uncertainty with almost all experiments. It is worth to mention that between 3 and 4.5 MeV neutron energies the results are in agreement within uncertainty with another high-resolution measurement performed at GELINA by Olacel et al. (2018) [39] using γ-spectrometry by employing the GAINS spectrometer. For incident energies above 4.5 MeV, the results of this work, while higher in magnitude, follow the trend of existing evaluations and show good agreement with the data from Boschung et al. (1971) [17] and Kinney et al. (1974) [19]. However, the data from Olacel are consistently higher, likely due to the poorly understood level scheme of the compound nucleus ^{55}Fe above this energy. This leads to unknown states populating the level under study, a contribution the authors could not correct for, as the levels remain unidentified.

Considering the overlapping energy region between the 1-8 MeV elastic scattering cross section and the 2.5-5.5 MeV partial inelastic scattering cross section that were extracted from the present experiment, there are some tests that can be made to validate the quality of the results. In the present work, the narrow energy region from 2.5 to 2.8 MeV was chosen to compare the results with the total cross section of ^{54}Fe. Taking into account the different reaction channels open in this energy region (see Fig. 3.23) the two dominant reaction mechanisms are the elastic scattering and the inelastic scattering from the first excited state. Other reaction channels are open in this region too, specifically the (n,p), (n,γ), (n,n$'_2$), and (n,n$'_3$) but their contribution to the total cross section was considered negligible in this test since the cross section of these reactions in the 2.5-2.8 MeV energy region is almost two orders of magnitude lower than the elastic scattering cross section. Nevertheless, the contribution of the non scattering reactions [(n,p) and (n,γ)], although negligible, was taken from the JEFF-3.3 evaluation and was added to the elastic and inelastic scattering cross sections of the present work. In Fig. 3.24 the extracted semi-experimental total cross section of ^{54}Fe in the energy region from 2.5 to 2.8 MeV is presented along with the total cross sections reported in the EXFOR library and the JEFF-3.3 and ENDF/B-VIII.0 evaluations. Only two total cross section measurements from Carlton et al.

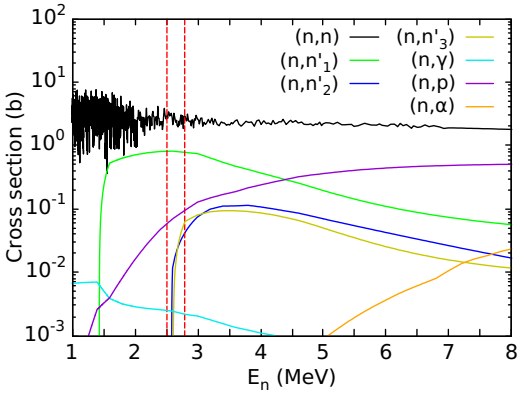

Figure 3.23: JEFF-3.3 [10] cross sections of the different reaction channels open in the 1 to 8 MeV energy region for ^{54}Fe. The red lines illustrate the energy region in which the semi-experimental total cross section was calculated.

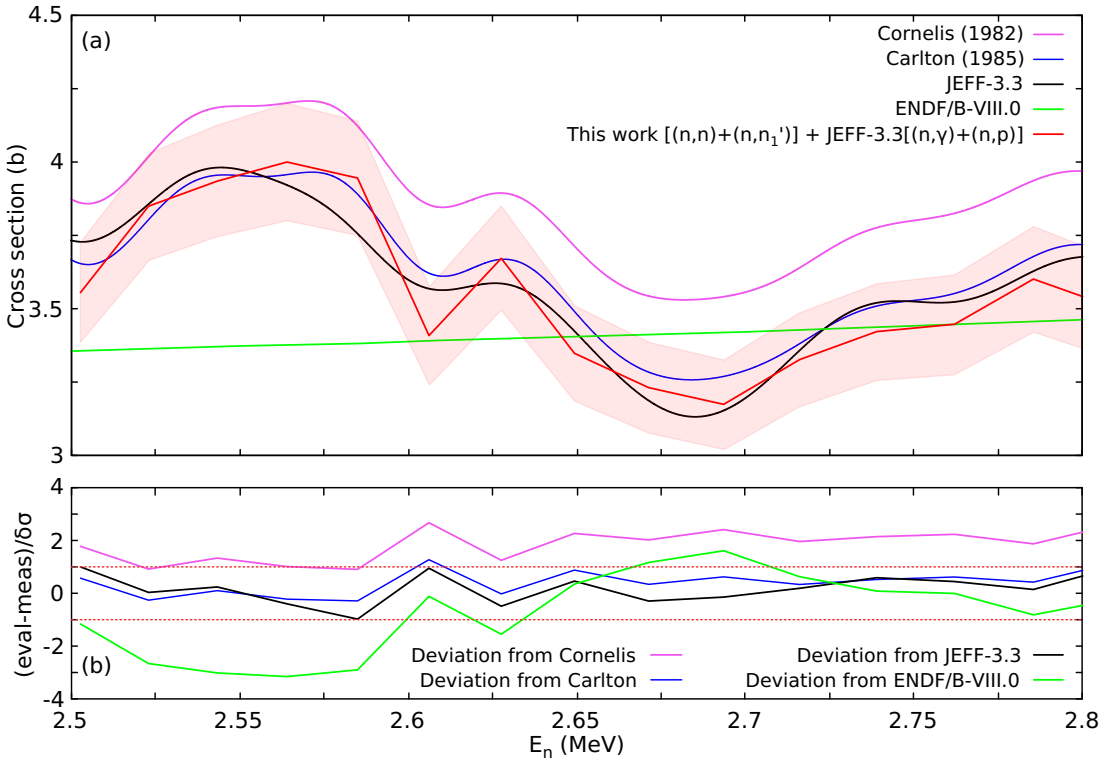

Figure 3.24: Semi-experimental total cross section of ^{54}Fe as a function of the incident neutron energy compared with the data available in the EXFOR library [13], and the JEFF-3.3 [10] and ENDF/B-VIII.0 [9] libraries all folded with the experimental energy resolution. In (b) the deviation of the experimental results from the evaluated and experimental values is presented as the difference between evaluation (or EXFOR data) and measurement divided by the experimental uncertainty ($\delta\sigma$).

(1985) [139] and Cornelis et al. (1982) [140] are available in EXFOR for this energy region. Both the evaluations and the EXFOR data were folded with the experimental energy resolution in order to make the comparison easier. It is observed that the results of this work are in excellent agreement within uncertainty with the JEFF-3.3 evaluation and the measurement by Carlton et al. (1985) [139], while the data of Cornelis et al. (1982) [140] are reporting systematically higher cross section. The fact that the semi-experimental total cross section is in such good agreement with the JEFF-3.3 evaluation and the high-resolution transmission measurement of Carlton et al. (1985) [139], validates the quality of the experimentally measured cross sections in the present work.

3.5 Results for neutron scattering on ^{56}Fe

From the ^{56}Fe experiment, elastic scattering angular distributions and angle integrated cross sections were produced in the energy range from 1 to 8 MeV and for inelastic scattering partial differential and angle integrated cross sections were estimated from the first excited state of ^{56}Fe in the energy range from 2 to 5 MeV and from the second excited state in the energy range from

3 to 6 MeV. The results are given below and are compared with the available experimental cross sections in the literature and the most recent evaluated nuclear data libraries.

3.5.1 Elastic scattering

The differential cross sections of neutron elastic scattering on ^{56}Fe are presented in Fig. 3.25 with respect to the incident neutron energy for the 8 different detection angles, in the energy range

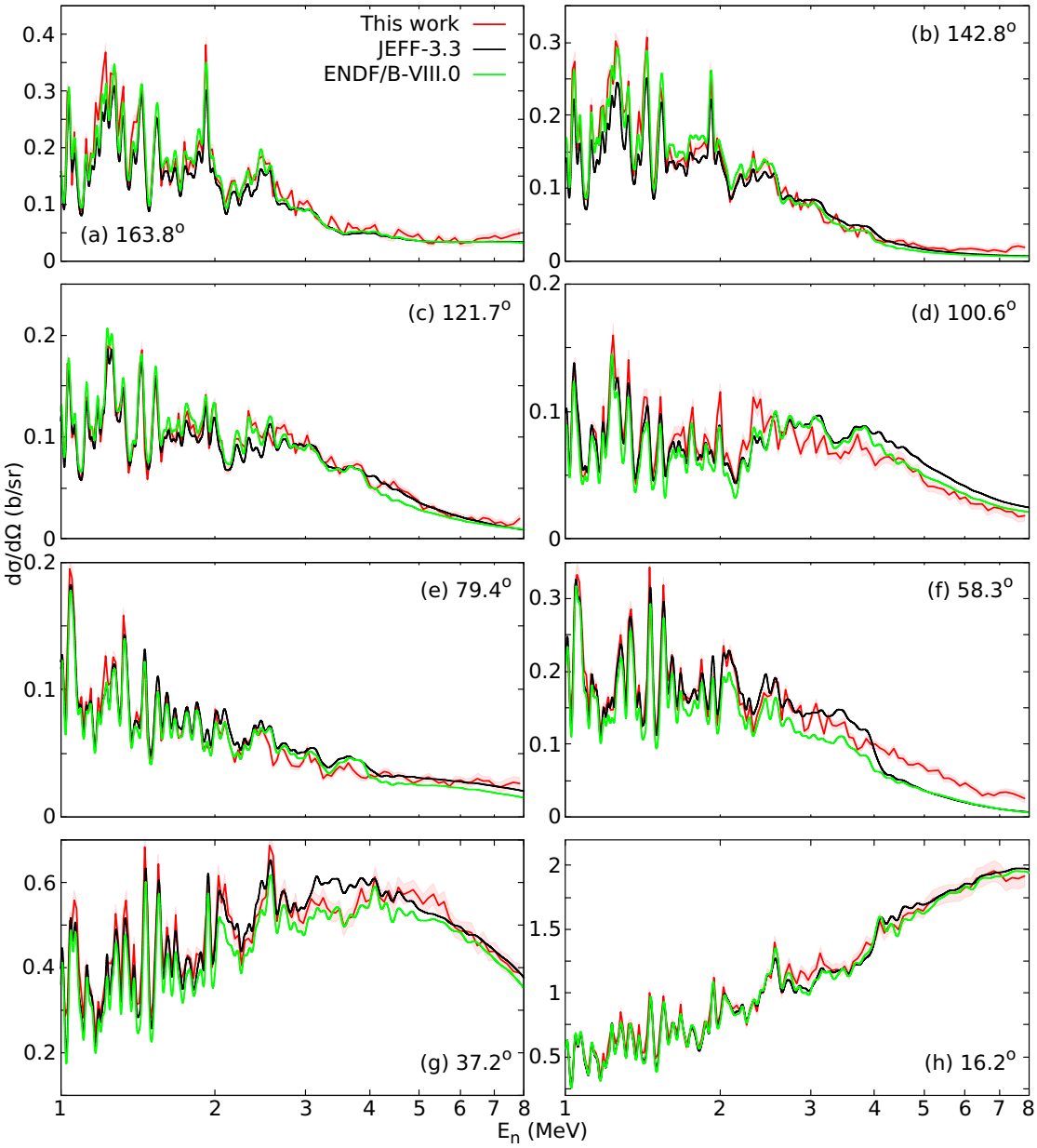

Figure 3.25: Differential cross sections of neutron elastic scattering on ^{56}Fe as a function of the incident neutron energy at the 8 detection angles. The experimental cross sections are compared with the evaluated values provided by the JEFF-3.3 [10] and ENDF/B-VIII.0 [9] libraries folded with the experimental energy resolution.

1-8 MeV. The results are compared with the JEFF-3.3 and ENDF/B-VIII.0 evaluations folded with the experimental energy resolution. In the case of the ^{56}Fe evaluations, ENDF/B-VIII.0 is strongly based on ^{nat}Fe high resolution measurements. Specifically, in the energy range from 1 to 2.5 MeV the angular distributions correspond to re-fitted Kinney et al. (1976) [141] ^{nat}Fe data with some adjustments that reduce the anisotropy, based on the comparison with Perey et al. (1991) [142] enriched ^{56}Fe data in the overlapping region. In the energy range from 2.5 to 4 MeV the angular distributions were taken from Smith et al. (1980) [143] and above 4 MeV neutron incident energy the distributions are based on calculations performed with the EMPIRE code. The JEFF-3.3 angular distributions were adopted by the JEFF-3.0 version which originates from the EFF-2.4 evaluation, updated by V. Pronyaev et al. (1995) [144]. The same approach as the one in ENDF/B-VIII.0 was followed, i.e. the high-resolution data from ORELA by Kinney et al. (1976) [141] were used up to 2.5 MeV. These data are given in 1 keV steps, were converted into relative Legendre coefficients and the resulting coefficients α_1-α_4 were used to create the file that correctly describes the fine structure of the elastic scattering angular distribution in the unresolved resonance range. In the energy region 2.5-4 MeV the data from ANL by Smith et al. (1980) [143] were used and for energies above 4 MeV the evaluation is based on theoretical calculations. There is a relatively good agreement between experimental and evaluated values over the whole neutron energy range. Especially in the 1-3 MeV energy region, where the angular distributions are fluctuating a lot, even though the resolution of this measurement is slightly worse compared to the one in the ^{54}Fe measurement, the agreement between experiment and evaluations, both in cross section behavior/trend and magnitude, is very good within the uncertainties. Again, in the case of the 58.3° detection angle, this time for energies approximately above 4 MeV, the experimental cross section is systematically higher than the values proposed by the evaluations. Along with the ^{54}Fe data mentioned above (see Fig. 3.17) and the ^{nat}Fe data by Pirovano et al. (2019) [62], this is the third measurement of iron where discrepancies have been observed in this detection angle, suggesting possible issues in the evaluated angular distributions of iron. The total uncertainties of the differential cross sections vary from 3% to 20%, and are mainly generated from the duration of the experiments and their related statistics.

In Fig. 3.26, the differential cross section is given as a function of the cosine of the detection angle θ. The results are compared with data available in the EXFOR library and the angular distributions provided by the JEFF-3.3 and ENDF/B-VIII.0 evaluations. Twelve 10 ns t.o.f. intervals have been selected aiming to cover most of the neutron incident energies measured in other experiments reported in EXFOR (Table 1.2) in the 1-8 MeV energy region. Overall, there is a favorable agreement between the cross sections of the present experiment and the experimental data found in the literature. The results align with the most recent measurements conducted by Ramirez et al. (2017) [28] utilizing quasi-monoenergetic neutron beams. In comparison with the evaluations, in the t.o.f. intervals that correspond to neutron incident energies below 2 MeV [see Fig. 3.26 (a) & (b)], even though the evaluations are following the same trend there are differences in the magnitude of the cross sections compared to the experimental data. For energies above 2 MeV, the JEFF-3.3 evaluations seem to be performing better than ENDF/B-VIII.0 with respect to the results

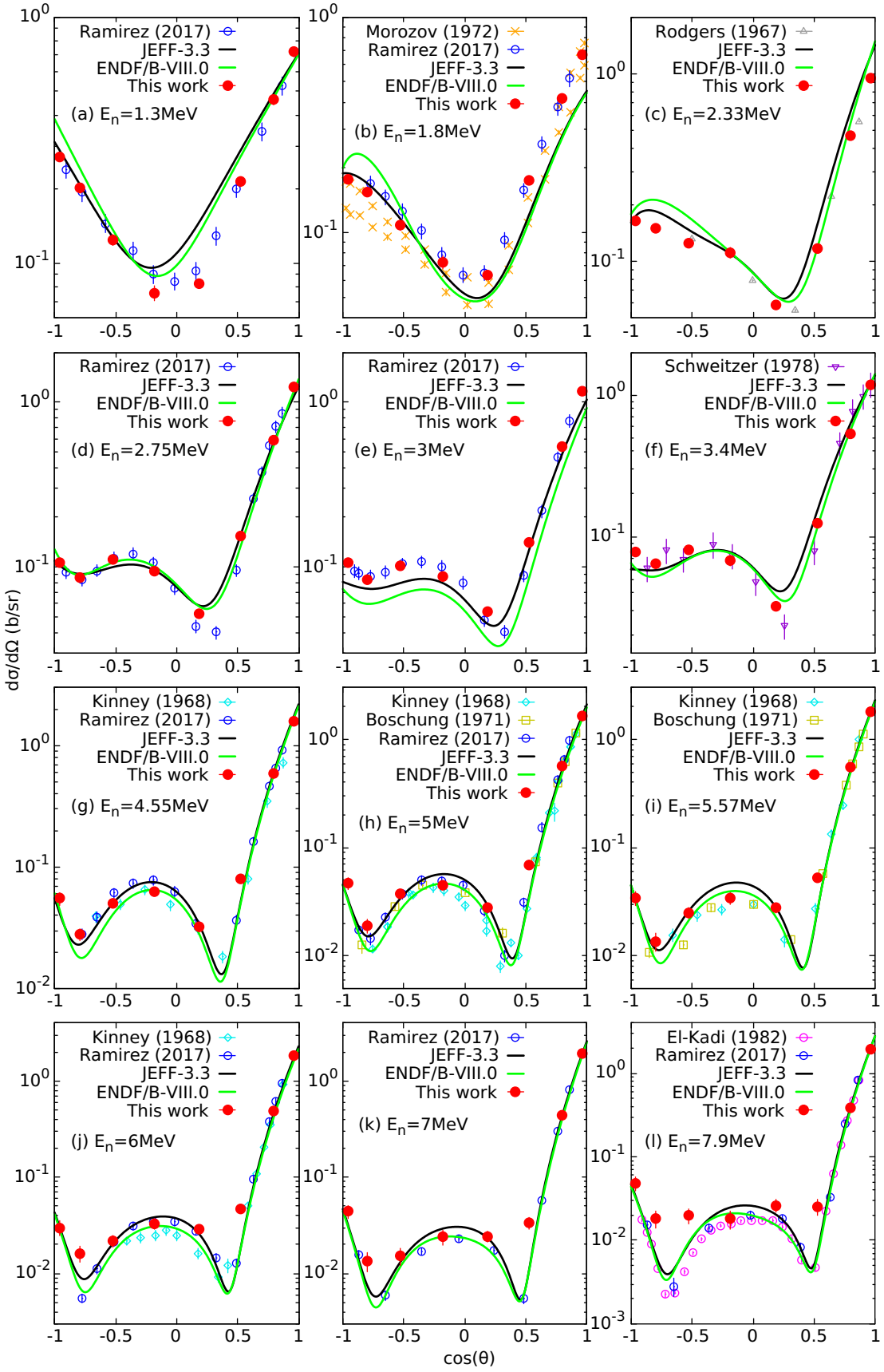

Figure 3.26: Comparison of differential cross sections of neutron elastic scattering on ^{56}Fe as a function of the cosine of the scattering angle θ, with data available in the EXFOR [13] library and the angular distributions provided in the JEFF-3.3 [10] and ENDF/B-VIII.0 [9] evaluations. Twelve 10 ns t.o.f. intervals have been selected. The corresponding incident neutron energy is reported in each graph.

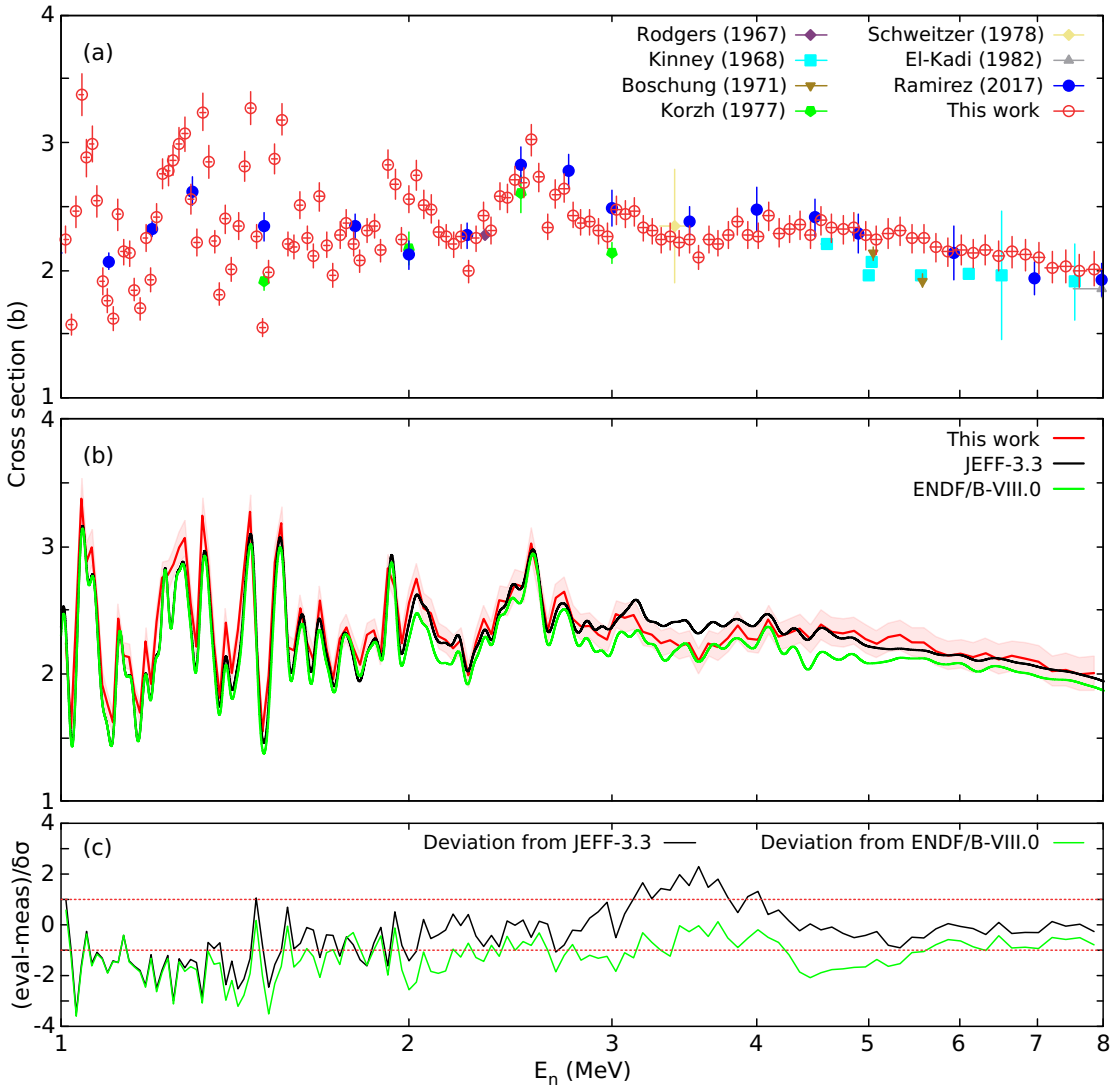

Figure 3.27: Angle-integrated cross section of neutron elastic scattering on ^{56}Fe as a function of the incident neutron energy compared with (a) the data available in the EXFOR library [13], and (b) the JEFF-3.3 [10] and ENDF/B-VIII.0 [9] libraries folded with the experimental energy resolution. In (c) the deviation of the experimental results from the evaluated values is presented as the difference between evaluation and measurement divided by the experimental uncertainty ($\delta\sigma$).

of this work and the majority of the experimental data in the EXFOR library.

The angle-integrated neutron elastic scattering cross section is presented in Fig. 3.27. The results are compared with the data available in the EXFOR library, and the JEFF-3.3 and ENDF/B-VIII.0 evaluations folded with the experimental resolution of the measurement. In both evaluations, the elastic scattering cross section was defined as the difference between the total and the remaining partial cross sections. In order to test the consistency, the cross section of the ENDF/B-VIII.0 evaluation was resolution broadened to 0.3%, achieving good agreement with the Kinney et al. (1968) [25] data in the 4-8 MeV region. The total cross section, in both evaluations, above the resonance range up to 10 MeV incident neutron energy was taken from the JEFF-3.2 evaluation,

which is essentially the Vonach-Tagesen evaluation with superimposed fluctuations derived from the Berthold et al. (1995) [29] transmission data on ^{nat}Fe with a correction for the presence of the minor isotopes. Even thought the same procedure was followed and the resulting total cross section is identical in both evaluations, when it comes to the resulting elastic scattering cross sections discrepancies are observed between the two. These discrepancies are originating from the different determination of the non-elastic cross sections that was adapted by the evaluations and then were subtracted by the total cross section. The results of this work are in overall good agreement within uncertainties with the handful of previous experimental values available in the EXFOR library, specifically with the most recent measurement performed by Ramirez et al. (2017) [28]. In comparison to the JEFF-3.3 and ENDF/B-VIII.0 evaluations, in the fluctuating region from 1 to 3 MeV the results of this work are following the same trend/behavior as the evaluations, although in some case are slightly higher in magnitude. In the remaining energy region from 4 to 8 MeV where discrepancies are observed between the evaluations, the present results are lying somewhat in the middle of the two with a better agreement with ENDF/B-VIII.0 in the 3-4 MeV region and with JEFF-3.3 in the 4-8 MeV range (see Fig. 3.27(c)). The total uncertainty of the experimental angle-integrated cross section of this work varies between 3% and 6%.

3.5.2 Inelastic scattering

The angular distributions of neutron inelastic scattering from the first excited state of ^{54}Fe (0.847 MeV), in the energy range from 2 to 5 MeV, are presented in Fig. 3.28. The cross sections are given with respect to the neutron incident energy at the 8 different detection angles. The results are compared with the JEFF-3.3 and ENDF/B-VIII.0 evaluated libraries folded with the experimental energy resolution. From the inelastic scattering threshold up to 4 MeV neutron incident energies fluctuations were imposed in the angular distributions of the first and the second excited state of ^{56}Fe based on the total inelastic scattering cross section data by Dupont et al. (1998) [35] and Negret et al. (2013) [34]. Above 4 MeV neutron incident energy the angular distributions of both evaluations are based on theoretical calculations. In most of the detection angles the measured values are slightly higher than the ones provided by the JEFF-3.3 and ENDF/B-VIII.0 evaluations over the whole neutron energy range. In comparison to the evaluations, the better agreement within the experimental uncertainties is observed with ENDF/B-VIII.0. The total uncertainties range from 5% to 35%. Similar to the inelastic scattering from the ^{54}Fe experiment, the highest uncertainties are observed in the two forward detectors. The reason for that is the same, i.e. the fact that at these angles, the inelastic scattering cross section is decreasing but the elastic scattering is increasing making it the predominant reaction in this energy range. Lower uncertainties can be achieved only by performing much longer measurements.

In Fig. 3.29 the differential inelastic scattering cross sections are presented as a function of the cosine of the detection angle θ, and compared with almost all the data available in the literature in the overlapping energy region and the JEFF-3.3 and ENDF/B-VIII.0 evaluations. Twelve 10 ns t.o.f. intervals have been selected, covering the majority of the incident neutron energies that have been measured in other experiments reported in EXFOR (Table 1.4). Based on Fig. 3.29 major

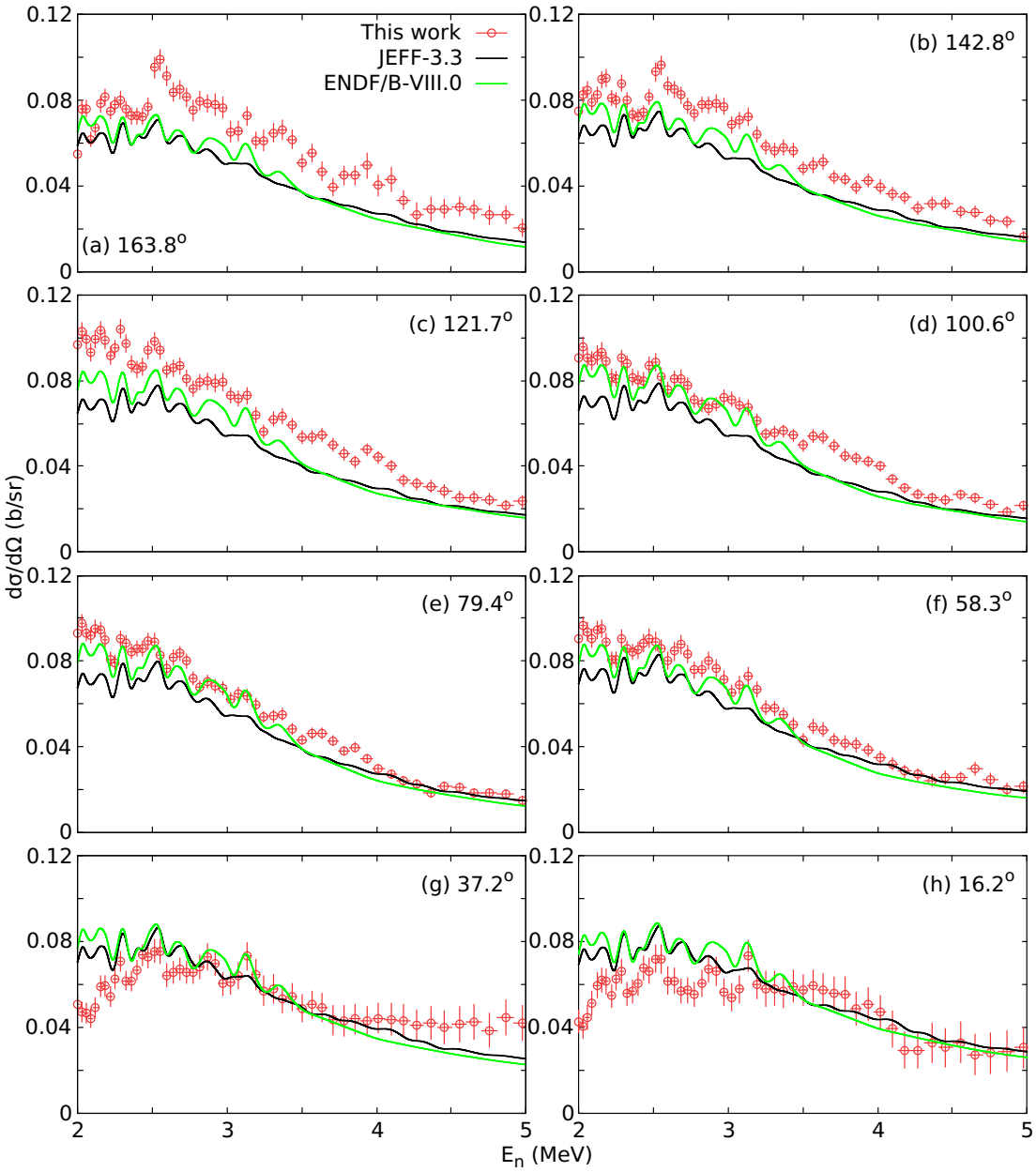

Figure 3.28: Differential cross sections of neutron inelastic scattering from the first excited state of ^{56}Fe as a function of the incident neutron energy at the 8 detection angles. The experimental cross sections are compared with the evaluated values provided by the JEFF-3.3 [10] and ENDF/B-VIII.0 [9] libraries folded with the experimental energy resolution.

issues are observed in the current state of the angular distributions of neutron inelastic scattering on ^{56}Fe. Big discrepancies between the two evaluations, but also between different experiments are noted. The results of this work are in agreement in some cases with values reported in other experiments. For the 10 ns t.o.f. intervals that correspond to neutron incident energies below 3 MeV the evaluations clearly deviate from the majority of the experimental cross sections. In the energies above 3 MeV there is a relatively better agreement between evaluations and experiments, including the results of this work, although it is clear that further investigation is needed to asses

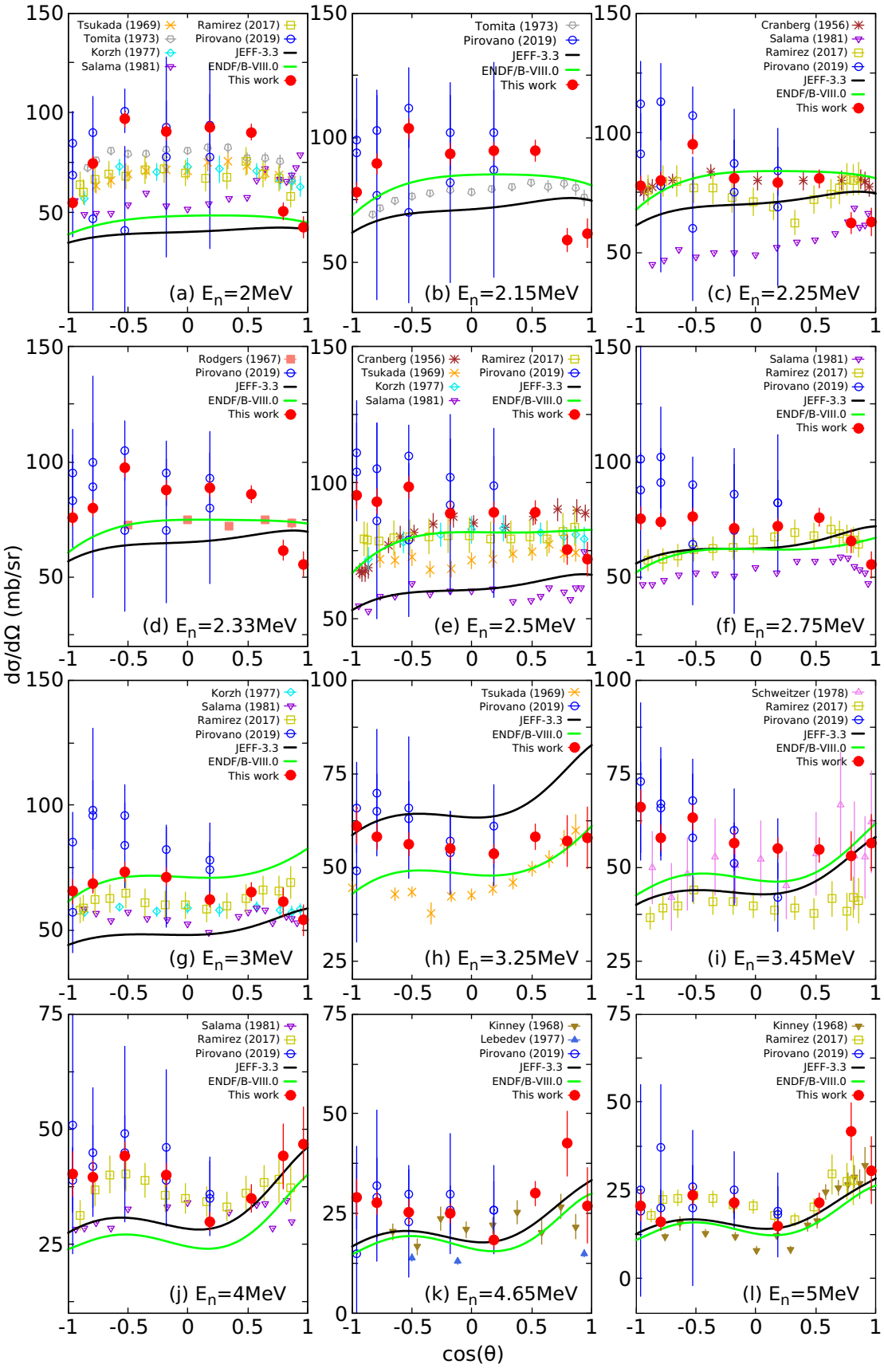

Figure 3.29: Comparison of differential cross sections of neutron inelastic scattering from the first excited state of ^{56}Fe as a function of the cosine of the scattering angle θ, with data available in the EXFOR [13] library and the angular distributions provided in the JEFF-3.3 [10] and ENDF/B-VIII.0 [9] evaluations. Twelve 10 ns t.o.f. intervals have been selected. The corresponding incident neutron energy is reported in each graph.

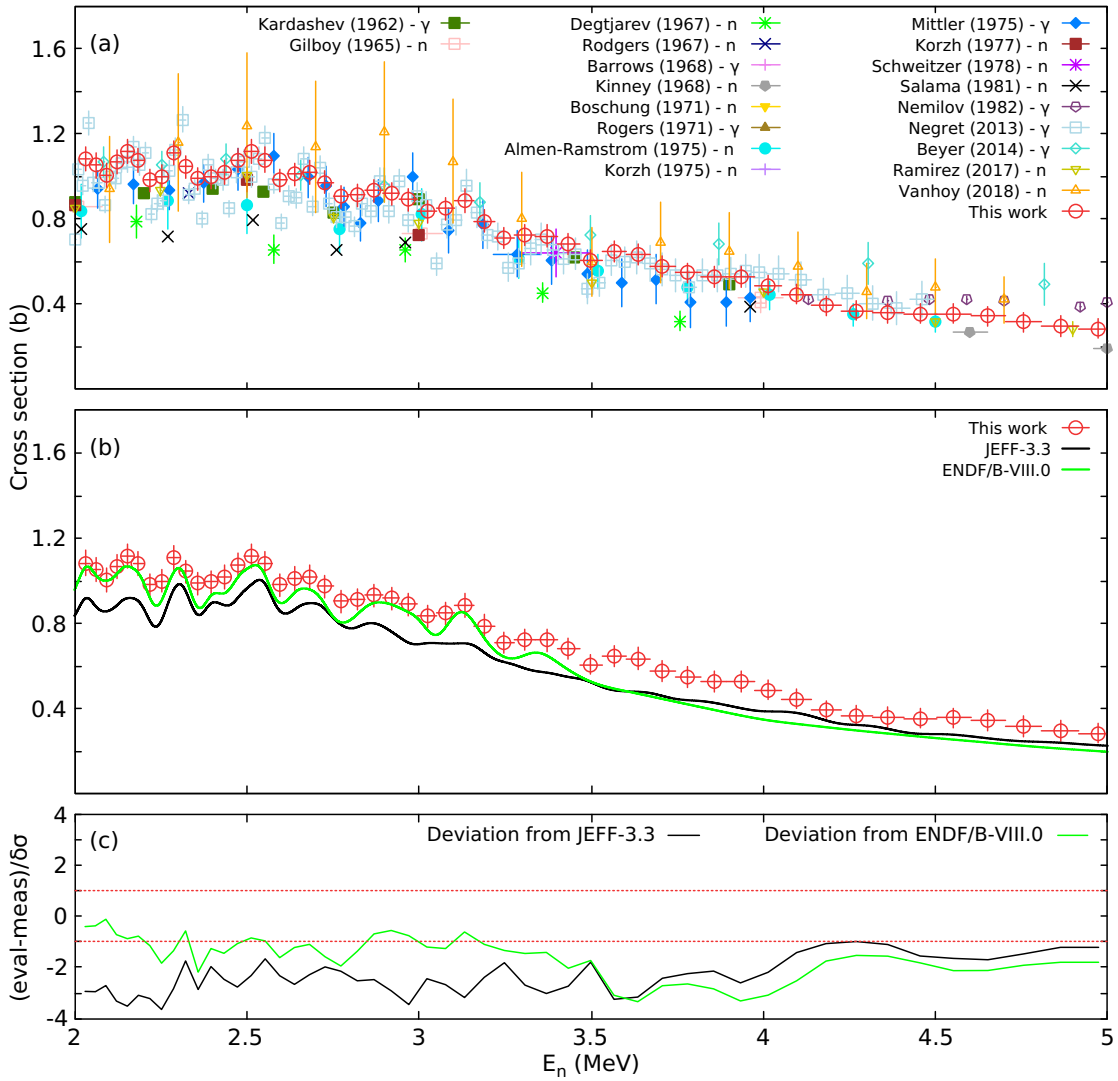

Figure 3.30: Angle-integrated cross section of neutron inelastic scattering from the first excited state of ^{56}Fe as a function of the incident neutron energy compared with (a) the data available in the EXFOR library [13], and (b) the JEFF-3.3 [10] and ENDF/B-VIII.0 [9] libraries folded with the experimental energy resolution. In (c) the deviation of the experimental results from the evaluated values is presented as the difference between evaluation and measurement divided by the experimental uncertainty ($\delta\sigma$).

the quality of both the evaluated and the experimental angular distributions in this energy region.

The results of the angle-integrated neutron inelastic scattering cross section from the first excited state of ^{56}Fe are presented in Fig. 3.30 in the energy range from 2 to 5 MeV. The results are compared with the data available in the literature, and the JEFF-3.3 and ENDF/B-VIII.0 evaluations folded with the experimental energy resolution. The total uncertainty of the cross section varies between 5% and 16%. There is a good agreement within uncertainties with the ENDF/B-VIII.0 evaluation in the energy range from 2 to 3 MeV. The JEFF-3.3 evaluation seem to support a lower cross section over the whole neutron energy region in contrast with the majority of the

experimental data in EXFOR. In comparison with the data available in the literature, there is an overall good agreement within uncertainty with almost all other experiments. It is important to mention that the results of this work are in agreement within uncertainty with the most recent experiments performed by Vanhoy et al. (2018) [24] and Ramirez et al. (2017) [114] using quasi-mononergetic beams at the tandem facility of the University of Kentucky, with the data of Beyer et al. (2014) [33] from an experiment that was performed at the nELBE facility, but also with another high-resolution measurement performed at GELINA by Negret et al. (2018) [34] using γ-spectrometry by employing the GAINS spectrometer.

In addition to the partial inelastic scattering cross section from the first excited state, an effort was made to extract information from the second excited state as well. In the end, partial inelastic scattering cross sections from the second excited state of ^{56}Fe (2.0851 MeV) were produced in the energy range from 3 to 6 MeV, although the uncertainties of these results are considerably high, especially for the angular distributions of the forward angles. In Fig. 3.31 the angular distributions in the energy range from 3-6 MeV, are presented. The total uncertainties range from 10% to 70%. The cross sections are given with respect to the neutron incident energy at the 8 different detection angles. The results are compared with the JEFF-3.3 and ENDF/B-VIII.0 evaluated libraries folded with the experimental energy resolution. In most of the detection angles the results are in agreement with the evaluations within the uncertainties, which as mentioned above are relatively large. In some angles (100.6°, 79.4°, 58.3°) above 4 MeV neutron incident energies the results of this work are systematically higher than the evaluations. Similar to the calculation of the inelastic scattering from the first excited state, the yields that correspond to the inelastic scattering from the second level were extracted by subtracting the contributions of elastic and inelastic scattering from the first level (see Fig. 3.6) which significantly increases the uncertainties of the resulting cross sections.

In Fig. 3.32 the differential inelastic scattering cross sections are presented as a function of the cosine of the detection angle θ and compared with the few experimental data available in the literature (see Table 1.5) in the overlapping energy region and the JEFF-3.3 and ENDF/B-VIII.0 evaluations. In the 10 ns interval that corresponds to 3.25 MeV neutron incident energy [Fig. 3.32(a)] ENDF/B-VIII.0 seems to follow the data of Tsukada et al. (1969) [41], while the results of the present work are in better agreement with the JEFF-3.3 evaluation. In the two remaining 10 ns t.o.f. intervals only data by Boschung et al. (1971) [17] are available for neutron incident energies at 5.05 MeV and 5.58 MeV. In those cases, the results of this work suggest higher cross sections in comparison to the data of Boschung and both the evaluations.

The angle-integrated neutron inelastic scattering cross section from the second level of ^{56}Fe is presented in Fig. 3.33 in the energy range from 3 to 6 MeV. The data are compared with the experimental cross sections available in the EXFOR library, and the JEFF-3.3 and ENDF/B-VIII.0 evaluations folded with the experimental energy resolution. The total uncertainty of the cross section varies between 20% and 45%. An agreement within uncertainties with the ENDF/B-VIII.0 evaluation in the energy range from 3 to 4 MeV is observed, while the JEFF-3.3 evaluation seem to suport a lower cross section in this region. Above 4 MeV, JEFF-3.3 supports a higher

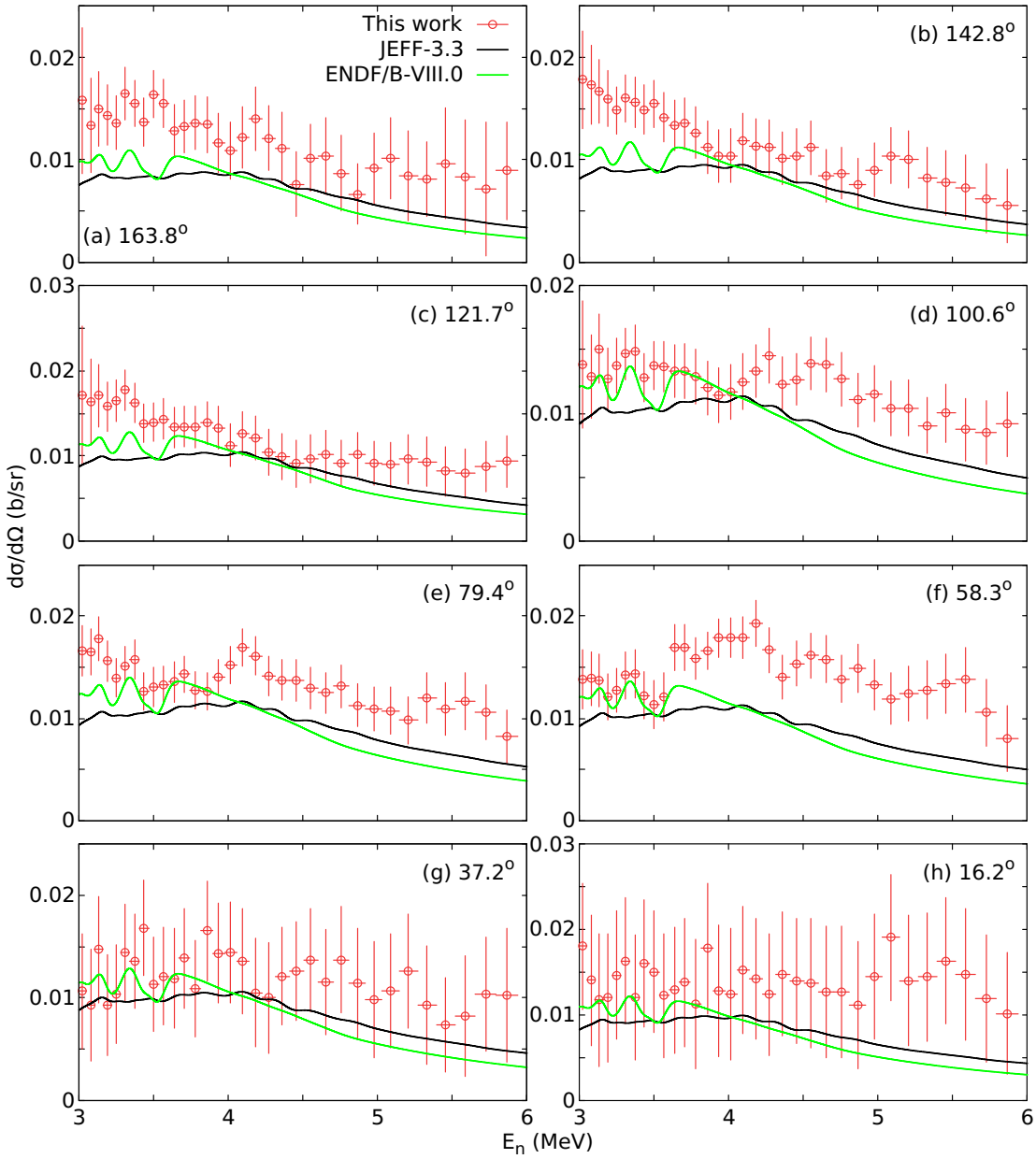

Figure 3.31: Differential cross sections of neutron inelastic scattering from the second excited state of ^{56}Fe as a function of the incident neutron energy at the 8 detection angles. The experimental cross sections are compared with the evaluated values provided by the JEFF-3.3 [10] and ENDF/B-VIII.0 [9] libraries folded with the experimental energy resolution.

cross section than ENDF/B-VIII.0, although both evaluations are underestimated in comparison with the results of the present work. In comparison with the data available in EXFOR, there is an overall good agreement within uncertainty with almost all other experiments, even though the present results seem to have the highest uncertainties compared to the cross sections from other experiments. Similar to the results from the first excited state, there is a good agreement within uncertainty with the most recent data by Vanhoy et al. (2018) [24] and Ramirez et al. (2017) [114], with the data of Beyer et al. (2014), and also with the high-resolution data of Negret

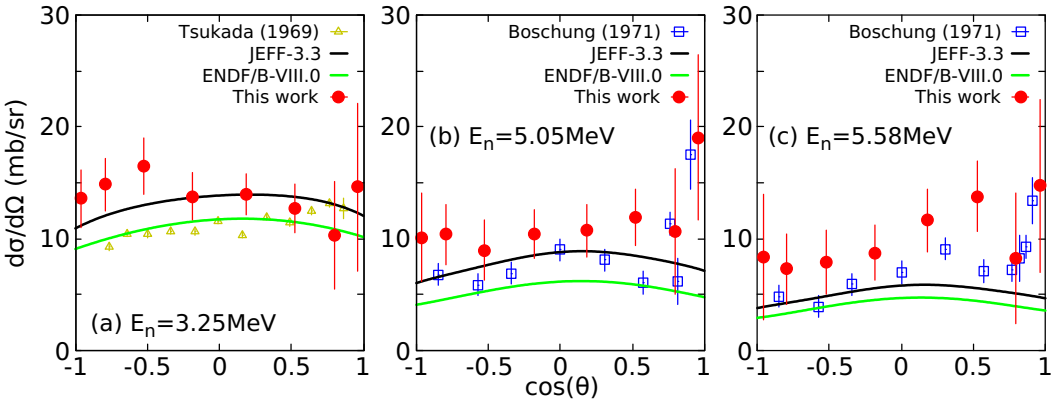

Figure 3.32: Comparison of angular distributions of neutron inelastic scattering from the second level of ^{56}Fe as a function of the cosine of the scattering angle θ.

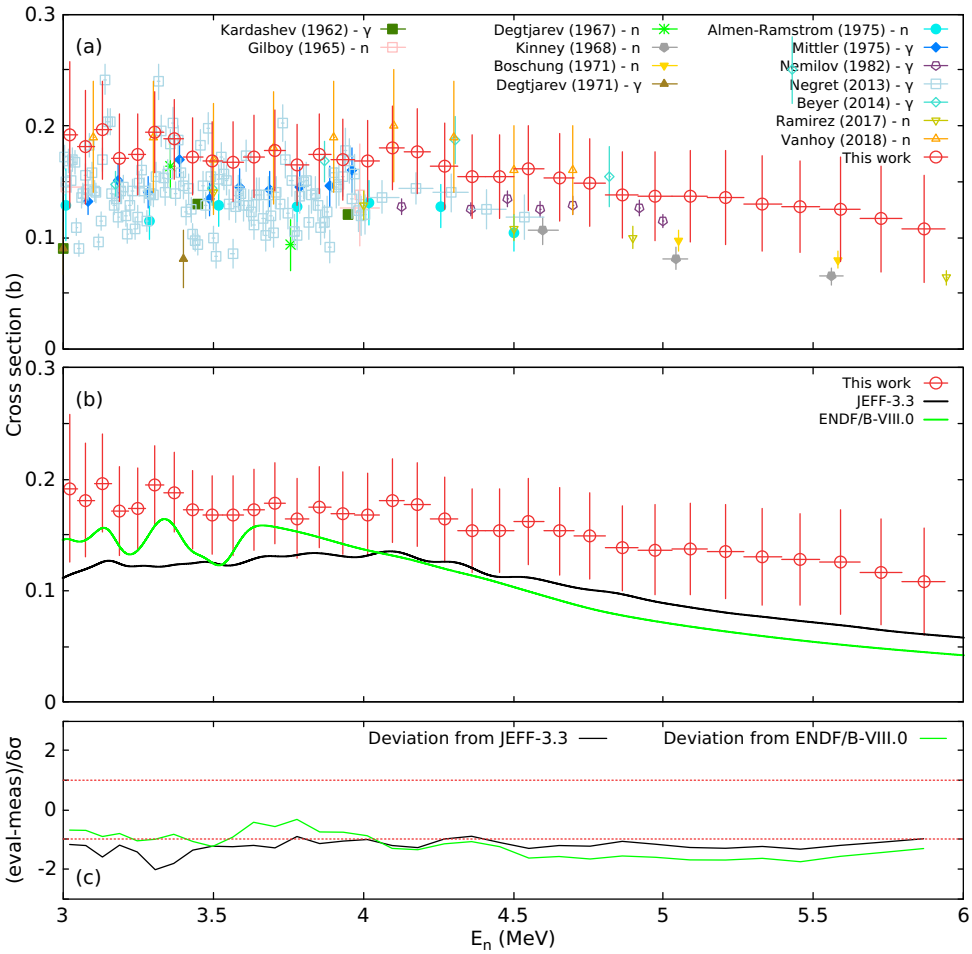

Figure 3.33: Angle-integrated cross section of neutron inelastic scattering from the second level of ^{56}Fe as a function of the incident neutron energy compared with (a) the data available in the EXFOR library [13], and (b) the JEFF-3.3 [10] and ENDF/B-VIII.0 [9] libraries folded with the experimental energy resolution. In (c) the deviation of the experimental results from the evaluated values is presented as the difference between evaluation and measurement divided by the experimental uncertainty ($\delta\sigma$).

et al. (2018) [34], although in absolute values the present cross sections are systematically higher.

Taking into account the overlapping energy region between the 1-8 MeV elastic scattering cross section, the 2-5 MeV partial inelastic scattering cross section from the first excited state, and the 3-6 MeV partial inelastic scattering from the second excited state that were extracted from the present experiment, a similar test with the one done above for the ^{54}Fe data was performed. In this case, the narrow energy region from 2 to 2.5 MeV was chosen to compare the results with the total cross section of ^{56}Fe. In this energy region the two dominant reaction mechanisms are the elastic scattering and the inelastic scattering from the first excited state (see Fig. 3.34). Other reaction channels are open in this region too, specifically the (n,γ) and (n,n$_2^{'}$), but their contribution to the total cross section was considered negligible in this test since the cross section of these reactions in this energy region is almost two orders of magnitude lower than the elastic scattering cross section. Nevertheless, the contribution of the (n,γ) reaction, although negligible was taken from the JEFF-3.3 evaluation and was added with the elastic and inelastic scattering cross sections of the present work. The extracted semi-experimental total cross section of ^{56}Fe in the energy region from 2 to 2.5 MeV is presented in Fig. 3.35 along with the total cross sections reported in the EXFOR library by Harvey et al. (1987) [145] and Cornelis et al. (1995) [146], the JEFF-3.3 and ENDF/B-VIII.0 evaluations folded with the experimental energy resolution. As mentioned above, both ENDF/B-VIII.0 and JEFF-3.3 evaluations of the total cross section are based on the Berthold et al. (1995) [29] ^{nat}Fe transmission data, corrected for the contribution of the minor isotopes, thus the resulting cross sections from both evaluations are identical. It is observed that the results of this work are in relatively good agreement within uncertainty with the data of Harvey et al. (1987) [145] and Cornelis et al. (1995) [146] above 2.25 MeV neutron incident energy. The semi-experimental total cross section of this work is overestimated over the whole neutron energy range compared to the evaluated cross sections, with limited agreement within uncertainties in the energy range above 2.2 MeV.

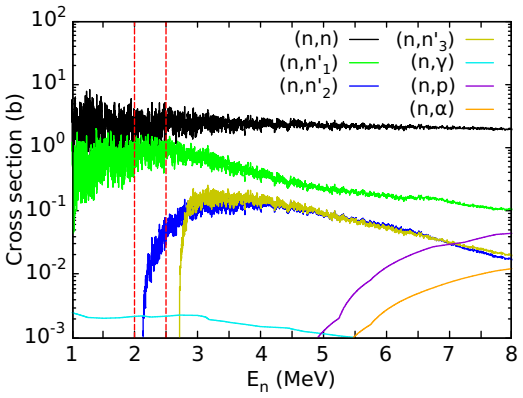

Figure 3.34: JEFF-3.3 [10] cross sections of the different reaction channels open in the 1 to 8 MeV energy region for ^{56}Fe. The red lines illustrate the energy region in which the semi-experimental total cross section was calculated.

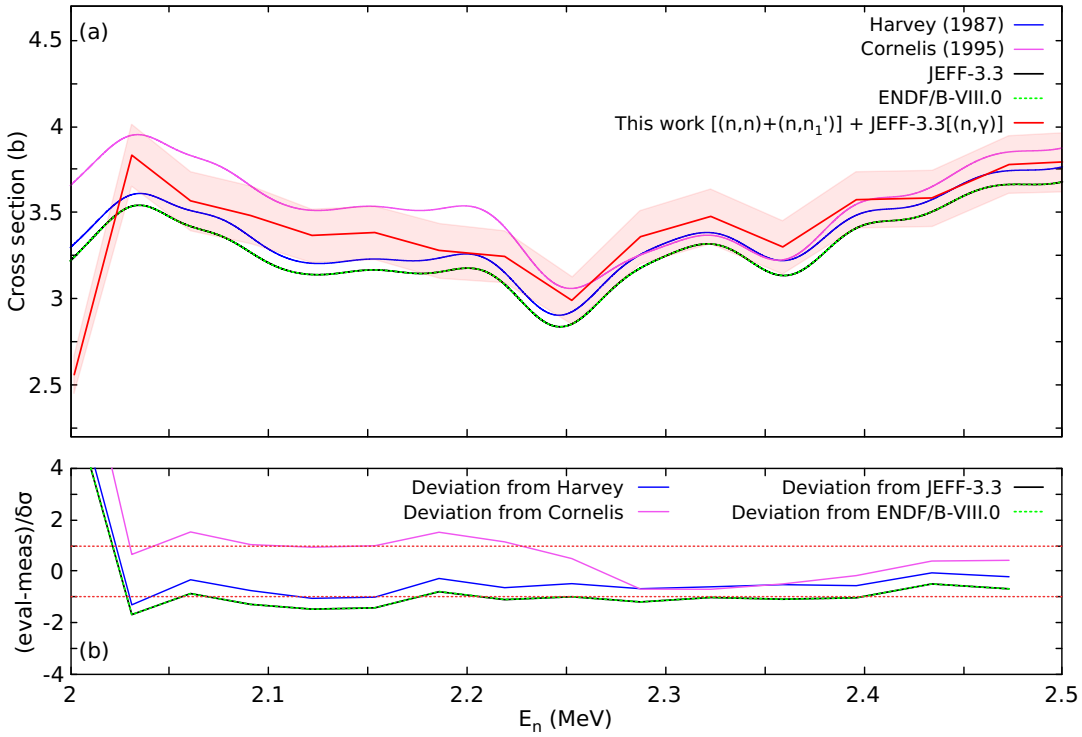

Figure 3.35: Semi-experimental total cross section of ^{56}Fe as a function of the incident neutron energy compared with the data available in the EXFOR library [13], and the JEFF-3.3 [10] and ENDF/B-VIII.0 [9] libraries all folded with the experimental energy resolution. In (b) the deviation of the experimental results from the evaluated and experimental values is presented as the difference between evaluation and measurement (or EXFOR data) divided by the experimental uncertainty ($\delta\sigma$).

3.6 Model calculations

The results of the present work are compared with theoretical reaction calculations performed with the TALYS 1.9 [147, 148] and EMPIRE 3.2 [30] codes. The codes are employing the conventional neutron optical model potential:

$$\begin{aligned} U(r,E) = &-V_V(E)f(r,R_V,\alpha_V) - iW_V(E)f(r,R_V,\alpha_V) + i4\alpha_D W_D(E)\frac{d}{dr}f(r,R_D,\alpha_D) \\ &+ V_{SO}(E)\left(\frac{\hbar}{m_\pi c}\right)^2 \frac{1}{r}\frac{d}{dr}f(r,R_{SO},\alpha_{SO})\hat{l}\cdot\hat{\sigma} \\ &+ iW_{SO}(E)\left(\frac{\hbar}{m_\pi c}\right)^2 \frac{1}{r}\frac{d}{dr}f(r,R_{SO},\alpha_{SO})\hat{l}\cdot\hat{\sigma} \end{aligned} \tag{3.8}$$

where the function f is the phenomenological Woods-Saxon potential with radius R and diffuseness α while V_V and W_V are the potential depths. The notation V, D, and SO refer to the volume, surface, and spin-orbit terms, respectively. In the present work, four different calculations were considered. The objective of these calculations is to check the predictive power of the codes by

performing calculations on the one hand using exclusively default parameters and on the other hand using parameters determined from microscopic models. It should be emphasized that in all calculations none of the parameters were fitted on the present data. The calculations were performed from 100 keV neutron incident energy up to 20 MeV.

The *"TALYS def."* calculation was based on the default parameters provided by the code. The optical model used is based on the Koning-Delaroche potential [6]. The discrete levels information was taken from the Reference Input Parameter Library (RIPL-3) [149] and for levels with unknown spins, parities or branching rations the code always assigned a value based on statistical rules. In the case of the ^{56}Fe calculation, the default Constant Temperature Model (CTM) as introduced by Gilbert and Cameron [150] was used for the level density description, and for the modeling of the γ-decay, the phenomenological γ-strength functions model of Kopecky and Uhl [151] was used. In the case of the ^{54}Fe calculation, these parameters were subsequently tuned in order to achieve an optimal agreement between experimental data and theoretical projections. For the level density description, instead of the phenomenological model used in the default calculation, a more microscopic approach was used, developed by S. Goriely on the basis of Hartree-Fock calculations [152, 153]. In addition, for the modeling of the γ-decay, the microscopic Skyrme-Hartree-Fock-Bogoliubov model was used [154]. The last two changes were made in order to better reproduce the (n,p) and (n,α) reaction cross sections.

In the *"TALYS mic.1-2"* calculations, the semi microscopic spherical optical model potential of Bauge et al. [155] was used. For the level density description the most recent microscopic approach based on Hartree-Fock-Bogoliubov calculations using the Gogny force was implemented [156], and for the γ-ray strength functions, the microscopic Gogny-Hartree-Fock-Bogoliubov model, developed based on the D1M version of the Gogny force, was used [157]. The difference between the two microscopic calculations *"mic.1"* and *"mic.2"* lies in the normalization factor used for the imaginary potential of the optical model. In the first case the default value is used, while in the second case an energy dependent factor is used, recommended for energies below 1 MeV.

In the case of ^{54}Fe, an additional calculation with the EMPIRE code was performed. The *"EMPIRE"* calculation was based on the parameters reported in the ENDF/B-VIII.0 evaluation for ^{54}Fe. This calculation was triggered by the fact that the elastic scattering cross section of ENDF/B-VIII.0, above 1 MeV neutron energy, was calculated using the EMPIRE code. The optical model potential of Koning-Delaroche was used for neutrons and protons, while for the description of alpha particles the potential of V. Avrigeanu et al. was used [158]. The optical model parameters of the potential (real/imaginary potential depth, diffuseness, radius), were re-scaled according to the values proposed in the evaluation file. For the pre-equilibrium emission the PCROSS phenomenological model, implemented in the code, was used with a mean free path parameter set to 2.4 [159, 160]. To address the correlation between incident and exit channels in elastic scattering the model developed by Hofmann, Richert, Tepel, and Weidenmueller (HRTW) was used for neutron incident energies up to 12.10 MeV [161]. The modified Lorentzian (MLO1) approach was used for the modeling of the γ-ray strength functions [162]. The level density was

calculated using the Gilbert and Cameron (GC) model, with some of the α-parameters modified according to the evaluation [150].

In Figs. 3.36 & 3.37 the results of the theoretical calculations are presented for the ^{54,56}Fe total, elastic, inelastic, (n,p), and (n,α) reaction cross sections. The calculations are compared with the results of this work and the available experimental data in the literature. In the case of the total cross section, to make the comparison easier, the experimental data were averaged over 100 keV energy bins. For the ^{54}Fe(n,tot) reaction [Fig. 3.36(a)] the calculations are compared with the high-resolution measurements of Cornelis et al. [140] and Carlton et al. [139]. It is observed that below 4 MeV neutron incident energy the theoretical calculations differ significantly in trend compared to the experimental data over the whole energy region. Above 4 MeV the *"TALYS def."* calculation is able to better reproduce the experimental data, while the *"EMPIRE"* calculation is systematically lower by 5% over the whole energy region. The microscopic approach *"TALYS mic.1"* is in agreement with the data of Cornelis between 4 and 20 MeV, and the *"TALYS mic.2"* calculation seems to produce higher results above 10 MeV. For the ^{56}Fe(n,tot) reaction [Fig. 3.36(b)] the calculations are compared with the high-resolution measurements of Harvey et al. (1987) [145] and Cornelis et al. (1995) [146]. It is observed that below 4 MeV neutron incident energy only the microscopic theoretical calculations are able to somewhat reproduce the experimental cross section. Above 4 MeV the *"TALYS def."* calculation is able to better reproduce the experimental data. In this region, the microscopic approach significantly differ in magnitude from the experimental data and only in energies above 14 MeV the *"TALYS mic.2"* calculation is giving results close to the data of Cornelis.

In Fig. 3.36(c) & (d) the elastic scattering cross section calculations are compared with the results of this work and the available data in the EXFOR library. For both isotopes, it is seen that below 2 MeV the results suggest higher cross section values than the ones produced in this work. Between 2 and 8 MeV the *"TALYS def."* calculation (and the *"EMPIRE"* in the case of ^{54}Fe) are in agreement within uncertainty with the data of this work, while the microscopic calculations seem to perform poorly in this region. Above 8 MeV, in the case of ^{54}Fe all calculations are in agreement within uncertainty with the only available experimental data in this region by El-Kadi et al. [21], while for ^{56}Fe the *"TALYS def."* calculation seems to be in agreement in both trend and magnitude with the handful of experimental data available in this region, while the microscopic calculations seem to be severely underestimated.

For the inelastic scattering cross sections [total in Fig. 3.36(e) & (f) and partial in Fig. 3.36(g) & (h), 3.37 (b)] the theoretical predictions are following the same trend as the experimental data. In the total inelastic scattering, for both isotopes, the codes are producing higher cross section compared to the EXFOR data in the energy range between 6 and 12 MeV where the cross section is reaching maximum values. In the case of the partial inelastic scattering cross section from the first excited state of ^{54,56}Fe, there is an overall good agreement between the theoretical calculations, the results of this work and the experimental data in the literature up to almost 4 MeV neutron incident energy. Above this energy, the TALYS calculations are in good agreement with the data available in literature.

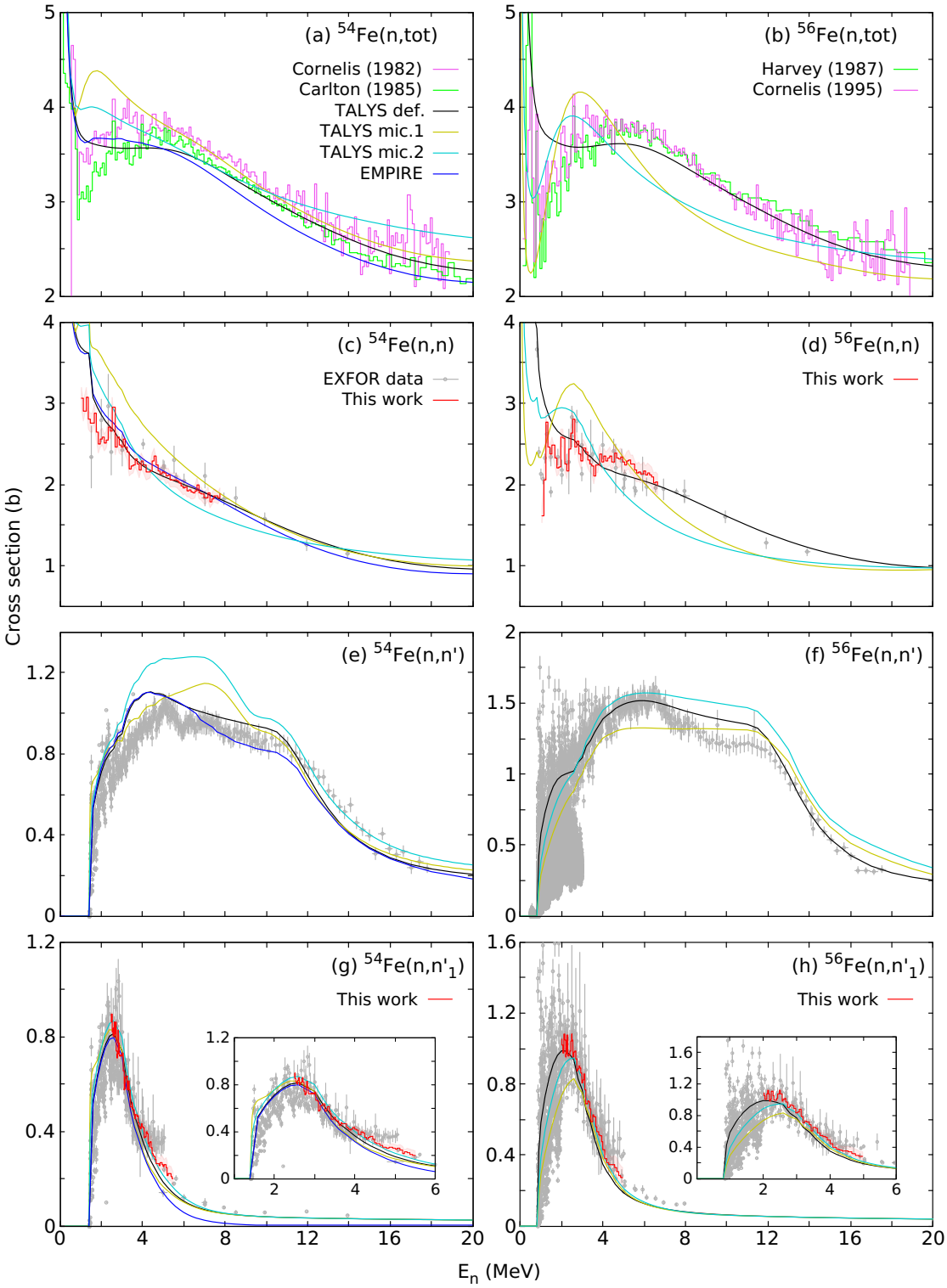

Figure 3.36: Comparison between the theoretical calculations and the available experimental data in the literature for the ^{54,56}Fe total, elastic, and inelastic reaction cross sections. The elastic and inelastic scattering data from this work are also included in the graphs. For the ^{54,56}Fe(n,n$'_1$) reaction cross section, a subplot is included focused on the neutron energy region studied in this work.

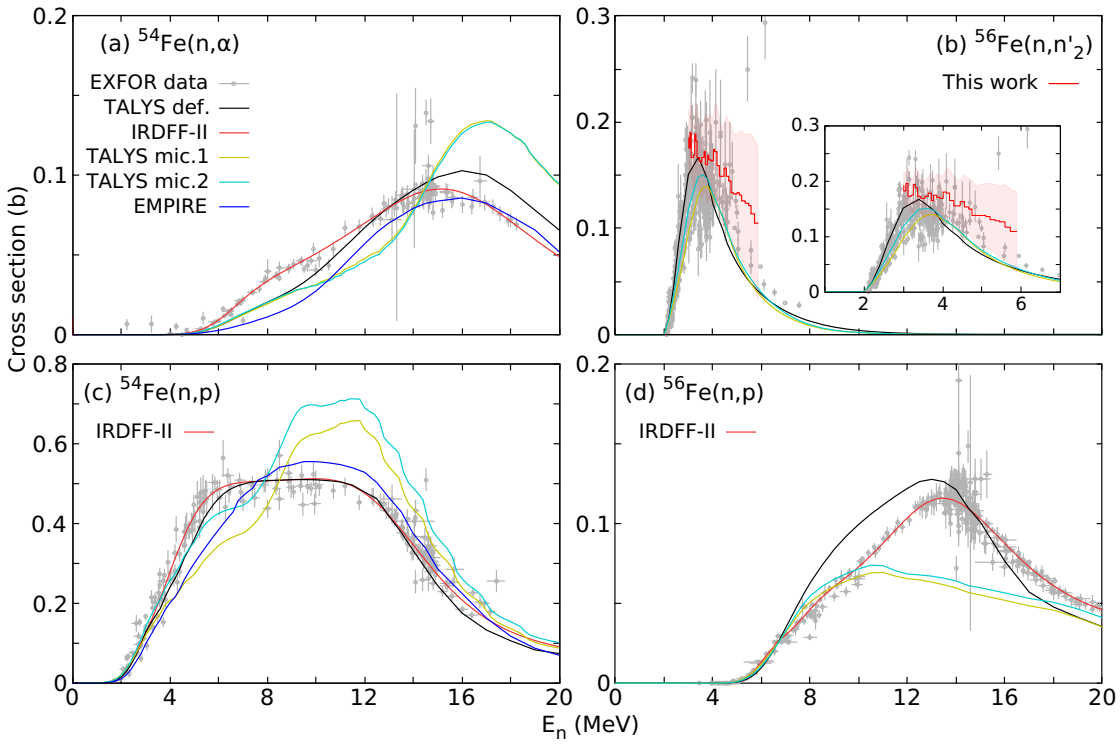

Figure 3.37: Comparison between the theoretical calculations and the available experimental data in the literature for the ^{54,56}Fe inelastic, (n,p), and (n,α) reaction cross sections. For the ^{56}Fe(n,n$'_2$) reaction cross section, a subplot is included focused on the neutron energy region studied in this work.

For the charged particle emitting reactions [(n,p) in Fig. 3.37(c) & (d) and (n,α) in Fig. 3.37(a)], the calculations are again compared with the data available in the EXFOR library [163–254], and the IRDFF-II evaluation library [255] since the ^{54,56}Fe(n,p) and ^{54}Fe(n,α) reactions are dosimetry standard reaction cross sections. In the case of ^{54}Fe, for the (n,p) reaction it is observed that the *"TALYS def."* calculation follows the same trend as the IRDFF-II evaluations and is able to reproduce the "flat" behavior of the cross section between 5 and 12 MeV, whereas *"EMPIRE"* is in agreement with the EXFOR data only above 12 MeV. In the case of the (n,α) reaction, it seems that both codes are performing poorly from the threshold up to 12 MeV, while in higher energies *"EMPIRE"* is closer to the experimental data. For both reactions, the microscopic predictions of TALYS are performing poorly over the whole energy range. In the case of ^{56}Fe, only the (n,p) reaction was considered. It is observed that the microscopic calculations are in agreement with the experimental data up to 10 MeV neutron energy, but above this energy they predict lower cross sections up to 50%. The *"TALYS def."* calculation follows the same trend as the IRDFF-II evaluations, but is overestimated in the 7-12 MeV region and underestimated in the 16-20MeV.

Overall, the results of these calculations show that default models, such as TALYS with the Koning-Delaroche potential, struggle to accurately describe cross sections in the 1–4 MeV range, as expected, indicating that while useful for broad predictions, these models lack the precision needed in this energy region. However, for energies above 6 MeV, the codes generally perform

well, showing good agreement with experimental data. Ultimately, a more detailed and comprehensive study is needed to refine the parameters and models to achieve optimal results from the codes.

3.7 Conclusions

In this chapter, the experimental details from the three different campaigns, on ^{54}Fe, ^{nat}C, and ^{56}Fe, were given. The data analysis followed to extract the final cross sections was layed out in a step by step detailed description. The analysis included the pulse shape discrimination for n-γ separation, the treatment of the data for the background contribution by subtracting the sample-out from the sample-in measurements, the elastic/inelastic separation by using kinematic calculations, the multiple scattering corrections via Monte Carlo simulations, and the analysis of the fission chamber data to extract the neutron fluence impinged on each sample. From each measurement, angular distributions and angle integrated cross section of neutron elastic scattering were extracted in the energy range from 1 to 8 MeV. In the iron measurements, inelastic scattering was also explored. The resulting angular distributions and the angle integrated cross sections were compared with data available in the EXFOR library, the JEFF-3.3 and ENDF/B-VIII.0 evaluations, and model calculations.

Chapter 4

Transmission measurements on iron

In addition to the scattering measurements, neutron transmission measurements were performed at the 50 m station of GELINA. For this purpose, two natural iron samples were measured. The objective of these measurements is to tackle discrepancies observed between nuclear data evaluations in the low neutron energy region. In the following chapter, the basic principle of transmission measurements, details of the performed experiments, the analysis of the acquired data, and the final results are presented.

4.1 Principle

Transmission experiments represent the most straightforward precise type of time-of-flight measurements. In a transmission experiment, the quantity of interest is the transmission factor T, which is defined as the fraction of the neutron beam that passes through the sample without interacting with it. The relation between the total cross section and the transmission factor is described by the formula:

$$T(E) = e^{-n\sigma_{tot}(E)}, \tag{4.1}$$

where n is the areal number density of the sample in atoms/barn and σ_{tot} is the Doppler broadened total cross section. The experimental transmission T_{exp} is obtained by the ratio of the counts of sample-in and sample-out measurements, both corrected for their respective backgrounds [256, 257]. Since the experimental transmission is calculated by the ratio of counting spectra, it is independent from the detector efficiency and neutron fluence. The optimal conditions for an experimental transmission are:

- the sample is perpendicular to the neutron beam,
- all detected neutrons have passed through the sample,
- neutrons that are scattered in the sample are not detected,
- the sample under study must have a constant homogeneous spatial distribution.

Optimal transmission geometry conditions can be attained through a proper collimation of the neutron beam both at the sample and detector positions.

4.2 Experimental conditions

The transmission experiments were performed at the 50 m measurement station of flight path 4 with the accelerator operating at 800 Hz repetition rate. The moderated neutron spectrum was used. A shadow bar made of Cu and Pb was placed close to the uranium target to reduce the intensity of the γ-flash and the fast neutron component. The flight path forms an angle of 9° with the direction normal to the face of the moderator viewing the flight path. The samples and detector were placed in an acclimatized room to keep them at a temperature of 20 °C. A schematic view of the experimental set-up is shown in Fig. 4.1.

The partially thermalized neutrons scattered from the moderators were collimated into the flight path through an evacuated aluminum pipe of 50 cm diameter with annular collimators, consisting of borated wax, copper and lead. Inside the pipe, a set of different materials are installed in order to optimize the size and energy spectrum of the neutron beam. Specifically, Pb, Ni and Cu annular collimators were used to reduce the neutron beam to a diameter of 45 mm at the sample position. Additional lithium and B_4C collimators were installed to absorb neutrons that are scattered by the collimators. A ^{10}B overlap filter with an areal density of about 0.08 at/b was placed close to the neutron target to minimize the contribution of slow neutrons coming from previous accelerator bursts and a 16 mm thick Pb filter was used to reduce the impact of the γ-flash in the neutron detector. To continuously monitor the neutron beam intensity BF_3 proportional counters mounted at different positions at the ceiling of the target hall are used. Each counter is a tube of 2.54 cm diameter and 63.2 cm length, filled with a BF_3 gas enriched in ^{10}B [259].

The neutron beam passing through the sample and filters was further collimated and detected by a 6.35 mm thick and 151.6 mm diameter NE912 Li-glass scintillator enriched to 95% in ^6Li (see Fig. 4.2). The scintillator was connected through a boron-free quartz window to a 127 mm

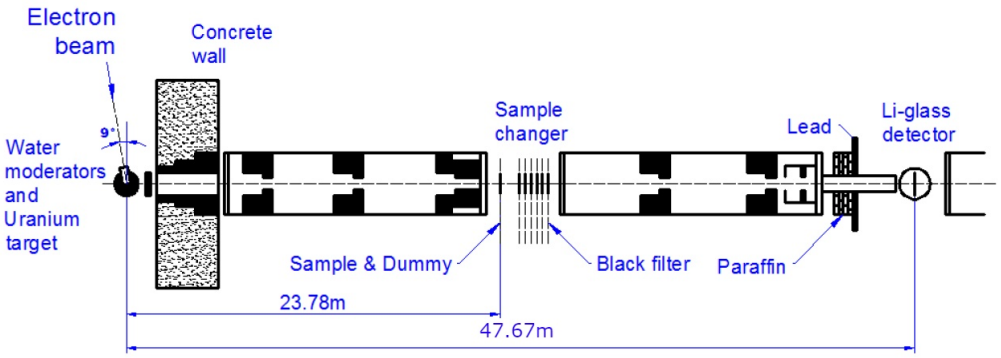

Figure 4.1: Schematic representation of the 50 m transmission measurement setup of flight path 4 at GELINA [258].

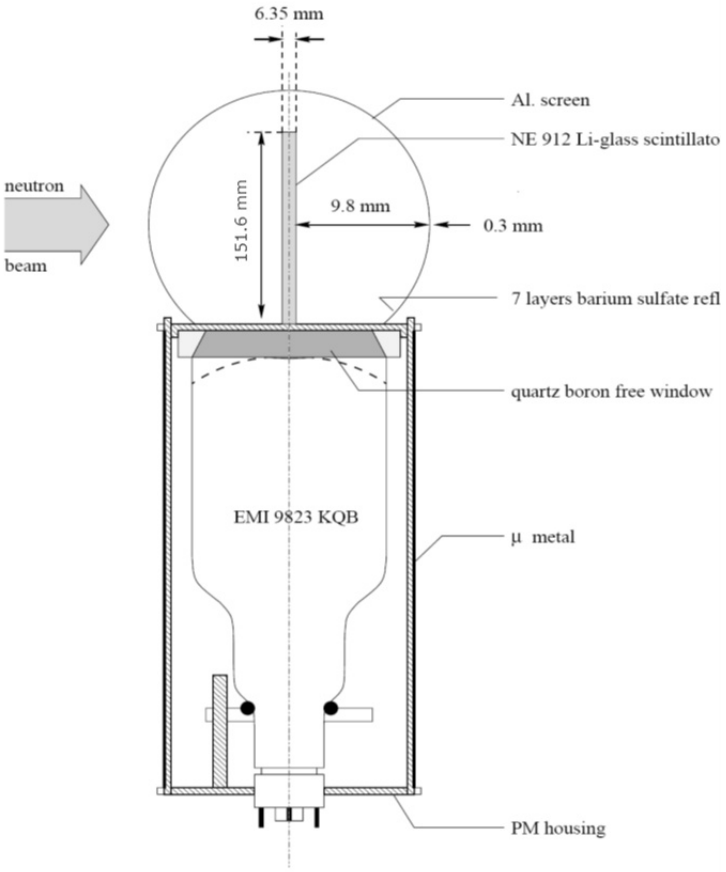

Figure 4.2: Schematic representation of the Li-glass scintillator detector used in the present experiment [260].

EMI 9823 KQB photomultiplier (PMT), surrounded by a reflector Al-case to improve the light collection. The detector was placed at a distance of 47.670(8) m from the neutron producing target.

The time-of-flight of the detected neutrons was derived from the time difference between the stop signal T_s, obtained from the anode pulse of the PMT, and the start signal T_0, given at each electron burst (see Sec. 2.2). This time difference was processed with a multi-hit fast time coder with a 1 ns time resolution. The time-of-flight and the pulse height of each detected event were recorded in list mode using a multi-parameter data acquisition system developed at the JRC-Geel. Each measurement was subdivided in different cycles. Only cycles for which the ratio between the total counts in the transmission detector and in the neutron monitor deviated by less than 1% were selected.

Two natural iron samples of more than 99.99% purity were acquired for the measurements. The main characteristics of the samples are reported in Table 4.1. The areal density of the samples was derived from a measurement of the weight and the area with an uncertainty better than 0.1%.

Table 4.1: Characteristics of the iron samples used for the experiments. Each areal density was calculated by using the experimentally determined mass and area.

ID	Thickness (mm)	Mass (g)	Area (mm^2)	Areal Density (at/b)
1	11.942(1)	677.00(5)	7093(15)	0.1014(2)
2	44.876(6)	2504.00(5)	7086(15)	0.3811(6)

The area was determined by an optical surface inspection with a microscope system from Mitutoyo [106]. The samples were mounted on an automatic exchange system that allows to alternate remotely the sample-in and sample-out configuration (see Fig. 4.3). The system was placed at the middle of the distance between the neutron producing target and the detector, at an approximate distance of 25 m. The measurements lasted six weeks in total, three weeks for each sample respectively. Throughout the text, the "thin" and "thick" labels are used to describe sample #1 and #2, respectively.

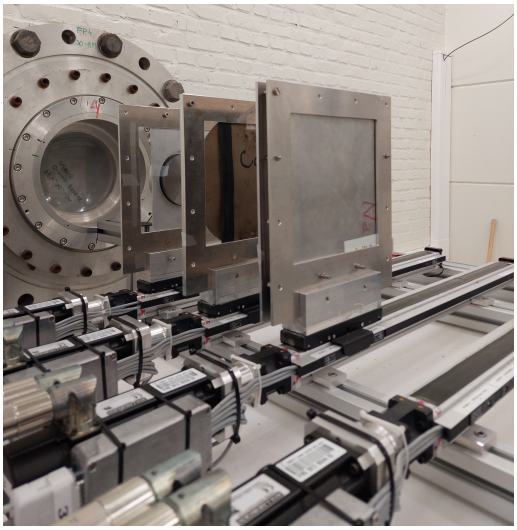

Figure 4.3: Picture of the sample exchanger system used in flight path 4 of GELINA.

4.3 Data analysis

The experimental transmission is calculated by the ratio of the counts from the sample-in (C_{in}) and sample-out (C_{out}) measurements, both corrected for their respective backgrounds (B_{in}, B_{out}). In addition, the time-of-flight spectra need to be corrected for losses due to the dead time in the detector and electronics chain and also normalized to the same neutron intensity. Thus, the experimental transmission was calculated using the formula:

$$T_{exp}(t_m) = N_T \frac{C_{in}(t_m) - k_T B_{in}(t_m)}{C_{out}(t_m) - k_T B_{out}(t_m)}, \tag{4.2}$$

where N_T is a normalization factor, k_T is a factor that accounts for the correlated uncertainty for systematic effects due to the background model, and t_m is the time-of-flight. The time-of-flight was determined using Eq. (2.4). The flight path length 47.670(8) m, i.e. the distance between the centre of the moderator viewing the flight path and the front face of the detector, was previously derived from results of transmission measurements using uranium standard references [261]. To extract the experimental transmission T_{exp} the data analysis was performed using the AGS (Analysis of Geel Spectra) code, developed at the JRC-Geel [262,263]. This code is able to perform corrections due to dead time, background fitting and subtraction, and normalize the data. The code is based on a compact formalism to propagate all uncertainties starting from uncorrelated uncertainties due to counting statistics.

All spectra were normalized to the same time-of-flight bin width structure and neutron beam intensity. The latter was derived from the response of the BF_3 beam monitors. To avoid systematic effects due to slow variations of both the beam intensity and detector efficiency as a function of time, data were taken by alternating sample-in and sample-out measurements in cycles of about 600 s. Such a procedure reduces the uncertainty on the normalization to the beam intensity to less than 0.25%. This uncertainty was evaluated from the ratio of counts in the ^{6}Li transmission detector and in the flux monitors. To account for this uncertainty the normalization factor N_T was set to 1.0000(25).

4.3.1 Dead time correction

The count rate spectra obtained in the present measurements require a correction due to the dead time of the detection and data acquisition system. The dead time of the detection chain t_d=3509(10) ns was derived from a spectrum of the time-interval between successive events. This correction is based on the formula provided by Moore [264] and it accounts for possible variations of the neutron beam intensity. In Fig. 4.4 the dead time correction factor as a function of the incident neutron energy is presented for the sample-in and sample-out measurements of both the thin and thick sample measurements. It is observed that for energies above 100 keV the dead time correction is becoming significant, above 20% thus the results of the present work were limited to energies only up to 100 keV.

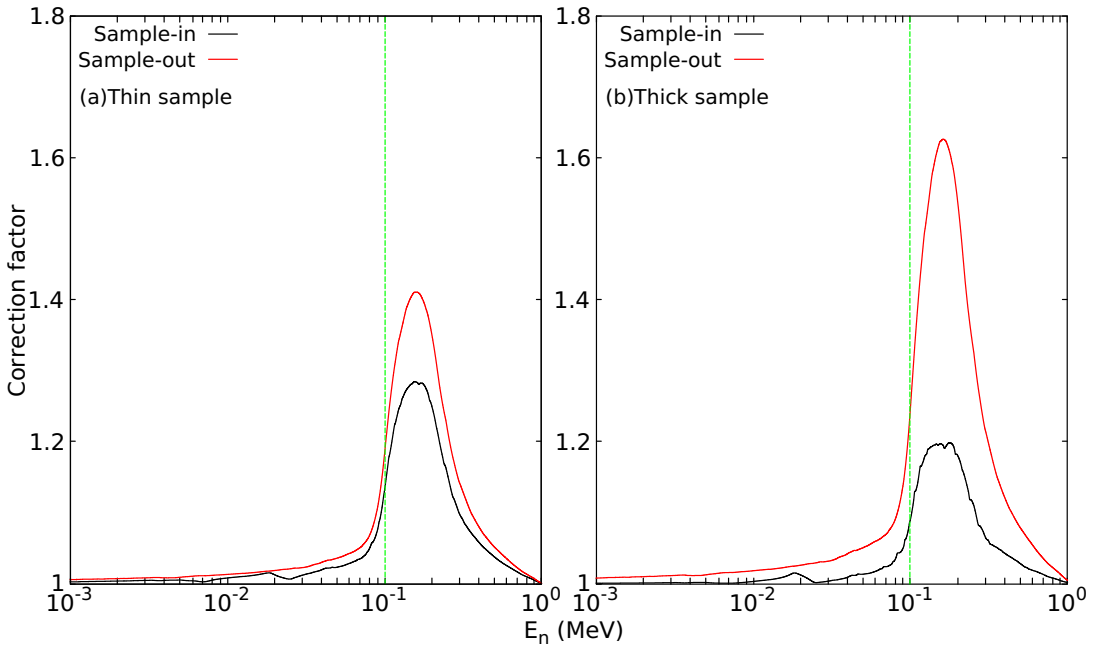

Figure 4.4: Dead time correction factor as a function of the neutron incident energy for the sample-in and sample-out measurements of both the thin and the thick sample measurements. The green line represents the 100 keV energy threshold due to dead-time.

4.3.2 Determination of the background

The background as a function of time-of-flight was approximated by an analytic expression applying the black resonance technique. To that end, samples of elements with strong absorption resonances (black resonances) are inserted into the beam. In the present work, during the measurements and close to the sample position Na, Co and W black resonance filters were mounted in an independent automatic filter changers to determine the background contribution at 2850 eV, 132 eV and 18 eV, respectively, and to obtain its time dependence. The Co filter is a permanent filter used to continuously monitor the background level and to account for the impact of the sample or other filters placed in the beam. The background as a function of the time-of-flight (t_m) was determined using the following analytical formula:

$$B(t_m) = b_0 + b_1 e^{-\lambda_1 t_m} + b_2 e^{-\lambda_2 t_m} + b_3 e^{-\lambda_3 (t_m + \tau_0)}. \tag{4.3}$$

The formula consists of a time independent and three time-dependent exponential terms. The time independent component b_0 is related to the ambient radiation and background contributions that lost any time correlation. The first time-dependent component is due to 2.2 MeV γ-rays resulting from neutron capture in hydrogen present in the moderator. This component has been extensively studied at GELINA by performing Monte Carlo simulations and measurements with polyethylene filters in the beam. In these measurements, polyethylene is used to scatter neutrons out of the beam path and enhance the ratio of the γ-ray to neutron intensity. The second exponential term is due to neutrons scattered inside the detector station and neutrons scattered at other flight paths, and the last one originates from slow neutrons coming from the previous accelerator pulse. The decay constants λ_1 and λ_2 were derived from transmission data measured with all the black resonance filters, while λ_3 was obtained by extrapolating the time-of-flight spectra at the end of the cycle. This procedure applied to each measurement also provides the amplitudes b_0 and b_3. The time-shift parameter τ_0 is related to the operating frequency of the accelerator and is set to τ_0=1.25 ms for the 800 Hz repetition rate. The time dependence of the first and the second time-dependent background components was studied by including short cycles with all the filters (Na-Co-W) in the beam. The b_1/b_2 ratio obtained in these short cycles was used for adjusting the amplitudes b_1 and b_2 together with the information of the black resonance dip of the permanent Co filter. The factor k_T in Eq. (4.2) was set to 1.00(3) and was introduced to account for systematic effects due to the background model. Its uncertainty was derived from a statistical analysis of the difference between the observed black resonance dips and the estimated background. This uncertainty is only valid for measurements with at least one fixed black resonance filters placed in the beam.

The dead time corrected sample-in and sample-out TOF-spectra of both configurations, the one with all the filters (All) and the one with only the cobalt filter (Co), for both the thin and thick natural iron samples, together with the resulting background contributions are shown in Figs. 4.5 and 4.6 respectively. Additionally, the fitting parameters describing the background contributions for all the measurements are provided in Table 4.2 and Table 4.3 for the thin and thick samples respectively.

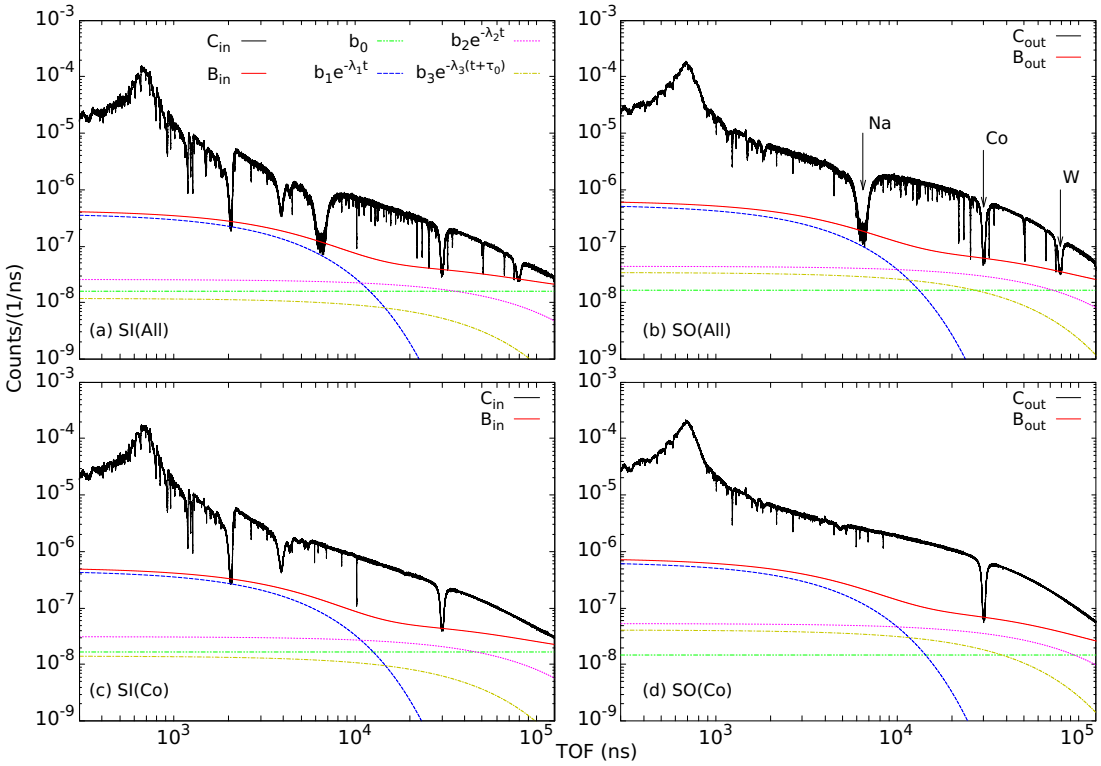

Figure 4.5: TOF-spectra resulting from the transmission measurement of the thin ^{nat}Fe sample at the 50 m station of GELINA. The sample-in (SI) and sample-out (SO) measurements of both configurations, the one will all the filters (All) and the one with only the cobalt filter (Co) are presented along with their respective total backgrounds. The individual time-independent and time-dependent background components are shown as well.

Table 4.2: Parameters for the analytical expressions of the background correction for the sample-in and sample-out measurements for the thin natural iron sample.

ID	$b_0/10^{-8}$	$b_1/10^{-7}$	$\lambda_1/10^{-5}$ (ns^{-1})	$b_2/10^{-8}$	$\lambda_2/10^{-6}$ (ns^{-1})	$b_3/10^{-6}$	$\lambda_3/10^{-6}$ (ns^{-1})
SI(All)	1.60	3.81	-2.65	2.57	-1.35	34.8	-2.70
SO(All)	1.63	5.47	-2.65	4.40	-1.35	1.00	-2.70
SI(Co)	1.65	4.63	-2.65	3.12	-1.35	41.4	-2.70
SO(Co)	1.50	6.61	-2.65	5.32	-1.35	1.20	-2.70

Table 4.3: Parameters for the analytical expressions of the background correction for the sample-in and sample-out measurements for the natural thick iron sample.

ID	$b_0/10^{-8}$	$b_1/10^{-7}$	$\lambda_1/10^{-5}$ (ns^{-1})	$b_2/10^{-8}$	$\lambda_2/10^{-6}$ (ns^{-1})	$b_3/10^{-8}$	$\lambda_3/10^{-6}$ (ns^{-1})
SI(All)	1.02	1.38	-3.08	1.57	-2.75	4.02	-2.70
SO(All)	1.27	6.31	-3.08	4.22	-1.35	94.0	-2.70
SI(Co)	1.07	1.53	-3.08	1.75	-2.75	4.43	-2.70
SO(Co)	1.15	7.34	-3.08	4.91	-1.35	110	-2.70

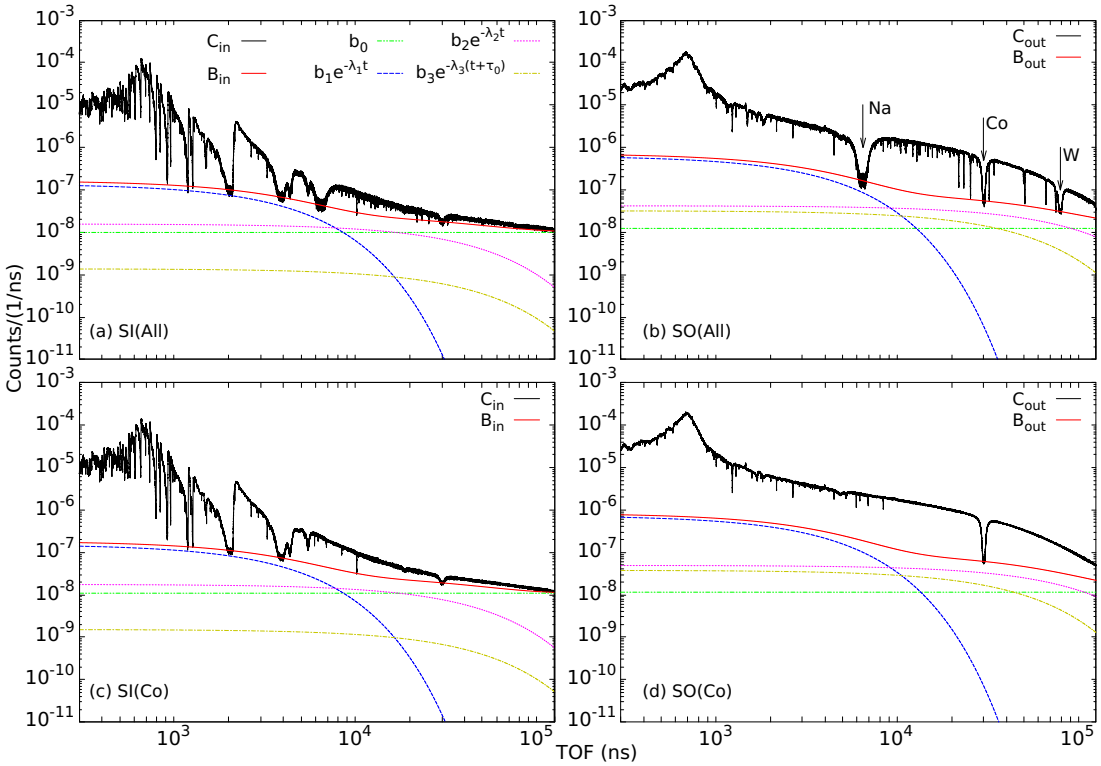

Figure 4.6: TOF-spectra resulting from the transmission measurement of the thick ^{nat}Fe sample at the 50 m station of GELINA. The sample-in (SI) and sample-out (SO) measurements of both configurations, the one will all the filters (All) and the one with only the cobalt filter (Co) are presented along with their respective total backgrounds. The individual time-independent and time-dependent background components are shown as well.

4.4 Results

The experimental transmission extracted using the AGS code for both the thin and thick samples are presented in Figs. 4.7 for incident neutron energies from 1 to 100 keV and in Fig. 4.8 for selected energy regions separately. The results are compared with the theoretical transmission based on the JEFF-3.3 and ENDF/B-VIII.0 evaluations calculated using Eq. (4.4) and the respective areal densities of each sample (see Table 4.1). The REFIT [265] code was used to account for effects due to the response function of the time-of-flight spectrometer by utilizing the following expression which is implemented into the code:

$$T(t_m) = \int R(t_m, E) e^{-n\sigma_{tot}(E)} dE, \tag{4.4}$$

where $R(t_m, E)$ is the response function and represents the probability that a neutron with energy E is detected with a time-of-flight t_m. The response function can be considered as the convolution of the duration of the accelerator burst, the time resolution of the detection system and the neutron transport in the neutron target and in the detector. It is important to mention that no fitting of the

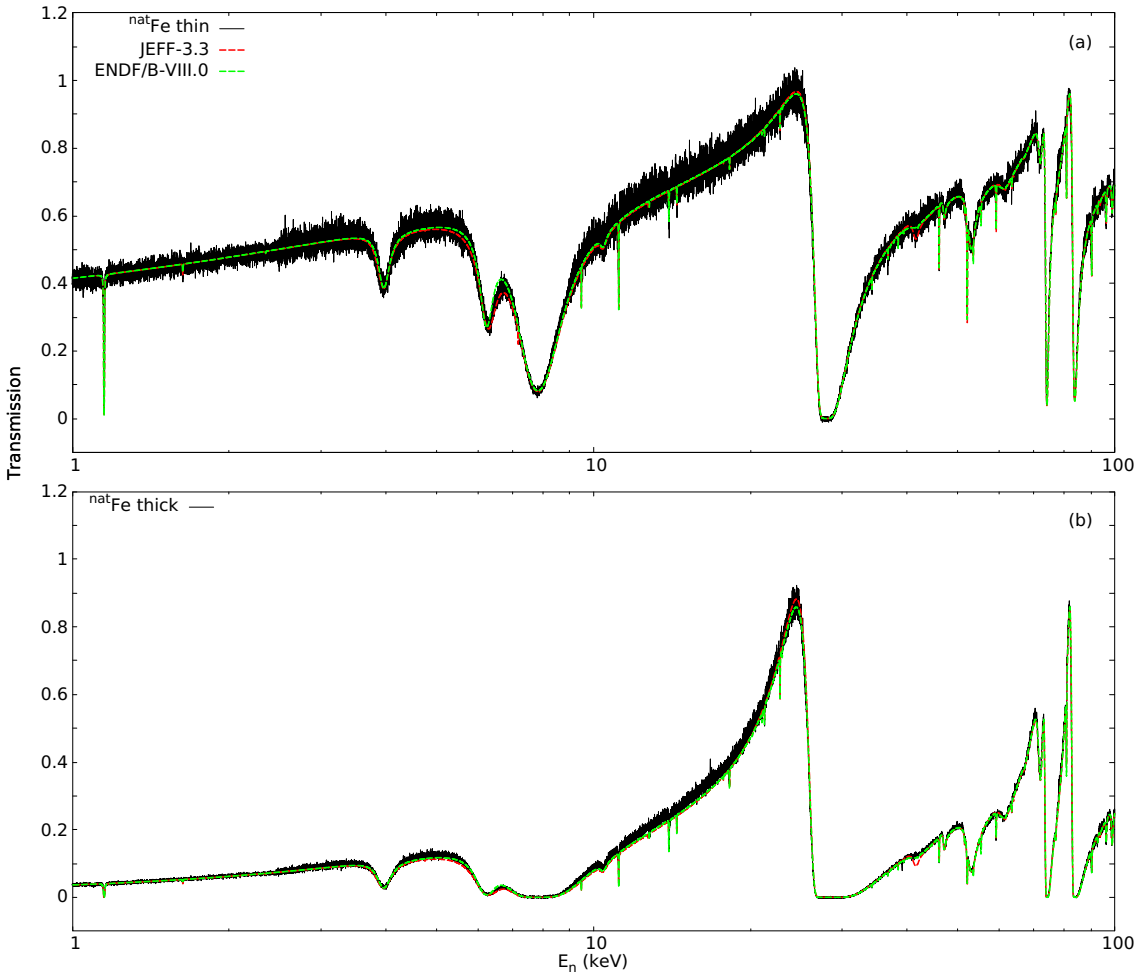

Figure 4.7: Experimental transmission obtained with the thin and thick natural iron sample compared with the JEFF-3.3 [10] and ENDF/B-VIII.0 [9] evaluations folded with the experimental resolution in the incident neutron energy range from 1 to 100 keV.

resonance parameters of the evaluations to the experimental data has been performed, so the results presented in Figs. 4.7 and 4.8 are a pure comparison between experiment and the present evaluations.

In the case of the thin sample data both evaluations are in relatively good agreement with the experimental transmission. Some discrepancies are observed in the 5 to 7 keV neutron energy region (see Fig. 4.8(c)) where JEFF-3.3 seems to be in better agreement with the results of this work. Furthermore, differences between the two evaluations are observed in the transmission maxima around the 24 to 25 keV energy region and at 42 keV where it seems that the JEFF-3.3 resonance file contains a resonance that is not included in the corresponding file of ENDF/B-VIII.0 and is also not observed in the present experiment (see Fig. 4.8(e)). In the results of the thick sample measurement the same discrepancies are observed. Additionally, it is observed that the resonance parameters files of both evaluations are not able to properly describe the transmission in the neutron energy region from 10 to 25 keV, resulting in a theoretical transmission that is lower compared to the experimental results of this work.

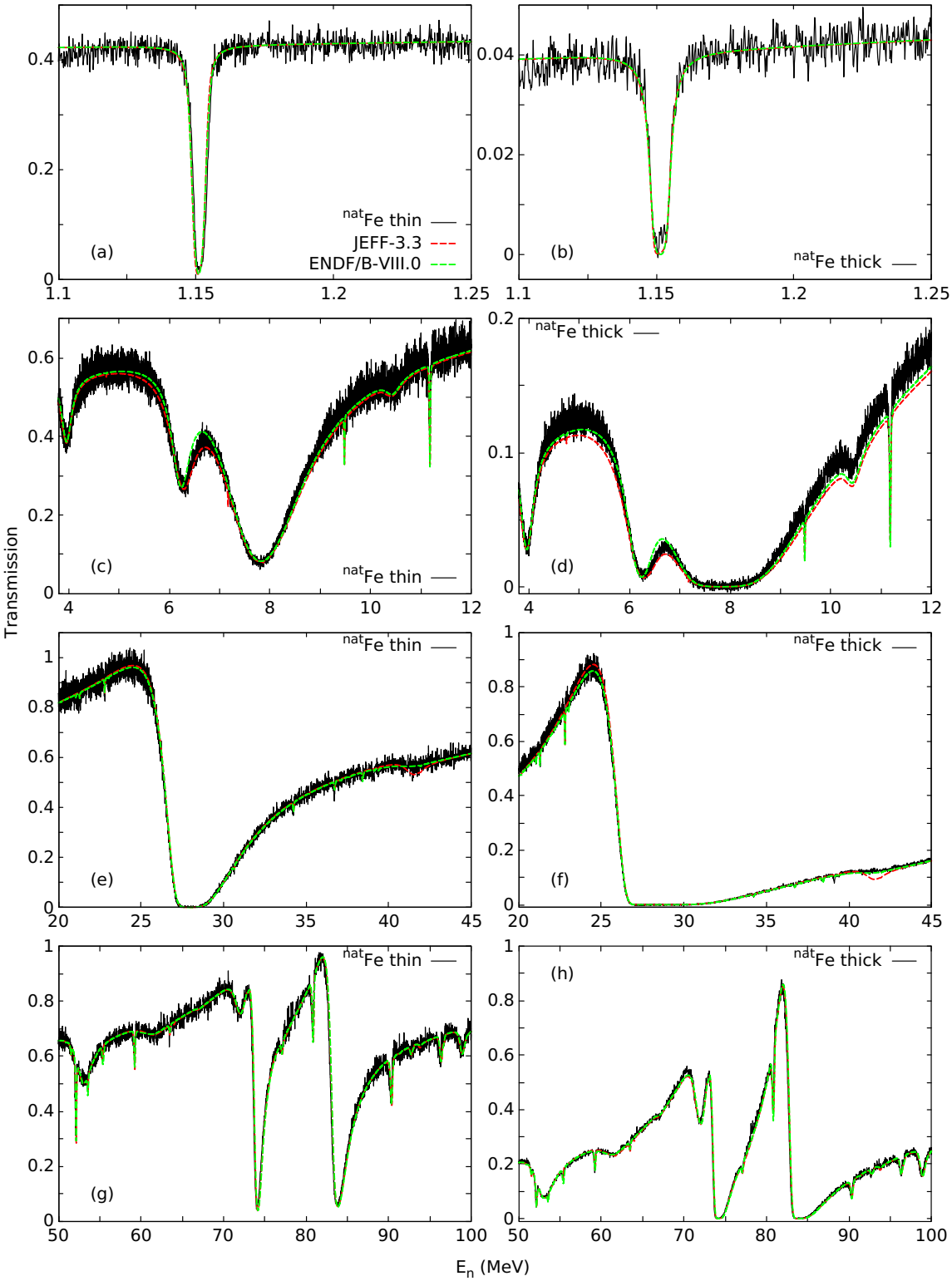

Figure 4.8: Experimental transmission obtained with the thin and thick natural iron sample compared with the JEFF-3.3 [10] and ENDF/B-VIII.0 [9] evaluations folded with the experimental resolution. In this figure attention is given to specific neutron energy regions.

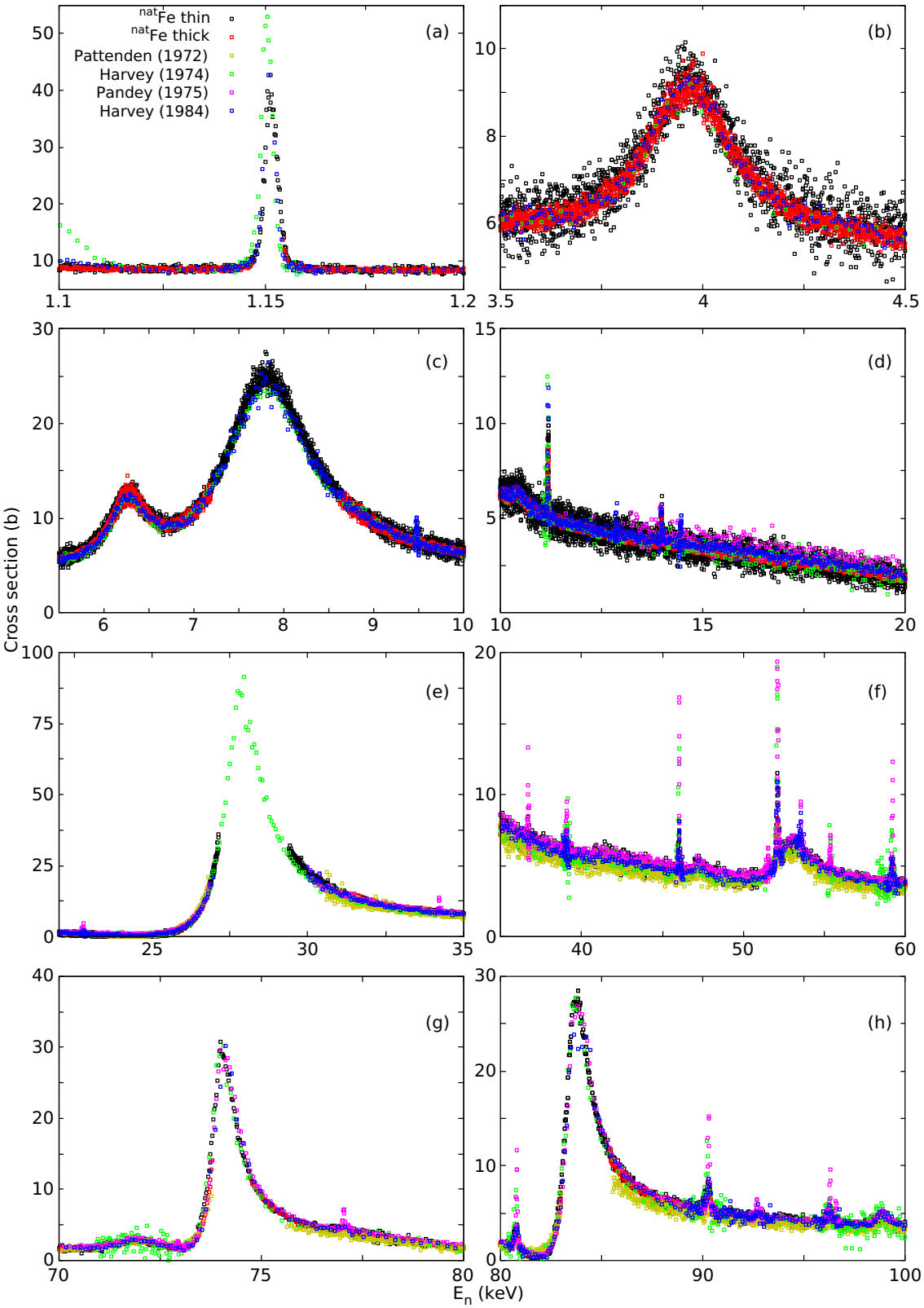

Figure 4.9: Comparison of the total cross sections of this work as a function of the incident neutron energy, with data available in the EXFOR [13] library. The results of this work are shown with black and red points for the thin and thick sample respectively. To enhance the resolution of the graphs all points are plotted without their respective uncertainties.

Table 4.4: Total cross section data of ^{nat}Fe available in the EXFOR library [13] for the neutron energy region from 1 to 100 keV. The name of the first author, the year of publication, the neutron energy range under study, the areal density of the sample, the flight path length and the number of points are listed.

Reference	E_n range (eV)	Sample (at/b)	FP length (m)	Points
Pattenden (1972) [266]	2.36E04-1.08E06	0.2546	97.43	7640
Harvey (1974) [267]	2.43E00-2.45E06	0.0545	78.203	3175
Pandey (1975) [268]	2.05E03-2.45E06	0.21787	198.733	11155
Harvey (1984) [269]	6.48E00-2.32E06	0.2179	80.2630	7037

In Fig. 4.9 the total cross section of this work, calculated with Eq. (4.1), is compared with other experimental cross sections reported in the EXFOR library for this neutron energy region (see Table 4.4). It needs to be clarified that this is a raw comparison between the different experimental data, not taking into account the different resolutions of each measurement. Although a proper comparison is difficult due to the high number of point reported in each work, it is observed that the results of the present experiments are in good agreement with the cross sections of Harvey et al. (1974/1985) [267, 269] and Pandey et al. [268], both experiment performed at the ORELA facility of the Oak Ridge National Laboratory. The data of Pattenden et al. [266] seem to be underestimated over the whole neutron energy region compared to the results of this work and the rest of the data reported in the EXFOR library.

4.5 Conclusions

In this chapter, the experimental details from the neutron transmission measurements on two natural iron samples were given. The data analysis followed to extract the experimental was described. The analysis included corrections for the dead-time in the detector and the contribution of the background. From each measurement, the experimental transmission was extracted in the energy region from 1 to 100 keV. The results were compared with the theoretical transmission based on the JEFF-3.3 and ENDF/B-VIII.0 evaluations and data available in the EXFOR library.

Chapter 5

Direct radiative capture calculations on ^{56}Fe

As already mentioned in Sec. 1.2, several changes were made in the evaluated cross section of neutron capture on ^{56}Fe. Specifically, a background component was added in the 10-100 keV energy region and a sudden increase in the cross section at the energy region around 850 keV was introduced based on experimental data provided by RPI. In an effort to provide a physical interpretation for these changes direct radiative capture (DRC) was explored. In this chapter, a short overview of the theory behind the direct capture cross section, the process of calculating it with the PDIX code and the results of both the direct capture and the total capture cross sections are presented.

5.1 DRC model calculations

The theoretical concept behind direct radiative capture is described in detail in Refs. [270–272]. In practice, two capture mechanisms exist. First is the *compound capture*, where the incident neutron is captured and a long-lived compound system is formed. This compound nucleus is typically in an excited state due to the addition of the neutron and it de-excites by releasing excess energy in the form of one or more gamma rays. Second is the *direct capture*, where the incident neutron is captured by the target without any compound state formation. Direct capture occurs by exciting a limited number of degrees of freedom within a shorter time frame, which reflects to the duration it takes for the projectile to traverse the target.

The compound capture cross section can be theoretically described using several formalisms. Statistical methods, such as the Hauser-Fesbach formalism, are used to calculate the probability of gamma-ray emission and predict the cross section based on the statistical properties of the compound nucleus. The R-Matrix formalism is used to describe the presence of nuclear resonances, where the cross section exhibits sharp energy-dependent variations. On the other hand, the theoretical model that is used to calculate the direct capture component considers the specific quantum mechanical properties of the neutron-target system. It takes into account the spatial distribution

of the nucleons within the target nucleus, their orbital angular momenta, and the properties of the neutron-nucleus potential. The direct capture cross section is proportional to the single-level electromagnetic transition matrix element. For the emission of an electric dipole radiation (E1) from the initial to final state, and for a specific neutron incident energy E_n, the cross section is given by:

$$\sigma_{n,\gamma} = \frac{16\pi}{9\hbar} k_\gamma^3 \bar{e}^2 |Q_{i\to f}^{(E1)}|, \tag{5.1}$$

where $k_\gamma = \varepsilon_\gamma/\hbar c$ is the wave number of the emitted γ-ray with energy ε_γ, and $\bar{e} = -Ze/A$ is the E1 effective charge of the neutron [271–273]. Based on Eq. (5.1), the cross section is primarily determined by the matrix element:

$$Q_{i\to f}^{(E1)} = < \Psi_i | \hat{T}^{E1} | \Psi_f >, \tag{5.2}$$

where $\hat{T}^{E1} = rY^{(E1)}(\theta,\phi)$ is the dipole operator with $Y^{(E1)}$ representing the spherical harmonic, Ψ_i represents the wave function of the initial state, and Ψ_f the wave function of the final state. The radial coordinate r denotes the distance of the incoming neutron with respect to the target nucleus. The entrance channel wave function can be decomposed into spherical (l-wave) components:

$$\Psi_{lm}(r) \equiv w_l(r) \frac{Y_{l,m}(\theta,\phi)}{ru^{1/2}}, \tag{5.3}$$

where $w_l(r)$ depends on the wave number k and is expressed as:

$$w_l(r) = \frac{i\sqrt{\pi}}{k} \sqrt{2l+1} i^l [I_l - U_l O_l], \tag{5.4}$$

where I_l and O_l represent the asymptotic forms of the incoming and outgoing waves, respectively and are determined using the following formulas:

$$I_l \sim exp\left(-ikr + \frac{1}{2} il\pi\right) \quad \text{and} \quad O_l \sim exp\left(+ikr - \frac{1}{2} il\pi\right). \tag{5.5}$$

Additionally, U_l represents the collision matrix for the scattering process in the entrance channel, u is the incoming neutron velocity, and k is the corresponding wave number. The matrix element in Eq. (5.2) can be expressed as the multiplication of three terms:

$$Q_{i\to f}^{(E1)} = \sqrt{S_f} \cdot I_{i,f} \cdot A_{i,f}, \tag{5.6}$$

where $I_{i,f}$ is the radial part of the transition matrix elements, $A_{i,f}$ is the angular coupling part, and S_f is the spectroscopic factor of each bound state. The radial part is given by:

$$I_{l_i,l_f} \equiv \int_0^\infty u_{l_f}(r) r w_{l_i}(r)\, dr \tag{5.7}$$

and can be easily calculated for any given single-particle radial wave function of the final state.

The angular part is given by:

$$A^2_{l_i,l_f} \equiv \frac{1}{2l_i+1}|<l_f||\hat{Y}_1||l_i>|^2 = \frac{3}{4\pi}(l_i 010|l_f 0)^2 \tag{5.8}$$

where $(l_i 010|l_f 0)$ is a Clebsh-Gordon coefficient. This leaves the spectroscopic factor S_f as the only quantity in Eq. (5.6) to be determined experimentally. This factor represents the single-particle strength of the final-state orbit and is usually derived from (d,p) stripping reactions. It should be mentioned that if the radial part of the matrix elements, Eq. (5.7), is calculated with reliable wave functions the spectroscopic factor can be derived from a DRC analysis of the experimental cross section.

5.2 DRC calculations with the PDIX code

The dedicated code (PDIX) used in the present work was developed by Dr. Alberto Mengoni. It performs the calculation in two steps. First, the bound state wave functions are determined based on available experimental data, and then the direct capture cross section is calculated for a given optical model potential. For the calculation of the bound state wave functions, 107 levels are available in ENSDF [107] for ^{57}Fe. The evaluation is based on experimental data obtained by three different reactions, namely ^{56}Fe(d,p), ^{57}Fe(p,p'), and ^{59}Co(d,α) [274–276]. In the present study, a grouped version of all the levels was used based on the work of Sen Gupta et al. (1971) [275] (see Table 5.1). Calculations were performed using either the 107 individual states available in ENSDF or the 6 group-states proposed by H. M. Sen Gupta. It was observed that both calculations provide similar results with differences of less than 0.5%.

Table 5.1: List of the bound states of ^{57}Fe that were used in this work along with their corresponding energy and spectroscopic factor [107].

State	Energy (MeV)	Spectroscopic factor (S_f)
$2p_{\frac{3}{2}}$	1.02	0.78
$2p_{\frac{1}{2}}$	2.97	1.26
$1f_{\frac{5}{2}}$	2.06	0.97
$1g_{\frac{9}{2}}$	4.03	0.61
$2d_{\frac{5}{2}}$	4.77	0.67
$3s_{\frac{1}{2}}$	5.06	0.11

Once the wave functions of the bound states have been calculated, the direct capture cross section can be determined for a specific optical model potential. As already described in Sec. 3.6 the phenomenological optical model potential for nucleon-nucleus scattering is given by:

$$U(r,E) = -V_V(r,E) - iW_V(r,E) - iW_D(r,E) + iW_{SO}(r,E).\mathbf{l}.\sigma + V_{SO}(r,E).\mathbf{l}.\sigma + V_C(r), \tag{5.9}$$

where V_C is the Coulomb term, $V_{V,SO}$ is the real part and $W_{V,D,SO}$ is the imaginary part of the volume-central (V), surface-central (D), and spin-orbit (SO) potentials. In the case of direct neutron capture, since their is no formation of a compound system, the imaginary part of the OMP is set to zero, and also the Coulomb potential is null because the projectile is not a charged particle. The remaining volume-central part was described as a Woods-Saxon potential of the type:

$$V_V(r) = \frac{-V_0}{1 + exp[(r-R)/a]}. \tag{5.10}$$

where $V_V(r)$ is the potential energy at a distance r from the nucleus, V_0 is the depth of the potential, r is the radial distance from the center of the nucleus, R is the nuclear radius, often parameterized as $R = r_0 A^{1/3}$, where A is the mass number of the nucleus and r_0 is a constant, and a is the diffuseness parameter, which controls how quickly the potential transitions from its central value to zero as you move away from the nucleus.

In the present work, several calculations were performed, testing different OMP parameters in order to study the sensitivity of the model and the effect the parameters have in the final outcome. In Fig. 5.1, some of the results from these test calculations are presented. Each line of graphs shows how the different partial components of the direct capture cross section are affected when tuning only one parameter of the OMP. The first line corresponds to changes in the volume potential (V_0), the second to changes in the radius (r_0), the third to changes in the diffuseness (α_0), and the fourth to changes in the depth of the spin-orbit potential (V_{SO}). This sensitivity analysis demonstrates that the magnitude of the direct capture cross sections is significantly affected by the choice of optical model potential (OMP) parameters. Variations in parameters led to noticeable differences in the cross section magnitudes. Despite these variations, the overall behavior of the cross sections remained consistent. Specifically, the s-wave direct capture consistently exhibited a $1/v$ dependence, and the d-wave direct capture showed a characteristic peak around 800 keV. This indicates that while precise tuning of OMP parameters is crucial for accurately predicting the magnitude of cross sections, the general trends and features of the cross sections are robust across different parameter choices. In the end, the OMP parameters proposed by Koning et al. (2003) [6] for the case of ^{56}Fe were used as the optimal choice. Specifically, the Woods-Saxon potential in Eq. (5.10) was parameterized as following: well depth of $V_0 = 53$ MeV, radius of $R = 4.759$ fm (corresponding to $r_0 = 1.244$ fm in $R = r_0 A^{1/3}$), diffuseness of $a = 0.603$ fm, and a spin-orbit coupling potential with strength $V_{SO} = 6$ MeV.

5.3 Results

In Fig. 5.2 the results of the calculated direct capture cross section are presented with respect to the neutron incident energy from thermal up to 2 MeV [277]. Additionally, the ENDF/B-VII.1 and ENDF/B-VIII.0 evaluations are included in the figure in order to have a qualitative comparison between the magnitude of the direct capture cross section and the changes that were made from one version of the evaluation to the other. Based on these results it is noticed that the *s-wave*

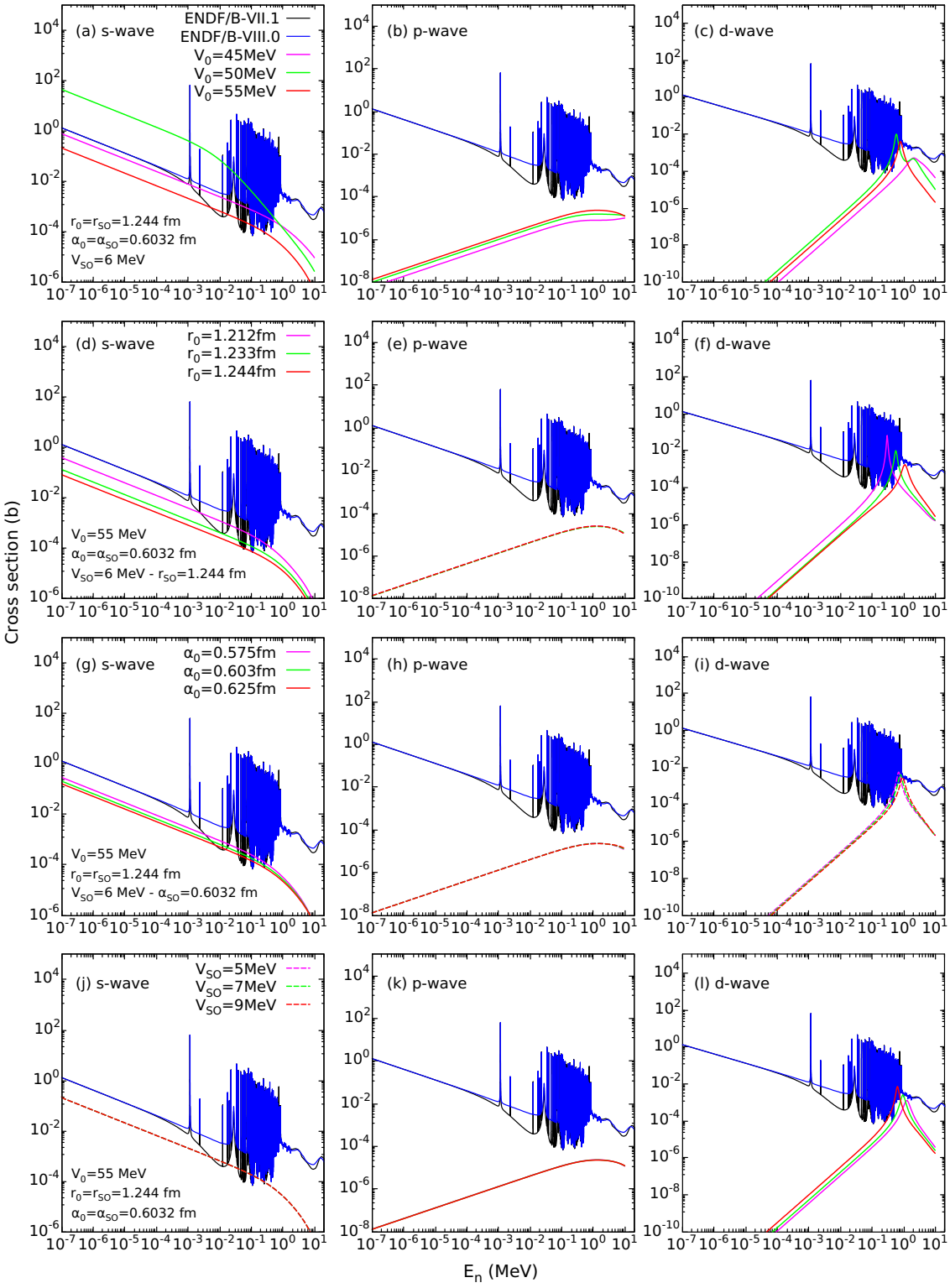

Figure 5.1: Comparison of the resulting direct capture components from calculations with different optical model parameters. The ENDF/B-VII.1 [63] and ENDF/B-VIII.0 [9] evaluations are included in the graphs to better understand the magnitude of the different direct capture cross section components.

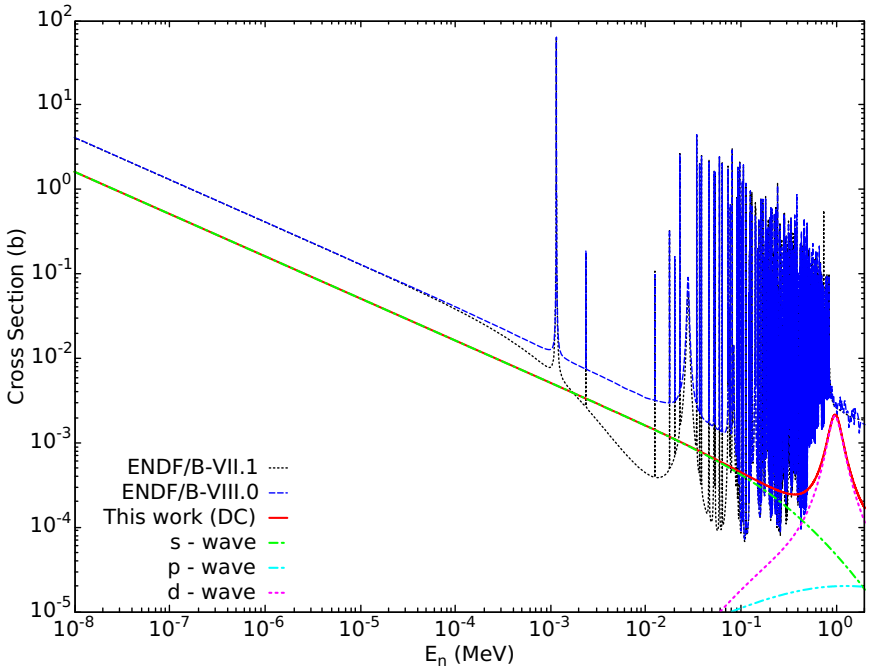

Figure 5.2: The results of the direct radiative capture cross section of ^{56}Fe (red) compared with the ENDF/B-VII.1 (black) [63] and ENDF/B-VIII.0 (blue) [9] evaluations from thermal up to 2 MeV neutron energy. The partial contributions of the s-wave (green), p-wave (cyan), and d-wave (magenta) direct capture are also presented with dash-lines.

direct capture is able to reproduce the trend of the 1/v background in the 10 to 100 keV energy region that was added in the ENDF/B-VIII.0 evaluation. Also, the *d-wave* direct capture looks like a prominent candidate in order to reproduce the "bump" in the cross section around 850 keV that was observed in the measurement performed at RPI (see Sec. 1.2). It needs to be clarified that in this calculation no interference effect between direct and compound capture was taken into account.

5.3.1 Comparison with TALYS

The nuclear reaction code TALYS is also able to calculate the direct capture cross section. The direct capture formalism that was implemented in the code is described in detail in Ref. [278]. TALYS has the capability to calculate both the direct and the semi-direct cross section for all transitions. Since the calculations performed in this work were focused only on the direct capture cross section for E1 transitions, a comparison with TALYS was made in order to examine the effect of the semi-direct and the other transitions to the final result. To be consistent, the default OMP parameters of TALYS were used in both calculations. In Fig. 5.3 the resulting direct capture cross sections of both TALYS and PDIX are presented.

The outcome of both codes illustrates that the E1 transitions are the main contributors to the direct capture cross section, since the TALYS cross sections for the E2 and M1 transitions are negligible. By comparing the results of both codes, it is obvious that the semi-direct part has a

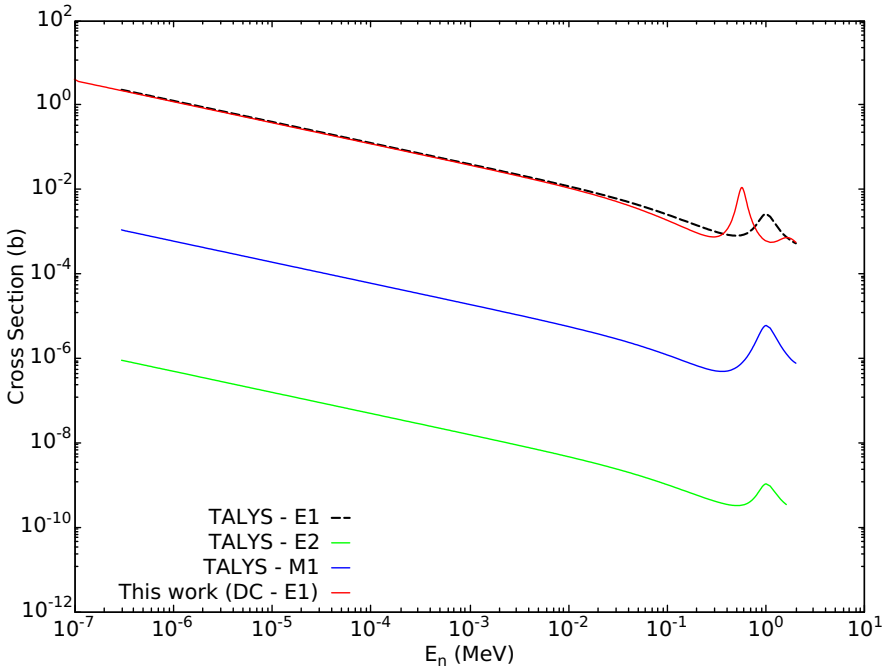

Figure 5.3: Comparison of the direct capture cross section of ^{56}Fe for an E1 transition between the TALYS code (black) and the PDIX code used in the present work (red). The cross sections of TALYS for E2 (green) and M1 (blue) transitions are also presented.

little or no impact on the final cross section until ∼0.5 MeV, since the 1/v s-wave component is the same in magnitude in both cases, and only a small difference in the d-wave "bump" of the cross section is observed, that might be caused by variations in the formalisms used in the two codes.

5.3.2 Calculation of the total capture cross section

In order to calculate the total capture cross section with PDIX, the direct radiative capture formalism was coupled to a Single-Level Breit-Wigner resonance model [279]. For the present calculations the resonance parameters provided by the JEFF-3.1.1 evaluation were used [280]. In this evaluation, a total of 317 resonances are available, going as high as 850 keV incident neutron energy. To simultaneously reproduce the coherent scattering length and the cross section at thermal energy the Γ_γ parameter of the -2.44 keV resonance was reduced by almost 50%. At the same time, the OMP parameters for the direct capture component where slightly modified in order to properly reproduce the cross section at thermal energy. The depth of the volume potential was reduced by 0.5 MeV compared to the value that was proposed by Koning et al. (2003) [6].

The PDIX code is able to calculate the total capture cross section only at 0 K temperature. To be able to properly compare the result with the evaluated data the Doppler broadening effect needs to be taken into account. To address that, the resulting cross section was folded with the Maxwell-Boltzman distribution:

$$\bar{\sigma}(E) \approx \frac{1}{\Delta_D\sqrt{\pi}} \int_{-\infty}^{\infty} dE' e^{\left(-\frac{E'-E}{\Delta_D}\right)^2} \sqrt{\frac{E'}{E}}\sigma(E'), \tag{5.11}$$

where Δ_D is the Doppler width defined as $\Delta_D = \sqrt{\frac{4Ek_BT}{M/m_n}}$ [281]. The cross section was then calculated for room temperature at 293 K.

In Figs. 5.4 and 5.5 the results of the total capture cross section are presented. It is observed that the results of this work support the intermediate choice of the background cross section component that was added in the 10 eV - 100 keV energy region, as already discussed in Sec. 1.2. Even though there are some small differences in this region between this work, INDEN-Aug2023, and JENDL-5 the trend of the cross section is the same in all cases. It is also interesting to mention that the present results are very close to the JENDL-5 evaluation, considering that in this evaluation direct and semi-direct calculations have been included for the first time. Additionally, in the resolved resonance region (see Fig. 5.5) it is observed that the direct capture component when coupled with the compound capture is able to reproduce the background cross section that was added up to 500 keV neutron incident energy, but above this energy the valleys between the resonances are underestimated compared to the other evaluations.

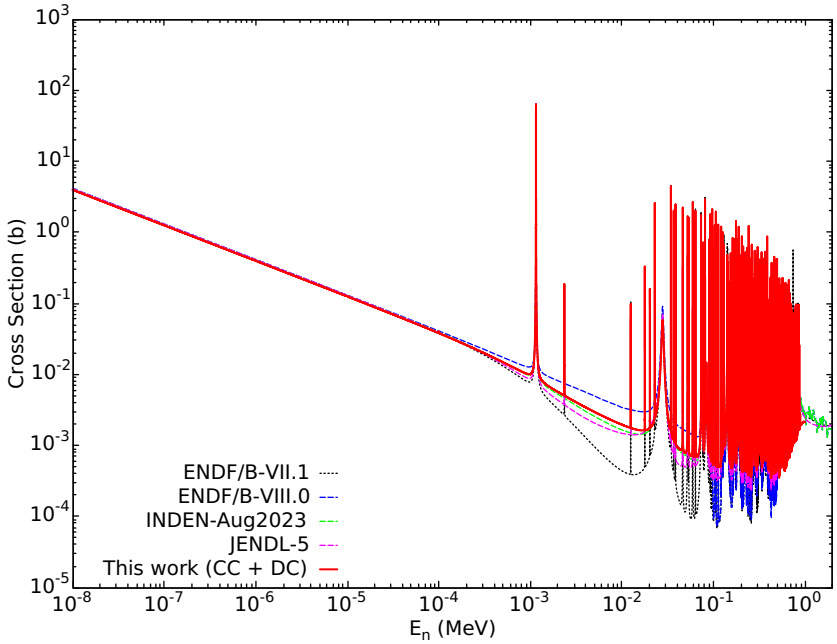

Figure 5.4: Result of the total capture cross section (red) from thermal up to 2 MeV neutron energy compared to the evaluated ^{56}Fe(n,γ) cross section of ENDF/B-VII.1 (black) [63], ENDF/B-VIII.0 (blue) [9], INDEN-Aug2023 (green) [65], and JENDL-5 (magenta) [66].

5.4 Conclusions

In this chapter, the direct radiative capture cross section for the case of ^{56}Fe was explored. A short description of the theoretical concept behind the direct capture process and the steps that were followed in order to calculate the cross section were given. Additionally, an attempt to calculate the total capture cross section (direct and compound capture) was made using the Single-Level

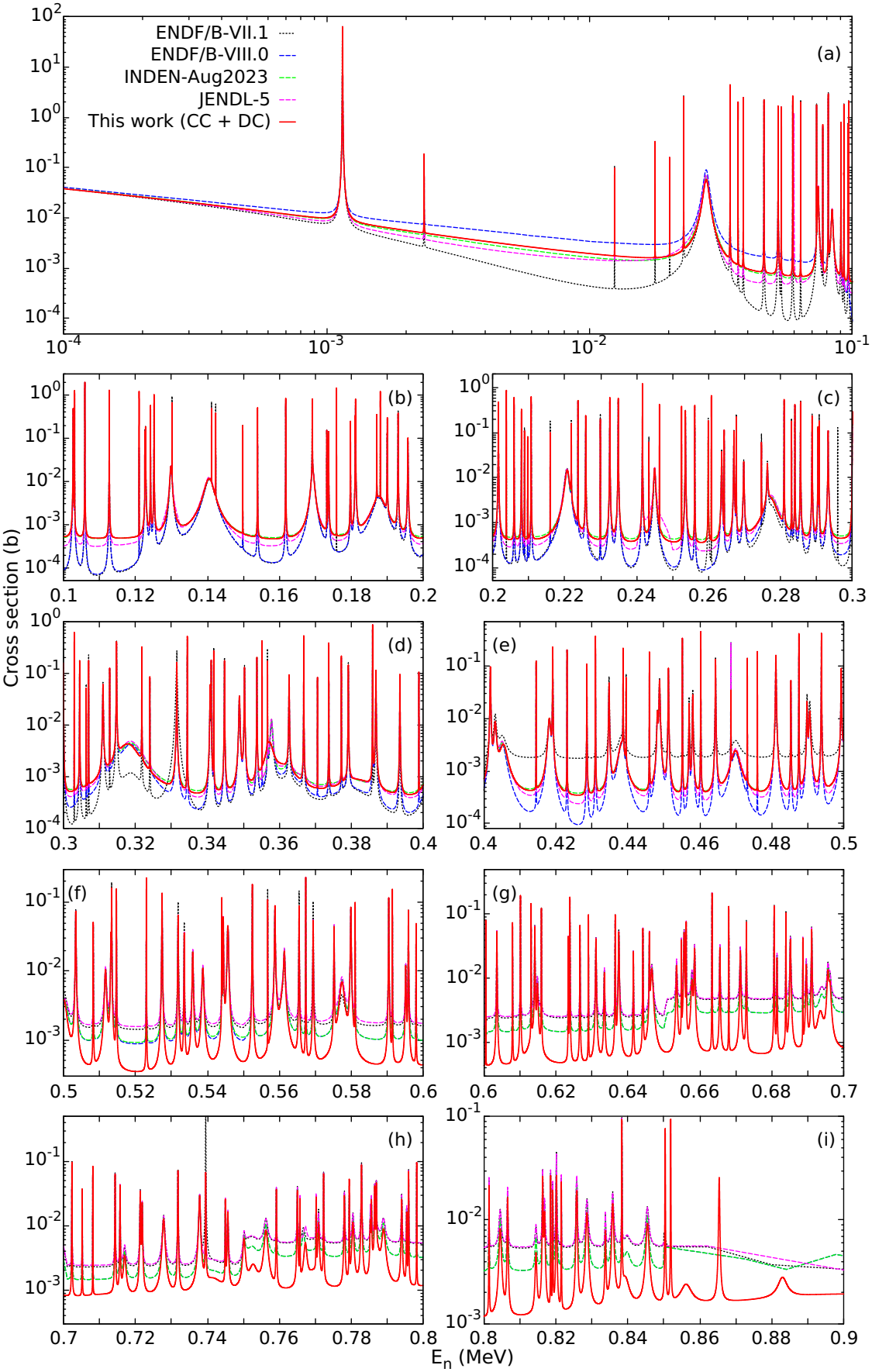

Figure 5.5: Comparison between the total capture cross section calculated with the PDIX code and the different evaluations in (a) the 10 eV-100 keV energy region and from (b) to (i) in the resolved resonance region up to 900 keV.

Breit-Wigner formalism to describe the resolved resonance region. Based on the first results, the s-wave direct capture is able to explain the background component that was added in the 10-100 keV energy region, while the d-wave direct capture seems to be a good candidate for the "bump" of the capture cross section around 850 keV that was observed at a recent experiment. The results were compared to the most recent evaluation data for the ^{56}Fe(n,γ) cross section provided by INDEN and JENDL and relatively good agreement was observed.

Chapter 6

Conclusions and future perspectives

6.1 Summary and conclusions

In the present work, new experiments were performed at the GELINA neutron time-of-flight facility to measure neutron induced reaction cross sections on iron in an effort to tackle issues reported in the evaluated files of iron by providing new experimental data for key reactions and neutron energy regions. First, angular distributions and cross sections of neutron elastic and inelastic scattering on ^{54,56}Fe in the fast neutron energy region were measured using highly enriched samples for both isotopes. For these measurements, the ELISA setup was used, a spectrometer consisting of 32 liquid organic scintillators for the detection of the scattered neutrons and a ^{235}U ionization chamber for the measurements of the neutron flux. The procedure for the characterization of the detectors installed at ELISA and the whole data analysis that followed for the extraction of the final results was described. This procedure includes the modeling of the response functions for each detector individually by combining experimental measurements and Monte Carlo simulation, the pulse shape analysis for n-γ separation, the treatment of the data for the background contribution by subtracting the sample-out from the sample-in measurements, the elastic/inelastic separation by using kinematic calculations, the multiple scattering corrections implementing a Monte Carlo simulation of the whole setup, and the analysis of the fission chamber data to extract the neutron fluence impinged on each iron sample. The differential cross sections were then calculated at 8 detection angles using Eq. (3.1) and the integral cross section using the Gauss-Legendre quadrature rule [Eq. (2.10)]. The whole analysis procedure was successfully validated using the ^{nat}C measurement by reproducing the well known ^{nat}C(n,n) reaction cross section. The results were compared with the data available in the EXFOR library, the JEFF-3.3 and ENDF-B/VIII.0 evaluations, and theoretical calculations using the TALYS and EMPIRE reaction codes.

For elastic scattering, these are the first experimental measurements providing high-resolution data in the energy range of 1 to 8 MeV. The total uncertainties for ^{54}Fe vary from 5% to 25% for the differential cross section, and from 5% to 8% for the angle integrated cross section, while for ^{56}Fe from 3% to 20% for the differential cross section, and the angle integrated from 3% to 6%. The results are in overall good agreement with the values proposed by the JEFF-3.3 and ENDF/B-

VIII.0 evaluations, other experimental data available in the EXFOR library, and the theoretical calculations above 2 MeV incident neutron energy. Some discrepancies in the angular distributions of some angles, above 3 MeV neutron incident energy, are observed and further investigation is needed to improve the quality of the evaluated libraries for neutron elastic angular distributions.

Regarding inelastic scattering, angular distributions and partial cross sections from the first excited state of ^{54}Fe and the first two excited states of ^{56}Fe were explored and good-quality results were extracted. For ^{54}Fe cross section were obtained in the energy range from 2.5 to 5.5 MeV, with total uncertainties varying from 7% to 50% for the differential, and from 6% to 20% for the angle integrated cross section. Results for the first excited state of ^{56}Fe were obtained in the energy range from 2 to 5 MeV, with total uncertainties varying from 5% to 35% for the angular distributions, and from 5% to 16% for the angle integrated cross section. For the second excited state of ^{56}Fe, partial cross sections were obtained in the energy region from 3 to 6 MeV with total uncertainties varying from 10% to 70% in the angular distributions, and from 20% to 45% in the angle integrated cross section. In all the inelastic scattering cases, high uncertainties are observed in the forward detection angles, where the difference between elastic and inelastic scattering cross section is considerable. All the inelastic scattering results were compared with the JEFF-3.3 and ENDF/B-VIII.0 evaluations and it was observed that in both the angular distributions and the angle integrated cross sections the evaluations were underestimated. All the results seem to be in good agreement within uncertainties with the majority of the other experimental data available in the EXFOR library.

Furthermore, neutron transmission experiments on ^{nat}Fe were performed with the goal to shed more light on the 24 keV energy region where issues have been identified by the evaluators working on the nuclear data of iron. The experiments were performed at the 50 m station GELINA and two natural iron samples of different thicknesses were measured. The basic principle behind transmission experiments and the details of the measurements were given. The analysis procedure, from sorting the raw data into time-of-flight histograms to the determination of the background contribution and the final calculation of the transmission was described. The final results were compared with the JEFF-3.3 and ENDF/B-VIII.0 evaluations and even thought both evaluations seem to perform relatively well over the whole neutron energy region, some discrepancies were observed especially around the 24 keV energy region. The results were also compared with experimental data available in the literature and seem to be in very good agreement.

Finally, the direct radiative capture mechanism for the case of ^{56}Fe was explored in this work. A short description of the steps needed to calculate the direct capture cross section was given and the first results of the direct capture were presented. Overall, the s-wave direct capture can explain the background component that was added in the 10 eV - 100 keV energy region, but it is not sufficient to simultaneously reproduce the cross section at thermal energies and the 10 eV - 100 keV region without the contribution of the negative resonances. Additionally, the d-wave direct capture seems to be a good candidate for the "bump" of the capture cross section around 850 keV that was observed at a recent experiment. An attempt to calculate the total capture cross section (direct and compound capture) was made using the Single-Level Breit-Wigner formalism,

available in the PDIX code, to describe the resolved resonance region. The final results of this work seem to be very close to the most recent evaluation data for the ^{56}Fe(n,γ) cross section provided by INDEN and JENDL.

All the results of this work, both experimental and theoretical, have been presented and communicated to the evaluation community through presentations at meetings of the JEFF project and the INDEN working group on structural materials. The experimental data have been submitted to the EXFOR library and have become available via private communication to the evaluators who are currently working on the nuclear data of iron, with the goal to provide important information that would assist in the improvement of the quality of the new evaluations.

6.2 Future perspectives

The future perspectives include further analysis of the obtained data, upgrades on the different detection systems, and new measurements. Specifically:

- Regarding the angular distributions of ^{54,56}Fe, the results of this work will be used to extract the experimental Legendre coefficients which are key information for the evaluation of angular distributions. Also the photon spectra of these measurements recorded by the scintillators of the ELISA spectrometer can be explored to see if useful information can be extracted on the neutron induced γ-emitting reactions, namely capture and inelastic scattering, in the fast neutron energy region.

- Upgrades of the ELISA spectrometer are planned. Specifically, 8 Li-glass detectors will be installed in an attempt to explore elastic scattering in the energy region below 1 MeV which is the detection threshold of the scintillators currently used at the ELISA setup. Additionally, NaI detectors will also be installed to explore n-γ coincidences and try to develop a technique that can be used to study nuclei with very low inelastic thresholds.

- Reducing the background contribution in the scattering measurements is also foreseen. As mentioned above, based on the measurements performed so far, the background contribution from the neutron beam scattering in the air accounts for almost 40% of the recorded signals. The plan is to minimize this effect by putting part of the ELISA spectrometer in vacuum conditions. This will be achieved by installing special structures around the setup or in the beam-path.

- New scattering measurements at the ELISA spectrometer are also planned. The measurements will be focused on medium-mass nuclei, where it has been proven that no theoretical model is able to reproduce the fluctuating behavior of the cross section in the 1 - 6 MeV region, meaning that only experimental data can sufficiently constrain the uncertainties on the evaluated files. The plan for the upcoming years is to continue the work on structural materials by measuring the cross sections of ^{63,65}Cu, but also explore heavy nuclei like ^{206,208}Pb,

all cases where there is almost no experimental data for elastic scattering available in the literature.

- An additional neutron transmission measurement on natural iron is also needed. The plan is to combine two of the samples used in the present work to study the transmission of a sample with a total thickness of 9 cm. This measurements will provide important information on the cross section minima and the valleys between the resonances.

- The development of a new transmission station at the flight path 4 of GELINA has already been initiated. The plan is to build a new station at the 200 m cabin and develop for the first time a digitizer based data acquisition system. With this system the dead time effect observed so far will be minimized allowing the measurement of transmission in energies up to several hundreds of keV.

- Finally, the implementation of the direct radiative capture formalism in a code that is able to do resonance fitting, a code like CONRAD which is developed at CEA Cadarache, will provide a more comprehensive approach in the calculation of the total capture cross section.

Appendices

Appendix A

Kinematic calculations

To determine the energy of the incoming neutrons, the time-of-flight method was employed. The fundamental concept of neutron spectroscopy using this technique involves measuring the time t it takes for a neutron to cover a specific distance L. The neutron's velocity u is straightforwardly calculated as:

$$u = \frac{L}{t} \tag{A.1}$$

When the velocity of a particle approaches the speed of light, we need to use relativistic mechanics to describe it's total energy. In special relativity, the total energy of a neutron is given by:

$$E_{\text{total}} = \gamma m_n c^2 \tag{A.2}$$

Where:

- $\gamma = \frac{1}{\sqrt{1-(u/c)^2}}$ is the Lorentz factor.
- u is the speed of the particle.
- c is the speed of light.
- m_n is the rest mass of the neutron.

The kinetic energy E_{kin} of the neutron is the total energy minus the rest energy:

$$\begin{aligned} E_{\text{kin}} &= E_{\text{total}} - E_{\text{rest}} \Rightarrow \\ E_{\text{kin}} &= \gamma m_n c^2 - m_n c^2 \Rightarrow \\ E_{\text{kin}} &= m_n c^2 (\gamma - 1) \end{aligned} \tag{A.3}$$

This is the relativistic expression for kinetic energy.

In our scattering experiments, the time-of-flight is calculated by adding the time it takes for the neutron to travel from the source to the scattering sample, and the time it takes for the scattered neutron to travel from the sample to the detector. The total time-of-flight is then given by the

formula:

$$t.o.f. = \frac{L}{u} + \frac{L'}{u'} \tag{A.4}$$

where L is the distance from the source to the sample, u is the initial velocity of the neutron, L' is the distance from the sample to the detector and u' is the velocity of the neutron after the scattering. In principle the velocity can be described with respect to the kinetic energy via the following formula:

$$E_{\text{total}} = E_{\text{rest}} + E_{\text{kin}} \Rightarrow \gamma m_n c^2 = m_n c^2 + E_{\text{kin}} \Rightarrow \frac{1}{\sqrt{1-(u/c)^2}} m_n c^2 = m_n c^2 + E_{\text{kin}} \Rightarrow$$

$$\frac{1}{\sqrt{1-(u/c)^2}} = 1 + \frac{E_{\text{kin}}}{m_n c^2} \Rightarrow \frac{1}{1-(u/c)^2} = \left(1 + \frac{E_{\text{kin}}}{m_n c^2}\right)^2 \Rightarrow 1-(u/c)^2 = \frac{1}{\left(1 + \frac{E_{\text{kin}}}{m_n c^2}\right)^2} \Rightarrow$$

$$\frac{u}{c} = \sqrt{1 - \frac{1}{\left(1 + \frac{E_{\text{kin}}}{m_n c^2}\right)^2}} \Rightarrow u = c\sqrt{1 - \frac{1}{\left(1 + \frac{E_{\text{kin}}}{m_n c^2}\right)^2}} \tag{A.5}$$

So Eq. (A.4) can be described as:

$$t.o.f. = \frac{L}{c\sqrt{1 - \frac{1}{\left(1+\frac{E_0}{m_n c^2}\right)^2}}} + \frac{L'}{c\sqrt{1 - \frac{1}{\left(1+\frac{E'}{m_n c^2}\right)^2}}} \tag{A.6}$$

where E_0 and E' is the kinetic energy before and after the collision. In elastic scattering, if we know the nuclear mass M of the scattering sample and the detection angle θ, the kinetic energy after the collision E' can be expressed as a function of the initial kinetic energy E_0 using the principles of energy and momentum conservation. From the conservation of energy we have:

$$E_{\text{initial}} = E_{\text{final}} \Rightarrow E_0 + Mc^2 = E' + Mc^2 + K \Rightarrow E_0 - E' = K \tag{A.7}$$

where K is the kinetic energy of the target nucleus. For the conservation of momentum we have the formula:

$$p_0 = p' + P \tag{A.8}$$

where p_0 is the initial momentum of the neutron, p' is the momentum after the scattering, and P is the momemntum of the target nucleus after the collision. Taking into account the scattering angle θ the formula above can be expressed as:

$$p_0^2 = p'^2 + P^2 + 2p'P\cos\theta \tag{A.9}$$

Using the relativistic relationship between energy and momentum we have:

$$\begin{aligned} E_0^2 &= (p_0 c)^2 + (m_n c^2)^2 \Rightarrow p_0 = \sqrt{\frac{E_0^2 - (m_n c^2)^2}{c^2}} \\ E'^2 &= (p' c)^2 + (m_n c^2)^2 \Rightarrow p' = \sqrt{\frac{E'^2 - (m_n c^2)^2}{c^2}} \end{aligned} \tag{A.10}$$

From Eq. (A.9) we have the momentum of the target nucleus:

$$p_0^2 = p'^2 + P^2 + 2p'P\cos\theta \Rightarrow P^2 = p_0^2 - p'^2 - 2p'P\cos\theta$$

and it's kinetic energy is given by:

$$K = \frac{P^2 c^2}{2M} \tag{A.11}$$

Going back to Eq. (A.7) and substitute the kinetic energy of the target nucleaus with Eq. (A.11) we have:

$$E_0 - E' = K \Rightarrow E_0 - E' = \frac{P^2 c^2}{2M} \Rightarrow E_0 - E' = \frac{c^2}{2M}(p_0^2 - p'^2 - 2p'P\cos\theta) \tag{A.12}$$

Assuming small scattering angles and elastic collisions, the momentum of the target nucleus can be expressed as $P = p_0 - p'$ thus:

$$\begin{aligned} E_0 - E' &= \frac{c^2}{2M}(p_0^2 - p'^2 - 2p'(p_0 - p')\cos\theta) \Rightarrow \\ E_0 - E' &= \frac{c^2}{2M}(p_0^2 - p'^2 - 2p'p_0\cos\theta + 2p_0^2\cos\theta) \Rightarrow \\ E_0 - E' &= \frac{c^2}{2M}\left(p_0^2 - p'^2(1 - 2\cos\theta) - 2p'p_0\cos\theta\right) \Rightarrow \end{aligned}$$

Substitute the expressions for p_0 and p' from Eq. (A.10) into the equation:

$$E_0 - E' = \frac{c^2}{2M}\left(\frac{E_0^2 + 2E_0 m_n c^2}{c^2} - \frac{E'^2 + 2E'm_n c^2}{c^2}(1 - 2\cos\theta) - 2\frac{\sqrt{E'^2 + 2E'm_n c^2}}{c}\frac{\sqrt{E_0^2 + 2E_0 m_n c^2}}{c}\cos\theta\right)$$

$$E_0 - E' = \frac{1}{2M}\left((E_0^2 + 2E_0 m_n c^2) - (E'^2 + 2E'm_n c^2)(1 - 2\cos\theta) - 2\sqrt{E'^2 + 2E'm_n c^2}\sqrt{E_0^2 + 2E_0 m_n c^2}\cos\theta\right)$$

After expanding and simplifying the terms, we arrive to the final equation:

$$E'(Mc^2 + m_n c^2) - E_0(Mc^2 - m_n c^2) + E_0 E' = c^2 p_0 p'\cos\theta \tag{A.13}$$

In the case of inelastic scattering, the excitation energy E^* of the target nucleus must be considered. From the conservation of energy and momentum we have:

$$E_0 = E' + E^* \tag{A.14}$$

and

$$p_0^2 = p'^2 + P^2 + 2p'P\cos\theta \tag{A.15}$$

While the formulas that describe the momentum of the neutron is given in Eq. (A.10) for the momentum of the target nucleus we have:

$$\begin{gathered}
E^2 = P^2c^2 + M^2c^4 \Rightarrow \\
((E_0 - E') + Mc^2)^2 = P^2c^2 + M^2c^4 \Rightarrow \\
(E_0 - E')^2 + 2(E_0 - E')Mc^2 + M^2c^4 = P^2c^2M^2c^4 \Rightarrow \\
(E_0 - E')^2 + 2(E_0E')Mc^2 = P^2c^2 \Rightarrow \\
P = \frac{\sqrt{(E_o - E')^2 + 2(E_0 - E')Mc^2}}{c}
\end{gathered}$$

Substitute the expressions for p_0, p', and P into the momentum conservation equation:

$$\left(\frac{\sqrt{E_0^2 + 2E_0mc^2}}{c}\right)^2 = \left(\frac{\sqrt{E'^2 + 2E'mc^2}}{c}\right)^2 + \left(\frac{\sqrt{(E_0 - E')^2 + 2(E_0 - E')Mc^2}}{c}\right)^2 + 2\frac{\sqrt{E'^2 + 2E'mc^2}}{c}\frac{\sqrt{(E_0 - E')^2 + 2(E_0 - E')Mc^2}}{c}\cos\theta \Rightarrow$$

Multiply through by c^2 to eliminate the denominators:

$$E_0^2 + 2E_0mc^2 = E'^2 + 2E'mc^2 + (E_0 - E')^2 + 2(E_0 - E')Mc^2 + 2\sqrt{(E'^2 + 2E'mc^2)((E_0 - E')^2 + 2(E_0 - E')Mc^2)}\cos\theta$$

Taking into account Eq. (A.14) we arrive to the final formula:

$$2E'(Mc^2 + mc^2) - 2E_0(Mc^2 - mc^2) + 2E_0E' + E^*(2Mc^2 + E^*) = 2c^2p_0p'\cos\theta \tag{A.16}$$

Bibliography

[1] K. Kolos, V. Sobes, R. Vogt, C. E. Romano, M. S. Smith, L. A. Bernstein, D. A. Brown, M. T. Burkey, Y. Danon, M. A. Elsawi, B. L. Goldblum, L. H. Heilbronn, S. L. Hogle, J. Hutchinson, B. Loer, E. A. McCutchan, M. R. Mumpower, E. M. O'Brien, C. Percher, P. N. Peplowski, J. J. Ressler, N. Schunck, N. W. Thompson, A. S. Voyles, W. Wieselquist, and M. Zerkle, "Current nuclear data needs for applications," *Phys. Rev. Res.*, vol. 4, p. 021001, 2022.

[2] R. Forrest, "Nuclear Science and Data Needs for Advanced Nuclear Systems," *Energy Procedia*, vol. 7, pp. 540–552, 2011.

[3] S. M. Qaim, "Nuclear data for production and medical application of radionuclides: Present status and future needs," *Nuclear Medicine and Biology*, vol. 44, pp. 31–49, 2017.

[4] IAEA, *Environmental and Source Monitoring for Purposes of Radiation Protection*. No. RS-G-1.8 in General Safety Guides, 2005.

[5] G. Aliberti, G. Palmiotti, M. Salvatores, T. K. Kim, T. Taiwo, M. Anitescu, I. Kodeli, E. Sartori, J. C. Bosq, and J. Tommasi, "Nuclear data sensitivity, uncertainty and target accuracy assessment for future nuclear systems," *Annals of Nuclear Energy*, vol. 33, no. 8, pp. 700–733, 2006.

[6] A. Koning and J. Delaroche, "Local and global nucleon optical models from 1 keV to 200 MeV," *Nuclear Physics A*, vol. 713, no. 3, pp. 231–310, 2003.

[7] M. Diakaki, S. Chen, G. Noguere, D. Bernard, P. Tamagno, and P. Archier, "Evaluation of neutron induced reactions on 56Fe with CONRAD," *EPJ Web of Conferences*, vol. 239, p. 11005, 2020.

[8] M. B. Chadwick, E. Dupont, E. Bauge, A. Blokhin, O. Bouland, D. A. Brown, R. Capote, A. Carlson, Y. Danon, C. De Saint Jean, M. Dunn, U. Fischer, R. A. Forrest, S. C. Frankle, T. Fukahori, Z. Ge, S. M. Grimes, G. M. Hale, M. Herman, A. Ignatyuk, M. Ishikawa, N. Iwamoto, O. Iwamoto, M. Jandel, R. Jacqmin, T. Kawano, S. Kunieda, A. Kahler, B. Kiedrowski, I. Kodeli, A. J. Koning, L. Leal, Y. O. Lee, J. P. Lestone, C. Lubitz, M. MacInnes, D. McNabb, R. McKnight, M. Moxon, S. Mughabghab,

G. Noguere, G. Palmiotti, A. Plompen, B. Pritychenko, V. Pronyaev, D. Rochman, P. Romain, D. Roubtsov, P. Schillebeeckx, M. Salvatores, S. Simakov, E. S. Soukhovitskii, J. C. Sublet, P. Talou, I. Thompson, A. Trkov, R. Vogt, and S. Van der Marck, "The CIELO Collaboration: Neutron Reactions on ^{1}H, ^{16}O, ^{56}Fe, ^{235,238}U, and ^{239}Pu," *Nuclear Data Sheets*, vol. 118, pp. 1–25, 2014.

[9] D. Brown, M. Chadwick, R. Capote, A. Kahler, A. Trkov, M. Herman, A. Sonzogni, Y. Danon, A. Carlson, M. Dunn, D. Smith, G. Hale, G. Arbanas, R. Arcilla, C. Bates, B. Beck, B. Becker, F. Brown, R. Casperson, J. Conlin, D. Cullen, M.-A. Descalle, R. Firestone, T. Gaines, K. Guber, A. Hawari, J. Holmes, T. Johnson, T. Kawano, B. Kiedrowski, A. Koning, S. Kopecky, L. Leal, J. Lestone, C. Lubitz, J. Márquez Damián, C. Mattoon, E. McCutchan, S. Mughabghab, P. Navratil, D. Neudecker, G. Nobre, G. Noguere, M. Paris, M. Pigni, A. Plompen, B. Pritychenko, V. Pronyaev, D. Roubtsov, D. Rochman, P. Romano, P. Schillebeeckx, S. Simakov, M. Sin, I. Sirakov, B. Sleaford, V. Sobes, E. Soukhovitskii, I. Stetcu, P. Talou, I. Thompson, S. van der Marck, L. Welser-Sherrill, D. Wiarda, M. White, J. Wormald, R. Wright, M. Zerkle, G. Žerovnik, and Y. Zhu, "ENDF/B-VIII.0: The 8th Major Release of the Nuclear Reaction Data Library with CIELO-project Cross Sections, New Standards and Thermal Scattering Data," *Nuclear Data Sheets*, vol. 148, pp. 1–142, 2018. Special Issue on Nuclear Reaction Data.

[10] A. Plompen, O. Cabellos, C. De Saint Jean, M. Fleming, A. Algora, M. Angelone, P. Archier, E. Bauge, O. Bersillon, A. Blokhin, F. Cantargi, A. Chebboubi, C. J. Diez, H. Duarte, E. Dupont, J. Dyrda, B. Erasmus, L. Fiorito, U. Fischer, D. Flammini, D. Foligno, M. Gilbert, J. R. Granada, W. Haeck, F. Hambsch, P. Helgesson, S. Hilaire, I. Hill, M. Hursin, R. Ichou, R. Jacqmin, B. Jansky, C. Jouanne, M. Kellett, D. H. Kim, H. I. Kim, I. Kodeli, A. J. Koning, A. Y. Konobeyev, S. Kopecky, B. Kos, A. Krasa, L. Leal, N. Leclaire, P. Leconte, Y. O. Lee, H. Leeb, O. Litaize, M. Majerle, J. Marquez Damian, F. Michel-Sendis, R. Mills, B. Morillon, G. Noguere, M. Pecchia, S. Pelloni, P. Pereslavtsev, R. Perry, D. Rochman, R. Roehrmoser, P. Romain, P. Romojaro, D. Roubtsov, P. Sauvan, P. Schillebeeckx, K. Schmidt, O. Serot, S. Simakov, I. Sirakov, H. Sjöstrand, A. Stankovskiy, J. C. Sublet, P. Tamagno, A. Trkov, S. Van Den Marck, F. Velarde, R. Villari, K. Yokoyama, and G. Zerovnik, "The Joint Evaluated Fission and Fusion Nuclear Data Library, JEFF-3.3," *European Physical Journal A*, vol. 56, p. 181, 2020.

[11] H. I. Liou, R. E. Chrien, R. C. Block, and U. N. Singh, "The Transmission of Neutrons Through Iron-56 at 24.37 keV," *Nuclear Science and Engineering*, vol. 70, no. 2, pp. 150–154, 1979.

[12] M. Herman, A. Trkov, R. Capote, G. P. A. Nobre, D. A. Brown, R. Arcilla, Y. Danon, A. Plompen, S. F. Mughabghab, Q. Jing, G. Zhigang, L. Tingjin, L. Hanlin, R. Xichao, L. Leal, B. V. Carlson, T. Kawano, M. Sin, S. P. Simakov, and K. Guber, "Evaluation of

Neutron Reactions on Iron Isotopes for CIELO and ENDF/B-VIII.0," *Nuclear Data Sheets*, vol. 148, pp. 214–253, 2018.

[13] N. Otuka, E. Dupont, V. Semkova, B. Pritychenko, A. I. Blokhin, M. Aikawa, S. Babykina, M. Bossant, G. Chen, S. Dunaeva, R. A. Forrest, T. Fukahori, N. Furutachi, S. Ganesan, Z. Ge, O. O. Gritzay, M. Herman, S. Hlavač, K. Katō, B. Lalremruata, Y. O. Lee, A. Makinaga, K. Matsumoto, M. Mikhaylyukova, G. Pikulina, V. G. Pronyaev, A. Saxena, O. Schwerer, S. P. Simakov, N. Soppera, R. Suzuki, S. Takács, X. Tao, S. Taova, F. Tárkányi, V. V. Varlamov, J. Wang, S. C. Yang, V. Zerkin, and Y. Zhuang, "Towards a More Complete and Accurate Experimental Nuclear Reaction Data Library (EXFOR): International Collaboration Between Nuclear Reaction Data Centres (NRDC)," *Nuclear Data Sheets*, vol. 120, pp. 272–276, 2014.

[14] P. Romojaro, F. Álvarez Velarde, O. Cabellos, N. García-Herranz, and A. Jiménez-Carrascosa, "On the importance of target accuracy assessments and data assimilation for the co-development of nuclear data and fast reactors: MYRRHA and ESFR," *Annals of Nuclear Energy*, vol. 161, p. 108416, 2021.

[15] J. Engelen, H. A. Abderrahim, P. Baeten, D. De Bruyn, and P. Leysen, "MYRRHA: Preliminary front-end engineering design," *International Journal of Hydrogen Energy*, vol. 40, no. 44, pp. 15137–15147, 2015.

[16] W. L. Rodgers, E. F. Shrader, and J. T. Lindow, "Neutron scattering from ^{12}C, ^{54}Fe, ^{56}Fe, ^{65}Cu, ^{58}Ni58, and ^{60}Ni," *Progress Report: Chicago Operations Office, A.E.C., No.*, vol. 1573-33, p. 2, 1967.

[17] P. Boschung, J. T. Lindow, and E. F. Shrader, "Scattering of fast neutrons by ^{12}C, ^{54}Fe, ^{56}Fe, ^{58}Ni and ^{60}Ni," *Nuclear Physics A*, vol. 161, no. 2, pp. 593–609, 1971.

[18] M. B. Fedorov and T. I. Jakovenko, "The Scattering of 2.9 MeV Neutrons by Even Even Isotopes of Iron, Chromium and Zinc," *Ukr. Fiz. Zh*, vol. 19, p. 152, 1974.

[19] W. E. Kinney and F. G. Perey, "^{54}Fe neutron elastic and inelastic scattering cross sections from 5.50 to 8.50 MeV," *Technical Report, Oak Ridge National Lab*, 1974.

[20] I. A. Korzh, V. A. Mishchenko, E. N. Mozhzhukhin, N. M. Pravdivyy, and I. E. Sanzhur, "Differential neutron scattering cross-sections at 1.5 to 3.0 MeV for titanium, iron and bismuth nuclei," *Ukr. Fiz. Zh*, vol. 22, p. 87, 1977.

[21] S. M. El-Kadi, C. E. Nelson, F. O. Purser, R. L. Walter, A. Beyerle, C. R. Gould, and L. W. Seagondollar, "Elastic and inelastic scattering of neutrons from ^{54,56}Fe and ^{63,65}Cu: (I). Measurements from 8 to 14 MeV and a spherical optical model analysis," *Nuclear Physics A*, vol. 390, no. 3, pp. 509–540, 1982.

[22] I. A. Korzh, V. A. Mishchenko, and N. M. Pravdivyi, "Fast neutron elastic and inelastic scattering cross sections of ^{54}Fe," *Sov. At. Energy*, vol. 62, no. 6, 1987.

[23] P. T. Guenther, D. L. Smith, A. B. Smith, and J. F. Whalen, "Total, scattering and gamma-ray-production cross sections for few-MeV neutrons on ^{54}Fe," *Annals of Nuclear Energy*, vol. 13, no. 11, pp. 601–610, 1986.

[24] J. R. Vanhoy, S. H. Liu, S. F. Hicks, B. M. Combs, B. P. Crider, A. J. French, E. A. Garza, T. Harrison, S. L. Henderson, T. J. Howard, M. T. McEllistrem, S. Nigam, R. L. Pecha, E. E. Peters, F. M. Prados-Estévez, A. P. D. Ramirez, B. G. Rice, T. J. Ross, Z. C. Santonil, L. C. Sidwell, J. L. Steves, B. K. Thompson, and S. W. Yates, "^{54}Fe neutron elastic and inelastic scattering differential cross sections from 2–6 MeV," *Nuclear Physics A*, vol. 972, pp. 107–120, 2018.

[25] W. E. Kinney, "Neutron Elastic and Inelastic Scattering from ^{56}Fe from 4.60 to 7.55 MeV," *Technical Report, Oak Ridge National Lab*, no. 4249, 1968.

[26] V. M. Morozov, Y. G. Zubov, and N. S. Lebedeva, "Two mechanisms of elastic scattering in nuclear optical model," *Technical Report, Yaderno-Fizicheskie Issledovaniya v SSSR*, no. 14, p. 8, 1972.

[27] T. Schweitzer, D. Seeliger, and S. Unholzer, "Elastic and inelastic scattering of 3.4 MeV neutrons by ^{23}Na, ^{24}Mg, ^{27}Al, ^{28}Si, ^{31}P-, ^{55}Mn, ^{56}Fe and ^{209}Bi," *Kernenergie*, vol. 20, p. 174, 1977.

[28] A. P. D. Ramirez, J. R. Vanhoy, S. F. Hicks, M. T. McEllistrem, E. E. Peters, S. Mukhopadhyay, T. D. Harrison, T. J. Howard, D. T. Jackson, P. D. Lenzen, T. D. Nguyen, R. L. Pecha, B. G. Rice, B. K. Thompson, and S. W. Yates, "Neutron scattering cross section measurements for ^{56}Fe," *Phys. Rev. C*, vol. 95, p. 064605, 2017.

[29] K. Berthold, C. Nazareth, G. Rohr, and H. Weigman, "HIGH-RESOLUTION FE TRANSMISSION DATA FROM GEEL," *Priv. Comm.*, 1995.

[30] M. Herman, R. Capote, B. Carlson, P. Obložinský, M. Sin, A. Trkov, H. Wienke, and V. Zerkin, "EMPIRE: Nuclear Reaction Model Code System for Data Evaluation," *Nuclear Data Sheets*, vol. 108, no. 12, pp. 2655–2715, 2007.

[31] M. Salvatores and R. Jacqmin, "Uncertainty and Target Accuracy Assessment for Innovative Systems Using Recent Covariance Data Evaluations," *NEA/WPEC subgroup 26 final report, OECD Nuclear Energy Agency*, 2008.

[32] OECD Nuclear Energy Agency - Nuclear Data High-Priority Request List, available at: https://www.oecd-nea.org/dbdata/hprl/ date accessed: 2024.

[33] R. Beyer, R. Schwengner, R. Hannaske, A. Junghans, R. Massarczyk, M. Anders, D. Bemmerer, A. Ferrari, A. Hartmann, T. Kögler, M. Röder, K. Schmidt, and A. Wagner, "Inelastic scattering of fast neutrons from excited states in 56Fe," *Nuclear Physics A*, vol. 927, pp. 41–52, 2014.

[34] A. Negret, C. Borcea, and A. J. M. Plompen, "Neutron inelastic scattering measurements for background assessment in neutrinoless double β decay experiments," *Phys. Rev. C*, vol. 88, p. 027601, 2013.

[35] E. Dupont, P. Ribon, H. Weigmann, and G. Vanpraet, "High Resolution Measurement of the Neutron Inelastic Scattering CrossSection of ^{56}Fe," *Conf. on Nucl. Data for Sci. and Techn.*, 1997.

[36] I. A. Korzh, V. A. Mishchenko, N. M. Pravdivy, N. T. Sklyar, D. A. Bazavov, and V. P. Lunyov, "Inelastic scattering of neutrons by nuclei Mo-94,Mo-96, Mo-98 near the first 2+level excitation threshold," *Ukrainskii Fizichnii Zhurnal*, vol. 39, 1994.

[37] F. G. Perey, W. E. Kinney, and R. L. Macklin, "High resolution inelastic cross section measurements for Na, Si, and Fe," *3rd Conf. Neutron Cross-Sections and Tech.*, vol. 1, 1971.

[38] T. W. Barrows, "A STUDY OF THE (N,N GAMMA) REACTIONS IN V51 AND MN55 AND THE REACTION F19(D,N)NE20," *PhD Thesis*, 1965.

[39] A. Olacel, C. Borcea, M. Boromiza, P. Dessagne, G. Henning, M. Kerveno, L. Leal, A. Negret, M. Nyman, and A. J. M. Plompen, "Neutron inelastic scattering on ^{54}Fe," *The European Physical Journal A*, vol. 54, pp. 1–15, 2018.

[40] A. Negret, M. Sin, C. Borcea, R. Capote, P. Dessagne, M. Kerveno, N. Nankov, A. Olacel, A. J. M. Plompen, and C. Rouki, "Cross-section measurements for the ^{57}Fe$(n,n\gamma)^{57}$Fe and ^{57}Fe$(n,2n\gamma)^{56}$Fe reactions," *Phys. Rev. C*, vol. 96, p. 024620, 2017.

[41] K. Tsukada, S. Tanaka, Y. Tomita, and M. Maruyama, "Elastic and inelastic scattering of fast neutrons from iron, nickel and tungsten," *Nuclear Physics A*, vol. 125, no. 3, pp. 641–653, 1969.

[42] E. Ramström, "A Systematic Study of Neutron Inelastic Scattering in the Energy Range from 2.0 MeV to 4.5 MeV," *Aktiebolaget Atomenergi,Stockholm/Studsvik Repts No.503*, 1975.

[43] A. Mittler, J. Nardini, and G. P. Couchell, "Measurements of neutron inelastic scattering cross sections for natural iron," *Data from CSISRS File, Accession*, no. 80257, 1975.

[44] P. H. Stelson and W. M. Preston, "The Inelastic Scattering of Fast Neutrons from Iron," *Phys. Rev.*, vol. 86, pp. 132–133, 1952.

[45] J. B. Weddell and B. Jennings, "SCATTERING OF 4.4-MEV NEUTRONS BY CR AND MO, AND OF 6.5-MEV NEUTRONS BY FE," *Private Communication*, 1956.

[46] L. Cranberg and J. S. Levin, "Neutron Scattering at 2.45 Mev by a Time-of-Flight Method," *Phys. Rev.*, vol. 103, pp. 343–352, 1956.

[47] D. A. Kardashev, V. S. Stavinskii, D. L. Broder, A. L. Lashuk, and I. P. Sadokhin, "Analysis of the excitation functions of the levels of the Fe-56 nucleus in inelastic scattering of neutrons in the optical model of the nucleus," *Atomnaya Energiya*, vol. 13, p. 587, 1962.

[48] D. J. Bredin, "Scattering and Polarization of Neutrons from Al, Si, Fe, and Co at 2 MeV," *Phys. Rev.*, vol. 135, pp. B412–B416, 1964.

[49] W. Gilboy and J. Towle, "A neutron scattering study of Fe56," *Nuclear Physics*, vol. 64, no. 1, pp. 130–146, 1965.

[50] A. B. Tucker, J. T. Wells, and W. E. Meyerhof, "Inelastic Neutron Scattering Near Threshold," *Phys. Rev.*, vol. 137, pp. B1181–B1187, 1965.

[51] A. B. Smith, D. Lister, and J. F. Whalen, "Microscopic Neutron Scattering Cross-Sections for Reactor Design," *Nuclear Data For Reactors Conf., Paris*, vol. 1, p. 399, 1966.

[52] J. G. Degtjarev and V. N. Protopopov, "Excitation of Al-27,Cr-52,Fe-56 and Bi-209 low levels at inelastic scattering of 1-4 MeV neutrons," *Atomnaya Energiya*, vol. 23, p. 568, 1966.

[53] A. Barrows, R. Lamb, D. Velkley, and M. McEllistrem, "Levels of 51V and 55Mn via (n, nγ) reactions," *Nuclear Physics A*, vol. 107, no. 1, pp. 153–169, 1968.

[54] V. C. Rogers, "Spin of the 3120 - keV Level in ^{56}Fe," *Phys. Rev. C*, vol. 6, pp. 801–805, 1972.

[55] Y. Tomita, "Intermediate structure in the neutron scattering cross sections of iron," *Nuclear Physics A*, vol. 210, no. 1, pp. 51–59, 1973.

[56] S. Elbakr, I. van Heerden, B. Robertson, W. McDonald, G. Neilson, and W. Dawson, "The energy level structure of 154Sm from the (n, nγ) reaction," *Nuclear Physics A*, vol. 211, no. 3, pp. 493–508, 1973.

[57] E. S. Konobeevskii, R. M. Musaelyan, V. I. Popov, V. M. Prokopenko, and I. V. Surkova, "Inelastic Neutron Scattering by Ti and Fe Isotopes in the Energy Region Near the Threshold," *Izv. Rossiiskoi Akademii Nauk, Ser.Fiz.*, vol. 37, p. 1973, 1973.

[58] I. A. Korzh, V. A. Mishchenko, E. N. Mozhzhukhin, A. A. Golubova, N. M. Pravdivyi, I. E. Sanzhur, and M. V. Pasechnik, "Neutron scattering in energy range 1.5-3.0 MeV on the even isotopes of Cr, Ni, Zn," *USSR report to the I.N.D.C.*, vol. 4, no. 099, p. 220, 1975.

[59] L. S. Lebedev, J. A. Nemilov, A. V. Orlovskij, and L. A. Pobedonostsev, "Inelastic scattering of the 4.7MeV neutrons by Al, Mn, Fe, Ni, Cu and Pb," *USSR report to the I.N.D.C.*, no. 114, p. 3, 1977.

[60] M. Salama, "Inelastic scattering of fast neutrons from iron," *Atomkernenergie*, vol. 37, p. 221, 1981.

[61] Y. A. Nemilov, L. A. Pobedonostsev, and E. L. Teterin, "Inelastic scattering of neutrons on 56Fe nuclei," *Atomnaya Energiya*, vol. 53, p. 194, 1982.

[62] E. Pirovano, R. Beyer, M. Dietz, A. R. Junghans, S. E. Müller, R. Nolte, M. Nyman, A. J. M. Plompen, M. Röder, T. Szücs, and M. P. Takacs, "Cross section and neutron angular distribution measurements of neutron scattering on natural iron," *Phys. Rev. C*, vol. 99, p. 024601, 2019.

[63] M. B. Chadwick, M. Herman, P. Obložinský, M. E. Dunn, Y. Danon, A. C. Kahler, D. L. Smith, B. Pritychenko, G. Arbanas, R. Arcilla, R. Brewer, D. A. Brown, R. Capote, A. D. Carlson, Y. S. Cho, H. Derrien, K. Guber, G. M. Hale, S. Hoblit, S. Holloway, T. D. Johnson, T. Kawano, B. C. Kiedrowski, H. Kim, S. Kunieda, N. M. Larson, L. Leal, J. P. Lestone, R. C. Little, E. A. McCutchan, R. E. MacFarlane, M. MacInnes, C. M. Mattoon, R. D. McKnight, S. F. Mughabghab, G. P. A. Nobre, G. Palmiotti, A. Palumbo, M. T. Pigni, V. G. Pronyaev, R. O. Sayer, A. A. Sonzogni, N. C. Summers, P. Talou, I. J. Thompson, A. Trkov, R. L. Vogt, S. C. van der Marck, A. Wallner, M. C. White, D. Wiarda, and P. G. Young, "ENDF/B-VII.1 Nuclear Data for Science and Technology: Cross Sections, Covariances, Fission Product Yields and Decay Data," *Nuclear Data Sheets*, vol. 112, no. 12, pp. 2887–2996, 2011. Special Issue on ENDF/B-VII.1 Library.

[64] B. McDermott, E. Blain, N. Thompson, A. Weltz, A. Youmans, Y. Danon, D. Barry, R. Block, A. Daskalakis, B. Epping, G. Leinweber, and M. Rapp, "56Fe capture cross section experiments at the RPI LINAC Center," *EPJ Web of Conf.*, vol. 146, p. 11038, 2017.

[65] INDEN - International Nuclear Data Evaluation Network available at: `https://www-nds.iaea.org/INDEN/` date accessed: 2024.

[66] O. Iwamoto, N. Iwamoto, S. Kunieda, F. Minato, S. Nakayama, Y. Abe, K. Tsubakihara, S. Okumura, C. Ishizuka, T. Yoshida, S. Chiba, N. Otuka, J.-C. Sublet, H. Iwamoto, K. Yamamoto, Y. Nagaya, K. Tada, C. Konno, N. Matsuda, K. Yokoyama, H. Taninaka, A. Oizumi, M. Fukushima, S. Okita, G. Chiba, S. Sato, M. Ohta, and S. Kwon, "Japanese evaluated nuclear data library version 5: JENDL-5, journal = Journal of Nuclear Science and Technology," vol. 60, no. 1, pp. 1–60, 2023.

[67] W. Mondelaers and P. Schillebeeckx, "GELINA, a neutron time-of-flight facility for high resolution neutron data measurements," *Notiziatio Neutroni e Luce di Sincratone*, vol. 11, p. 19, 2006.

[68] A. Bensussan and J. Salome, "GELINA: A modern accelerator for high resolution neutron time of flight experiments," *Nuclear Instruments and Methods*, vol. 155, no. 1, pp. 11–23, 1978.

[69] D. Tronc, J. Salomé, and K. Böckhoff, "A new pulse compression system for intense relativistic electron beams," *Nuclear Instruments and Methods in Physics Research Section A: Accelerators, Spectrometers, Detectors and Associated Equipment*, vol. 228, no. 2, pp. 217–227, 1985.

[70] J. Salome and R. Cools, "Neutron producing targets at GELINA," *Nuclear Instruments and Methods*, vol. 179, no. 1, pp. 13–19, 1981.

[71] M. Flaska, A. Borella, D. Lathouwers, L. Mihailescu, W. Mondelaers, A. Plompen, H. van Dam, and T. van der Hagen, "Modeling of the GELINA neutron target using coupled electron–photon–neutron transport with the MCNP4C3 code," *Nuclear Instruments and Methods in Physics Research Section A: Accelerators, Spectrometers, Detectors and Associated Equipment*, vol. 531, no. 3, pp. 392–406, 2004.

[72] D. Ene, C. Borcea, S. Kopecky, W. Mondelaers, A. Negret, and A. Plompen, "Global characterisation of the GELINA facility for high-resolution neutron time-of-flight measurements by Monte Carlo simulations," *Nuclear Instruments and Methods in Physics Research Section A: Accelerators, Spectrometers, Detectors and Associated Equipment*, vol. 618, no. 1, pp. 54–68, 2010.

[73] Pirovano, Elisa, *Neutron scattering cross section measurements with a new scintillator array*. PhD thesis, Ghent University, 2017.

[74] E. Pirovano, R. Beyer, A. Junghans, R. Nolte, M. Nyman, and A. Plompen, "Measurements of neutron scattering angular distributions with a new scintillator setup," *EPJ Web of Conferences*, vol. 146, p. 11008, 2017.

[75] M. Nyman, T. Adam, C. Borcea, M. Boromiza, P. Dessagne, G. Henning, M. Kerveno, A. Negret, A. Olacel, E. Pirovano, *et al.*, "New equipment for neutron scattering cross-section measurements at GELINA," *EPJ Web of Conferences*, vol. 239, p. 17003, 2020.

[76] E. Dekempeneer, H. Liskien, L. Mewissen, and F. Poortmans, "A spectrometer for double-differential neutron-emission cross section measurements in the energy range 1.6 to 16 MeV," *Nuclear Instruments and Methods in Physics Research Section A: Accelerators, Spectrometers, Detectors and Associated Equipment*, vol. 256, no. 3, pp. 489–498, 1987.

[77] Eljen Technology, "EJ301, EJ309 data sheet available at `https://eljentechnology.com/products/liquid-scintillators/ej-301-ej-309`," date accessed: 2024.

[78] Eljen Technology, "EJ315 data sheet available at `https://eljentechnology.com/products/liquid-scintillators/ej-315`," date accessed: 2024.

[79] G. Dietze and H. Klein, "Gamma-calibration of NE 213 scintillation counters," *Nuclear Instruments and Methods in Physics Research*, vol. 193, no. 3, pp. 549–556, 1982.

[80] A. Tomanin, J. Paepen, P. Schillebeeckx, R. Wynants, R. Nolte, and A. Lavietes, "Characterization of a cubic EJ-309 liquid scintillator detector," *Nuclear Instruments and Methods in Physics Research Section A: Accelerators, Spectrometers, Detectors and Associated Equipment*, vol. 756, pp. 45–54, 2014.

[81] H. Klein and S. Neumann, "Neutron and photon spectrometry with liquid scintillation detectors in mixed fields," *Nuclear Instruments and Methods in Physics Research Section A: Accelerators, Spectrometers, Detectors and Associated Equipment*, vol. 476, no. 1, pp. 132–142, 2002. Int. Workshop on Neutron Field Spectrometry in Science, Technology and Radiation Protection.

[82] N. Kornilov, I. Fabry, S. Oberstedt, and F.-J. Hambsch, "Total characterization of neutron detectors with a ^{252}Cf source and a new light output determination," *Nuclear Instruments and Methods in Physics Research Section A: Accelerators, Spectrometers, Detectors and Associated Equipment*, vol. 599, no. 2, pp. 226–233, 2009.

[83] H. Klein, "Neutron spectrometry in mixed fields: NE213/BC501A liquid scintillation spectrometers," *Radiation Protection Dosimetry*, vol. 107, no. 1-3, pp. 95–109, 2003.

[84] J. Birks, "The Theory and Practice of Scintillation Counting," *International Series of Monographs in Electronics and Instrumentation, Pergamon*, 1964.

[85] D. Gedcke and W. McDonald, "A constant fraction of pulse height trigger for optimum time resolution," *Nuclear Instruments and Methods*, vol. 55, pp. 377–380, 1967.

[86] L. Bardelli, G. Poggi, M. Bini, G. Pasquali, and N. Taccetti, "Time measurements by means of digital sampling techniques: a study case of 100ps FWHM time resolution with a 100MSample/s, 12bit digitizer," *Nuclear Instruments and Methods in Physics Research Section A: Accelerators, Spectrometers, Detectors and Associated Equipment*, vol. 521, no. 2, pp. 480–492, 2004.

[87] M. A. Nelson, B. D. Rooney, D. R. Dinwiddie, and G. S. Brunson, "Analysis of digital timing methods with BaF2 scintillators," *Nuclear Instruments and Methods in Physics Research Section A: Accelerators, Spectrometers, Detectors and Associated Equipment*, vol. 505, no. 1, pp. 324–327, 2003. Proceedings of the tenth Symposium on Radiation Measurements and Applications.

[88] V. Modamio, J. Valiente-Dobón, G. Jaworski, T. Hüyük, A. Triossi, J. Egea, A. Di Nitto, P.-A. Söderström, J. Agramunt Ros, G. de Angelis, G. de France, M. Erduran, S. Ertürk, A. Gadea, V. González, J. Kownacki, M. Moszynski, J. Nyberg, M. Palacz, E. Sanchis, and R. Wadsworth, "Digital pulse-timing technique for the neutron detector array NEDA,"

Nuclear Instruments and Methods in Physics Research Section A: Accelerators, Spectrometers, Detectors and Associated Equipment, vol. 775, pp. 71–76, 2015.

[89] I. Pawełczak, S. Ouedraogo, A. Glenn, R. Wurtz, and L. Nakae, "Studies of neutron–γ pulse shape discrimination in EJ-309 liquid scintillator using charge integration method," *Nuclear Instruments and Methods in Physics Research Section A: Accelerators, Spectrometers, Detectors and Associated Equipment*, vol. 711, pp. 21–26, 2013.

[90] F. Brooks, "A scintillation counter with neutron and gamma-ray discriminators," *Nuclear Instruments and Methods*, vol. 4, no. 3, pp. 151–163, 1959.

[91] J. Polack, M. Flaska, A. Enqvist, C. Sosa, C. Lawrence, and S. Pozzi, "An algorithm for charge-integration, pulse-shape discrimination and estimation of neutron/photon misclassification in organic scintillators," *Nuclear Instruments and Methods in Physics Research Section A: Accelerators, Spectrometers, Detectors and Associated Equipment*, vol. 795, pp. 253–267, 2015.

[92] P. Sparrman, J. Lindskog, and A. Marelius, "An electron scintillation detector with good energy resolution," *Nuclear Instruments and Methods*, vol. 41, no. 2, pp. 299–304, 1966.

[93] H. Schölermann and H. Klein, "Optimizing the energy resolution of scintillation counters at high energies," *Nuclear Instruments and Methods*, vol. 169, no. 1, pp. 25–31, 1980.

[94] R. Batchelor, W. Gilboy, J. Parker, and J. Towle, "The response of organic scintillators to fast neutrons," *Nuclear Instruments and Methods*, vol. 13, pp. 70–82, 1961.

[95] R. Craun and D. Smith, "Analysis of response data for several organic scintillators," *Nuclear Instruments and Methods*, vol. 80, no. 2, pp. 239–244, 1970.

[96] S. Mouatassim, G. Costa, G. Guillaume, B. Heusch, A. Huck, and M. Moszyński, "The light yield response of NE213 organic scintillators to charged particles resulting from neutron interactions," *Nuclear Instruments and Methods in Physics Research Section A: Accelerators, Spectrometers, Detectors and Associated Equipment*, vol. 359, no. 3, pp. 530–536, 1995.

[97] D. Schmidt, B. Asselineau, R. Böttger, H. Klein, L. Lebreton, S. Neumann, R. Nolte, and G. Pichenot, "Characterization of liquid scintillation detectors," *Nuclear Instruments and Methods in Physics Research Section A: Accelerators, Spectrometers, Detectors and Associated Equipment*, vol. 476, no. 1, pp. 186–189, 2002. Int. Workshop on Neutron Field Spectrometry in Science, Technolog y and Radiation Protection.

[98] N. Hawkes, J. Adams, D. Bond, S. Croft, O. Jarvis, and N. Watkins, "Measurements of the proton light output function of the organic liquid scintillator NE213 in several detectors," *Nuclear Instruments and Methods in Physics Research Section A: Accelerators, Spectrometers, Detectors and Associated Equipment*, vol. 476, no. 1, pp. 190–194, 2002. Int. Workshop on Neutron Field Spectrometry in Science, Technolog y and Radiation Protection.

[99] G. Dietze, "Energy calibration of NE-213 scintillation counters by γ-rays," *IEEE Transactions on Nuclear Science*, vol. 26, no. 1, pp. 398–402, 1979.

[100] C. J. Werner, J. Bull, C. Solomon, F. Brown, G. McKinney, M. Rising, D. Dixon, R. Martz, H. Hughes, L. Cox, *et al.*, "MCNP6. 2 release notes," *Los Alamos National Laboratory, report LA-UR-18-20808*, 2018.

[101] C. J. Werner *et al.*, "MCNP users manual-code version 6.2," *Los Alamos national laboratory, report LA-UR-17-29981*, 2017.

[102] G. T. Wright, "Scintillation Response of Organic Phosphors," *Phys. Rev.*, vol. 91, pp. 1282–1283, 1953.

[103] C. N. Chou, "The Nature of the Saturation Effect of Fluorescent Scintillators," *Phys. Rev.*, vol. 87, pp. 904–905, 1952.

[104] W. Tornow, W. Arnold, J. Herdtweck, and G. Mertens, "Measurement of the response of the deuterated scintillators NE 232 and NE 230 to protons and deuterons," *Nuclear Instruments and Methods in Physics Research Section A: Accelerators, Spectrometers, Detectors and Associated Equipment*, vol. 244, no. 3, pp. 477–482, 1986.

[105] R. Madey, F. M. Waterman, A. R. Baldwin, J. N. Knudson, J. Carlson, and J. Rapaport, "The response of NE-228A, NE-228, NE-224, and NE-102 scintillators to protons from 2.43 to 19.55 MeV," *Nuclear Instruments and Methods*, vol. 151, no. 3, pp. 445–450, 1978.

[106] Mitutoyo, "website available at `https://www2.mitutoyo.co.jp/eng/`," date accessed: 2024.

[107] "From ENSDF database `https://www.nndc.bnl.gov/ensdf/`," date accessed: 2024.

[108] C. Budtz-Jørgensen, H. Knitter, and G. Bortels, "Assaying of targets for nuclear measurements with a gridded ionization chamber," *Nuclear Instruments and Methods in Physics Research Section A: Accelerators, Spectrometers, Detectors and Associated Equipment*, vol. 236, no. 3, pp. 630–640, 1985.

[109] A. Carlson, V. Pronyaev, R. Capote, G. Hale, Z.-P. Chen, I. Duran, F.-J. Hambsch, S. Kunieda, W. Mannhart, B. Marcinkevicius, R. Nelson, D. Neudecker, G. Noguere, M. Paris, S. Simakov, P. Schillebeeckx, D. Smith, X. Tao, A. Trkov, A. Wallner, and W. Wang, "Evaluation of the Neutron Data Standards," *Nuclear Data Sheets*, vol. 148, pp. 143–188, 2018. Special Issue on Nuclear Reaction Data.

[110] C. Y. Fu, "Evaluated Cross Sections for Neutron Scattering from Natural Carbon below 2 MeV Including R Matrix Fits to ^{13}C Resonances," *Nuclear Science and Engineering*, vol. 106, no. 4, pp. 494–500, 1990.

[111] C.Y. Fu and F.G. Perey, "Neutron scattering cross sections of carbon below 2 MeV recommended from R-matrix fits to data," *Atomic Data and Nuclear Data Tables*, vol. 22, no. 3, pp. 249–267, 1978.

[112] D.C. Dodder and G.M. Hale and K. Witte, "The Energy Dependent Analysis Code," *Los Alamos National Laboratory*, unpublished.

[113] G. Hale and P. Young, "n+^{12}C Cross Sections from an R-matrix Analysis of Reactions in the ^{13}C System," *Nuclear Data Sheets*, vol. 118, pp. 165–168, 2014.

[114] A. Ramirez, E. Peters, J. Vanhoy, S. Hicks, L. Alasagas, D. Alcorn-Dominguez, S. Block, S. Byrd, E. Chouinard, B. Combs, B. Crider, E. Derdyn, L. Downes, J. Erlanson, S. Evans, A. French, E. Garza, J. Girgis, T. Harrison, S. Henderson, T. Howard, D. Jackson, L. Kersting, A. Kumar, S. Liu, C. Lueck, E. Lyons, P. McDonough, M. McEllistrem, T. Morin, S. Mukhopadhyay, T. Nguyen, M. Nickel, S. Nigam, R. Pecha, J. Potter, F. Prados-Estévez, B. Rice, T. Ross, Z. Santonil, J. Schneiderjan, L. Sidwell, A. Sigillito, J. Steves, B. Thompson, D. Watts, Y. Xiao, and S. Yates, "Neutron elastic and inelastic scattering differential cross sections on carbon," *Nuclear Physics A*, vol. 1023, p. 122446, 2022.

[115] M. R. MacPhail, "Anomalous Scattering of Fast Neutrons," *Phys. Rev.*, vol. 57, pp. 669–676, 1940.

[116] R. N. Little, B. P. Leonard, J. T. Prud'homme, and L. D. Vincent, "Liquid Scintillator Measurements of Angular Elastic Scattering of Neutrons from Carbon, Aluminum, and Sulfur," *Phys. Rev.*, vol. 98, pp. 634–638, 1955.

[117] B. Jennings, J. Weddell, I. Alexeff, and R. L. Hellens, "Scattering of 4.4-Mev Neutrons by Iron and Carbon," *Phys. Rev.*, vol. 98, pp. 582–585, 1955.

[118] M. Walt and J. R. Beyster, "Interaction of 4.1-Mev Neutrons with Nuclei," *Phys. Rev.*, vol. 98, pp. 677–684, 1955.

[119] H. B. Willard, J. K. Bair, and J. D. Kington, "Elastic Scattering Angular Distributions of Fast Neutrons on Light Nuclei," *Phys. Rev.*, vol. 98, pp. 669–673, 1955.

[120] C. O. Muehlhause, S. D. Bloom, H. E. Wegner, and G. N. Glasoe, "Neutron Scattering from Iron and Carbon by Time-of-Flight," *Phys. Rev.*, vol. 103, pp. 720–726, 1956.

[121] J. R. Beyster, M. Walt, and E. W. Salmi, "Interaction of 1.0-, 1.77-, 2.5-, 3.25-, and 7.0-Mev Neutrons with Nuclei," *Phys. Rev.*, vol. 104, pp. 1319–1331, 1956.

[122] A. Langsdorf, R. O. Lane, and J. E. Monahan, "Angular Distributions of Scattered Neutrons," *Phys. Rev.*, vol. 107, pp. 1077–1087, 1957.

[123] J. E. Wills, J. K. Bair, H. O. Cohn, and H. B. Willard, "Scattering of Fast Neutrons from C^{12} and F^{19}," *Phys. Rev.*, vol. 109, pp. 891–897, 1958.

[124] M. Hosoe and S. Suzuki, "Gamma Rays from Neutron Inelastic Scattering of Magnesium, Aluminum, Iron and Bismuth," *Journal of the Physical Society of Japan*, vol. 14, no. 6, pp. 699–707, 1959.

[125] E. Haddad and D. D. Phillips, "Elastic and Inelastic Scattering of Neutrons from C^{12}," *Bull. Am. Phys. Soc.*, vol. 4, pp. No.6, 358, J2, 1959.

[126] N. Bostrom, I. Morgan, J. Prud'homme, P. Okhuysen, and O. Hudson, "Neutron interactions in Lithium, Carbon, Nitrogen, Aluminum, Argon, Manganese, Yttrium, Zirconium, Radiolead and Bismuth," *Wright Air Devel. Centre Reports*, pp. 59–107, 1959.

[127] R. Lane, A. Langsdorf, J. Monahan, and A. Elwyn, "The angular distributions of neutrons scattered from various nuclei," *Annals of Physics*, vol. 12, no. 2, pp. 135–171, 1961.

[128] R. O. Lane, R. D. Koshel, and J. E. Monahan, "Polarization and Differential Cross Section for Neutrons Scattered from ^{12}C," *Phys. Rev.*, vol. 188, pp. 1618–1625, 1969.

[129] F. G. Perey and W. E. Kinney, "Carbon neutron elastic-and inelastic-scattering cross sections from 4.5 to 8.5 MeV," *Oak Ridge National Lab. Reports,*, vol. No.4441, 1969.

[130] N. Ahmed, M. Coppola, and H. H. Knitter, "Measurements of neutron elastic scattering from carbon in the energy region of 0.50 to 2.00 MeV," *Nuclear Data for Reactors Conf.*, vol. 1, p. 177, 1970.

[131] F. D. McDaniel, M. W. McDonald, M. F. Steuer, and R. M. Wood, "Spin-Flip Probability in the Inelastic Scattering of 7.48-MeV Neutrons from the 4.43-MeV State of ^{12}C," *Phys. Rev. C*, vol. 6, pp. 1181–1191, 1972.

[132] W. Galati, J. D. Brandenberger, and J. L. Weil, "Scattering of Neutrons by Carbon from 3 to 7 MeV," *Phys. Rev. C*, vol. 5, pp. 1508–1529, 1972.

[133] H. Knox, J. Cox, R. Finlay, and R. Lane, "Differential cross section and polarization for 2.63 MeV neutrons scattered from 12C," *Nuclear Physics A*, vol. 217, no. 3, pp. 611–627, 1973.

[134] D. E. Velkley, J. D. Brandenberger, D. W. Glasgow, M. T. McEllistrem, J. C. Manthuruthil, and C. P. Poirier, "Scattering of Neutrons by Carbon from 7 to 9 MeV," *Phys. Rev. C*, vol. 7, pp. 1736–1742, 1973.

[135] C. E. Hollandsworth, W. P. Bucher, J. Youngblood, and A. Niiler, "Cross Sections for Forward-Angle Elastic Scattering of 7.55 MeV Neutrons- A survey," *Ballistic Research Labs Reports*, vol. No.1764, 1975.

[136] F. G. Perey and W. E. Kinney, "Elastic and inelastic scattering cross sections in the energy range 5.2 - 8.7 MeV," *U.S.AEC Nucl. Cross Sections Advisory Comm. Repts,*, vol. No.42, p. 190, 1978.

[137] A. Smith, R. Holt, and J. Whalen, "Neutron Interaction with Carbon-12 in the Few-MeV Region," *Nuclear Science and Engineering*, vol. 70, no. 3, pp. 281–293, 1979.

[138] G. Gkatis, M. Diakaki, G. Noguere, M. Nyman, A. Oprea, C. Paradela, E. Pirovano, and A. J. M. Plompen, "Cross section measurements of neutron elastic and inelastic scattering on ^{54}Fe," *Phys. Rev. C*, vol. 109, p. 034612, 2024.

[139] R. Carlton, J. Harvey, and B. Castel, "Single Particle Strength in 55Fe," *Bulletin of the American Physical Society Ser.II*, vol. 30, p. 1252, 1985.

[140] E. Cornelis, L. Mewissen, and F. Poortmans, "Neutron resonance structure of Fe-54 and Fe-56 from high resolution total cross section measurements," *Conf. on Nucl. Data for Sci. and Technol.*, p. 135, 1982.

[141] W. E. Kinney and J. W. McConnell, "High Resolution Neutron Scattering Experiments at ORELA," *Int. Conf. on Interact. of Neutr. with Nuclei*, p. 1319, 1976.

[142] C. M. Perey, F. G. Perey, J. A. Harvey, N. W. Hill, and N. M. Larson, "^{56}Fe and ^{60}Ni resonance parameters," *Conf. on Nucl. Data for Sci. and Technol.*, p. 41, 1991.

[143] A. Smith and P. Guenther, "Scattering of MeV Neutrons from Elemental Iron," *Nuclear Science and Engineering*, vol. 73, no. 2, pp. 186–195, 1980.

[144] V. Pronyaev, S. Tagesen, H. Vonach, and S. Badikov, "Improvement of the EFF-2 evaluations for 52Cr, 56Fe, 58 Ni and 60Ni," *Final Report for NET contract No. ERB 5000 CT 940031*, 1995.

[145] J. A. Harvey *Priv. Comm.*, 1987.

[146] G. Rohr, R. Shelley, and C. Nazareth, "TOTAL NEUTRON CROSS SECTION MEASUREMENT OF VANADIUM," *Priv. Comm.*, 1995.

[147] A.J. Konning and S. Hilaire and M.C. Duijvestijn, "TALYS-1.0," *EDP Sciences, Les Ulis, France*, p. 211, 2008.

[148] TALYS 1.9, "website available at `https://www-nds.iaea.org/talys/`," date accessed: 2024.

[149] R. Capote, M. Herman, P. Obložinský, P. Young, S. Goriely, T. Belgya, A. Ignatyuk, A. Koning, S. Hilaire, V. Plujko, M. Avrigeanu, O. Bersillon, M. Chadwick, T. Fukahori, Z. Ge, Y. Han, S. Kailas, J. Kopecky, V. Maslov, G. Reffo, M. Sin, E. Soukhovitskii, and P. Talou, "RIPL – Reference Input Parameter Library for Calculation of Nuclear Reactions and Nuclear Data Evaluations," *Nuclear Data Sheets*, vol. 110, no. 12, pp. 3107–3214, 2009. Special Issue on Nuclear Reaction Data.

[150] A. Gilbert and A.G.W. Cameron, "A COMPOSITE NUCLEAR-LEVEL DENSITY FORMULA WITH SHELL CORRECTIONS," *Canadian Journal of Physics*, 1972.

[151] J. Kopecky and M. Uhl, "Test of gamma-ray strength functions in nuclear reaction model calculations," *Phys. Rev. C*, vol. 41, pp. 1941–1955, 1990.

[152] S. Goriely, S. Hilaire, and A. J. Koning, "Improved microscopic nuclear level densities within the Hartree-Fock-Bogoliubov plus combinatorial method," *Phys. Rev. C*, vol. 78, p. 064307, 2008.

[153] S. Goriely, F. Tondeur, and J. Pearson, "A HARTREE–FOCK NUCLEAR MASS TABLE," *Atomic Data and Nuclear Data Tables*, vol. 77, no. 2, pp. 311–381, 2001.

[154] S. Goriely, E. Khan, and M. Samyn, "Microscopic HFB + QRPA predictions of dipole strength for astrophysics applications," *Nuclear Physics A*, vol. 739, no. 3, pp. 331–352, 2004.

[155] E. Bauge, J. P. Delaroche, and M. Girod, "Lane-consistent, semimicroscopic nucleon-nucleus optical model," *Phys. Rev. C*, vol. 63, p. 024607, 2001.

[156] S. Hilaire, M. Girod, S. Goriely, and A. J. Koning, "Temperature-dependent combinatorial level densities with the D1M Gogny force," *Phys. Rev. C*, vol. 86, p. 064317, 2012.

[157] S. Goriely, S. Hilaire, S. Péru, and K. Sieja, "Gogny-HFB+QRPA dipole strength function and its application to radiative nucleon capture cross section," *Phys. Rev. C*, vol. 98, p. 014327, 2018.

[158] V. Avrigeanu, P. E. Hodgson, and M. Avrigeanu, "Global optical potentials for emitted alpha particles," *Phys. Rev. C*, vol. 49, pp. 2136–2141, 1994.

[159] J. J. Griffin, "Statistical Model of Intermediate Structure," *Phys. Rev. Lett.*, vol. 17, pp. 478–481, 1966.

[160] C. Cline, "The Pauli exclusion principle in pre-equilibrium decay," *Nuclear Physics A*, vol. 195, no. 2, pp. 353–360, 1972.

[161] H. Hofmann, J. Richert, J. Tepel, and H. Weidenmüller, "Direct reactions and Hauser-Feshbach theory," *Annals of Physics*, vol. 90, no. 2, pp. 403–437, 1975.

[162] V. Plujko, "A New Closed-Form Thermodynamic Approach for Radiative Strength Functions," *Acta Phys. Pol. B*, vol. 31, p. 435, 2000.

[163] A. Filatenkov, "Neutron activation cross sections measured at KRI in neutron energy region 13.4 - 14.9 MeV," *USSR report to the I.N.D.C.*, no. 0460, 2016.

[164] W. Mannhart and D. Schmidt, "Measurement of neutron activation cross sections in the energy range from 8 MeV to 15 MeV," *Phys. Techn. Bundesanst., Neutronenphysik Reports*, no. 53, 2007.

[165] T. Shimizu, H. Sakane, M. Shibata, K. Kawade, and T. Nishitani, "Measurements of activation cross sections of (n,p) and (n,a) reactions with d-D neutrons in the energy range of 2.1–3.1 MeV," *Annals of Nuclear Energy*, vol. 31, no. 9, pp. 975–990, 2004.

[166] J. Meadows, D. Smith, L. Greenwood, R. Haight, Y. Ikeda, and C. Konno, "Measurement of fast-neutron activation cross sections for copper, europium, hafnium, iron, nickel, silver, terbium and titanium at 10.0 and 14.7 MeV and for the Be(d,n) thick-target spectrum," *Annals of Nuclear Energy*, vol. 23, no. 11, pp. 877–899, 1996.

[167] A. Grallert, J. Csikai, C. Buczko, and I. Shaddad, "Investigations on the systematics in (n,a) cross sections at 14.6 MeV," *IAEA Nucl. Data Section report to the I.N.D.C., No.286*, p. 131, 1993.

[168] I. Garlea, C. Miron-Garlea, H. Rosu, G. Fodor, and V. Raducu, "Integral Neutron Cross Sections Measured Around 14 MeV," *Revue Roumaine de Physique*, vol. 37, p. 19, 1992.

[169] S. K. Saraf, C. E. Brient, P. M. Egun, S. M. Grimes, V. Mishra and R. S. Pedroni, "Cross Sections and Spectra for the ^{54}Fe and ^{56}Fe (n,xp) and (n,xa) Reactions Between 8 and 15 MeV," *Nuclear Science and Engineering*, vol. 107, no. 4, pp. 365–373, 1991.

[170] J.W. Meadows, D.L. Smith, L.R. Greenwood, L.P. Geraldo, W. Mannhart, G. Boerker, and G. Mueller, "Measurements of the neutron cross section for Fe-54(n,alpha)Cr-51 between 5.3 and 14.6 MeV," *Conf. on Nucl. Data for Sci. and Technol.*, p. 288, 1991.

[171] A. Ercan, M.N. Erduran, M. Subasi, E. Gueltekin, G. Tarcan, A. Baykal, and M. Bostan, "14.6 MeV neutron induced reaction cross section measurements," *Conf. on Nucl. Data for Sci. and Technol.*, p. 376, 1991.

[172] G. P. M. Viennot, M. Berrada and S. Joly, "Cross-Section Measurements of (n,p) and (n,np + pn + d) Reactions for Some Titanium, Chromium, Iron, Cobalt, Nickel, and Zinc Isotopes around 14 MeV," *Nuclear Science and Engineering*, vol. 108, no. 3, pp. 289–301, 1991.

[173] I. Kimura and K. Kobayashi, "Calibrated Fission and Fusion Neutron Fields at the Kyoto University Reactor," *Nuclear Science and Engineering*, vol. 106, no. 3, pp. 332–344, 1990.

[174] Y. Ikeda, C. Konno, K. Kosako, and K. Oishi, "Activation cross section measurement at a neutron energy range from 2.1 to 3.0 MeV by d-d neutron source at FNS," *Japanese report to NEANDC*, no. 155, p. 11, 1990.

[175] L.R. Greenwood, "Recent research in neutron dosimetry and damage analysis for materials irradiations," *American Soc. of Testing and Materials Reports*, no. 956, p. 743, 1987.

[176] B.M. Bahal, and R. Pepelnik, "Cross section measurements of Cr, Mn, Fe, Co, Ni for an accurate determination of these elements in natural and synthetic samples using a 14 MeV neutron generator," *Ges.Kernen.-Verwertung, Schiffbau and Schiffahrt*, no. 85-E-11, 1985.

[177] F. Peiguo, Z. Wenrong, T. Dan, and L. Hanlin, "Measurements of Cross Sections for Some Reactions Induced by 8.62 MeV Neutrons," *Chinese J. of Nuclear Physics*, vol. 7, p. 242, 1985.

[178] I. Garlea, C. Miron-Garlea, H.N. Rosu, M. Ion, and V. Raducu, "Neutron cross sections measured at 14.8 MeV," *Zentralinst. f. Kernforschung Rossendorf Reports*, no. 562, p. 126, 1985.

[179] O.I. Artem'ev, I.V. Kazachevskii, V.N. Levkovskii, V.L. Poznyak, and V.F. Reutov, "Cross sections for (n,p) and (n,alpha) reactions on chromium, iron, copper, and molybdenum nuclei at a neutron energy of 14.8 MeV," *Soviet Atomic Energy*, vol. 49, p. 655, 1980.

[180] A. Paulsen, R. Widera, F. Arnotte and H. Liskien, "Cross Sections for the Reactions 54Fe(n,a)51Cr, 54Fe(n,p)54Mn, and 56Fe(n,p)56Mn," *Nuclear Science and Engineering*, vol. 72, no. 1, pp. 113–116, 1979.

[181] K. Fukuda, K. Matsuo, S. Shirahama, and I. Kumabe, "Activation cross sections on Fe, Co, Ni, Zr and Mo for 14.6 MeV neutrons," *Japanese report to NEANDC*, no. 56, p. 44, 1978.

[182] Chi-Fong Ai, Mien-Win Wu, and Jen-Chang Chou, "Measurements of Al-27(n,p)Mg-27 and Fe-54(n,p)Mn-54 cross sections," *Nuclear Science*, vol. 14, p. 1, 1977.

[183] D. L. Smith and J. W. Meadows, "Cross-Section Measurement of (n,p) Reactions for ^{27}Al, ^{46,47,48}Ti, ^{54,56}Fe, ^{58}Ni, ^{59}Co, and ^{64}Zn from Near Threshold to 10 MeV," *Nuclear Science and Engineering*, vol. 58, no. 3, pp. 314–320, 1975.

[184] J.J. Singh, "Neutron Reaction Cross Sections of Iron at 14.5 MeV," *Transactions of the American Nuclear Society*, vol. 15, p. 147, 1972.

[185] A. Paulsen, and R. Widera, "Ni-58(N,P)Co-58 and Fe-54(N,P)Mn-54 cross-section measurements for use as threshold detectors," *Chemical Nucl. Data Conf.*, p. 129, 1971.

[186] S.M. Qaim, R. Woelfle, and G. Stoecklin, "Activation cross sections of fast neutron induced nuclear reactions: precision measurements and systematics," *Chemical Nucl. Data Conf.*, p. 121, 1971.

[187] R.C. Barrall, J.A. Holmes, and M. Silbergeld, "High energy neutron cross section validation and neutron flux spectrum using the HENRE source," *Air Force Spec. Weap. Center Kirtland A.F.B. Repts.*, no. 68, p. 134, 1969.

[188] R.C. Barrall and M. Silbergeld and D.G. Gardner, "Cross sections of some reactions of Al, S, Mn, Fe, Ni, In and I with 14.8 MeV neutrons," *Nuclear Physics A*, vol. 138, no. 2, pp. 387–391, 1969.

[189] Rao, P. Venugopala and Fink, R. W., "Neutron Reaction Cross Sections of Selenium and Iron at 14.4 MeV," *Phys. Rev.*, vol. 154, pp. 1023–1028, 1967.

[190] E. E. Carroll and G. G. Smith, "Iron-54(n,p) Cross-Section Measurement," *Nuclear Science and Engineering*, vol. 22, no. 4, pp. 411–415, 1965.

[191] S. R. Salisbury and R. A. Chalmers, "^{54}Fe(n,p), (n,a), (n,2n) Cross Sections," *Phys. Rev.*, vol. 140, pp. B305–B310, 1965.

[192] A. Lauber and S. G. Malmskog, "Measurements of the ^{54}Fe(n,p)^{54}Mn reaction cross section in the neutron energy range 2.3–3.8 MeV," *Nuclear Physics*, vol. 73, no. 1, pp. 234–240, 1965.

[193] W.G. Cross, and H.L. Pai, "Activation cross sections in Ti for 14.5 MeV neutrons," *Canadian report to EANDC*, no. 16, p. 1, 1963.

[194] H. Pollehn and H. Neuert, "Bestimmung von Wirkungsquerschnitten einiger Kernreaktionen durch 14 MeV-Neutronen nach einer Aktivierungsmethode," *Zeitschrift für Naturforschung A*, vol. 16, no. 3, pp. 227–231, 1961.

[195] J. Van Loef, "Activation cross sections for (n,p) reactions in some medium-weight nuclei with D+D neutrons," *Nuclear Physics*, vol. 24, no. 2, pp. 340–345, 1961.

[196] D. Allan, "The energy and angular distribution of protons from 14 MeV neutron reactions with Fe54," *Nuclear Physics*, vol. 10, pp. 348–359, 1959.

[197] H. Bai, H. Jiang, Y. Lu, Z. Cui, J. Chen, G. Zhang, Y. M. Gledenov, M. V. Sedysheva, G. Khuukhenkhuu, X. Ruan, H. Huang, J. Ren, and Q. Fan, "^{56,54}Fe$(n,\alpha)^{53,51}$Cr cross sections in the MeV region," *Phys. Rev. C*, vol. 99, p. 024619, 2019.

[198] T. Khromyleva, I. Bondarenko, A. Gurbich, V. Ketlerov, V. Khryachkov and P. Prusachenko, "Investigation of (n,a) Reaction Cross Sections for a Number of Structural Material Isotopes," *Nuclear Science and Engineering*, vol. 191, no. 3, pp. 282–290, 2018.

[199] Wang, Zhimin and Fan, Xiao and Zhang, Luyu and Bai, Huaiyong and Chen, Jinxiang and Zhang, Guohui and Gledenov, Yu. M. and Sedysheva, M. V. and Krupa, L. and Khuukhenkhuu, G., "Cross sections of the ^{56}Fe$(n,\alpha)^{53}$Cr and ^{54}Fe$(n,\alpha)^{51}$Cr reactions in the MeV region," *Phys. Rev. C*, vol. 92, p. 044601, 2015.

[200] Yu.M. Gledenov, M.V. Sedysheva, G. Khuukhenkhuu, S. Bao, G. Tang, Z. Chen, Y. Chen, "Study of the Fast Neutron Induced (n,a) Reaction for Middle-Mass Nuclei," *Conf. on Nucl. Data for Sci. and Techn.*, vol. 1, p. 514, 1997.

[201] N.I. Molla and S.M. Qaim, "A systematic study of (n,p) reactions at 14.7 MeV," *Nuclear Physics A*, vol. 283, no. 2, pp. 269–288, 1977.

[202] G.N. Maslov, F. Nasyrov, N.F. Pashkin, "Experimental cross-sections for nuclear reactions involving neutrons with energies of about 14 MeV," *USSR report to the I.N.D.C.*, no. 42, p. 10, 1974.

[203] Y. Ikeda, C. Konno, K. Oishi, T. Nakamura, H. Miyade, K. Kawade, H. Yamamoto, and T. Katoh, "Activation cross section measurements for fusion reactor structural materials at neutron energy from 13.3 to 15.0 MeV using FNS facility," *JAERI Reports*, no. 1312, 1988.

[204] L. Hanlin, L. Jizhou, F. Peiguo, and H. Jianzhou, "Measurements of Cross Sections of Reactions (n,p) and (n,a) for ^{54}Fe, ^{181}Ta," *Chinese J. of Nuclear Physics*, vol. 4, p. 272, 1982.

[205] M. Kostal, T. Czakoj, P. Alexa, J. Šimon, M. Zmeškal, M. Schulc, A. Krechlerová, T. Peltán, F. Mravec, F. Cvachovec, V. Rypar, R. Uhlář, O. Harkut, and Z. Matěj, "Measurement of dosimetrical cross sections with 14.05 MeV neutrons from compact neutron generator," *Annals of Nuclear Energy*, vol. 191, p. 109904, 2023.

[206] A. A. Filatenkov, "Neutron activation cross sections measured at KRI in neutron energy region 13.4 - 14.9 MeV," *USSR report to the I.N.D.C.*, no. 0460, 2016.

[207] V. K. Mulik, H. Naik, S. V. Suryanarayana, S. D. Dhole, P. M. Prajapati, B. S. Shivashankar, K. C. Jagadeesan, S. V. Thakre, V. N. Bhoraskar, and A. Goswami, "Measurement of 56Fe(n, p)56Mn reaction cross-section at E n = 5.9, 9.85, 14.8 and 15.5 MeV," *J. Radioanal. Nucl. Chem.*, vol. 296, pp. 1321–1329, 2013.

[208] A. Fessler, A. J. M. Plompen, D. L. Smith, J. W. Meadows, and Y. Ikeda, "Neutron Activation Cross-Section Measurements from 16 to 20 MeV for Isotopes of F, Na, Mg, Al, Si, P, Cl, Ti, V, Mn, Fe, Nb, Sn, and Ba," *Nuclear Science and Engineering*, vol. 134, no. 2, pp. 171–200, 2000.

[209] Y. IKEDA, C. KONNO, Y. OYAMA, K. KOSAKO, K. OISHI, and H. MAEKAWA, "Absolute Measurements of Activation Cross Sections of 27Al(n, p)27Mg, Al27(n, a)24Na, 56Fe(n, p)56Mn, 90Zr(n, 2n)89m+gZr and 93Nb(n, 2n)92mNb at Energy Range of 13.3–14.9 MeV," *Journal of Nuclear Science and Technology*, vol. 30, no. 9, pp. 870–880, 1993.

[210] B. Zongyu, R. Chaofan, Y. Xiaoyun, Z. Shuping, D. Shengyao, and Y. Yiguan, "Absolute measurement of cross sections of 27Al(n,a)24Na and 56Fe(n,p)56Mn at En=14.6 MeV," *Chinese J. of Nuclear Physics*, vol. 15, 1993.

[211] M. Belgaid, M. Siad, and M. Allab, "Measurement of 14.7 MeV neutron cross sections for several isotopes," *J. Radioanal. Nucl. Chem.*, vol. 166, pp. 493–502, 1992.

[212] P. Fuga, "Study of the excitation function of 56Fe(n, p) 56Mn threshold reaction," *Nuclear Instruments and Methods in Physics Research Section A: Accelerators, Spectrometers, Detectors and Associated Equipment*, vol. 309, no. 3, pp. 500–502, 1991.

[213] J. Meadows, D. Smith, M. Bretscher, and S. Cox, "Measurement of 14.7 MeV neutron-activation cross sections for fusion," *Annals of Nuclear Energy*, vol. 14, no. 9, pp. 489–497, 1987.

[214] Z. Muyao, Z. Yongfa, W. Chuanshan, Z. Lu, C. Yitai, Z. Shuxin, Z. Shenjun, X. Kuanzhong, Z. Shenmuo, C. Xueshi, Z. Yiping, and Y. Qinguan, "Shell Effect from the Cross Section of the (n,2n) Reaction Produced by 14.6 MeV Neutron," *Chinese J. of Nuclear Physics*, vol. 9, p. 34, 1987.

[215] J. P. Gupta, H. D. Bharwaj, and R. Prasad, " Pre-equilibrium emission effect in (n, p) reaction cross-sections at 14.8 MeV," *Pramana J. of Phys.*, vol. 24, pp. 637–642, 1985.

[216] K. Kudo, "CROSS SECTION MEASUREMENTS OF 56-FE(N,P)56-MN AND 27-AL(N,A)24-NA BETWEEN 14.0 AND 19.9 MEV," *Priv. Comm.*, 1984.

[217] P. N. Ngoc, L. L. Bach, N. V. Do, T. T. Vinh, and I.Ribansky, "Neutron activation cross section for 56Fe(n,p) and 87Rb(n,2n) reactions," *Vietnam report to the I.N.D.C.*, no. 2, 1983.

[218] K. Kudo, "56Fe(n,p)56Mn Cross Section at 14.60 MeV," *Japanese report to NEANDC*, no. 83/U, 1982.

[219] P.N.Ngoc, S.Gueth, F.Deak, and A.Kiss, "Investigations of (n,p), (n,a) and (n,2n) reactions around 14 MeV," *PhD Thesis, Eotvos Lorand Univ.*, 1980.

[220] T. B. Ryves, P. Kolkowski, and K. J. Zieba, "Cross Section Measurements of 56Fe(n, p)56Mn, 63Cu(n, 2n)62Cu and 65Cu(n, 2n)64Cu between 14 and 19 MeV," *Metrologia*, vol. 14, no. 3, p. 127, 1978.

[221] L. Chi-Chou, L. Han-Lin, F. Pei-Kuo, M. Hung-Chang, and L. Yeh-Sha, "Cross section measurement for the reaction 56Fe(n,p)56Mn," *High Energy Physics and Nucl. Physics, Chinese ed.*, vol. 2, 1978.

[222] D. Sharma, M. G. Shahani, U. Y. Phadnis, and S. K. Sadavarte, "Absolute measurements of Fe-56(n,p)Mn-56 cross-section at 14.7 MeV using a neutron telescope," *21 Nucl. Phys. and Solid State Phys. Symp.*, vol. 2, 1978.

[223] Y. A. Nemilov and Y. N. Trofimov, "Cross-sections of (n,p) reactions in the isotopes 58Ni, 56Fe and 64Zn for neutron energies of 7.6 - 9.3 MeV," *Yaderno-Fizicheskie Issledovaniya v SSSR*, no. 26, 1978.

[224] S. L. Sothras, "A Study of the Systematics for (n,2n) Reactions," *PhD Thesis, Southern Methodist University*, 1977.

[225] K. Kudo, "Absolute measurement of the 56Fe(n,p)56Mn cross section at 14.8 MeV using an on-line monitoring system for the time variation of neutron flux," *Nuclear Instruments and Methods*, vol. 141, no. 2, pp. 325–328, 1977.

[226] Z. A. Ramendik, G. M. Stukov, and V. T. Shchebolev, "Determination of the 56Fe(n,p)56Mn Cross Section at 14.8 MeV," *Atomnaya Energiya*, vol. 42, 1977.

[227] A. B. M. G. Mostafa, "Measurements of Relative Neutron Activation Cross Sections of 27Al(n,p)27Mg, 27Al(n,a)24Na, 24Mg(n,p)24Na and 56Fe(n,p)56Mn Reactions in the Energy Range of 4.5 to 8.35 MeV," *Nuclear Science and Applications B*, vol. 9, 1976.

[228] R. Spangler, E. L. D. Jr, and T. A. Parish, "14-MeV cross section measurements of threshold reactions for seven metals," *Transactions of the American Nuclear Society*, vol. 22, 1975.

[229] J. C. Robertson, B. N. Audric, and P. Kolkowski, "The 56Fe(n, p)56Mn and 27Al(n, a)24Na cross sections at 14·78 MeV," *Journal of Nuclear Energy*, vol. 27, no. 3, pp. 139–149, 1973.

[230] N. C. Dyer and J. H. Hamilton, "56Fe and 58Fe(n, p) cross sections for 14·4 MeV neutrons," *Journal of Inorganic and Nuclear Chemistry*, vol. 34, no. 4, pp. 1119–1120, 1972.

[231] V. Levkovsky, G. E. Kovelskaya, G. P. Vinitskaya, V. M. Stepanov, and V. V. Sokolsky, "Cross Sections of the (n,p) and (n,a) Reactions at 14.8 MeV," *Soviet Journal of Nuclear Physics*, vol. 8, 1969.

[232] H. K. Vonach, W. G. Vonach, H. Muenzer, and P. Schramel, "Precision measurements of excitation functions of (n,p),(n,alpha) and (n,2n) reactions induced by 13.5 - 14.7 MeV neutrons," *Nuclear Cross-Sections Techn. Conf.*, vol. 2, 1968.

[233] P. Cuzzocrea, E. Perillo, and S. Notarrigo, "Some excitation functions of neutron-induced reactions around 14 MeV," *Il Nuovo Cimento B*, vol. 54, pp. 53–60, 1968.

[234] J. A. Grundl, "A Study of Fission-Neutron Spectra with High-Energy Activation Detectors—Part I. Detector Development and Excitation Measurements," *Nuclear Science and Engineering*, vol. 30, no. 1, pp. 39–53, 1967.

[235] H. Liskien and A. Paulsen, "CROSS SECTIONS FOR THE CU63(N,A)CO60, NI60(N,P)CO60 AND SOME OTHER THRESHOLD REACTIONS USING NEUTRONS FROM THE BE9(A,N)C12 REACTION," *Nukleonik*, vol. 8, p. 315, 1966.

[236] J. D. Hemingway, R. H. James, E. B. M. Martin, and G. R. Martin, "The determination of the cross sections for the reactions 27Al(n, a) and 56Fe(n, p) for 14 MeV neutrons by an absolute method," *Royal Society*, vol. 292, 1966.

[237] H. Liskien and A. Paulsen, "Cross-section measurement for the threshold reactions 56Fe (n, p) 56Mn, 59Co (n, a) 56Mn and 63Cu (n, 2n) 62Cu between 12·6 and 19·6 MeV neutron energy," *Journal of Nuclear Energy. Parts A/B. Reactor Science and Technology*, vol. 19, no. 2, pp. 73–80, 1965.

[238] M. Bormann, E. Fretwurst, P. Schehka, G. Wrege, H. Büttner, A. Lindner, and H. Meldner, "Some excitation functions of neutron induced reactions in the energy range 12.6–19.6 MeV," *Nuclear Physics*, vol. 63, no. 3, pp. 438–448, 1965.

[239] D. C. Santry and J. P. Butler, "EXCITATION CURVES FOR THE REACTIONS Fe56(n, p)Mn56 AND Co59(n, a)Mn56," *Canadian Journal of Physics*, vol. 42, no. 6, 1964.

[240] G. Bonazzola, P. Brovetto, E. Chiavassa, R. Spinoglio, and A. Pasquarelli, "The measurement by activation of cross sections for 14.7 MeV neutrons," *Nuclear Physics*, vol. 51, pp. 337–344, 1964.

[241] W. G. Cross and H. L. Pai, "Activation cross sections in Ti for 14.5 MeV neutrons," *Canadian report to EANDC*, no. 16, 1963.

[242] F. Gabbard and B. D. Kern, "Cross Sections for Charged Particle Reactions Induced in Medium Weight Nuclei by Neutrons in the Energy Range 12-18 MeV," *Phys. Rev.*, vol. 128, pp. 1276–1281, 1962.

[243] M. Bormann, S. Cierjacks, R. Langkau, and H. Neuert, "Über die Wirkungsquerschnitte einigern, n a-Reaktionen für Neutronenenergien zwischen 12 und 19 MeV," *Zeitschrift für Physik*, vol. 166, 1962.

[244] D. M. Chittenden, D. G. Gardner, and R. W. Fink, "New Isotope of Manganese; Cross Sections of the Iron Isotopes for 14.8-Mev Neutrons," *Phys. Rev.*, vol. 122, pp. 860–861, 1961.

[245] M. J. Depraz, G. Legros, and M. R. Salin, "Mesure des sections efficaces de quelques réactions (n, p), (n, a), (n, 2n)," *J. Phys. Radium*, vol. 21, no. 5, pp. 377–379, 1960.

[246] B. Kern, W. Thompson, and J. Ferguson, "Cross sections for some (n, p) and (n, a) reactions," *Nuclear Physics*, vol. 10, pp. 226–234, 1959.

[247] J. Terrell and D. M. Holm, "Excitation Function for $Fe^{56}(n,p)Mn^{56}$," *Phys. Rev.*, vol. 109, pp. 2031–2035, 1958.

[248] S. Yasumi, "Nuclear Reactions induced by the 14 MeV Neutrons," *Journal of the Physical Society of Japan*, vol. 12, no. 5, pp. 443–453, 1957.

[249] D. L. Allan, "Protons from the Interaction of 14 MeV Neutrons with Medium Weight Nuclei," *Proceedings of the Physical Society. Section A*, vol. 70, no. 3, p. 195, 1957.

[250] G. W. Mcclure and D. W. Kent, "Inelastic scattering of 14 MeV neutrons," *Journal of the Franklin Institute*, vol. 260, 1955.

[251] E. B. Paul and R. L. Clarke, "CROSS-SECTION MEASUREMENTS OF REACTIONS INDUCED BY NEUTRONS OF 14.5 MEV. ENERGY," *Canadian Journal of Physics*, vol. 31, no. 2, 1953.

[252] S. G. Forbes, "Activation Cross Sections for 14-Mev Neutrons," *Phys. Rev.*, vol. 88, pp. 1309–1311, 1952.

[253] Z. Wang, X. Fan, L. Zhang, H. Bai, J. Chen, G. Zhang, Y. M. Gledenov, M. V. Sedysheva, L. Krupa, and G. Khuukhenkhuu, "Cross sections of the ^{56}Fe$(n, \alpha)^{53}$Cr and ^{54}Fe$(n, \alpha)^{51}$Cr reactions in the MeV region," *Phys. Rev. C*, vol. 92, p. 044601, 2015.

[254] H. Bai, H. Jiang, Y. Lu, Z. Cui, J. Chen, G. Zhang, Y. M. Gledenov, M. V. Sedysheva, G. Khuukhenkhuu, X. Ruan, H. Huang, J. Ren, and Q. Fan, "^{56,54}Fe$(n,\alpha)^{53,51}$Cr cross sections in the MeV region," *Phys. Rev. C*, vol. 99, p. 024619, 2019.

[255] A. Trkov, P. Griffin, S. Simakov, L. Greenwood, K. Zolotarev, R. Capote, D. Aldama, V. Chechev, C. Destouches, A. Kahler, C. Konno, M. Koštál, M. Majerle, E. Malambu, M. Ohta, V. Pronyaev, V. Radulović, S. Sato, M. Schulc, E. Šimečková, I. Vavtar, J. Wagemans, M. White, and H. Yashima, "IRDFF-II: A New Neutron Metrology Library," *Nuclear Data Sheets*, vol. 163, pp. 1–108, 2020.

[256] S. Kopecky, I. Ivanov, M. Moxon, P. Schillebeeckx, P. Siegler, and I. Sirakov, "The total cross section and resonance parameters for the 0.178eV resonance of 113Cd," *Nuclear Instruments and Methods in Physics Research Section B: Beam Interactions with Materials and Atoms*, vol. 267, no. 14, pp. 2345–2350, 2009.

[257] P. Schillebeeckx, B. Becker, Y. Danon, K. Guber, H. Harada, J. Heyse, A. Junghans, S. Kopecky, C. Massimi, M. Moxon, N. Otuka, I. Sirakov, and K. Volev, "Determination of Resonance Parameters and their Covariances from Neutron Induced Reaction Cross Section Data," *Nuclear Data Sheets*, vol. 113, no. 12, pp. 3054–3100, 2012. Special Issue on Nuclear Reaction Data.

[258] I. Sirakov, B. Becker, R. Capote, E. Dupont, S. Kopecky, C. Massimi, and P. Schillebeeckx, "Results of total cross section measurements for 197Au in the neutron energy region from 4 to 108 keV at GELINA," *Eur. Phys. J. A*, vol. 49, no. 11, p. 144, 2013.

[259] G. Noguere, "Measurements and Analysis of the ^{127}I and ^{129}I Neutron Capture and Total Cross Sections," *PhD Thesis, Université Louis Pasteur*, 2005.

[260] P. Schillebeeckx, "Neutron Resonance Experiments," presented at the 4th Summer School on Neutron Detectors and Related Applications, Riva del Garda, June-July 2022.

[261] H. Derrien, "Neutron Resonance Parameters of 238U and the Calculated Cross Sections from the Reich-Moore Analysis of Experimental Data in the Neutron Energy Range from 0 keV to 20 keV," *ORNL/TM-2005/241*, 2005.

[262] B. Becker, C. Bastian, F. Emiliani, F. Gunsing, J. Heyse, K. Kauwenberghs, S. Kopecky, C. Lampoudis, C. Massimi, N. Otuka, P. Schillebeeckx, and I. Sirakov, "Data reduction and uncertainty propagation of time-of-flight spectra with AGS," *Journal of Instrumentation*, vol. 7, no. 11, p. P11002, 2012.

[263] B. Becker, "AGS-Analysis of Geel Spectra User's Manual," *NEA/DB/DOC*, 2014.

[264] M. Moore, "Rate dependence of counting losses in neutron time-of-flight measurements," *Nuclear Instruments and Methods*, vol. 169, no. 1, pp. 245–247, 1980.

[265] M. C. Moxon, T. C. Ware, and C. J. Dean, "REFIT-2009: A Least-Square Program for Resonance Analysis of Neutron Transmission, Capture, Fission and Scattering Data Users' Guide for REFIT-2009-2009-10," *OECD/NEA*, 2010.

[266] N. J. Pattenden, I. T. Belcher, I. M. Blair, P. H.Bowen, G. C.Cox, P. E. Dolley, and W. R. Mcmurray, "A PRELIMINARY MEASUREMENT OF THE NEUTRON TOTAL CROSS-SECTION OF IRON FROM 24 KEV TO 1000 KEV USING THE HARWELL SYNCHRO-CYCLOTRON," *A.E.R.E. Harwell Reports*, no. 7425, 1973.

[267] J. A. Harvey and D. C. Larson *Priv. Comm.*, 1974.

[268] M. S. Pandey, J. B. Garg, J. A. Harvey, and W. M.Good, "High resolution total neutron cross-section in 54Fe and 56Fe," *Conf. on Nucl. Cross-Sect. and Techn.*, vol. 2, 1975.

[269] J. A. Harvey, F. G. Perey, and J. A. Hill, "The 56Fe 1.15 keV resonance parameters from transmission measurements at ORELA," *U.S. D.O.E. Nuclear Data Committee Reports*, no. 33, 1984.

[270] A. Lane and J. Lynn, "Theory of radiative capture in the resonance region," *Nuclear Physics*, vol. 17, pp. 563–585, 1960.

[271] J. Lynn, "The Theory of Neutron Resonance Reactions," *Oxford: Clarendon P.*, 1968.

[272] A. Mengoni, T. Otsuka, and M. Ishihara, "Direct radiative capture of p-wave neutrons," *Phys. Rev. C*, vol. 52, pp. R2334–R2338, 1995.

[273] T. Kikuchi, Y. Nagai, T. S. Suzuki, T. Shima, T. Kii, M. Igashira, A. Mengoni, and T. Otsuka, "Nonresonant direct p- and d-wave neutron capture by ^{12}C," *Phys. Rev. C*, vol. 57, pp. 2724–2730, 1998.

[274] A. Sperduto and W. W. Buechner, "Reaction Energies and Energy Levels from Proton and Deuteron Bombardment of the Iron Isotopes," *Phys. Rev.*, vol. 134, pp. B142–B163, 1964.

[275] H. Sen Gupta, A. Majumder, and E. Lin, "A study of the level structure in 57Fe from the (d, p) reaction on 56Fe," *Nuclear Physics A*, vol. 160, no. 3, pp. 529–549, 1971.

[276] J. Bjerregaard, P. Dahl, O. Hansen, and G. Sidenius, "Energy levels from (p, p'), (d, p) and (d, a) reactions on the stable isotopes between Sc45 and Ni58," *Nuclear Physics*, vol. 51, pp. 641–666, 1964.

[277] G. Gkatis, M. Diakaki, G. Noguere, and A. Mengoni, "Direct radiative capture calculations on 56Fe," *EPJ Web of Conferences*, vol. 294, p. 04002, 2024.

[278] Y. Xu and S. Goriely, "Systematic study of direct neutron capture," *Phys. Rev. C*, vol. 86, p. 045801, 2012.

[279] Y. Nagai, M. Kinoshita, M. Igashira, Y. Nobuhara, H. Makii, K. Mishima, T. Shima, and A. Mengoni, "Nonresonant p-wave direct capture and interference effect observed in the $^{16}\mathrm{O}(n,\gamma)^{17}\mathrm{O}$ reaction," *Phys. Rev. C*, vol. 102, p. 044616, Oct 2020.

[280] A. Santamarina, D. Bernard, P. Blaise, M. Coste, A. Courcelle, T. D. Huynh, C. Jouanne, P. Leconte, O. Litaize, S. Mengelle, G. Noguere, J.-M. Ruggieri, O. Serot, J. Tommasi, C. Vaglio, and J.-F. Vidal, "The JEFF-3.1.1 Nuclear Data Library," *JEFF Report*, no. 22, 2009.

[281] F. H. Frohner, "Evaluation and Analysis of Nuclear Resonance Data," *JEFF Report*, no. 18, 2000.